Flashback investigations in a premixed swirl burner by high-speed laser imaging

Vom Fachbereich Maschinenbau
an der Technischen Universität Darmstadt
zur
Erlangung des Grades eines Doktor-Ingenieurs (Dr.-Ing.)
genehmigte

D I S S E R T A T I O N

vorgelegt von

Dipl.-Ing. Christof Heeger

aus Freiburg i. Br.

Berichterstatter:	Prof. Dr. rer. nat. A. Dreizler
1. Mitberichterstatter:	Assistant Professor M. J. Tummers
2. Mitberichterstatter:	Prof. Dr.-Ing. J. Janicka
Tag der Einreichung:	1. November 2011
Tag der mündlichen Prüfung:	15. Dezember 2011

Darmstadt 2011

D 17

Contents

Nomenclature

Some variables in the following will have a double meaning which cannot be prevented if standard conventions are used. A dash (−) in the *Unit* column indicates a dimensionless variable. The Einstein summation convention is used for the indices i, j, k.

Upper-case Latin letters		**Unit**
A	pre-exponential factor	$\mathrm{m^3\ s^{-1}\ kmol^{-1}}$
A	area	$\mathrm{m^2}$
A_0	cross sectional area	$\mathrm{m^2}$
B	second constant in boundary layer log law $B = 5.2$	–
B_{12}	Einstein absorption coefficient	$\mathrm{s^{-1}}$
C_b	empirical flashback model constant [112]	–
D_α	mass diffusivity	$\mathrm{m^2\ s^{-1}}$
D_Γ	general diffusivity	$\mathrm{m^2\ s^{-1}}$
D_λ	thermal diffusivity	$\mathrm{m^2\ s^{-1}}$
E	energy	$\mathrm{J = kg\ m^2\ s^{-2}}$
$E(1/l)$	energy spectral density	$\mathrm{J/m = kg\ m\ s^{-2}}$
F_fl	overlapping spectral fraction of the fluorescence	–
G	Gibb's free energy	$\mathrm{J/kmol = kg\ m^2\ s^{-2}\ kmol^{-1}}$
H	moveable block channel height	m
I, I'	two-dimensional grayscale arrays	–
I_L	normalized spectral laser irradiance	–
L	characteristic length	m
M	magnification of an imaging system $M = l_\mathrm{pix}/\Delta x$	–
N	number density	$\mathrm{m^{-3}}$
N_a	number of active pixels	–
N_f	f-number	–
N_tot	total number	–
P	rate of production of turbulent kinetic energy	$\mathrm{W = kg\ m^2\ s^{-3}}$
P_th	thermal power	$\mathrm{W = kg\ m^2\ s^{-3}}$
$\mathfrak{R}$	universal gas constant $\mathfrak{R} = 8.314462\ \mathrm{J\ mol^{-1}\ K^{-1}}$	$\mathrm{kg\ m^2\ s^{-2}\ K^{-1} kmol^{-1}}$
R	radius of the burner nozzle	m
R_{ij}	normalized correlation coefficient	–
R_pix	pixel rate	$\mathrm{s^{-1}}$
S	swirl number	–
S_g	geometrical swirl number	–
S_I	normalized signal strength in imaging experiments	–
S_LIF	normalized signal strength in LIF measurements	–
S_Γ	source term in the general transport equation	$\mho$

T	temperature	K
V	volume	m^3
$\dot{V}$	volumetric flow rate	$m^3\ s^{-1}$
Y	mass fraction	–

Lower-case Latin letters

		Unit
a, b	real numbers	–
c_p	specific heat capacity at constant pressure	$J/K = kg\ m^2\ s^{-2}\ K^{-1}$
d	diameter	m
f	focal length	m
f_B	Boltzmann fraction	–
f_c	coherent frequency	s^{-1}
f_N	Nyquist frequency	s^{-1}
f_s	sampling frequency	s^{-1}
f_{uc}	sampling frequency for uncorrelated data	s^{-1}
g	velocity gradient at the wall	s^{-1}
g_i	gravity vector	$m\ s^{-2}$
h_s	sensible enthalpy	$J = kg\ m^2\ s^{-2}$
i, j, k	integer numbers	–
k	specific turbulent kinetic energy	$J = kg\ m^2\ s^{-2}$
$k(T)$	temperature dependent reaction rate coefficient	$m^3\ s^{-1} kmol^{-1}$
l	length or length scale	m
l_0	integral length scale	m
l_f	laminar flame thickness	m
l_{chip}	detector chip size	m
l_{FOV}	side length of a square field of view	m
l_δ	inner reaction zone thickness of a premixed flame	m
m, n	integer numbers	–
$\dot{m}$	mass flow rate	$kg\ s^{-1}$
n_x	pixel number along x direction	–
p	gage pressure	$Pa = kg\ m^{-1}\ s^{-2}$
$\dot{q}'$	heat release fluctuations	$W = kg\ m^2\ s^{-3}$
r	radial coordinate	m
s	slip (normalized velocity difference)	–
s	flame speed	$m\ s^{-1}$
s_b	flame propagation speed inside a vortex	$m\ s^{-1}$
t	time	s
t_L	laser pulse duration	s
t_{rec}	recording duration	s
u, v, w	velocity components	$m\ s^{-1}$
$\vec{u}$	velocity vector	$m\ s^{-1}$
u^+	velocity normalized by the wall friction velocity u_*	–
u_*	friction velocity	$m\ s^{-1}$
u_0	characteristic velocity based on l_0	$m\ s^{-1}$
u_0	free stream velocity	$m\ s^{-1}$
u_i	velocity component in index notation	$m\ s^{-1}$

$w_{\max}$	maximum tangential velocity	$\mathrm{m\,s^{-1}}$
x, y, z	spatial coordinates	m
x_i	spatial coordinate in index notation	m
y	coordinate normal to the bounding wall	m
y^+	wall normal coordinate y normalized by τ_w	–
y_q	quenching distance	m

Upper-case Greek letters

		Unit
Γ	general transported property	$\mho$
$\Gamma_{12,\mathrm{L}}$	integral of laser and absorption bandwidth	–
Ω	collection angle of the imaging optics	sr
Φ	equivalence ratio	–
Ψ	mole fraction	–

Lower-case Greek letters

		Unit
α	specific reacting species	–
α_1, α_2	horizontal viewing angles of Stereo-PIV config.	sr
β	tangential channel wall angle of the swirler	sr
β_1, β_2	vertical viewing angles of Stereo-PIV configuration	sr
γ_1, γ_2	Scheimpflug angles of Stereo-PIV configuration	sr
δ	boundary or shear layer thickness	m
δ_DOF	depth of field	m
ε	rate of dissipation of turbulent kinetic energy	$\mathrm{W = kg\,m^2\,s^{-3}}$
ε_r	residual of PIV data processing	–
ϑ	angle of moveable block rotation	sr
κ	von Karman constant $\kappa = 0.41$	–
λ	mean free path length between molecules	m
λ	thermal conductivity	$\mathrm{W/m\,K = kg\,m\,s^{-3}\,K^{-1}}$
μ	dynamic viscosity	$\mathrm{N\,s/m^2 = kg\,m^{-1}\,s^{-1}}$
ν	kinematic viscosity	$\mathrm{m^2\,s^{-1}}$
ξ	quantum efficiency	–
ρ	density	$\mathrm{kg\,m^{-3}}$
τ	time scale	s
τ_{ij}	viscosity stress tensor	$\mathrm{N\,/m^2 = kg\,m^{-1}\,s^{-2}}$
τ_pro	process time scale	s
τ_u	flow time scale	s
τ_w	wall shear stress	$\mathrm{N\,/m^2 = kg\,m^{-1}\,s^{-2}}$
υ	stoichiometric coefficient	–
ϕ	fluorescence quantum yield	–
φ	arbitrary quantity	$\mho$
χ	responsivity of the detection system	–
ω	tangential velocity in cylindrical coordinates	$\mathrm{sr\,/s^{-1}}$
$\vec{\omega}$	vorticity vector	$\mathrm{sr\,/s^{-1}}$
$\dot{\omega}_\alpha$	source term of chemical reaction (mole fraction)	$\mathrm{s^{-1}}$
$\dot{\omega}_\mathrm{r}$	source term of chemical reaction (heat)	$\mathrm{W = kg\,m^2\,s^{-3}}$

Indices

0	characteristic value of the quantity
2C	quantity refers to two-component velocity data
3C	quantity refers to three-component velocity data
8	quantity refers to 8×8 interrogation area size
16	quantity refers to 16×16 interrogation area size
∞	quantity refers to a state close to infinity
a	quantity refers to activation or active
ad	quantity refers to adiabatic conditions
b	quantity refers to the burnt state
bar	quantity refers to baroclinity
c	quantity refers to the chemical reaction
crit	quantity refers to the critical state
f	quantity refers to the flame
f	quantity refers to focal length f
i	quantity refers to the inner position
l	quantity refers to laminar conditions
limit	quantity is a limiting value
m,n	integer numbers
max	maximum value of the quantity
min	minimum value of the quantity
o	quantity refers to the inner position
p	quantity refers to the particle
pix	quantity refers to the pixel
r	quantity refers to the reaction
rms	root mean square value of the quantity
st	quantity refers to stoichiometric condition
T	quantity refers to thermophoresis
u	quantity refers to the unburnt state
α	quantity refers to a specific species
Γ	quantity refers to the general transported property
η	quantity refers to the Kolmogorov scale

Definitions and Conventions

$h\nu$	energy of a photon of wavelength ν	kg m^2 s^{-2}
$\mho$	arbitrary unit	$\mho$
$[\alpha]$	concentration of the species α	kmol m^{-3}
$(\alpha_T D)_T$	diffusion coefficient of thermophoresis	m^2 s^{-1}
δ_{ij}	Kronecker delta	–
$\Delta\varphi$	difference between two values of φ	$\mho$
$\overline{\varphi}$	mean value of $\varphi = \overline{\varphi} + \varphi'$	$\mho$
φ'	fluctuating part of $\varphi = \overline{\varphi} + \varphi'$	$\mho$
$\widehat{\varphi}$	Reynolds (time) average of φ	$\mho$
$\widetilde{\varphi}$	approximate value of φ	$\mho$
$\lvert\varphi\rvert$	absolute value of φ	$\mho$
$\max(\varphi)$	maximum value of φ	$\mho$

$\nabla \times \varphi$	curl of φ	$\mho$

Dimensionless Numbers

Da	Damköhler number
Ka	Karlovitz number
Ka_δ	Karlovitz number based on the inner reaction layer
Kn	Knudsen number
Le	Lewis number
Pr	Prandtl number
Re	Reynolds number
Sc	Schmidt number

Abbreviations

2C	Two-Component
2D	Two-Dimensional
3C	Three-Component
3D	Three-Dimensional
`30iso`	Isothermal configuration corresponding to 30 kW
ADC	Analog-to-Digital Converter
AOM	Acousto-Optical Modulator
CCD	Charge-Coupled Device
CFD	Computational Fluid Dynamics
CL	Chemiluminescence
CMOS	Complementary Metal-Oxide Semiconductor
DEHS	Di-(2-Ethyl-Hexyl)-Sebacat
DNS	Direct Numerical Simulation
DPSS	Diode-Pumped Solid State
FBN	Fuel-Bond Nitrogen
HS	High Speed
IC	Internal Combustion
ICCD	Intensified Charge-Coupled Device
IRO	Intensified Relay Optics
IRZ	Internal Recirculation Zone
LDA	Laser Doppler Anemometry
LED	Light-Emitting Diode
LES	Large Eddy Simulation
LIF	Laser-Induced Fluorescence
LPP	Lean Premixed Pre-vaporized
$\mathrm{NO_x}$	Nitric Oxides (NO, $\mathrm{NO_2}$)
PIV	Particle Image Velocimetry
PLIF	Planar Laser-Induced Fluorescence
PSD	Power Spectral Density
`PSF30`	Premixed Swirl Flame at 30 kW
PTV	Particle Tracking Velocimetry
PVC	Precessing Vortex Core
RET	Rotational Energy Transfer

RMS	Root Mean Square
RQL	Rich-burn / Quick-quench / Lean-burn operation
sCMOS	Scientific grade CMOS cameras
SNR	Signal-to-Noise Ratio
UV	Ultra-Violet
VET	Vibrational Energy Transfer

1 Introduction

Energy supply is one of the primary building blocks of our society. Worldwide, and especially in rapidly developing countries, e.g. China and India, the demands of energy for housing, industry, transportation and communication are constantly increasing [83]. The global energy supply is currently dominated by combustion of fossil fuels. In 2008, 85.1% of the global primary energy supply was produced from the combustion of oil (34.6%), coal (28.4%) and natural gas (22.1%). From the 12.4% of renewable energy sources, 82% (in total 10.2%) was bioenergy based on burning renewable rescources [45]. Recent reports confirm that a dramatic shift towards CO_2 neutral energy supply is required to stop the current trend of global warming [135]. Nevertheless, the slow developement of renewable energies over the last decades as well as the absence of large technological advancements in nuclear fusion technology indicate that this structure will not substantially change in the coming decades.

Besides emissions of CO_2, further pollutants are formed during the combustion of fossil or biofuels. From these emissions, nitric oxides (NO_x) have been identified as a major problem of practical combustion processes [214]. In the recent decades nitric oxides became a significant contributor to photochemical smog and ozone in urban air [180]. It further participates in the chain reaction removing ozone form the stratosphere with the consequence of increased ultraviolet radiation reaching earth's surface [90]. NO_x is generally formed during the oxidation process of nitrogen containing fuels such as coal and oil. However, the gross NO_x emissions are created at high combustion temperatures from nitrogen in the air. These are typical for hard coal plants, internal combustion engines and gas turbines. Hence, it is essential to understand the physico-chemical processes of NO_x formation and concepts to reduce or even eliminate NO_x emissions.

1.1 Background

A significant amount of NO_x formed during a combustion process stems from the *thermal* NO production. One of the most primary techniques to prevent this formation mechanism is lean premixed combustion [211]. Thereby fuel and oxidizer are perfectly mixed prior to reaction which leads to reduced flame temperature. Application of this combustion technology to gas turbine combustors makes the flame prone to the so called *flashback* problem.

Mixing fuel and oxidizer upstream of the combustion chamber enables the flame to propagate upstream. As a result, the vital burner parts prior to the combustor can be damaged, since they are not designed for flame temperatures. Hence, flashback can be a major operational problem for aero engines, land-based gas turbines and industrial burners.

Flashback can principally occur if the flame propagation against the approaching premixed gas flow is faster than the local flow velocity ahead of the flame. Most often turbulent flows are found in practical burners. Turbulence can enhance the flame propagation speed and add complexity to the flashback problem. Further complexity is introduced if the premixed flame is stabilized by a swirl motion, which is commonly utilized to widen the operational range of

gas turbine combustors. Here, the formation of an internal recirculation zone (IRZ) is exploited which includes a region of low flow velocity and facilitates upstream transport of heat and radicals. Based on the burner type and operating conditions, several flashback mechanisms have been identified through experimental and numerical investigations. These explain the upstream propagation of a flame in a vortex or in swirl tubes.

Initially, the research on flame flashback was driven by experimental studies in laminar flames. These experiments have been extended to turbulent reactive flows, similar to those found in technical applications [12, 105]. With the advent of large computational power during the 80s, turbulent combustion research by numerical calculations (CFD: Computational Fluid Dynamics) became feasible. Over the last two decades non-stationary numerical techniques, e.g. direct numerical simulations (DNS) [153] or large eddy simulation (LES) [86], have been implemented which enabled the investigation of transient phenomena such as flashback.

Nowadays, laser-based combustion diagnostics are commonly used for experimental analysis. These techniques use light for measuring the chemical and physical properties, such as radical concentrations or velocity fields. In comparison to intrusive techniques, laser diagnostics have a negligible influence on the measured properties of the reactive flow. Pulsed laser systems allow for instantaneous measurements at single points or planar domains at acquisition rates of 10 Hz. Statistical analysis of stationary combustion is conducted by calculating means and variances. This provides information on the time-averaged and fluctuating parameters. The results can be subsequently used for modeling purposes or validation of CFD simulations. Recently, kilohertz laser systems became commercially available, but their application has not emerged into combustion diagnostics, yet.

1.2 Aim of this Work

Certain types of premixed gas turbine combustors feature a central bluff body to extend a stable combustion over a wide operational range [121]. In addition to a swirl-induced large scale central recirculation zone, a second stabilization region with low local flow velocities is generated on top of the bluff body. Flashback in these types of burners has so far not received much attention. This has resulted in the following shortcomings:

- Fundamental investigations that characterize the stability against flashback in terms of the operational parameters of Reynolds number, swirl number and equivalence ratio are rare.
- There is a lack of experimental data of the flow and flame structure within the nozzle of swirl burners in which the flame propagates upstream during flashback.
- Existing flashback mechanisms in vortical flows or in swirl tubes do not include the influence of the boundary layer in the vicinity of the bluff body wall. Hence, new mechanisms are needed to predict the onset of flashback in swirling flows in the presence of a boundary layer.

One focus of this work is the experimental investigation of flashback processes to acquire results that allow for the identification of new driving mechanisms. On the other hand, appropriate datasets have to be obtained in order to analyze the processes that happen within milliseconds. Therefore, the second goal is the development of methods to capture the individual flashback

events and to analyze the acquired data adequately. In contrast to stationary combustion, transient processes in turbulent flames, such as flashback, are unique events with an individual time history. Hence, the temporal evolution of the events needs to be assessed. The following issues in the context of measuring transient combustion events are addressed within this work:

- Attempts to capture transient phenomena by laser diagnostics are limited to oscillating systems which are quasi-stationary, e.g. reciprocating engines and thermo-acoustic instabilities. The process of interest has to exhibit distinct coherent cycles, such that phase averaging can be applied to obtain cycle-conditioned data.

- Conventional laser diagnostics encounter their limitations when turbulent transient processes under investigation occur within millisecond durations and are unpredictable in their onset. The required kilohertz acquisition rates for temporally correlated sampling of turbulent processes cannot be achieved with these systems.

- Existing data evaluation strategies for stationary turbulent flames are based on means and variances of data in a fixed coordinate systems. Phenomena that feature a transition from an initial state into a final state with an unpredictable onset cannot be adequately described with this approach.

Recent developments in camera and laser technology enable the enhancement of these conventional measurement techniques towards kilohertz sampling rates. The second focus of this thesis is on the application of these high-speed laser imaging techniques. The aim is to introduce new measurement and data evaluation concepts which provide a new perspective on turbulent flame diagnostics using temporally correlated imaging. The potential of these concepts is illustrated through applying them to the challenging problem of flame flashback. In the course of the present work, multi-parameter high-speed imaging diagnostics, such as simultaneous flow field and two-dimensional species concentration measurements, were developed and successfully applied.

1.3 Outline

The thesis is structured as follows. In Chapter 2 the physical background of flame flashback in premixed swirl burners with central bluff body will be described. A practical flame is a reacting turbulent flow. Thus, fluid dynamical fundamentals of turbulent flows and swirl flows will be summarized, and a brief introduction to boundary layers will be given. Successively, the combustion process will be detailed, with an emphasis on methane oxidation. This involves NO_x formation and premixed combustion as the most relevant aspects within the framework of this thesis. A literature review on mechanisms of flashback in premixed swirling flames completes the chapter.

A detailed description of the investigated burner is given in Chapter 3. The TECFLAM burner emerged from a previous research project to investigate swirled combustion. The specific design of the variable swirl generator as well as the applied modifications to experimentally capture the flashback inside the exit nozzle of the burner are introduced. This follows by the definition of the conditions and procedures. Finally, the infrastructure of the laser laboratory to conduct the experimental investigations under constant environmental conditions is briefly stated.

One of the major scientific contributions of this thesis is the development and application of planar high-speed multi-parameter laser diagnostics. Chapter 4 is dedicated to this new methodology. Starting with the basic concepts of the measurement techniques that were used, the extension of these techniques towards kilohertz repetition rates is discussed. The new aspects of high-speed diagnostics include general concepts, hardware and data processing techniques. These have been applied in three different experimental setups to investigate flashback, which will be detailed subsequently. The section ends with the description of the data processing of the simultaneously acquired multi-parameter data and assessing the accuracy and the precision of the measurements.

Chapter 5 presents the results of the series of measurements. The general stabilization locations of the flame inside the burner are discussed. While marking the transition from a metastable location to global flashback into the swirl generator, stability maps are generated and compared to a new flashback model in premixed swirl burners. The main section examines the temporally correlated results collected during flame upstream propagation. Velocity fields, flame structure and pressure series are discussed which result in the development of a new hypothesis for the flashback mechanism. The hypothesis is discussed and classified within the framework of flashback theory of swirling flames.

Finally, the main conclusions are summarized in Chapter 6 and an outlook for further experimental and numerical investigations will be given.

2 Fundamentals

This chapter is a survey of the current knowledge on turbulent swirled combustion and the associated phenomenon of flame flashback. It is divided into three major sections which will explain the physical background of the most relevant processes and concepts and their mathematical description. The conservation equations for reacting flows will be presented and the theory of turbulence, swirling flows and boundary layers will be introduced. The chemistry of methane oxidation, including the formation mechanism of nitric oxides and the concept of premixed combustion to reduce the NO_x emissions are presented in the following section. The final section closes this chapter with an overview of the research in the field of flashback mechanisms, which are the result of the interactions between the previously presented physicochemical processes.

2.1 Fluid Dynamics

Combustion of gaseous fuel consist of a huge number of chemical reactions in an environment that is determined by fluid mechanics. Hence, in the context of this thesis it is essential to understand the flow theory. In contrast to ordered laminar flows, practical combustion applications are dominated by highly irregular turbulent flow fields. Two reasons for this situation are pointed out by Peters [151]. Firstly, turbulence increases mixing, which in turn enhances combustion. This is of importance in the context of non-premixed flames (see Section 2.2). In premixed turbulent combustion the rate of heat release is increased through wrinkling of the flame. Secondly, fluctuations of the heat release generate flow instabilities. These instabilities in turn accelerate the transition from the laminar to the turbulent regime. Further, swirling flows can create large volumes of recirculating fluid. This is a successfully applied feature to stabilize premixed flames in a wide range of flow rates and thermal powers, as it is required in gas turbine combustors.

In practical flames, such as in the investigated burner, the reacting gaseous flow can be assumed to be a Newtonian fluid. This classification incorporates two important constraints. The word 'fluid' refers to the assumption, that gaseous flows in combustion can be treated as a continuum, although having a discrete molecular nature. The validity of this assumption is confirmed by the Knudsen number. It is defined by

$$\mathrm{Kn} = \frac{\lambda}{L} \tag{2.1}$$

where λ is the mean free path length between the molecules of the fluid and L a characteristic length scale of the flow. Hence, for $\mathrm{Kn} \ll 1$ the flow features characteristics of a continuum [155]. Furthermore, isotropic properties of the fluid are assumed. The word 'Newtonian' implies that the viscous stresses τ_{ij} on a fluid element are linearly proportional to the spatial velocity gradients

$(\partial u_j/\partial x_i)$ at its surfaces and can be mathematically described by[1]

$$\tau_{ij} = \mu \left(\frac{\partial u_j}{\partial x_i} + \frac{\partial u_i}{\partial x_j} - \frac{2}{3} \frac{\partial u_k}{\partial x_k} \delta_{ij} \right) \tag{2.2}$$

with the dynamic viscosity μ being the proportionality constant. Typical examples of Newtonian fluids are familiar gases such as air, methane, water vapor, gas mixtures and also liquids with low molecular weight [190]. Their motion can be mathematically described by the Navier-Stokes equations [155]. This is a set of second order differential equations which describe the conservation of mass and momentum. Additional conservation equations are needed to describe reacting flows. Depending on the complexity of the reaction mechanism that is modeled, the inclusion of up to several hundred equations for the conservation of the reacting species have to be considered. The associated heat release of the usually exothermic combustion reactions also demands an equation for the conservation of energy to be taken into account.

The structure of these equations is similar and they contain the same physical transport mechanisms. Thus, a general approach to describe their properties seems appropriate. The general Eulerian form of a conservation equation for a fixed Cartesian reference coordinate system is [147]

$$\frac{\partial}{\partial t}(\rho\Gamma) + \frac{\partial}{\partial x_j}(\rho u_j \Gamma) = \frac{\partial}{\partial x_j} \left(D_\Gamma \frac{\partial}{\partial x_j} \Gamma \right) + S_\Gamma. \tag{2.3}$$

The first term on the left hand side represents the local change of the product of the physical property Γ and the density ρ of an infinitesimal Cartesian element ∂x_j. For the equations of interest Γ can be a velocity component, a species concentration or even unity as we will see below. The second term describes the convective transport by the flow field. Both terms together represent the material derivative $(\mathrm{D}\Gamma/\mathrm{D}t)$ which refers to a Lagrangian perspective and expresses the change of Γ of a fluid element that moves with the flow field. In the first term on the right hand side the effect of diffusion due to spatial gradients of Γ is included with the general diffusion constant D_Γ. The last term S_Γ is called 'source' term and describes the change of Γ by sources (positive contribution) and sinks (negative contribution), in contrast to convection or diffusion, which only redistribute the property within the considered domain. In the following each equation pertinent to turbulent combustion, including the flashback phenomenon, will be briefly discussed.

CONSERVATION OF MASS. In combustion reactions no nuclear physical processes are involved and, thus, the mass of the chemically reacting system is conserved. The density ρ is the local mass per volume element. Hence, Γ is unity and the source term is zero in the general transport equation. As a consequence diffusion is also zero. Thus to describe the conservation of mass, which is also called the continuity equation, Eq. (2.3) reduces to

$$\frac{\partial \rho}{\partial t} + \frac{\partial}{\partial x_j}(\rho u_j) = 0. \tag{2.4}$$

MOMENTUM CONSERVATION. The so-called *Navier-Stokes equations* and simplifications of them are the building block of various flashback models and elementary for the understanding of the flashback mechanisms based on aerodynamics (see Section 2.3). They consist of three equations which relate the acceleration of a fluid element to the surface and body forces acting

[1] Index notation according to the *Einstein summation convention* has been used to express coordinate formulae. The reader is referred to Spurk [190]

on it. This relation is modeled via the already mentioned symmetric stress tensor τ_{ij} and normal stresses represented by pressure p. Momentum is a vector as it is defined as $\rho \cdot u_i$ with u_i being a vector of the velocity components in $\mathbb{R}^3$. The set of equations is defined as

$$\frac{\partial}{\partial t}(\rho u_i) + \frac{\partial}{\partial x_j}(\rho u_i u_j) = -\frac{\partial p}{\partial x_i} + \frac{\partial \tau_{ij}}{\partial x_j} + \rho g_i \quad \text{with} \quad i = [1,3] \tag{2.5}$$

where g_i is the gravity vector. The first term on the right hand side describes the diffusion of momentum by the viscous stress term τ_{ij} (see Eq. (2.2)). This process can be physically interpreted as diffusion of fluid particles carrying different momentum and it is proportional to the momentum diffusion coefficient μ – the viscosity of the fluid. The isotropic part of the stresses acting on a fluid element (pressure) and gravitational forces act as source terms in the conservation equation.

SPECIES MASS CONSERVATION. In contrast to the total mass of the system, described by the continuity equation (2.4), the mass of a specific reacting species α changes due to the redistribution of atoms during chemical reactions. Therefore, each species mass fraction Y_α must be described by an additional transport equation with a source term that accounts for the formation and destruction of the species. The equation for the conservation of the species mass fraction has the form

$$\frac{\partial}{\partial t}(\rho Y_\alpha) + \frac{\partial}{\partial x_j}(\rho Y_\alpha u_j) = \frac{\partial}{\partial x_j}\left(\rho D_\alpha \frac{\partial Y_\alpha}{\partial x_j}\right) + \dot{\omega}_\alpha \tag{2.6}$$

with the chemical source term $\dot{\omega}_\alpha$. Species diffusion is modeled by Fick's law, which determines the diffusion to be proportional to the concentration gradient with the species diffusion coefficient D_α. It should be noted that D_α depends on the sort of molecule, temperature and composition of the gas. These differential diffusion effects change the behavior of reacting systems. Especially for pure hydrogen combustion these effects become important, where hydrogen as a major component diffuses much faster than the rest of the reactants. However, in the context of methane-air combustion a Lewis number (see Eq. (2.11)) of unity can be assumed due to the canceling effects of the contributions from the various diffusion coefficients [36].

CONSERVATION OF ENERGY. The final transport equation accounts for the first law of thermodynamics. The purpose of a combusting flow is to transfer chemical energy into heat. In order to fulfill the conservation of energy a final equation needs to be considered. Besides using temperature T it is convenient to chose the sensible enthalpy h_s as transported property ($\Gamma = h_\mathrm{s}$), which is the sensible form of the energy and does not include the energy of formation. It is defined as

$$h_\mathrm{s} = \int_{T_0}^{T} c_p \, dT \tag{2.7}$$

where T_0 is a reference temperature and c_p is the heat capacity at constant pressure. It is appropriate to assume a low Mach number and constant volumetric forces for the system under investigation [154]. Further, the large heat release of the flame compared to external heat sources, viscous heating and additional source terms simplify the energy conservation equation. Under these assumptions and using the definition in Eq. (2.7) it becomes

$$\frac{\partial}{\partial t}(\rho h_\mathrm{s}) + \frac{\partial}{\partial x_j}(\rho h_\mathrm{s} u_j) = \frac{\partial}{\partial x_j}\left(c_p \rho D_\lambda \frac{\partial T}{\partial x_j}\right) + \dot{\omega}_\mathrm{r} \tag{2.8}$$

with the thermal diffusivity D_λ and the heat release due to combustion $\dot{\omega}_\mathrm{r}$.

Huge efforts have been undertaken to fully understand the Navier-Stokes and the additional transport equations due to their enormous relevance in all kinds of practical applications. However, there is yet no mathematical proof that a general analytical solution of the Navier-Stokes equations for given initial conditions exists and that this solution can be determined. It is one of the six remaining Millennium Prize Problems stated by the Clay Mathematics Institute in 2000[2]. The award honors any substantial development or hint towards an understanding of the Navier-Stokes existence and smoothness problem [54]. However, due to its omnipresent relevance great efforts have been spent to determine approximate solutions with numerical methods. Various recent examples can be found in [98, 100, 104].

Depending on the specific problem in hand, it is possible to simplify the set of equations due to their similar structure. An important method is to introduce dimensionless numbers that represent the ratios between the various diffusion coefficients. By introducing the kinematic viscosity $\nu = \mu/\rho$, a set of three dimensionless numbers can be defined

$$\mathrm{Pr} = \frac{\nu}{D_\lambda} = \text{momentum diffusion/thermal diffusion} \tag{2.9}$$

$$\mathrm{Sc} = \frac{\nu}{D_\alpha} = \text{momentum diffusion/species diffusion} \tag{2.10}$$

$$\mathrm{Le} = \frac{D_\lambda}{D_\alpha} = \text{thermal diffusion/species diffusion.} \tag{2.11}$$

The Prandtl, Schmidt and Lewis numbers describe the relations between the different diffusion coefficients. These, are momentum and thermal diffusion, momentum and species diffusion, and thermal and species diffusion, respectively. In combustion modeling the dimensionless numbers can be used to simplify the set of equations that have to be solved. E.g. this is utilized in the context of flamelet modeling assuming $\mathrm{Le} = 1$ [151]. The technique helps reducing the numerical costs, which is especially important in the context of LES and DNS.

2.1.1 Turbulent Flows

After the fundamental mathematical equations to describe the physics of reactive flows are introduced, this section focuses on the character of the flow. The flashback phenomena occur in a turbulent flow as present in most practical applications. This features some fundamental differences compared to laminar systems. Here, turbulence is explained according to the fundamental work of Reynolds [164], which is summarized in Pope [155]. The most important dimensionless number to characterize the general flow behavior is the Reynolds number

$$\mathrm{Re} = \frac{uL}{\nu} \tag{2.12}$$

with the characteristic velocity u, a characteristic length scale L and the kinematic viscosity ν. The Reynolds number describes the ratio between destabilizing flow momentum and stabilizing viscous forces. Starting at a relatively low Reynolds number, e.g. 100, for a given flow geometry and continuously increasing the flow velocity Osborne Reynolds in 1883 [164] observed the

[2] In 2000 the Clay Mathematics Institute (CMI) established seven Millennium Prize Problems in order to celebrate mathematics in the new millennium. Each solution of the classic questions is rewarded $1 million. Besides the Navier-Stokes existence and smoothness problem, also the Riemann hypothesis from 1859 is among the list of problems.

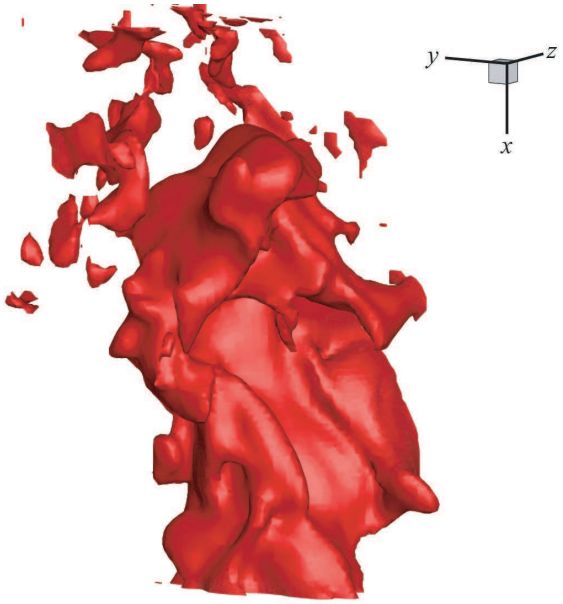

Figure 2.1: Snapshot of a turbulent flow. The isosurface of an arbitrary mixture state between two coaxial swirling flows is shown. The structure was recorded using Mie-scattering of droplets in combination with a light sheet scanning technique [213].

transition from ordered stationary laminar flows to unsteady and highly three dimensional flows with irregular flow structures. At that point the critical Reynolds number is reached and the flow is called turbulent. An example of a turbulent swirled jet is shown in Fig. 2.1. The three dimensional structures represent isosurfaces of concentration during mixing of a droplet seeded central jet with a coaxial surrounding swirled jet. A continuous range of spatial structures from large to small is visible.

The most peculiar property of the Navier-Stokes equations in the turbulent regime is their sensitivity to tiny changes in initial conditions. This circumstance results in the following characteristics for turbulent flows [155]:

- Significant and irregular variations of the velocity field in space and time
- Three dimensional flow structures
- Vortical structures of various scales
- Increased transport and fluid mixing compared to laminar flows

A deterministic prediction of the flow field $u_i(x_j,t)$ is impossible due to the random nature of turbulence. Therefore, it is appropriate to describe the flow statistically by probability distributions and the corresponding statistical moments. Hence, comparison of statistical moments is the only way of validating results of numerical calculations. However, close examination of a turbulent flow reveals a spectrum of vortical flow patterns of size l, called *eddies*. Their size can vary over a wide range from large anisotropic structures (e.g. Kelvin-Helmholtz instability, Precessing Vortex Core) determined by the geometrical scales of the domain, to small vortices that behave isotropic below a certain length scale. This concept of different length scale regimes is exploited in a variety of mathematical approaches for numerical simulations such as Large Eddy Simulation (LES). This numerical approach seems appropriate to numerically investigate

transient processes such as flashback. It is based on solving the time-dependent Navier-Stokes equations directly for the large eddies while modeling the impact of the smaller ones onto larger structures [170].

A cascaded energy transfer from the large to the smaller coherent structures is the fundamental modeling concept of turbulence. In 1922 Richardson [165] was the first to present the concept of the energy cascade shown in Fig. 2.2. The basic idea is that kinetic energy of the mean flow is transferred by a production term P into large anisotropic eddies. These eddies are characterized by the integral length scale l_0 which is in the order of the characteristic length scale L of the flow geometry. Based on l_0 the characteristic velocity of the integral length scales is given as

$$u_0 = u(l_0) \tag{2.13}$$

Hence, the specific Reynolds number of these eddies is large and can be defined as

$$\mathrm{Re}_0 = \frac{u_0 l_0}{\nu}. \tag{2.14}$$

As a consequence the large eddies are unstable due to the relatively small damping effect of viscosity compared to the momentum of the eddies and break up. Thereby they transfer their energy to smaller eddies still associated with large Reynolds numbers. Consequently, they undergo a similar break-up process. The cascaded process continues until the Reynolds number of the eddies is sufficiently small. When the molecular viscosity is large enough with respect to the momentum of the eddies the flow stabilizes. At that stage the turbulent kinetic energy is dissipated into heat. As a consequence of this linear energy transfer, the rate of dissipation ε is determined by the production term, thus $P = \varepsilon$.

To determine the sizes of the different scales l it is adequate to estimate the scaling of the production rate using the integral scales by

$$P = \varepsilon \propto \frac{u_0^2}{\tau_0} \tag{2.15}$$

which is proportional to the order of kinetic energy u_0^2 divided by characteristic timescale $\tau_0 = l_0/u_0$ of the large scale eddies. Thus, the rate of dissipation scales according to

$$\varepsilon \propto \frac{u_0^3}{l_0}. \tag{2.16}$$

This is consistent with experimental results in free shear flows (e.g. in round jets) [155]. In 1941 Kolmogorov postulated his famous theory to estimate the characteristic scales of turbulent flows. It is formulated as three hypotheses for high Reynolds number flows [108]. The first two state the following:

- Small scale eddies ($l \ll l_0$) are statistically isotropic, which means that they lost their directional memory.
- The smallest scales (Kolmogorov scales) are in equilibrium with energy transfer from larger scales and lose energy by viscous dissipation.

Consequently, the Kolmogorov scales can be uniquely described by the dissipation rate ε and the viscosity ν. They are defined in terms of length, time and velocity as

$$l_\eta = \left(\frac{\nu^3}{\varepsilon}\right)^{1/4} \qquad \tau_\eta = \left(\frac{\nu}{\varepsilon}\right)^{1/2} \qquad u_\eta = (\varepsilon\nu)^{1/4}, \tag{2.17}$$

respectively. The Reynolds number based on the Kolmogorov scales becomes unity

$$\mathrm{Re}_\eta = \frac{u_\eta l_\eta}{\nu} = 1. \tag{2.18}$$

It becomes clear that at these scales viscous forces play the dominant role and dissipate the turbulent energy into heat. From the scaling law for the rate of dissipation ε in Eq. (2.16), the ratio between large integral scales and the small dissipative scales can be expressed as a function of the Reynolds number

$$\frac{l_0}{l_\eta} \propto \mathrm{Re}^{3/4} \qquad \frac{u_0}{u_\eta} \propto \mathrm{Re}^{1/4} \qquad \frac{\tau_0}{\tau_\eta} \propto \mathrm{Re}^{1/2}. \tag{2.19}$$

Thus, high Reynolds number flows span a wide spectrum of scales. The final hypothesis states:

- In the subrange where $l_0 \gg l \gg l_\eta$ eddies are still much larger than dissipative eddies.

Therefore, eddies are not affected by viscosity and thus determined solely by the dissipation ε and eddy size l. Their velocity and time scales decrease as l decreases with a constant transfer of energy from large to small scales. For fully developed isotropic turbulence the energy cascading process can be summarized as shown in Fig. 2.2. Here, $E(1/l)$ is the energy spectral density which is the relative energy content of eddies of size l. Three ranges of different behavior can be identified. An energy-containing range where kinetic turbulent energy is produced and transferred to large eddies. This range comprises the most turbulent kinetic energy of the spectrum with its corresponding eddies potentially participating in the mechanism of flame flashback. The inertial range is characterized by the energy transport from large to small scales due to inertial forces. For the sake of completeness the slope of $-5/3$ for the transfer process is plotted. The derivation is beyond the scope of this introduction on turbulence and can be found in [155]. Finally, the dissipation range marks the part of the scale spectrum where turbulent kinetic energy is dissipated into heat. This range contains only a small fraction of turbulent kinetic energy. However, the small scale eddies can strongly influence the structure of the flame as we will see in Section 2.2.3.

A quantification of the turbulent break-up process and its scales can be determined experimentally. From Fig. 2.2 one can see that the integral length scale l_0 plays a central role as it carries the most turbulent kinetic energy. In Section 5.3.1 from the results chapter, it will become clear that large coherent structures also seem to play an important role in the mechanism of flame flashback. These structures can be determined by calculating correlations in space and time [190]. Generally, a correlation expresses the similarity of two variables. Here, the correlated variables will naturally originate from the flow field u_i. A general normalized correlation function R_{ij} of two velocity components u_i and u_j at the time t and a location x in the flow field, which are shifted in space and time by l and τ respectively, is given by

$$R_{ij}(x,t,l,\tau) = \frac{\overline{u_i(x,t)u_j(x+l,t+\tau)}}{\sqrt{\overline{u_i^2(x,t)}}\sqrt{\overline{u_j^2(x+l,t+\tau)}}} \tag{2.20}$$

where the overbar signals a mean value. For the special case $\tau = 0$ and correlating the same component of the velocity u_i Eq. (2.20) yields the spatial autocorrelation function (also called cross correlation function)

$$R_{ii}(x,t,l,0) = \frac{\overline{u_i(x,t)u_i(x+l,t)}}{\sqrt{\overline{u_i^2(x,t)}}\sqrt{\overline{u_j^2(x+l,t)}}}. \tag{2.21}$$

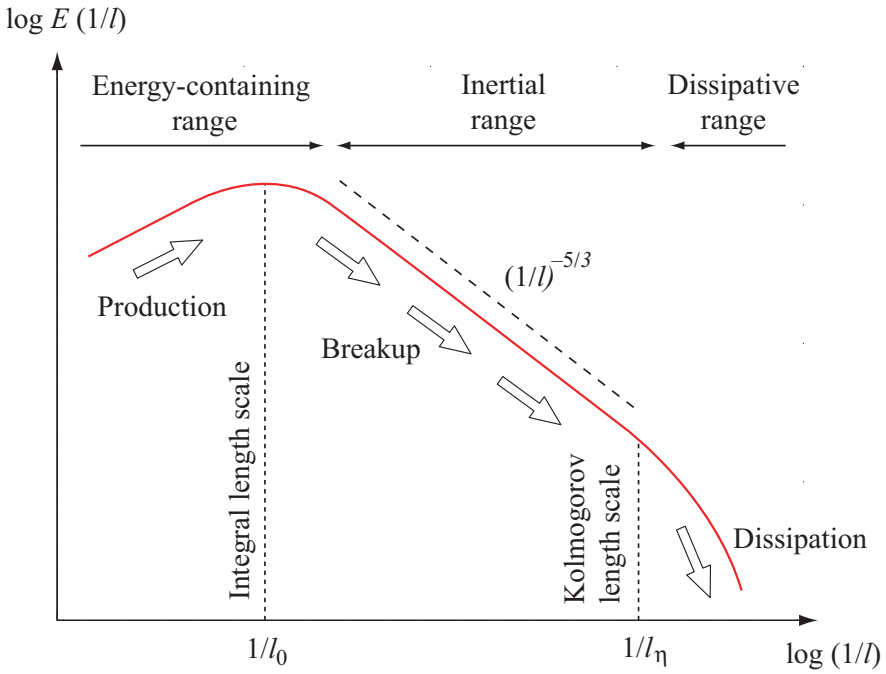

Figure 2.2: Schematic of the energy spectrum of fully developed turbulence according to Kolmogorov [155].

from which the integral length scale l_0 is calculated by

$$l_0(x) = \int_0^\infty R_{ii}(x,t,l,0)dl. \tag{2.22}$$

In analogy to the integral length scale, for $r = 0$ and identical velocity component u_i the integral time scale τ_0 can be obtained by

$$\tau_0(x) = \int_0^\infty R_{ii}(x,t,0,\tau)d\tau. \tag{2.23}$$

Note that the indices of the spatial and temporal autocorrelation coefficients have become identical, as the correlated velocity components are the same. A typical sample of a temporal autocorrelation function in homogeneous isotropic turbulence is shown in Fig. 2.3. The integral time scale is determined by the area delimited by the coordinate axes and the curve. Its value is illustrated by the vertical line at τ_0 that creates a rectangle with the coordinate axes of an area equal to τ_0.

The kinetic energy of the flow field is contained in the fluctuating part of the velocity field u_i. This can be expressed by the Reynolds decomposition

$$u_i' = u_i - \overline{u}_i, \tag{2.24}$$

with the fluctuating velocity u_i' and the temporal mean flow $\overline{u}_i$. A measure of the fluctuating part u_i' is the root mean square value $u_{i,\mathrm{rms}}'$. Hence, the turbulent Reynolds number can be defined as

$$\mathrm{Re_t} = \frac{u_{\mathrm{rms}}' l_0}{\nu}. \tag{2.25}$$

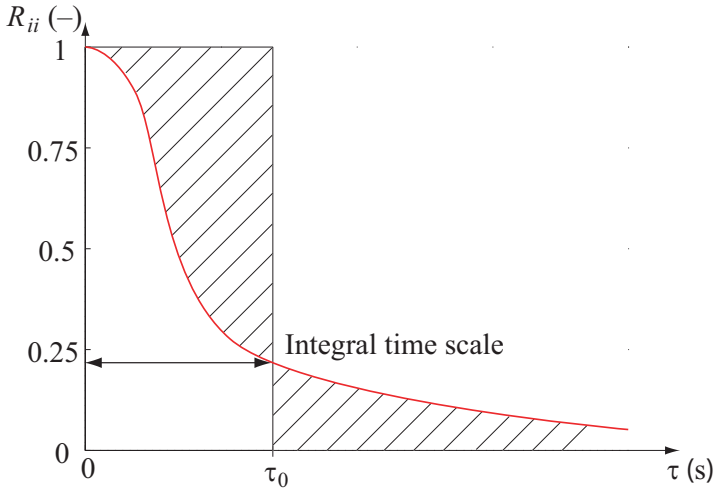

Figure 2.3: Sample of a temporal autocorrelation function R_{ii} in homogeneous isotropic turbulence

This important number expresses the ratio of the turbulent structures' inertial forces to viscous forces in contrast to the Reynolds number of the whole flow Re. Using the decomposition from Eq. 2.24 the specific turbulent kinetic energy (per unit mass) can be directly obtained by

$$k = \frac{1}{2}\overline{u_i' u_i'}. \tag{2.26}$$

Finally, the dissipation rate can be obtained by

$$\varepsilon = \frac{k^{3/2}}{l_0} \tag{2.27}$$

and the various turbulent scales can be estimated according to Eq. 2.17.

2.1.2 Swirl Flows

Swirl flows are characterized by an angular momentum, which can be created by geometrical deflection of the flow with a swirl generator or other mechanisms (e.g. Coriolis effect). The angular momentum results in a velocity component that is tangential to the main direction of the flow. It has a substantial impact on the general flow behavior and the created turbulence structures [48] which play an important role in the investigated type of flashback. Swirl flows have been studied experimentally and numerically during the last sixty years. In the articles of Lucca-Negro and O'Doherty [128] and Syred [199], a large number of publications have been summarized.

To characterize the swirl strength the swirl number S is defined as the ratio of tangential and axial momentum flux. A common definition by Gupta [70] is

$$S = \frac{\int_0^\infty \rho(\widehat{uv} + \widehat{u'v'}) r^2 \mathrm{d}r}{L \int_0^\infty \rho(\widehat{uu} + \widehat{u'u'}) + (p - p_\infty) r \mathrm{d}r}, \tag{2.28}$$

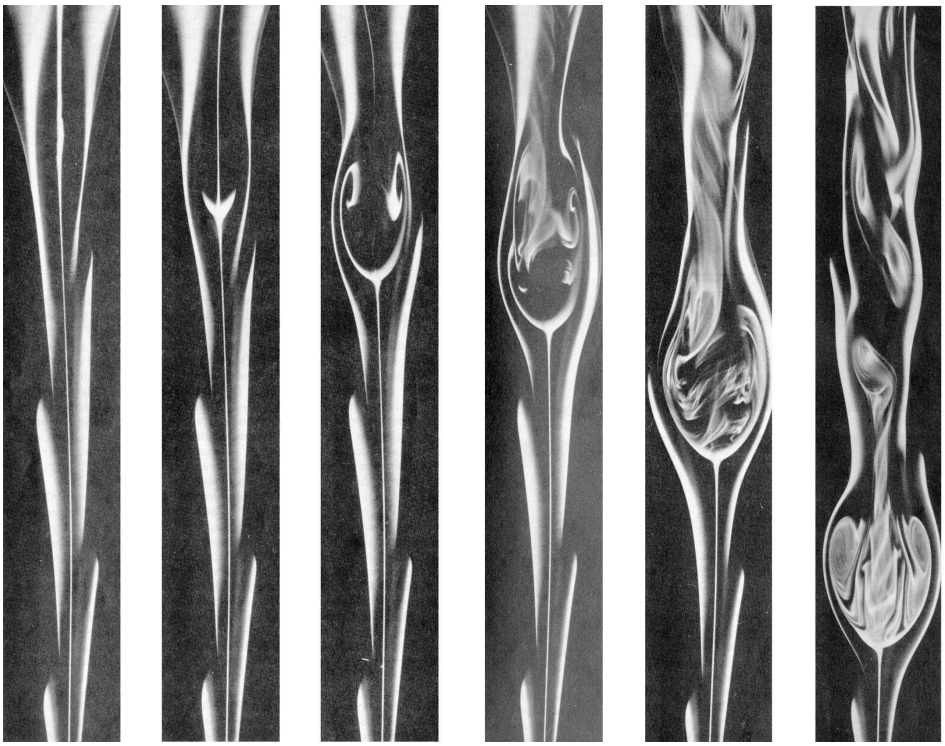

Figure 2.4: Example sequence of vortex breakdown in a laminar swirled flow [128]

where L denotes a characteristic length scale, e.g the hydraulic nozzle diameter. In any given flow configuration it is difficult to exactly determine the swirl number by experimental techniques. Therefore, simplifications or geometrical constraints have been used frequently to estimate S. To distinguish these from the exact definition they will be label S_g in the following.

A characteristic phenomenon of swirl flows is vortex breakdown. It develops an internal recirculation zone (IRZ) on the swirl axis and diverging streamlines around it. Often, these form a bubble like structure that can propagate along the central swirl axis. Even in the laminar case, the IRZ comprises complex and highly irregular fluid motion and its underlying physics are still far from being understood. However, many theories exist that attribute this phenomenon to the generation of a positive axial pressure gradient due to centrifugal forces. According to Lucca-Negro et al. [128] vortex breakdown can be used to classify weak and strong swirl flows. Figure 2.4 shows an example of this phenomenon.

Common literature states that the occurrence of a positive axial pressure gradient is a consequence of a chain of events and can be explained as followed. The radial pressure gradient and the centrifugal force are the dominating forces in the conservation of radial momentum. They are in equilibrium as given by

$$\frac{\partial p}{\partial r} = \frac{\rho v^2}{r}. \tag{2.29}$$

As a consequence the pressure on the central axis is smaller compared to larger radii. Hence, a positive radial pressure gradient exists that leads to entrainment of non-swirled ambient fluid into the vortex core. The resulting decrease of swirl along the axis causes the pressure to increase. Far away from the axis $p = p_\infty$. Thus, the change in radial pressure gradient leads to a positive axial pressure gradient on the central axis. It was observed that for $S > 0.6$ fluid elements cannot flow against the local pressure gradient on the axis and a longitudinal IRZ occurs. A similar phe-

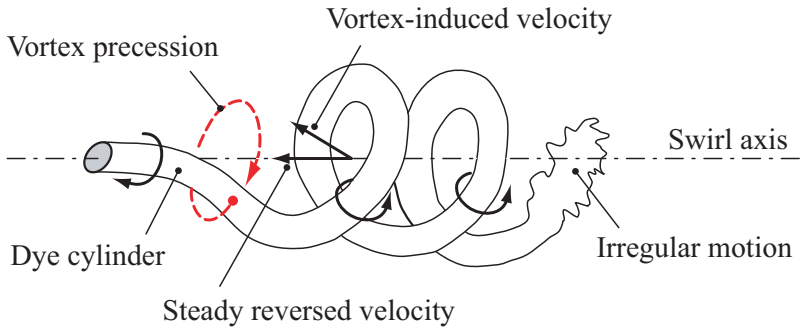

Figure 2.5: Sketch of the precessing motion of the vortex core within a swirling flow (adapted from Chanaud [23]).

nomenon can also be observed in diffusers that exhibit opening angles exceeding $\approx 15^\circ$ as shown later in Section 2.1.3. For laminar flows seven specific modes of vortex breakdown have been observed [128]. However, for turbulent flows it is still unclear to what extent mechanisms for laminar type vortex breakdown can be transferred to large Reynolds numbers [137]. A detailed description of the vortex breakdown phenomena can be found in [53] and [200].

A second phenomenon in swirl flows are rotating helical vortices also called precessing vortex cores (PVC). In gas turbines these occur frequently in combination with vortex breakdown phenomena. PVCs are large coherent flow structures which originate from the swirl generator and rotate around the central flow axis. They were investigated for the first time by Chanaud in 1965 [23]. The general structure as sketched in Fig. 2.5 was observed in isothermal as well as in premixed and non-premixed combusting flows. The position and structure of the PVC is connected to the occurrence of the IRZ [59]. The mutual interactions lead to a distortion of the recirculation zone, which was observed as a 'kidney-shape' [128, 199]. It was also discovered, that the size of the PVC scales directly with the extent of the recirculation zone [55]. The large size of the PVC is associated with a high energetic content. Due to this fact, Hussain [82] claimed that for modeling turbulence in such flows the classical Reynolds decomposition is violated.

Indeed, in the case of large coherent flow motion predominant frequencies of these structures remain in autocorrelation functions as shown in the examples in Fig. 2.6. Clearly, the correlation coefficient is not decreasing monotonously as in isotropic turbulence, but fluctuate around zero with the dominant frequency of the structure itself. Therefore, the definition of τ_0 (resp. l_0) according to Eqs. (2.22) and (2.23) is difficult. To circumvent this difficulty, the first 'zero crossing' on the time axis is defined as the end of the integration. Thus, it marks the time span τ in which the correlation between the two velocities vanishes. The characteristic coherent frequency f_c can be obtained from a Fourier transformation [127] of the autocorrelation function, which results in the power spectral density (PSD). Both, the integral time scale τ_0 and the coherent frequency f_c will be utilized in the analysis of the flashback data and for CFD validation purposes in Chapter 5.

In the context of combustion, swirl features several beneficial characteristics. Firstly, it can enhance mixing drastically, which is utilized in modern gas turbine combustors and also internal combustion engines. Especially in premixed flames the recirculation zone can act as reservoir for heat and radicals, which is advantageous for stabilization (see Section 2.2.3). As it comprises lower velocity regions, it further facilitates the stabilization of these type of flames. The impact of the interactions of premixed flames and turbulent swirl flows is detailed in Section 2.3.

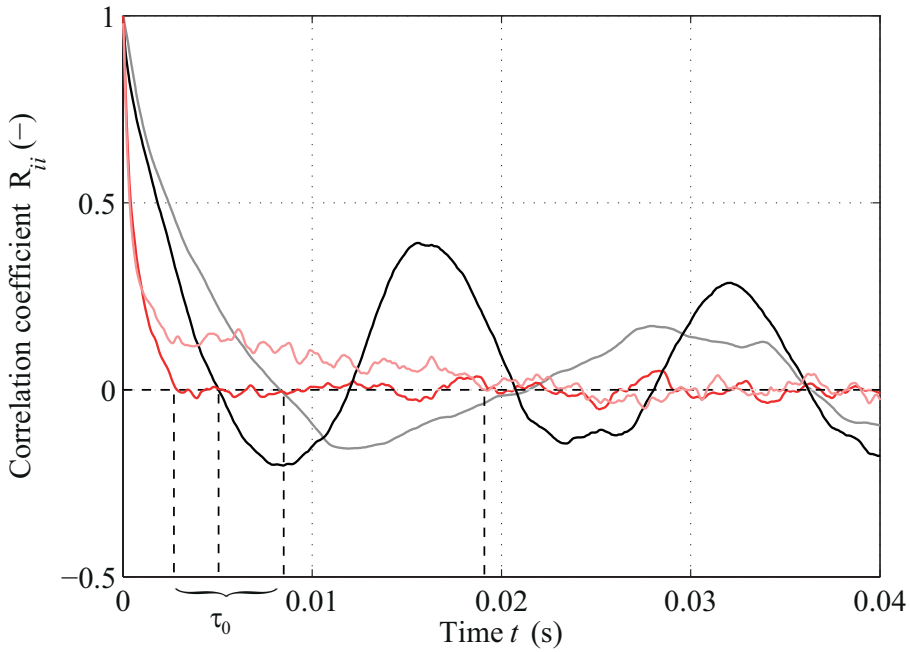

Figure 2.6: Various examples of coherent structures within autocorrelation functions. The results are obtained through the data analysis which will be presented in Section 4.4. The 'zero crossing' approach to estimate the integral time scale is depicted as dashed lines.

2.1.3 Boundary Layers

The layer of fluid in the immediate vicinity of a bounding solid surface is called boundary layer. Inside the nozzle of the investigated burner such a boundary layer is additionally introduced by the central bluff-body. It should be noted that this circumstance differentiates the present investigations from previous flashback research. In the boundary layer effects of viscosity of the fluid start to play the dominant role. It reduces the mean velocity of the free flow until it comes to a rest at the solid surface due to the no slip condition[3]. The left hand side of Fig. 2.7 shows the velocity profile of a laminar boundary layer. The thickness of a boundary layer δ is defined as the distance from the surface or wall where the mean velocity is as high as 99% of the free stream velocity u_0, expressed as

$$\delta = y(u = 0.99u_0). \tag{2.30}$$

In a fully developed flow region of a duct, channel or annular slot the entire flow can be type of a boundary layer flow and may be laminar or turbulent. In the laminar case the profile of u is parabolic for channel (Poisseuille flow) or duct flows (Hagen-Poisseuille flow) and analytical solutions of the Navier-Stokes equations (see Section 2.1) exist of the form

$$u = f(y^2). \tag{2.31}$$

A fully developed turbulent boundary layer profile which is normalized by the turbulent stress at the wall τ_w is depicted in the right hand side of Fig. 2.7. Here, u^+ is the flow velocity normalized by the friction velocity $u_* = \sqrt{\tau_w/\rho}$ and y^+ is the wall distance normalized by $y^+ = u_* y/\nu$.

[3]The no slip condition refers to the resting of fluid particles directly at the solid boundary.

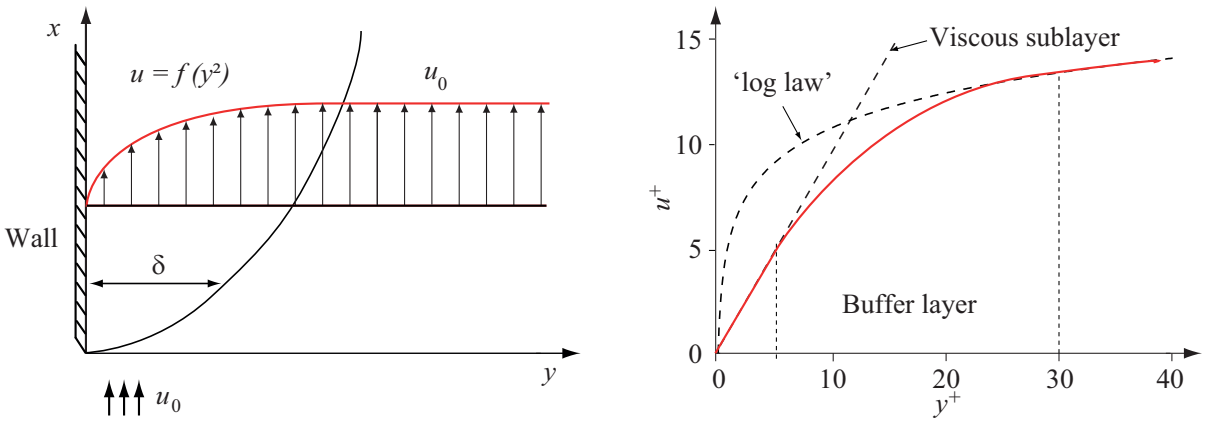

Figure 2.7: Schematic of a laminar boundary layer (left) and normalized transversal velocity profile of a turbulent boundary layer (right). The velocities are marked as red lines. The dashed lines represent the specific models to describe the viscous sublayer and the *log law* region of the boundary layer.

According to Pope [155] the region close to the wall ($y^+ < 5$) is called viscous sublayer. In 1904 Prandtl found that in this layer momentum exchange in y direction (normal to the wall) happens only due to viscous forces and turbulence is negligible. Thus, the velocity increases linearly with the wall distance yielding

$$u^+ = y^+. \tag{2.32}$$

Further away from the wall ($y^+ > 30$, $y/\delta < 0.3$) the empirical *log law* holds, which is defined as

$$u^+ = \frac{1}{\kappa} \ln y^+ + B \tag{2.33}$$

with the von Karman constant κ and another constant B being

$$\kappa = 0.41 \qquad \text{and} \qquad B = 5.2. \tag{2.34}$$

The transition region between the viscous sublayer and the log law region $5 < y^+ < 30$ is called the buffer layer.

In the presence of an adverse pressure gradient, as it is found in swirl flows or diffusers, the flow is decelerated. Due to the no slip condition at the wall and the viscous forces, the lower flow momentum near the wall may result in a stagnation of the flow or even flow reversal. In this situation flow separation from the wall occurs at a location where the oncoming and the reversed flow converge. The situation is depicted in Fig. 2.8 where boundary layer separation appears due to a strong enlargement of the flow's cross section. As mentioned before, mass conservation results in the ejection of fluid from the wall where the approaching fluid encounters the reversed flow. Subsequently this leads to the formation of vortices adjacent to the boundary. Classical flow configurations with positive axial pressure gradients in flow direction are diverging channels or diffusers, bends, and junctions. Besides the aerodynamically created pressure gradients, also combustion-induced adverse pressure gradients can occur, which will be explained in Section 2.3.3.

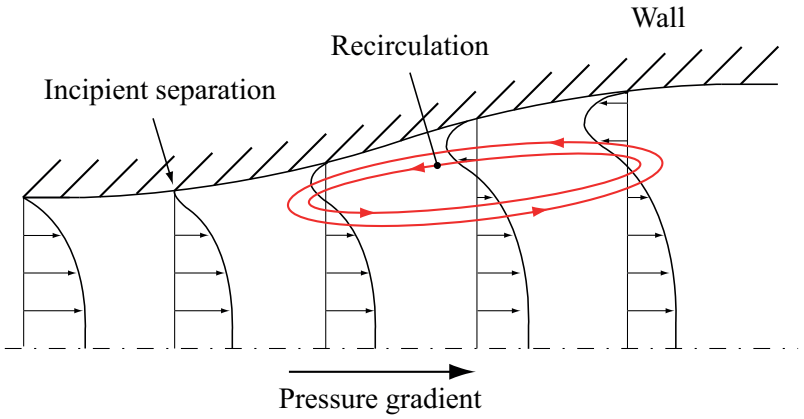

Figure 2.8: Schematic of a boundary layer separation with flow reversal in a diffuser

2.2 Combustion

Combustion is an exothermic self-sustaining chemical reaction of fuel and an oxidizer [204]. In practical gaseous combustion processes molecules are mainly composed of hydrogen H and carbon C (i.e. hydrocarbons). These react with oxygen from the air to form carbon dioxide (CO_2) and water (H_2O). Besides oxidation by diatomic oxygen O_2 the chemical process is also possible with other sorts of molecules, such as fluoride, chloride, etc. For instance, Fluorine can oxidize hydrogen to form Hydrogen Fluoride. Practical applications of combustion aims at transferring chemical energy into heat. Often the heat is directly used for heating purposes, e.g. for housing and materials production. The second major application is to further transfer the heat into kinetic energy in order to create momentum. This can be used for transport purposes such as in airborne gas turbines, where the investigated type of burner is applied. Also, the momentum can be transferred further to electrical energy by coupling a generator to a stationary gas turbine.

The various reactions during the process of hydrocarbon oxidation lead to the electronic excitation of molecules within the reaction zone, which in turn emit light when returning to their ground states. The reaction volume of emitted light, colloquial called the 'flame', is the heat release zone. There, temperatures can reach up to 2000 °C in premixed methane-air systems. The effect of light emission is exhibited in a utilized measurement technique. Hence, the details of this flame or chemiluminescence (CL) will be explained in Section 4.1.1. The structure, shape, size and temperature of a flame can vary strongly by the physicochemical processes within the reaction zone. These processes are mainly determined by the mode of fuel and oxidizer supply, which is principally the a premixed or non-premixed combustion mode. The two extremes are sketched in Fig. 2.9.

In the premixed mode, fuel and oxidizer are perfectly mixed on the molecular level before they enter the combustion zone. Hence, the resulting flame propagates from the region of burnt products towards the fresh gas mixture. The thickness of the reaction zone is typically a fraction of a millimeter and characterized by a steep temperature gradient. In the non-premixed mode, or 'diffusion' flame, the fuel and air streams are supplied from individual ports. The reaction zone is located where fuel and oxidizer are mixed. In a laminar flame this occurs exclusively through diffusion. The reaction zone can be up to a millimeter thick located at the temperature peak. In between the two extreme modes the field of partially premixed combustion is settled.

Methane was used in the experiments which facilitates the modeling of the chemical reac-

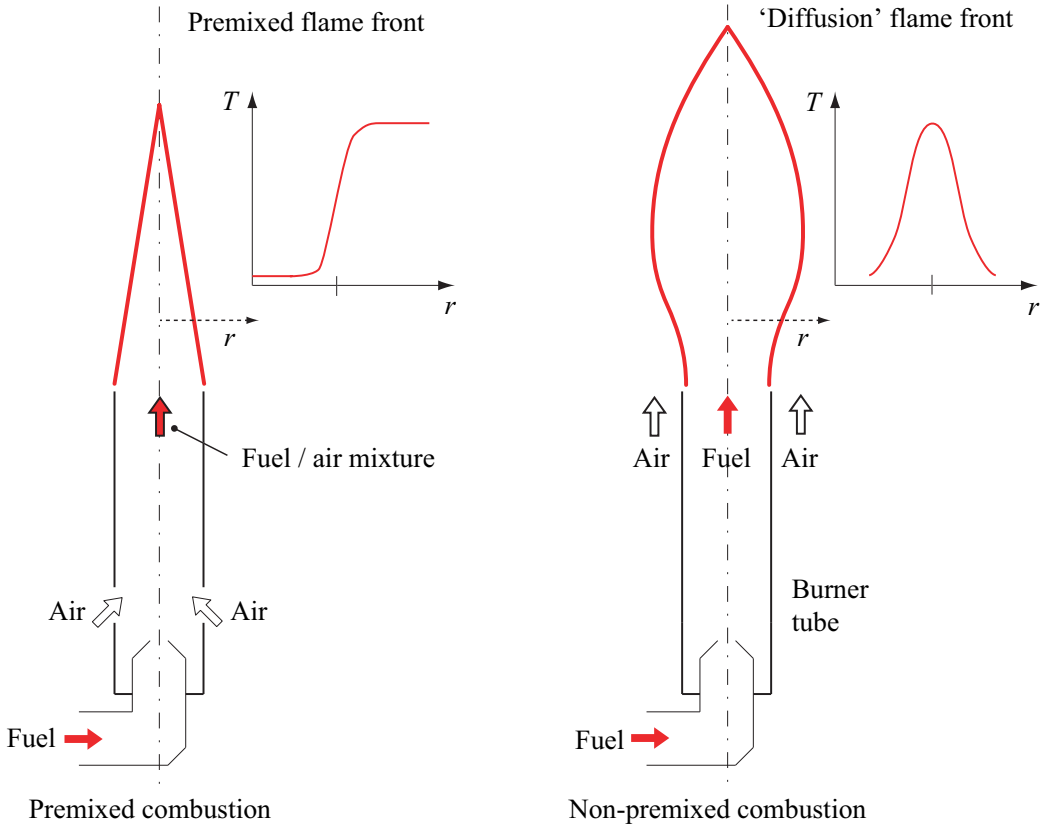

Figure 2.9: Premixed and non-premixed mode of combustion

tions as it is the most simple hydrocarbon. In the next section the oxidation of methane will be described by the global reaction, but also by chemical kinetics. The latter is able to describe the formation of minor species. They depend on the specific combustion configuration and are mainly unburnt hydrocarbons (UHC), carbon monoxide (CO), soot and nitric oxides (NO_x). They are considered as pollutant emissions, since they are harmful to the environment and are therefore unwanted. The investigations in this thesis aim at the understanding of the flame flashback mechanism in the special type of swirl burners with central bluff-body. The burners are utilized to reduce nitric oxides emissions in gas turbines by the lean premixed combustion concept. Therefore, Section 2.2.2 will describe the formation paths of NO_x in detail. In the last section on combustion premixed flames are detailed, which hold the potential to significantly decrease the formation of NO_x emissions.

2.2.1 Oxidation of Methane

The following section provides the most basic concepts of methane oxidation that can be found in various references. The explanations and statements reflect the descriptions in the textbooks of Warnatz [211], Peters [151], and Turns [204]. Generally, the oxidation of any hydrocarbon C_nH_m consisting of n C atoms and m H atoms can be described macroscopically by the following global reaction equation

$$\upsilon_{C_nH_m} C_nH_m + \upsilon_{O_2} O_2 \longrightarrow \upsilon_{CO_2} CO_2 + \upsilon_{H_2O} H_2O. \tag{2.35}$$

The stoichiometric coefficients υ_α, put in front of the sort of molecules describe the ratio between the numbers of molecules that participate during the reaction. The right arrow indicates that during this reaction all of the reactants will be consumed to form the products. It should be noted that this is an approximation and backward reaction also occurs, though its reaction rate is negligible. The coefficients for a stoichiometric oxidation of a hydrocarbon molecule can be calculated as

$$\upsilon_{C_nH_m} = 1 \qquad \upsilon_{O_2} = (n + m/4) \qquad \upsilon_{CO_2} = n \qquad \upsilon_{H_2O} = m/2. \tag{2.36}$$

Eq. (2.35) describes the redistribution of C, H and O atoms during the oxidation process globally. It is assumed that all fuel and O_2 molecules react to form CO_2 and H_2O. Hence, the global description is not sufficient for the prediction of minor species such as the pollutants NO_x and CO. In reality the reaction process is complex and consists of a large number of elementary reactions, which describe the reactive collision of single molecules on the microscopic level. Thereby, intermediate species such as NO_x and CO are formed that are again partially or totally consumed in the course of subsequent reactions. Reaction mechanisms are used to simulate the complex chemical processes. These are subsets of rate-limiting elementary reactions which determine the global chemical time scale. The `GRI Mech 3.0` reaction mechanism can be applied to model the chemistry of the relatively simple CH_4 molecule, which was used in the experiments. The `GRI Mech 3.0` is a detailed mechanism for CH_4 oxidation that incorporates more than 50 species and over 300 reactions including NO_x [184]. The global reaction for methane oxidation reads

$$CH_4 \; + \; 2\,O_2 \longrightarrow CO_2 \; + \; 2\,H_2O \tag{2.37}$$

with the stoichiometric coefficients

$$\upsilon_{CH_4} = 1 \qquad \upsilon_{O_2} = 2 \qquad \upsilon_{CO_2} = 1 \qquad \upsilon_{H_2O} = 2. \tag{2.38}$$

A mixture of fuel and oxidizer is defined as *stoichiometric* if the reactants consume each other completely. Hence, the methane mole fraction Ψ_{CH_4} of the stoichiometric methane-oxygen mixture can be calculated by

$$\Psi_{CH_4,st} = \frac{1}{1 + \frac{\upsilon_{O_2}}{\upsilon_{CH_4}}}. \tag{2.39}$$

For ideal gases this equals the ratio in volumetric flow rate, which yields $1/3$ for the oxidation of CH_4 with pure oxygen. In the case of air as oxidizer the gas composition has to be taken into account. Dry air contains about 21% O_2, 78% N_2 and 1% noble gases. According to the composition Eq. (2.39) has to be modified when using air and becomes

$$\Psi_{CH_4,st} = \frac{1}{1 + 4.762\frac{\upsilon_{O_2}}{\upsilon_{CH_4}}}. \tag{2.40}$$

For a mixture of methane and air a stoichiometric volumetric mole fraction of 9.5 mol% is calculated. However, practical flames exhibit varying fuel and oxidizer flow rates. In case of an excess of air the mixture is called *lean*. For values of mole fraction larger than 9.5 mol% the mixture is called *rich*. The state of the mixture can easily be characterized by the equivalence ratio Φ, which can be described by the ratio of the actual fuel mole fraction to the stoichiometric

mole fraction[4]

$$\Phi = \frac{\Psi_{CH_4}}{\Psi_{CH_4,st}}. \tag{2.41}$$

Hence, stoichiometric, lean, and rich mixtures will give $\Phi = 1$, $\Phi < 1$, and $\Phi > 1$, respectively. The flame characteristics (e.g. flame speed or temperature) can be parameterized by the equivalence ratio Φ in the context of the premixed combustion. It is one of the major parameters in these investigations and further details of its impact will be provided in Section 2.2.3.

The speed of the global reaction process is given by the global reaction rate r. Here, it describes the change of the methane concentration in time and is defined as

$$r = \frac{\mathrm{d}[CH_4]}{\mathrm{d}t} = k(T)\ [CH_4]^a\ .[O_2]^b \tag{2.42}$$

The parameters a and b, as well as the temperature dependent reaction rate coefficient $k(T)$ for various hydrocarbon fuels are determined either from molecular dynamical and kinetic calculations or from experiments. In the case of global reactions the exponential coefficients a and b are real numbers since a huge number of various elementary reactions is involved. $k(T)$ can be modeled by the Arrhenius law

$$k(T) = A^T \exp\left(\frac{G}{\Re T}\right), \tag{2.43}$$

where A is the pre-exponential factor, G the Gibb's free energy, $\Re$ the universal gas constant and T temperature. Often, the global reaction approach is satisfactory to model the heat release of a combustion system. However, no information about the detailed chemical processes is obtained which is relevant for the formation of pollutants. If we consider the oxidation of hydrogen, which is a sub-mechanism of the methane oxidation, the global reaction can be described by the equation [204]

$$2\ H_2\ +\ O_2 \longrightarrow 2\ H_2O. \tag{2.44}$$

In reality the redistribution of H and O atoms does not happen instantaneously. This is a fact that does not become clear from Eq. (2.44). Instead a highly non-linear system of elementary reactions called reaction mechanism runs. The elementary reactions describe the bond breaking between atoms and the formation of new molecules by collisions of single molecules. An example of such an elementary reaction [184] is

$$H_2\ +\ O_2 \rightleftharpoons HO_2\bullet\ +\ H\bullet, \tag{2.45}$$

where a hydrogen atom is transferred from the diatomic hydrogen to the diatomic oxygen molecule. Radicals (marked by a black dot) are formed and recombine in the course of a reaction mechanism such as O, H, and OH. They are highly reactive due to unpaired electrons and, hence, are the sustaining element in the chain of elementary reactions. Regarding radicals four different types of elementary reactions can be classified:

1. Chain initiation reactions form radicals from the stable reactants.

2. Chain Propagation reactions sustain the reaction chain by destruction and formation of a radical.

[4] It is also possible to describe the equivalence ratio in terms of mass fractions. The molecular weight, which relates moles and masses, cancels out during the transformation from mole-based to mass-based equivalence ratio, or vice versa.

3. Chain branching reactions create new radicals. While one (or no) radical is consumed, two are formed.

4. Chain termination reactions stop the reaction mechanism by recombination of radicals without producing a new one. Usually a high heat release is associated with this type of reactions.

Especially during methane oxidation radicals such as single O or H atoms are needed in order to break the bonds in the symmetric and therefore highly stable CH_4 molecule.

Similar to the global reaction (see Eq. 2.43) the rate of the elementary reactions can also be described by the Arrhenius law

$$k(T) = A \exp\left(\frac{-E_a}{\Re T}\right). \tag{2.46}$$

In contrast to the reaction rate coefficient of a global reaction which is a function of the Gibb's free energy, the temperature influence of elementary reactions is given by the activation energy E_a. The values of E_a are typically high for high temperature oxidation.

The most dominant pathway for CH_4 oxidation at 2200 K in a well-stirred reactor [204] is

$$CH_4 \xrightarrow{OH,\,H,\,O} CH_3 \xrightarrow{O} CH_2O \xrightarrow{OH,\,H,\,O} CHO \xrightarrow{H_2O,\,M,\,OH} CO \xrightarrow{OH,\,O+M} CO_2\,. \tag{2.47}$$

The pathway follows a successive dehydration of the CH_4 molecule by various radicals. It also highlights the importance of the hydroxyl radical (OH) during the breakup process. Hence, the OH radical is a good indicator for the reaction processes in the flame. Its application in combustion laser diagnostics will be highlighted in Section 4.1.2 through Laser-Induced Fluorescence (LIF) of the hydroxyl radical. At lower temperatures different pathways become more dominant. These are important in auto-ignition processes, but do not play a significant role as no auto-ignition was observed during the investigations. The formation of nitric oxides described by elementary reactions will be detailed in following section.

2.2.2 NO Formation and Reduction Principles

Nitric oxides are pollutants from combustion processes. They became an issue in the second half of the 20th century. Nitrogen dioxide (NO_2) is a reddish-brown toxic gas. Epidemiological studies provide some evidence that long-term NO_2 exposure may decrease lung function and increase the risk of respiratory symptoms [214]. NO and NO_2, collectively called NO_x, are also major contributors to photochemical smog and ozone (O_3) in the troposphere, which is the layer of the atmosphere closest to the ground ($0-15$ km). The UV photons of the sun spectrum supply the energy to dissociate NO_2 to NO and O. The latter combines with another O_2 molecule to form O_3, which subsequently reacts with NO to form again NO_2 and O_2. The mechanism is given as

$$NO_2 + h\nu \rightleftharpoons NO + O\bullet \tag{2.48}$$

$$O\bullet + O_2 \rightleftharpoons O_3 \tag{2.49}$$

$$O_3 + NO \rightleftharpoons O_2 + NO_2 \tag{2.50}$$

Hence, during high sun light intensities the formation of ozone is favored, e.g. during hot summer days. This results in the so-called 'summer smog'. Long-term exposure to high ozone concentrations can lead to asthma, a decreased lung function growth and lung cancer, which appears to be

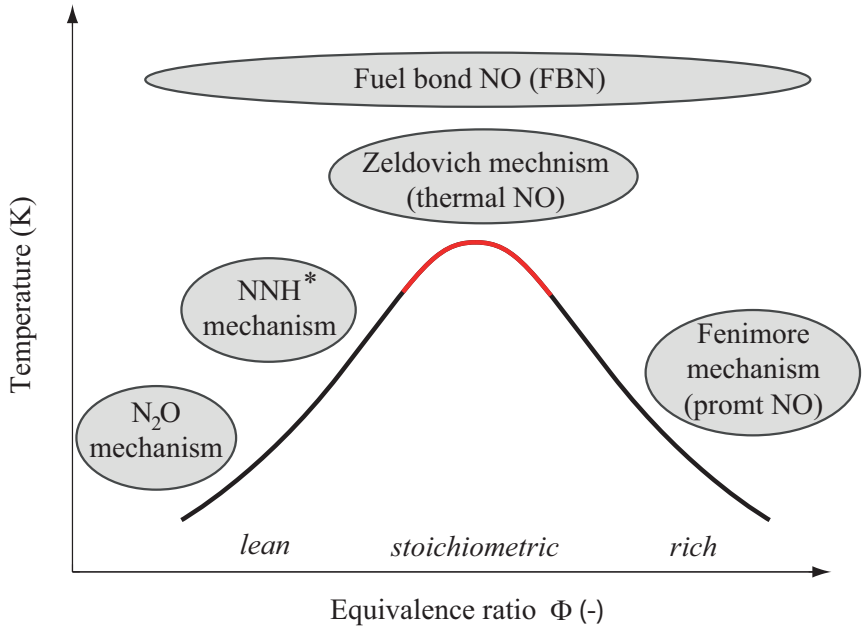

Figure 2.10: Formation paths for nitric oxides as a function of the equivalence ratio Φ according to Joos [91]

dependent based on genetic differences. The effects of these pollutants on the human organism are still under investigation, especially as there is evidence of interactions between them [214].

In contrast to the effect of O_3 in the troposphere, ozone absorbs harmful UV radiation in the stratosphere above $(15-50\,\text{km})$. Unfortunately, NO_x also participates in a chain reaction removing ozone at this altitude, with the consequence of increased UV radiation reaching the earth's surface. Thus, the mechanisms of formation of NO_x must be understood to essentially avoid formation of this pollutant. A global equilibrium approach cannot be assumed due to relatively slow rates of formation and chemical kinetics have to be taken into account. So far five major routes for the formation of nitric oxides have been identified:

1. Zeldovich mechanism
2. Fenimore mechanism
3. N_2O mechanism
4. NNH radical mechanism
5. Formation of Fuel-Bond NO (FBN)

The formation paths depend on the equivalence ratio and temperature of the flame. This is summarized in Fig. 2.10. The following provides a brief overview of the mechanisms of formation. Further details can be found in [138, 167].

The Zeldovich mechanism, or 'thermal' NO mechanism, forms NO from atmospheric nitrogen at temperatures above 1800 K [204]. The mechanism is named after J. B. Zel'dovich, who

postulated the mechanism in his doctor dissertation in 1939.

$$\mathrm{O\bullet} + \mathrm{N_2} \xrightarrow{k_1} \mathrm{NO} + \mathrm{N\bullet} \qquad A_1 = 1.8 \cdot 10^{14} \, \frac{\mathrm{cm}^3}{\mathrm{mol \cdot s}} \qquad E_{\mathrm{a},1} = 318 \, \frac{\mathrm{kJ}}{\mathrm{mol}} \tag{2.51}$$

$$\mathrm{N\bullet} + \mathrm{O_2} \xrightarrow{k_2} \mathrm{NO} + \mathrm{O\bullet} \qquad A_2 = 6.4 \cdot 10^{9} \, T \, \frac{\mathrm{cm}^3}{\mathrm{mol \cdot s}} \qquad E_{\mathrm{a},2} = 26 \, \frac{\mathrm{kJ}}{\mathrm{mol}} \tag{2.52}$$

$$\mathrm{N\bullet} + \mathrm{OH\bullet} \xrightarrow{k_3} \mathrm{NO} + \mathrm{H\bullet} \qquad k_3 = 3.8 \cdot 10^{13} \, \frac{\mathrm{cm}^3}{\mathrm{mol \cdot s}} \tag{2.53}$$

The first reaction in Eq. (2.51) has a very high activation energy due to the strong triple bond of the N_2 molecule. This leads to a strong temperature dependence. Hence, the N radical is only formed at high temperatures. Its reaction rate coefficient k_1 is small compared to the other two reactions in (2.52) and (2.53). Therefore, Eq. (2.51) is the rate-limiting reaction, which runs slowest. Consequently, the assumption is valid that the concentration of N is quasi steady state, i.e. $\mathrm{d[N]/d[t]} = 0$. By this assumption, the rate of formation of NO can be simplified to yield

$$\frac{\mathrm{d[NO]}}{\mathrm{d}t} = 2k_1 \, [\mathrm{O}] \, [\mathrm{N_2}]. \tag{2.54}$$

As a consequence NO formation can be minimized by decreasing either [O], [N_2] and/or k_1 by decreasing the temperature. The nitrogen concentration in the air is usually no free parameter for airborne gas turbine operation. However, the O radical concentration is affected by various parameters, such as temperature and equivalence ratio. In practice, NO reduction is mainly achieved through the decrease in temperature, thereby exploiting the highly non-linear dependency of temperature on k_1. This is often realized by lean premixed combustion, which will be discussed in the following section.

The mechanism of formation of 'prompt' NO was postulated by Fenimore in 1979 [91]. His observations in laminar flames revealed that the concentration of NO does not go to zero as the measurement probe approaches the flame front from the downstream side. This was contrary to Zel'dovich's theory. He proposed a new mechanism, which describes the production of NO from intermediate CH radicals inside the flame front, including the formation of the hydrogen cyanide radical (HCN). This is formed by the reaction

$$\mathrm{CH\bullet} + \mathrm{N_2} \rightleftharpoons \mathrm{HCN\bullet} + \mathrm{N\bullet} \, . \tag{2.55}$$

This reaction is a fast process and the participating CH radicals are only present in the flame front. HCN is a relatively stable component which reacts further at flame temperatures also forming NO. The N radical which was formed in Eq. (2.55) is oxidized to NO by

$$\mathrm{N\bullet} + \mathrm{O_2} \rightleftharpoons \mathrm{NO} + \mathrm{O\bullet} \tag{2.56}$$

$$\mathrm{N\bullet} + \mathrm{OH\bullet} \rightleftharpoons \mathrm{NO} + \mathrm{H\bullet} \, . \tag{2.57}$$

This mechanism is favored during rich combustion where more CH is formed than in the lean due to the absence of oxygen atoms.

However, in the previously mentioned lean premixed combustion at low temperatures the major source of NO production remains the nitrous oxide mechanism (N_2O mechanism) that was postulated by Wolfrum in 1972 [29, 221]. It was initiated by the following observation. If temperature is decreased under lean premixed conditions ($\Phi < 0.66$), where the Zel'dovich NO is

reduced to a minimum, still a significant nitric oxide concentration can be measured. The authors found out that it can be attributed to the formation of nitrous oxide (N_2O). The N_2O mechanism is similar to the Zel'dovich mechanism as O atoms oxidize N_2 from the air [131],

$$N_2 + O\bullet + M \rightleftharpoons N_2O + M \tag{2.58}$$

$$N_2O + O\bullet \rightleftharpoons NO + NO. \tag{2.59}$$

As Eq. (2.58) is a termolecular reaction type high pressure favors this mechanism. Again, N_2O reacts further to ultimately form NO. Usually N_2O is an insignificant contributor, but lean premixed conditions suppresses the production of CH. In turn this leads to less formation of NO by the Fenimore mechanism and the suppression of thermal NO due to low temperatures. Furthermore, the low activation energy of Eq. (2.58) favors the N_2O mechanism in the low temperature region. Thus, it is the main source of NO production in lean premixed combustors of gas turbines.

A small fraction of NO is furthermore formed under lean conditions by the NNH radical mechanism [91]. Hereby, diatomic nitrogen reacts with hydrogen radicals to form the NNH radical according to

$$N_2 + H\bullet \rightleftharpoons NNH\bullet \tag{2.60}$$

$$NNH\bullet + O\bullet \rightleftharpoons NO + NH\bullet. \tag{2.61}$$

In subsequent steps NNH is oxidized to form another NO molecule.

Finally, for the sake of completeness the NO production from the nitrogen contained in the fuel itself shall be mentioned. A certain content of nitrogen is typical for fossil fuels that have been biologically formed in air. Coal and crude oil comprise about 1% of nitrogen containing molecules aside from jet fuel and refined hydrocarbons where nitrogen has been removed during the refinement process. Under stoichiometric and lean conditions fuel-bound nitrogen (FBN) is almost completely oxidized to NO via the oxidation of HCN during combustion.

In the atmosphere, nitric oxide ultimately oxidizes to form nitrogen dioxide. The following elementary reactions are responsible for the formation of NO_2 prior to the exhausting of the combustion products into atmosphere [204]

$$NO + HO_2\bullet \rightleftharpoons NO_2 + OH\bullet \tag{2.62}$$

$$NO_2 + H\bullet \rightleftharpoons NO + OH\bullet \tag{2.63}$$

$$NO_2 + O\bullet \rightleftharpoons NO + O_2. \tag{2.64}$$

The HO_2 radical is formed by the following reaction in relatively low-temperature regions

$$H + O_2 + M \rightleftharpoons HO_2\bullet + M. \tag{2.65}$$

Thus, the formation of NO_2 occurs in zones of high HO_2 concentrations and relatively low temperature. In hot regions NO_2 is destroyed by the reactions in Eq. (2.63) and Eq. (2.64). Ultimately, NO_2 is formed where NO is transported from high into low temperature zones.

One goal is to inhibit or at least minimize NO_x emissions because of the adverse environmental impacts. To achieve this, primary reduction strategies are favored that try to reduce the formation of NO_x to a minimum. Secondary reduction strategies destroy the already formed NO_x molecules and come along with larger instrumental efforts and thus higher costs. Thermal De-NOx and RAPRENOx mechanisms [130] for fuel-bond nitrogen emissions are examples of this class of

strategies. A widely used primary reduction strategy is the exhaust gas recirculation (EGR). The physical principle is based on mixing the combustion air with inert cooled exhaust gas. The heat of combustion is then transferred to relatively more mass (combustion air and fuel plus inert gas). This leads to lower temperatures and thus lower emission. Also, the global oxygen concentration is reduced as the exhaust gas contains less oxygen than fresh air. From Eq. (2.54) one can see that NO formation is thereby further reduced. The EGR principle is already applied in internal combustion engines, furnaces and stationary gas turbines. In airborne gas turbine combustors exhaust gas recirculation is hindered by the additional weight of the structure to recirculate the gas. Instead a sequential rich-burn, quick-quench, lean-burn strategy (RQL) is followed. Hereby the influence of the equivalence ratio on the adiabatic flame temperature is exploited which will be detailed in the next section. The principle of RQL is to firstly burn the fuel under rich conditions at low temperatures, resulting in high emissions of unburnt hydrocarbons. Quick mixing with secondary air keeps the residence time for the reactants low as they pass the peak temperature region of the stoichiometric mixture. Afterwards, a lean environment results again in low combustion temperatures while the unburnt hydrocarbons from the primary rich stage are oxidized. However, there is still a period of high temperatures that result in high NO_x formation. Unfortunately this cannot be avoided by this strategy. The most promising primary strategy is the already mentioned lean premixed combustion. In the context of gas turbine combustions this strategy has been utilized in various technological concepts. These are Lean Premixed Prevaporized combustion (LPP), Partial Evaporating and Rapid Mixing (PERM) and Lean Direct Injection (LDI) [142].

2.2.3 Premixed Combustion

The implementation of premixed combustion is a key strategy to reduce nitric oxides emissions of high temperature combustion systems. In premixed combustion fuel and oxidizer, usually air, are perfectly premixed on a molecular level before supplied to the combustion chamber. This is in contrast to non-premixed combustion where fuel and oxidizer are injected separately. The ratio of fuel and oxidizer can be characterized by the equivalence ratio Φ which has been already been introduced in Section 2.2. The mixture has to be within the flammability limits to sustain a continuous, thus, stable combustion reaction. Pressure, temperature and equivalence ratio influence the flammability. For a methane-air mixture under normal conditions these range from $\Phi = 0.46 - 1.64$ [13], which correspond to a volumetric fraction of methane between 4.61% – 14.7%. A reaction front divides the combustion region into two characteristic states after ignition by a thermal source: the burnt and the unburnt state. In the course of the chemical reactions the flame front moves towards the unburnt mixture leaving products in the burnt region. The ignition can initiate a supersonic shock which leads to *detonation*, associated with a strong pressure rise over the reaction front. In this case the density of the mixture stays relatively constant. Here, the propagation of the flame is mainly controlled by the speed of sound and not by the reaction mechanism of combustion. However, this is not the focus of this work and mentioned only for the sake of completeness. Instead, subsonic upstream propagation of the flame during flashback is investigated. The so-called *deflagration* is characterized by a relatively constant pressure over the flame front and the density of the mixture changes according to the ideal gas law by a factor of ≈ 7 for stoichiometric methane-air mixtures. The reaction volume where combustion takes place is a very thin zone between burnt and unburnt mixture. Figure 2.11 depicts the structure of such a flame front normal to its propagation direction. It shows the temperature, concentrations of reactants and products as well as intermediate species across the premixed flame for a laminar

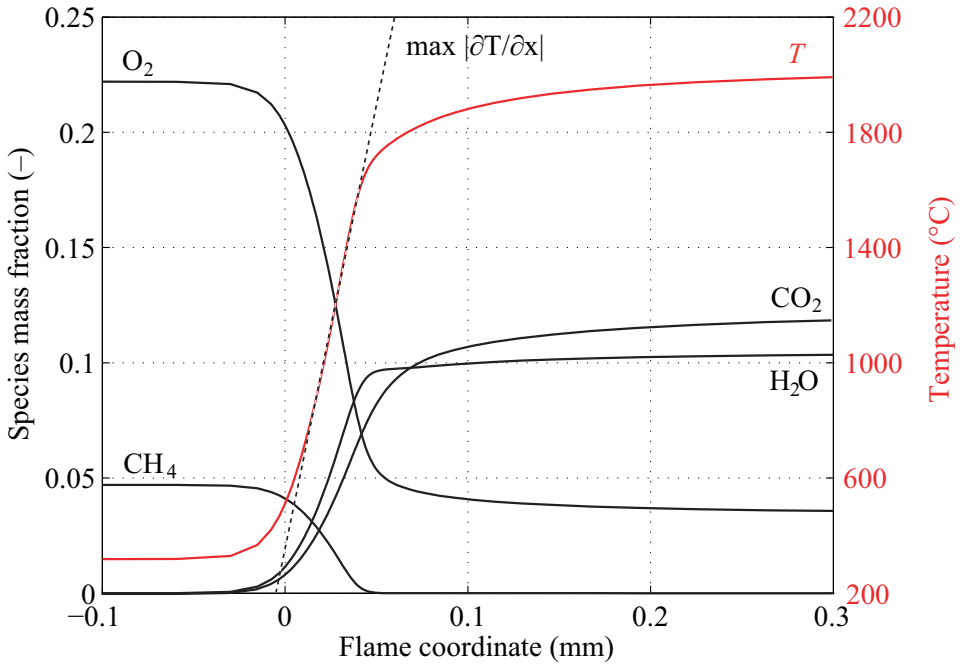

Figure 2.11: The structure of a premixed laminar methane-air flame at an equivalence ratio $\Phi = 0.833$

methane-air flame of $\Phi = 0.833$. The profiles have been determined by detailed chemical kinetics calculations using the program CHEM1D [25, 189]. This incorporates the detailed chemical mechanism `GRI Mech 3.0` (see Section 2.2.1). The thickness of the laminar flame l_f can be estimated from the profiles in various ways [154]. The most widely used one seems to be the following form

$$l_f = \frac{T_b - T_u}{\max|\frac{\partial T}{\partial x}|}. \tag{2.66}$$

Here, the burnt and unburnt gas temperatures T_b and T_u, respectively, and the steepest temperature gradient are taken into account. In the case of the depicted methane-air flame at $\Phi = 0.833$ the laminar flame thickness can be estimated to yield $l_f = 0.5$ mm.

The flame front itself can be divided into three zones which are governed by different physical mechanisms [149]. These are the preheat zone, the inner reaction layer and the oxidation zone. In the preheat zone only slow low temperature reactions take place. There, the approaching mixture is continually heated by diffusion of thermal energy from the adjacent inner reaction layer downstream. Physics is governed by the equilibrium of convective and diffusive transport processes. The thickness of the preheat zone is in the order of l_f. Above 1000 K chain branching reactions start (see Section 2.2.1). These are attributed to the beginning of the inner reaction layer of the thickness l_δ. This second zone is characterized by very fast chemistry in which the fuel molecules are destroyed and many intermediate species like CO, H_2 and OH are created. The latter is a very important species for experimental investigations of flames. It can be detected and also quantified by Planar Laser-Induced Fluorescence (PLIF). The steepest gradient of the OH concentration can be used as flame front marker. In this zone the heat release is at its maximum. Fast bimolecular reactions dominate the chemical process. The thickness of the inner reaction layer is approximately $l_\delta \sim 0.1 l_f$. Because this zone is thin, temperature and

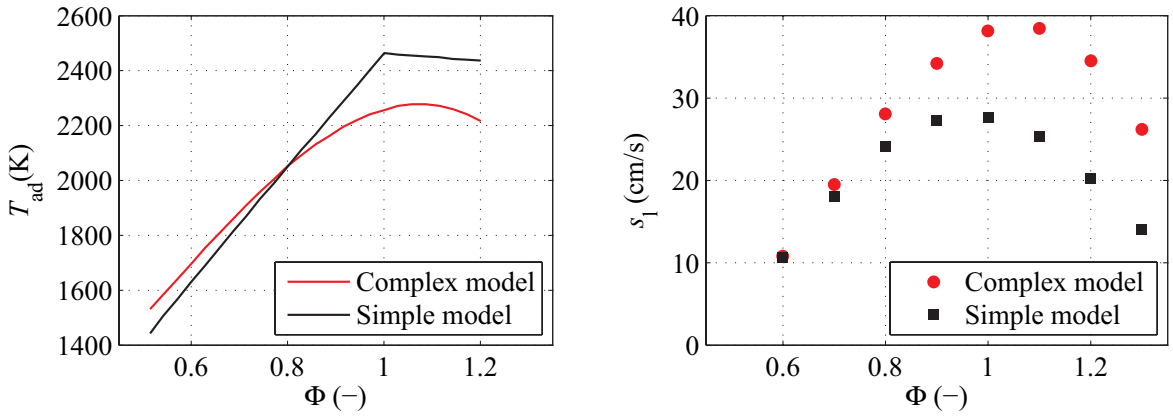

Figure 2.12: Dependency of laminar flame speed s_l and adiabatic temperature T_{ad} as a function of the equivalence ratio Φ [154]. T_{ad} has been calculated with full chemistry and variable c_p marked with the red line. The effect of reduced complexity using one-step chemistry and constant c_p is shown as the black line. s_l has been calculated with a complex transport model (red dots) and a simplified model assuming $\mathrm{Le} = 1$ (black dots).

species concentration gradients are very steep. The very large gradients are the driving force of a self-sustaining premixed flame, because these gradients promote the diffusion processes into the preheat zone. The third region is the oxidation zone. Its extent is largely influenced by the final oxidation of CO [204] by the reaction

$$\mathrm{CO} + \mathrm{OH}\bullet \xrightarrow{k} \mathrm{CO_2} + \mathrm{H}\bullet\,. \tag{2.67}$$

The comparably small reaction rate coefficient k leads to an oxidation zone that may extend several millimeters in atmospheric flames. Termolecular radical recombination reactions dominate the chemistry within this zone, such as [211]

$$\mathrm{H}\bullet + \mathrm{O_2} + \mathrm{M} \rightleftharpoons \mathrm{H0_2}\bullet + \mathrm{M}. \tag{2.68}$$

These are much slower than bimolecular reactions that are statistically more likely to happen.

For an adiabatic system the temperature continuously increases over the flame front until the adiabatic flame temperature T_{ad} is reached. The dependency of T_{ad} on the equivalence ratio Φ is a fundamental requisite for the principle of thermal NO_x reduction by premixed combustion. The functionality for methane-air flames is illustrated in Fig. 2.12 [154]. Therein, T_{ad} has been modeled and calculated with different levels of complexity. The red line in the graph on the left hand side shows results for a detailed reaction mechanism (`GRI Mech 3.0`) and variable heat capacity c_p. The influence of the reduced complexity using one-step chemistry and constant c_p is shown as black line. In both approaches T_{ad} decreases from the point of the stoichiometric mixture towards the lean and the rich mixture. As already pointed out in Section 2.2.2 the lean (LPP, LDI, PERM) as well as the rich branch (RQL) are utilized to reduce NO_x emission. T_{ad} for both levels of complexity was estimated to be approximately 2100 K for the system under investigation in its basic configuration at $\Phi = 0.833$. Clearly, the simple model overestimates the maximum temperature by 200 K. This indicates the importance of choosing the right level of detail when setting up numerical calculations, such as flashback in premixed burners. The

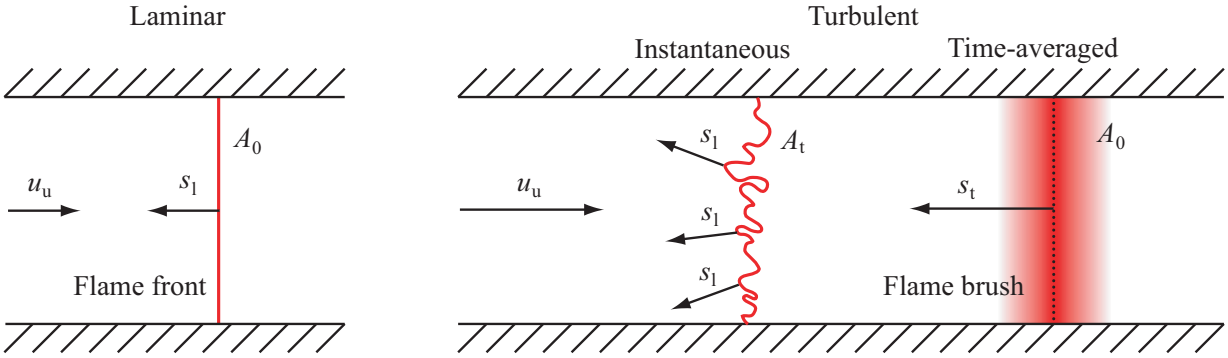

Figure 2.13: Stabilization mechanisms for a laminar and turbulent premixed flame inside a tube

simplifications can significantly influence the result. This can be observed later in Section 2.3 where flashback models will be presented that depend on the density ratio ρ_b/ρ_u which is directly influenced through temperature.

The propagation speed of the flame front is controlled by the equilibrium between the generation of heat during the oxidation of hydrocarbons inside the flame front and the diffusion of heat into the unburnt gas. The mechanism is determined by the thermal diffusivity D_λ of the mixture. The propagation velocity of the flame front towards the fuel-air mixture is called the laminar flame speed s_l. Considering a tube with negligible wall friction and no thermal conductivity, it is possible to stabilize a flame at a fixed position inside the tube. In case of a laminar flat flame and hence at a low Reynolds number there is no transversal mass or momentum transfer. The approaching unburnt mixture velocity equals the laminar flame speed, hence $s_l + u_u = 0$. This equilibrium is sketched on the left hand side of Fig. 2.13. Inside the tube the premixed flow is approaching from the left hand side with the uniform velocity u_u. The laminar flame that has a cross sectional area of A_0 is propagating with the laminar flame speed against the oncoming fresh gas. Since the vectors of both velocities have the same length and opposite directions the flame maintains its position. It is an experimental practice to define the laminar flame speed s_l based on the gas velocity of the unburnt mixture. Hence, the definition of s_l is given by

$$s_l = \frac{\dot{m}}{\rho_u A_0} \tag{2.69}$$

where $\dot{m}$ is the mass flow rate that crosses the cross sectional area of the laminar flame front A_0. The laminar flame speed is influenced by several parameters. Besides the initial temperature of the mixture, pressure and the fuel type, the equivalence ratio is also an important parameter. The right hand side of Fig. 2.12 shows the variation of the laminar flame speed as a function of the equivalence ratio Φ for an unstrained laminar methane-air flame [154]. The data has been calculated with different levels of model complexity as for the adiabatic flame temperature. The results of the complex transport model (red dots) show a peak of the laminar flame speed of almost 40 cm/s in the slightly rich region. These results are in very good agreement with experimental findings [151]. In contrast, significant deviations can be observed when using the same molecular diffusion coefficient for all species by setting $\mathrm{Le} = 1$. The simplified model shows the peak flame speed in the slightly lean branch and generally reduced flame speeds. It is clear that the assumption seems to influence the calculated results to a certain extent. Again, depending on the actual aim of the numerical investigation it is important to choose the right

level of modeling detail. All experiments in this thesis were conducted in a range between $\Phi = 0.7$ and $\Phi = 1.0$. Using the complex mechanism this results in significantly varying laminar flame speeds between $s_l = 20\,\mathrm{cm/s}$ and $s_l = 40\,\mathrm{cm/s}$, respectively. For the simplified model the predicted flame speed reduces to values between $s_l = 18\,\mathrm{cm/s}$ and $s_l = 28\,\mathrm{cm/s}$, which is up to 30% lower than with the complex model. Hence, for numerical investigations of flashback (e.g. using LES) detailed chemistry and transport modeling should be implemented.

In the laminar case the propagation velocity depends uniquely on the thermal and chemical properties of the mixture. In contrast, a turbulent premixed system depends additionally on the flow field. The turbulent flame front is wrinkled by the velocity fluctuations. Hence, the effective cross sectional area of the turbulent flame A_t crossed by mass is significantly increased. A much higher mass flow rate is needed to stabilize a turbulent flame. Hence, with respect to Eq. (2.69) which is based on the cross section of the tube, there will be an apparent increase in the flame propagation velocity. In this situation the nominal cross section can be interpreted as a time averaged flame front or 'flame brush'. Thereby it is recognized that the instantaneous flame front my be highly wrinkled and fluctuating wildly. The velocity is then called turbulent flame speed s_t and is sketched on right hand side of Fig. 2.13. In summary, a premixed flame can be stabilized in a region where the local flow velocities match the flame propagation speed. From continuity considerations the ratio between s_t and s_l can be expressed as the ratio between the wrinkled flame front A_t, caused by velocity fluctuations u' of the flow, and the tube's cross sectional area A_0

$$\frac{s_t}{s_l} = \frac{A_t}{A_0}. \tag{2.70}$$

For large fluctuations of u' with respect to s_l Damköhler [33] proposed the functional relationship

$$\frac{s_t}{s_l} = 1 + \frac{u'_{rms}}{s_l}. \tag{2.71}$$

The relation describes the impact of large vortex structures that wrinkle the flame front by a purely kinematic approach. Hence, Eq. (2.71) models the influence of *large scale turbulence* on the propagation speed of the flame front. If the size of the vortex structures is in the order of the flame thickness l_f or less, they can penetrate into the flame front. Thereby an intense turbulent transport inside the flame front can be observed. In addition to the flame wrinkling mechanism it alters the flame structure and the propagation speed. Damköhler [33] identified the ratio between laminar and turbulent flame speed dominated by *small scale turbulence* to behave according to

$$\frac{s_t}{s_l} = \left(\frac{u'_{rms} l_0}{s_l l_f}\right)^{1/2}. \tag{2.72}$$

A classification of premixed combustion under the influence of large or small scale turbulence can be pursued. This is useful to identify whether the structure of the flame front and its thermo-chemical state is altered by the penetration of eddies or if the flame front, though wrinkled, can be still treated as laminar. Damköhler [33] was the first to propose a scale comparison which is expressed by the non-dimensional Damköhler number

$$\mathrm{Da} = \frac{\tau_t}{\tau_c} = \frac{(l_0/u'_{rms})}{(l_f/s_l)}. \tag{2.73}$$

This expression is the ratio between the turbulent time scale of the flow field τ_t and the time scale of the chemical reactions τ_c. Both can be expressed by a characteristic length and velocity scale, namely (l_0/u'_{rms}) for the turbulence and (l_f/s_l) for the chemistry.

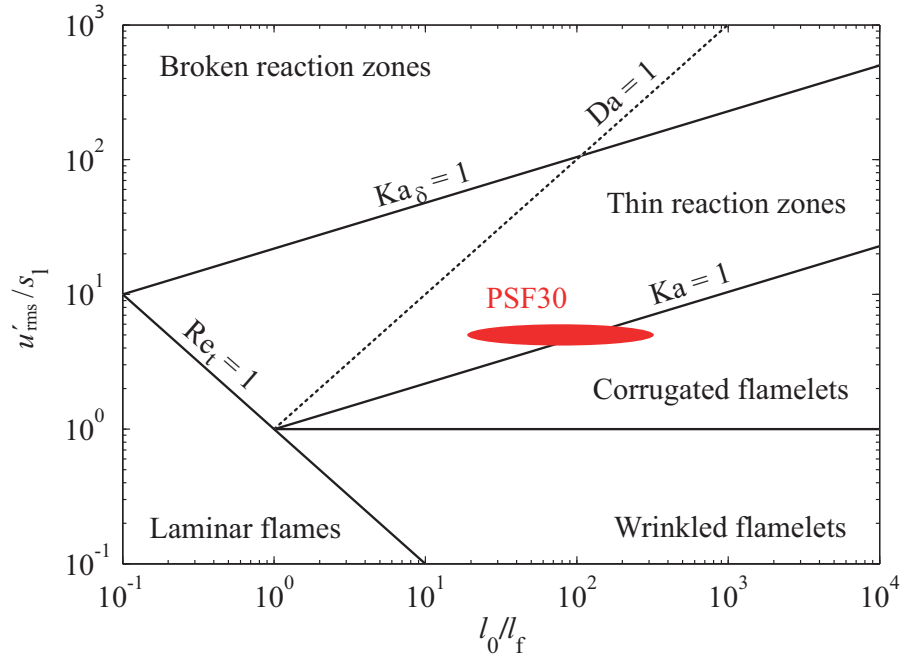

Figure 2.14: Borghi-Peters regime diagram for premixed flames under the influence of turbulence

To allow for a refined classification of turbulence-flame interaction the Karlovitz numbers were introduced. By comparing the laminar flame thickness l_l and the thickness of the inner reaction layer l_δ to the dissipative Kolmogorov scales of the flow, the turbulent Karlovitz numbers can be defined as [211]

$$\mathrm{Ka} = \frac{{l_f}^2}{{l_\eta}^2} \tag{2.74}$$

and

$$\mathrm{Ka}_\delta = \frac{{l_\delta}^2}{{l_\eta}^2}. \tag{2.75}$$

Using the equations (2.74), (2.75), and (2.73) a classification of premixed flames can be pursued as shown in Fig. 2.14. The *regime diagram* is originally based on the work of Borghi [18] and later modified by Peters [150]. It classifies premixed flames based on the ratio of turbulent and chemistry length and velocity scales. Therefor the non-dimensional parameters (l_0/l_f) and (u'_{rms}/s_l) are used. In the double logarithmic representation of Fig. 2.14 the regime of purely laminar flames is demarcated from turbulent flames by the $\mathrm{Re}_t = 1$ line. According to Peters [150] turbulent premixed flames can be classified into three different regimes by the previously defined Karlovitz numbers Ka and Ka_δ.

The *flamelet* regime is characterized by a very thin flame front compared to the smallest dissipative structures of the flow field ($l_f < l_\eta$). These can only kinematically wrinkle the flame front, thus changing the large scale appearance while its laminar structure is maintained. According to Damköhler it represents the regime of large scale turbulent structures. This regime can be further divided into *wrinkled* and *corrugated* flamelets. In the former the flame front is merely stretched and wrinkled by fluctuations smaller than the laminar flame speed ($u'_{rms} < s_l$). The latter however characterizes the regime of flamelets where the turbulent fluctuations exceed the laminar

flame speed ($u'_{\mathrm{rms}} > s_{\mathrm{l}}$). In this regime fluctuations larger than s_{l} can partially breach the flame front, modifying its topology. Thereby detached flame fronts can occur while the laminar flame structure is still maintained. This class of premixed flame is present in the *corrugated* flamelet regime.

The transition from the class of corrugated flamelets to *thin reaction zones* is delineated by the straight line where $\mathrm{Ka} = 1$. Following the Klimov-Williams-criterion [218] this line describes the equality of size of the Kolmogorov vortices and the flame thickness. $\mathrm{Ka} > 1$, hence $l_\eta < l_{\mathrm{f}}$, denotes the regime where the smallest vortices can penetrate into the preheat zone of the flame. Thus, it is dominated by small scale turbulence according to Damköhler. Thereby the equilibrium between the previously laminar convective transport and thermal diffusion upstream of the flame is altered by turbulent transport processes inside the preheat zone. However, the laminar structure of the inner reaction layer (l_δ) remains unchanged.

In case of very high fluctuations of the flow field even the inner reaction layer l_δ of the flame is affected by vortices. At $\mathrm{Ka}_\delta > 1$, which is associated with $l_\eta < l_\delta$, the smallest eddies can penetrate into the inner reaction layer. Thereby, the transport of heat into the preheat zone as well as the chemical processes inside the layer are modified by convective transport processes. This results in an increased flame thickness. The spreading of the reaction zone leads to a reduction in maximum heat levels if the total heat is assumed to remain constant. The reaction rates will decrease reducing the amount of newly formed radicals that promote the break up of fuel molecules. As a consequence, this can lead to local quenching of the flame and even to global extinction. *Broken reaction zones* are the result of the interactions of turbulence with the inner layer, which give the regime its name.

The classification of the investigated TECFLAM burner configurations [174] is marked by the red oval in Fig. 2.14. A detailed description of the burner and its operating conditions will be given in Chapter 3. The burner is operated in the regime of large scale turbulence in the transition region between corrugated flamelets and thin reaction zones. There the laminar flame structure is maintained and the flamelet model for numerical investigations seems to be adequate.

2.3 Flashback Mechanisms in Premixed Flames

With the possibility to reduce thermal $\mathrm{NO_x}$ emissions by premixed combustion the intrinsic problem of flame flashback arises. As fuel and oxidizer are already mixed to form a flammable mixture upstream of the combustion chamber, interactions between the flame and flow structures can enable the flame to propagate upstream into the fuel injection nozzle. This is detrimental to burner operation and longevity. Despite the difficulties the concept of premixed combustion has already been successfully applied to stationary gas turbines. These are typically operated at stationary conditions or in a narrow operational range. However, airborne gas turbine combustors have to cover a much wider operational range than stationary turbines. There, the parameters of the flow field inside the combustion chamber and the thermal power change significantly during a duty cycle of take-off, flight and landing. These requirements hamper the utilization of premixed combustion in airborne gas turbines. Therefore, this thesis aims at the investigation of flow and flame parameters on the flashback behavior of burners, typical for combustion chambers in stationary and airborne gas turbines.

The phenomenon of flashback is complex, not yet fully understood, and can occur through a variety of mechanisms. The next section will briefly summarize the most relevant mechanisms that can occur in technical premixed combustors.

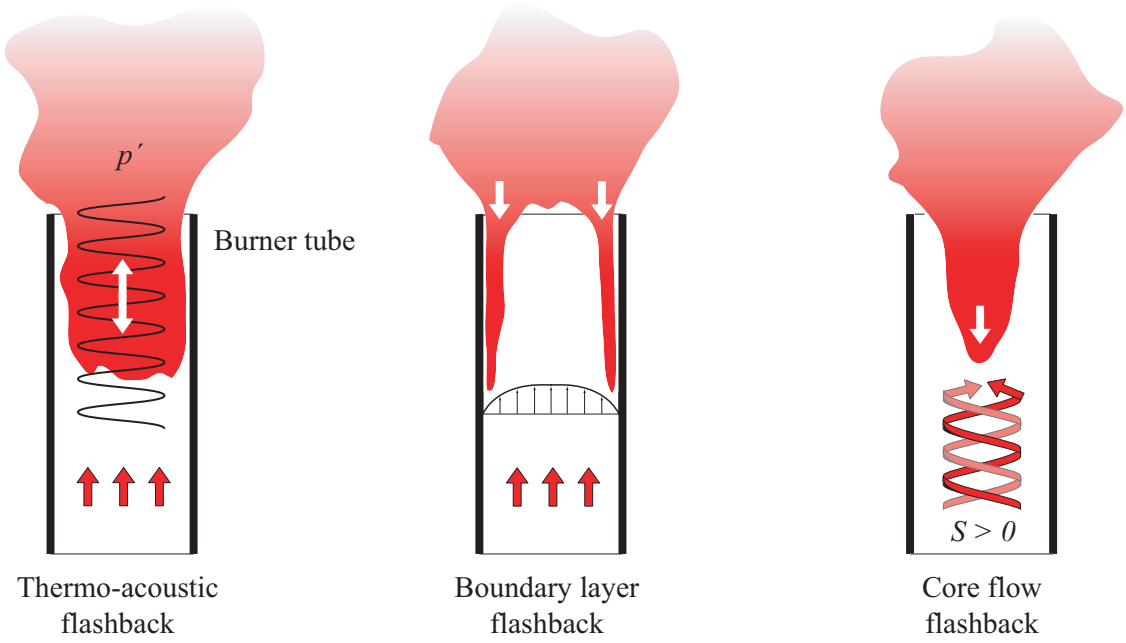

Figure 2.15: Overview of three different flashback classes

Some general challenges of premixed combustion have to be met in order to exploit the potential to reduce the emission of nitric oxides. Fuel-air mixtures within the flammability limits do not automatically produce a stable flame. Considering a simple lean premixed jet burner (e.g. a Bunsen burner) that stabilizes a cone-shaped flame at the burner exit, blow-off occurs when the gas flow rates are increased above a certain limit. In this situation there are no low velocity regions close to the burner exit region that match the flame speed. With larger distance from the burner dilution by ambient air reduces the equivalence ratio below the lean flammability limit, prohibiting a stable combustion. Hence, the previously stable burning flame lifts off and quenches due to mixing with ambient air. On the contrary, reducing the flow rates and thus the exit velocities below a critical limit enables the flame to move upstream into the fuel injector. The propagation of the flame into the burner parts upstream of the actual combustion chamber is known as flame flashback. In this case the turbulent flame speed s_t exceeds the local mean velocity $\overline{u}$, which can be formulated as the fundamental flashback criterion

$$s_t > \overline{u}. \tag{2.76}$$

This mechanism of bulk velocity flashback is one of the several types of flashback mechanisms that can occur in premixed combustors. In order to produce a stable flame in gas turbine combustion chambers the phenomenon of vortex breakdown of turbulent swirling flows is utilized (see Section 2.1.2). Hereby, a zone of rather low velocities inside the combustion chamber can be generated by the development of an IRZ to match the local flame speed over a wide operational range. The interactions of the turbulent swirl flow and the flame give rise to further complex mechanisms that enable the flame front to propagate upstream. In order to classify the state-of-knowledge of flame flashback, the following subsections will give an overview on the so far identified flashback mechanisms. These include *thermo-acoustic* flashback, flashback *in boundary layers* and flashback *in the core flow*. A rudimentary picture of the three classes of mechanisms are shown in Figure 2.15.

2.3.1 Thermo-Acoustic Flashback

Flashback as a consequence of thermo-acoustic instabilities can be observed in enclosed flames. Here, turbulent combustion generates acoustic waves that are in resonance with an acoustical mode of the combustion chamber. In 1878 Lord Rayleigh was the first to investigate the phenomenon analytically [159]. He posed that the thermo-acoustical coupling occurs if pressure and heat release fluctuations are in phase. This results in an energy gain of the instability. The relationship is mathematically described by the Rayleigh criterion

$$\int p' \dot{q}' dV > 0, \tag{2.77}$$

where p' and q' denote the pressure and heat release fluctuations, respectively, within the control volume V. The various mechanisms that generate thermo-acoustic instabilities are summarized in [24, 103, 154] and are still under investigation. Thermo-acoustic instabilities in gas turbines appear preferentially in lean premixed systems [28, 103, 125, 181]. They can be initiated, when acoustic pressure fluctuations interact with the air and fuel feed system of the combustion chamber. The principle mechanism of thermo-acoustic instabilities is briefly described as such limit cycle pressure fluctuations have been observed in the experiments. In the course of these interactions fluctuations in the mass flows arise that generate either perturbations of the global inlet flow of premixed gas or of the equivalence ratio. The latter can occur when the acoustic impedance of air and fuel feed system vary significantly from each other. Both kinds of fluctuations result in oscillations of the heat release. In turn, these oscillations amplify the acoustic fluctuations. The feedback loop can be described by the following mechanism

$$p' \quad \rightarrow \quad u' \quad \rightarrow \quad \dot{q}' \quad \rightarrow \quad p' \tag{2.78}$$

where u' is the unsteady velocity as a consequence of mass flux fluctuations. During excitation of a resonant chamber mode the pressure fluctuations can grow to such an extent that the resulting velocity fluctuations exceed the bulk velocities in the fuel-air injection system. Hence, the flame is convected up and downstream with an amplitude that it can reach vital burner parts adjacent to the actual combustion chamber. Usually these parts of the structure are not designed for exposure to the flame temperatures. Apart from the role of acoustics in the generation of thermo-acoustic instabilities, there can be other sources that provoke the occurrence of these kinds of instabilities [24]. Among the many possible causes, some are of special relevance since these cause fluctuations in heat release or generate pressure perturbations. The most important are:

- Unsteady strain rate
- Flame–vortex interactions
- Acoustic–flame coupling
- Interactions of perturbed flames with the boundaries
- Flame response to the incident composition inhomogeneities

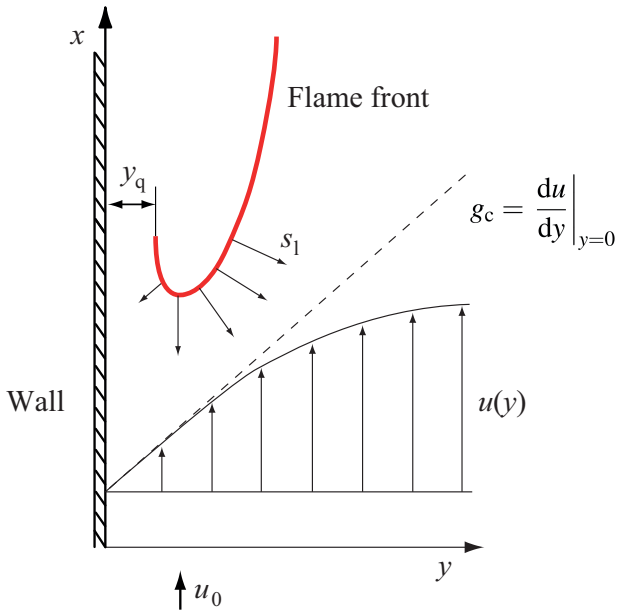

Figure 2.16: Schematic of the mechanism for flashback inside a boundary layer

2.3.2 Flashback in Boundary Layers

Within a wall boundary layer Eq. (2.76) is seemingly fulfilled as the velocity near the wall approaches zero. Thus the flame speed exceeds the local flow velocity. However, the effect of wall quenching can prevent the upstream propagation of the flame near a wall. As the flame approaches a wall it experiences a loss of both, heat and radicals. The closer the distance of the flame to the wall, the slower are the local flow velocities in the boundary layer. At the same time the reaction rates decrease due to an increase in heat loss to the wall and an increase in chain termination reactions. This continues until a distance is reached where the flame cannot be sustained anymore and extinguishes locally within the quenching distance l_q. The effect of the boundary layer velocity profile, quenching distance and its consequences on the flame propagation within a laminar boundary layer have been extensively studied by Lewis and von Elbe [123]. They define a velocity gradient g_c at the wall that results in an equilibrium of the local laminar flame speed and flow velocity at the flame's quenching distance from the wall $u(y_q) = s_l$. It can be stated as

$$g_{crit} = \left.\frac{du}{dy}\right|_{y=0} = \frac{s_l(y = y_q)}{y_q} \tag{2.79}$$

The critical velocity gradient g_c generally depends on many parameters. These are the fuel-oxidizer kinetics, the equivalence ratio, the temperatures of the flow and the wall, the pressure, the state of the boundary layer, and the flow geometry. Fig. 2.16 depicts the situation that defines the critical gradient. In the case that a given wall profile $u(y)$ comprises a wall gradient which is below the critical value g_c, the flame is able to propagate upstream inside the boundary layer causing a flashback. Harris et al. [73] found a critical gradient of $g_c = 400\ s^{-1}$ for a stoichiometric methane-air flame in the specific case of a cylindrical Bunsen burner. The quenching distance was experimentally determined to be $y_q = 2.4$ mm.

Turbulent transport inside the boundary layer considerably increases the flashback propensity [56, 57, 99]. In the past only tube burner setups were investigated, and thus turbulent flashback

limits were only derived for a fully developed Blasius wall friction profile. Details of the flame propagation in the proximity of the wall remain unclear for turbulent flows [46].

2.3.3 Flashback in the Core Flow

Apart from thermo-acoustic flashback and propagation inside the wall boundary layer, flashback in the core of the flow can also be observed. The problem of flashback of premixed flames inside laminar Hagen-Poiseuille flows was investigated by Daou et al. [35] and Dery [38]. It will not be detailed further since the focus of this thesis is on highly turbulent combustion in airborne gas turbines. Turbulent flow in combination with a swirling motion, gives rise to a number of different mechanisms that enable the flame front to propagate towards the oncoming gas mixture in the core flow region.

For high levels of turbulence it can be imagined that the flame front can propagate upstream according to Eq. (2.76) even without a swirling motion. The estimation of Damköhler's turbulent flame speed according to equation (2.71) enables a simple approach to derive a flashback criterion based on the turbulence level [109]. For typical turbulence levels in practical burners $T_u = u'_{\mathrm{rms}}/\overline{u} = 10-20\ \%$ one obtains

$$s_{\mathrm{t}} \approx s_{\mathrm{l}} + \frac{u'_{\mathrm{rms}}}{\overline{u}} \cdot \overline{u} \approx s_{\mathrm{l}} + [0.1-0.2] \cdot \overline{u}. \tag{2.80}$$

Since the laminar flame speed of a methane-air mixtures is one order of magnitude smaller than typical bulk velocities in practical combustion systems Eq. (2.80) simplifies to the final form

$$s_{\mathrm{t}} \approx T_u \cdot \overline{u} < \overline{u}. \tag{2.81}$$

Hence, the flashback criterion (2.76) is not fulfilled and upstream flame propagation in the core flow is therefore unlikely. However, the picture is different for the combustion of hydrogen containing fuels. The increased reactivity and thus higher flame speeds as well as effects of preferential diffusion have to be taken into account.

The theory of flame flashback under the influence of a swirling motion is crucial in the context of this work. It is significantly different from the previously mentioned theory of non-swirled propagation in the core. Literature review reveals a vast number of theories to explain the mechanism. The spectrum of different explanations for flashback vary from 'fundamentally different' to 'principally the same' [84]. The following sections provide an overview of the theory of flame propagation along the axis of a vortex tube. It is noted that in the current study the presence of a bluff-body (see Section 3.1) modifies the investigated configuration with respect to the vortex tube theory. However, two classes of mechanisms will be presented: mechanisms driven by classical aerodynamics and mechanisms that are based on baroclinic torque in the context of the vorticity conservation equation.

Mechanisms based on Aerodynamics

The class of mechanisms that are based on aerodynamical forces constitutes on the generation of a positive pressure gradient along the vortex axis in the presence of the flame [84]. The influence of the flame is taken into account by the theories in form of the density gradient across the flame front. In these mechanisms a pressure gradient pushes the fluid upstream against the approaching flow. Consequently, this enables the flame front to propagate upstream. It is basically a similar

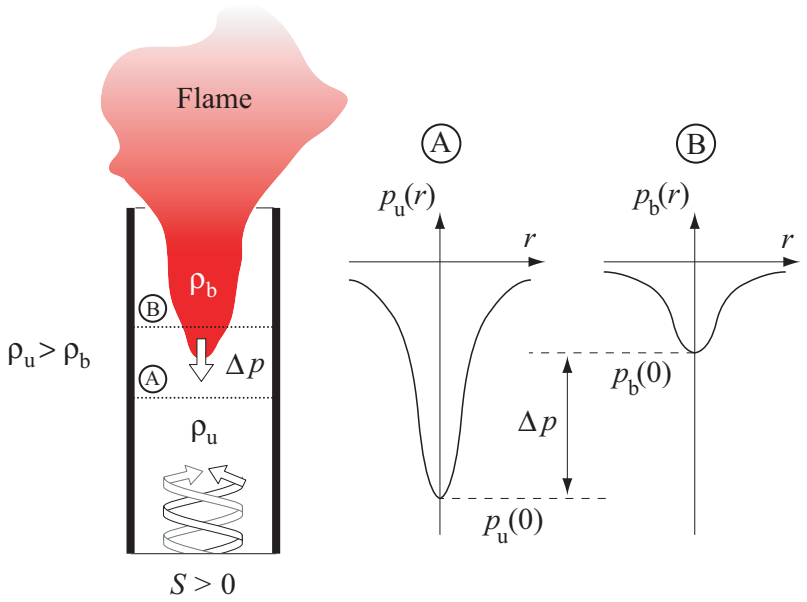

Figure 2.17: Schematic of the mechanism of flashback by the vortex bursting theory

effect as in the vortex breakdown mechanism described in Section 2.1.2. The various theories mainly differ in the modeling of the propagation speed. However, they are all based on the same physical mechanism.

In 1974 McCormack [133] considered the density jump between burnt and unburnt mixture in vortex rings to induce an instability that leads to rapid upstream flame propagation. However, he rejected this as a full mechanism to explain the upstream propagation. Chomiak [26] was the first to develop a mechanism based on the density jump within a vortex which explains an increase in velocity on the vortex axis. His postulated *vortex bursting* theory, termed in analogy to the purely aerodynamic 'vortex breakdown' mechanism, has received considerable interest from many researchers since its publication in 1977. Based on McCormacks observations he proposed the model that is depicted in Fig. 2.17. Disregarding the axial and radial velocities, the pressure distribution of an assumed Rankine vortex [2] can be obtained from the simplified form of the Navier-Stokes equation (see Eq. (2.5)) in cylindrical coordinates to read

$$\frac{1}{\rho_i}\frac{\partial p}{\partial r} = \frac{\omega^2}{r}, \tag{2.82}$$

where ω is the tangential velocity. Equation (2.82) integrates to yield the difference in pressure between p_i in the inner region (on the axis) and p_o in the outer regions of the vortex as

$$p_\mathrm{o} - p_\mathrm{i} = \rho_i \int_0^\infty \frac{\omega^2}{r}\mathrm{d}r = \rho_i w_\mathrm{max}^2. \tag{2.83}$$

For a Rankine vortex the integral of the second term yields the squared maximum tangential velocity w_max^2. The density jump across the flame leads to a large pressure difference $\Delta p = p_\mathrm{b} - p_\mathrm{u}$ on the axis of the vortex. Assuming an equilibrium between the pressure forces caused by the vortex and the momentum flux due to the 'pulling' of the flame inside the vortex, the

upstream flame propagation velocity s_b, or bursting velocity, can be expressed by

$$s_b = w_{\max}\sqrt{\frac{\rho_u}{\rho_b}}. \tag{2.84}$$

Similarly, Hanson and Thomas in 1984 [71] argued that the flame speed enhancement along the axis is no more than the effect of the centrifugal force. It flings out components of higher density, i.e. the cold gas, and attracts the hot and therefore lighter components to the axis. There, it extends along the axis according to the fact that a light density burnt gas will be forced towards the center. They termed their model *penciling effect*. Their paper shows that if a constant pressure at the wall is assumed, there exists a higher pressure in the less dense medium at the centerline. As it is described in Chomiak's theory this pressure difference on the axis drives the flame upstream.

In 1987 Daneshyar and Hill [34] published a refined theory of the vortex bursting concept using the angular momentum conservation equation. This finally models the propagation speed almost identical to Chomiak's theory.

In his experiments in 1992 Asato [8] found out that the flame speeds were much slower than predicted by the developed theories. They modified the theories to match their experiments. This was done by taking the flame diameter into account along with an average pressure difference – a concept already introduced in [34]. Their *finite flame diameter* model overestimated the flame speeds compared to their experiments.

A steady state model which takes the axial flow velocity into account was proposed in 1994 by Atobiloye and Britter [10]. Using Bernoulli's equation in the limit of an unconfined free vortex flow they obtained an expression which gives much lower flame speeds than the previous models.

In 1996, Sakai and Ishizuka [171] proposed a model that for the first time was able to describe experimental results qualitatively as well as quantitatively. Their *back pressure* theory considers mass and angular momentum conservation as well as axial momentum conservation through Bernoulli's equation and also the burning rate.

A final mechanism which is based on the breakdown of the vortex is the *azimuthal vorticity evolution* model by Umemura and Tomita in 2001 [205]. In their model the authors explain the vortex breakdown in the core flow through the azimuthal vorticity production. This is in contrast to the previous argumentation where vortex breakdown is induced by an axial pressure gradient. However, they obtain the same equations as presented in the back pressure mechanism. Hence, this azimuthal vorticity evolution mechanism can be categorized as a sub-class of the vortex bursting mechanism, based on the pressure difference [84].

The predicted flame speeds of the various models are summarized in Table 2.1.

Mechanisms based on Baroclinic Torque

In contrast to the previous, this class of flashback mechanisms disregards pressure as the driving force of flashback. The physics governing these mechanisms emerge from a different perception than considering the momentum conservation in a Cartesian or cylindrical coordinate system. The basis of the theoretical considerations is the vorticity field, which is a physical quantity

[5] Propagation speed of the flame within a turbulent swirl flow.
[6] Propagation speed for a flame tip radius smaller than the vortex core radius ($\alpha \leq a$).
[7] Propagation speed according to the condition $s_\mathrm{b} \geq \rho_\mathrm{u} s_\mathrm{b}/\rho_\mathrm{b}$. σ is an arbitrary constant.

Table 2.1: Overview of various aerodynamic flashback mechanisms with their associated flame propagation speeds

Author	Year	Description	Model	Ref.
Chomiak	1977	Vortex bursting	$s_\mathrm{b} = w_\mathrm{max}\sqrt{\frac{\rho_\mathrm{u}}{\rho_\mathrm{b}}}$	[26]
Hanson et al.	1984	Pencilling effect	$\Delta p = \frac{1}{2}\rho_\mathrm{u} w_\mathrm{max}^2\left(1-\frac{\rho_\mathrm{b}}{\rho_\mathrm{u}}\right)$	[71]
Daneshyar et al.	1987	Steady state[5]	$s_\mathrm{b} = w_\mathrm{max}\sqrt{\frac{2}{3}\frac{\rho_\mathrm{u}}{\rho_\mathrm{b}}}$	[34]
Asato et al.	1992	Finite flame diameter[6]	$s_\mathrm{b} = \frac{\alpha}{2a} w_\mathrm{max}\sqrt{\left(\frac{\rho_\mathrm{u}}{\rho_\mathrm{b}}-1\right)\left(1-\frac{\alpha^2}{4a^2}\right)}$	[8]
Atobiloye et al.	1994	Steady, immiscible	$s_\mathrm{b} \propto w_\mathrm{max}\sqrt{1-\frac{\rho_\mathrm{b}}{\rho_\mathrm{u}}}$	[10]
Ishizuka et al.	1998	Back pressure[7]	$s_\mathrm{b} = \sqrt{\frac{\rho_\mathrm{u}}{\rho_\mathrm{b}} s_\mathrm{l}^2 + (1+\sigma) w_\mathrm{max}^2}$	[85]

derived from the velocity field u_i as[8]

$$\vec{\omega} = \nabla \times \vec{u}. \tag{2.85}$$

Using Eq. (2.85) a flow can be described by the vorticity transport equation of a rotational symmetric, inviscid, compressible flow. That is

$$\frac{\mathrm{D}\vec{\omega}}{\mathrm{D}t} = (\vec{\omega}\cdot\nabla)\vec{u} - \vec{\omega}(\nabla\cdot\vec{u}) + \frac{1}{\rho^2}\nabla\rho\times\nabla p. \tag{2.86}$$

Following the structure of a general transport equation as defined in Eq. (2.3) the left hand side of Eq. (2.86) represents the material derivative of vorticity. It expresses the change of vorticity that a particle experiences moving with the flow. The terms on the right hand side describe the change of vorticity due stretching and tilting of the streamlines (first term), volumetric expansion (second term) and the so-called *baroclinic torque* (third term). While stretching and tilting of the streamlines is inherent in turbulent flows, the second and the third terms on the right hand side gain importance in reacting flows with large density gradients. Neglecting the first two terms Ashurst [9] in 1996 was the first to focus on the baroclinic torque to account for rapid upstream flame propagation. The expression for the baroclinic production of vorticity as

$$\left(\frac{\mathrm{d}\vec{\omega}}{\mathrm{d}t}\right)_\mathrm{bar} = \frac{1}{\rho^2}\nabla\rho\times\nabla p, \tag{2.87}$$

was first derived by Silberstein [183] in 1896 and two years later used by Bjerknes [17] to explain the properties of geophysical fluids. The equation describes the production of vorticity due to the misalignment between the local density and pressure gradient. If the local pressure and density gradient vectors span a plane in vector space, the fluid element is exposed to a rotational force, resulting in a vorticity vector perpendicular to the created plane. For an alignment of 90° the baroclinic vorticity or 'torque' is maximum, whereas a parallel alignment of the density jump in a flame and the local pressure gradient does not create vorticity. The influence of baroclinic torque on a propagating premixed flame inside a vortex tube is schematically shown in Fig. 2.18.

[8] For convenience vector notation is used to mathematically express the flow physics from the perspective of the vorticity transport equation.

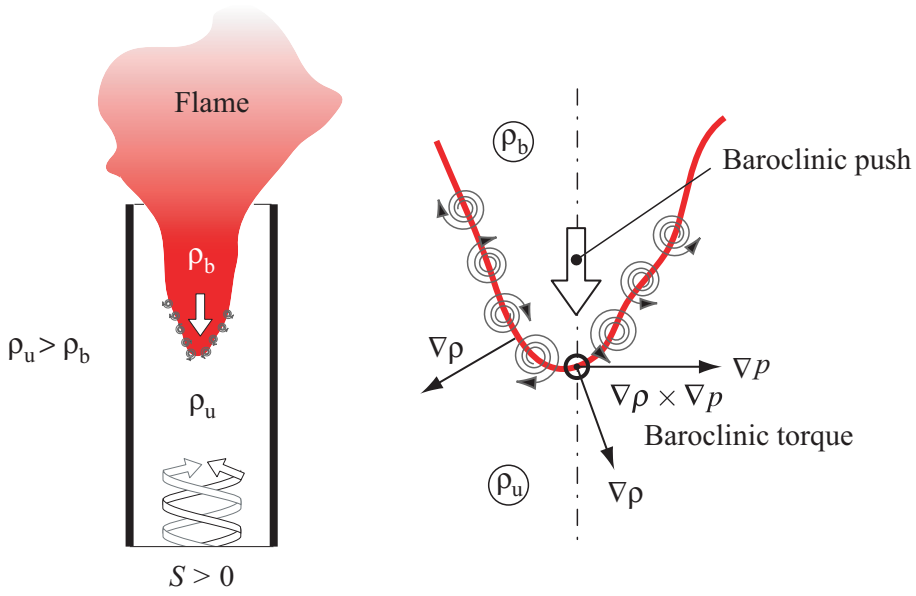

Figure 2.18: Schematic of vorticity production due to baroclinic torque [9]

Baroclinic torque is created due to the inclination between pressure gradient ∇p and density gradient $\nabla\rho$ of the axially propagating flame. The generated vorticity field can be transformed into an axial velocity at a certain distance from the center of vorticity by the law of Bio-Savart [190]. Thereby, it reveals a negative axial component on the axis that 'pushes' the flame upstream towards the fresh gas mixture. The mechanism is therefore termed *baroclinic push* by Ashurst [9]. However, he also states that this is not the only reason for flame upstream propagation but an important contribution.

In 2003 Fritz and Kröner [60] identified the baroclinic push to play an important role in flashback inside the premixing tube of a model gas turbine combustion. In their investigated swirl configuration the presence of the flame leads to vortex breakdown inside the tube that is not present in the isothermal flow field. Hence, they termed the phenomenon *Combustion-Induced Vortex Breakdown* (CIVB).

In a subsequent study Kiesewetter [101] investigated numerically the contribution of the three terms on the right hand side of the vorticity transport equation (2.86). He found that for a stable configuration the stretching and tilting dominates the vorticity generation whereas volumetric expansion and baroclinic torque contribute very little. However, during the transition from the stable combustion to an upstream propagating flame, he could show that volumetric expansion and baroclinic torque have a significant influence. Further analysis showed that volumetric expansion hinders upstream propagation while baroclinic torque promotes it. Thus, both terms are in competition and the net effect determines whether the flame following the IRZ can move upstream or is convected out of the mixing tube.

The influence of turbulence-chemistry interactions on the flashback behavior according to CIVB were investigated further by Konle [110–112]. His studies resulted in a broadly applicable flashback model (see section 5.2).

3 Swirl Burner

This chapter introduces the swirl burner in which the phenomenon of flashback has been investigated. Swirl-stabilized combustion is a broadly utilized technique in gas turbine combustors, internal combustion engines, power station burners and many more. The mechanism of swirl-stabilized combustion as well as its advantages are well documented [199]. Flame stabilization can be achieved over a wide operational range through the formation of flow regions with low velocities which can be matched by the turbulent flame speed. It relies on the formation of a central recirculation zone which, furthermore, recirculates heat and radicals.

In this chapter the geometrical parameters as well as the special method of initiating the swirled fluid motion will be detailed. Modifications have been applied to its original configuration in order to enable the application of the various optical measurement techniques which will be thoroughly described in Section 4.1. The modifications will be highlighted before the operating conditions and the procedure to initiate the flashback are explained. Finally, an overview of the infrastructure is provided that complements the test rig.

3.1 TECFLAM Burner

The burner is a part of the TECFLAM work group which is a national collaboration to investigate swirled combustion under gas turbine conditions. In Fig. 3.1 a schematic of the burner is shown. It was originally operated in a non-premixed mode and was investigated experimentally as well as numerically [96, 163, 176]. To allow for premixed operation the burner was later redesigned by Schneider [173].

As illustrated by the arrows in Fig. 3.1 air is supplied from the bottom and mixes with methane which is injected from a circular manifold. The manifold is located 70 mm upstream of the moveable block swirl generator. A large number of small holes in the circular manifold guarantee the proper mixing of methane and air around the annulus. The mixture enters the swirl generator after a 90° deflection of the flow towards the central axis. The flow exits the swirler in axial direction into an annular slot. This has an outer diameter of 60 mm and a slot width of 15 mm. The stabilization of the premixed flame is provided by the initiated swirl, which forms a central recirculation zone above a swirl number of $S_g = 0.5$ [78]. The presence of the bluff-body defines the axial location of the recirculation zone and creates another smaller recirculation zone on its top, which is similar to a backward facing step. The bluff-body fills the central space on the axis up to the exit of the burner nozzle and is water-cooled, such that effects of increasing wall temperatures during the measurements could be neglected. As required in gas turbine combustors, this burner geometry provides a stable and stationary combustion over a wide operational range [122].

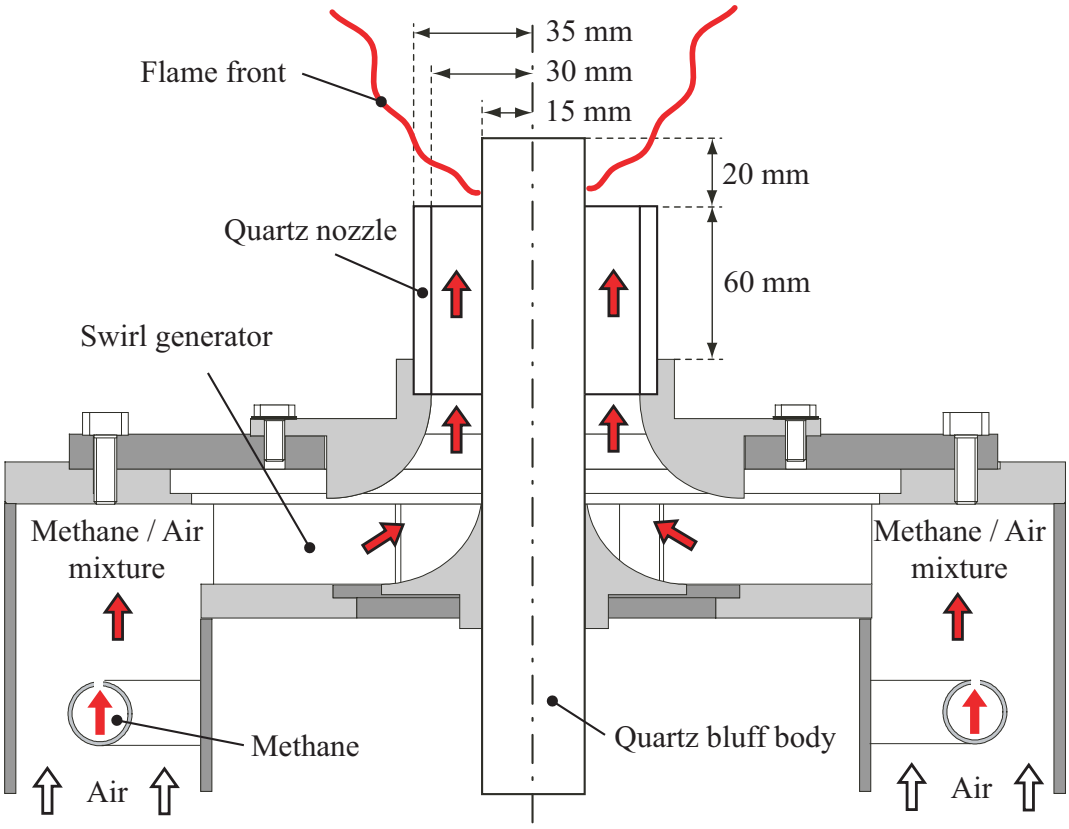

Figure 3.1: The TECFLAM burner in its investigated configuration

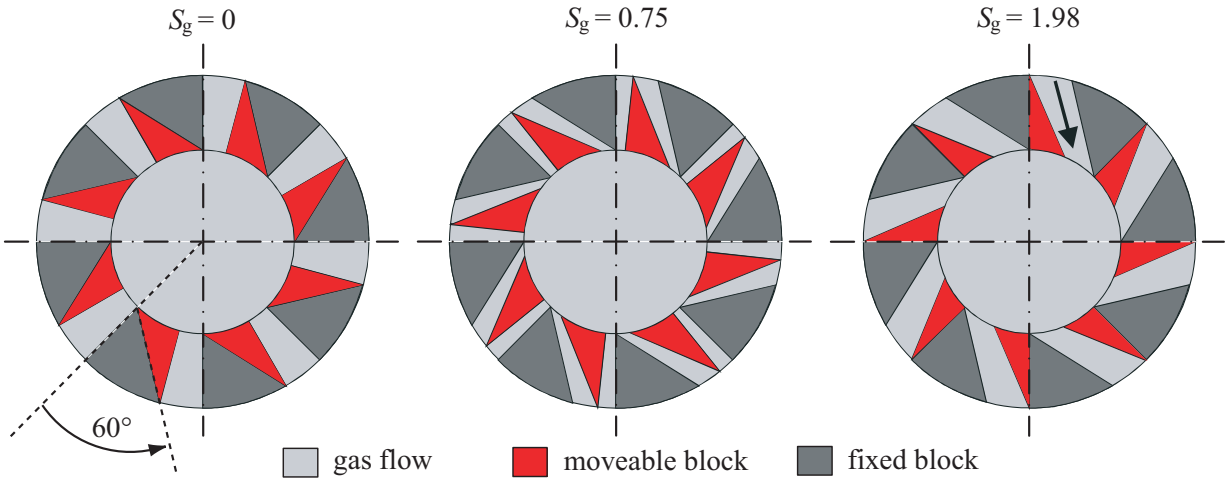

Figure 3.2: Moveable block design of the swirl generator

Table 3.1: Variables for determining the geometrical swirl number S_g

Geometrical parameters	Symbol	Value
Number of channels	n	8
Tangential channel wall angle	β	60°
Maximum rotation of moveable block	ϑ_{max}	15°
Channel height	H	24 mm
Inner radius of outlet area	R_i	15 mm
Outer radius of outlet area	R_o	30 mm

3.1.1 Swirler Design

The initiation of the swirl is based on the *moveable block* principle [121], which is shown in Fig. 3.2. The flow enters the moveable block in negative radial direction towards the axis and exits in axial direction as indicated by the arrows. The block consists of an upper and lower segment in which radial and tangentially inclined channels are shaped. The inclination of the latter type of channels is 60° with respect to the radius. Continuously variable swirl numbers S_g can be produced by the rotation of the lower moveable segment. S_g is defined by the geometrical properties of the swirl generator and can be estimated as a function of the moveable block rotation ϑ by the expression [121]

$$S_g(\vartheta) = \frac{\pi}{n\vartheta_m} \frac{\sin(\beta)\cos(\beta)(1+\tan(\beta)\tan(\vartheta/2))\frac{\vartheta}{\vartheta_{max}}}{\left[1-[1-\cos(\beta)(1+\tan(\beta)\tan(\vartheta/2))]\frac{\vartheta}{\vartheta_{max}}\right]^2} \frac{R_o}{H}\left[1-\left(\frac{2R_i}{2R_o}\right)^2\right], \qquad (3.1)$$

Here, n is the number of channels, H is the channel height, ϑ_m is the maximum angle of the moveable block, R_o and R_i are the outer and inner radii, and β is the inclination of the tangential channel walls. The different parameters in Eq. (3.1) are listed in Table 3.1 which are needed in order to calculate the geometrical swirl number of this specific burner. In the case of a purely radial inflow the geometrical swirl number is zero. A maximum swirl number of $S_g = 1.98$ can be achieved by turning the lower segment such that the radial flow channels are fully closed.

The moveable block was equipped with an electrical stepper motor to control the swirl number. By an additional gear reduction the theoretical swirl number could be changed in increments of $\Delta S_g = 0.02$ [141]. This was sensitive enough to reproduce the various operational modes of the flame as detailed in Section 5.1.

3.1.2 Burner Modifications

Several modifications were made to enable flame flashback observation. These are summarized in Fig. 3.3. In the original design increasing S_g until the critical swirl number is reached causes a sudden and rapid flashback upstream into the annular slot. This prohibits a thorough investigation of the transition from stable to flashback conditions. For this reason the original design with a flush-mounted central bluff-body (shown on the left hand side of Fig. 3.3) was modified by extending it 20 mm above the nozzle exit (shown on the right hand side). Through this measure the transitional regime between stable combustion and flashback (see Section 5.1) was extended and made experimentally accessible for sufficiently long observation times.

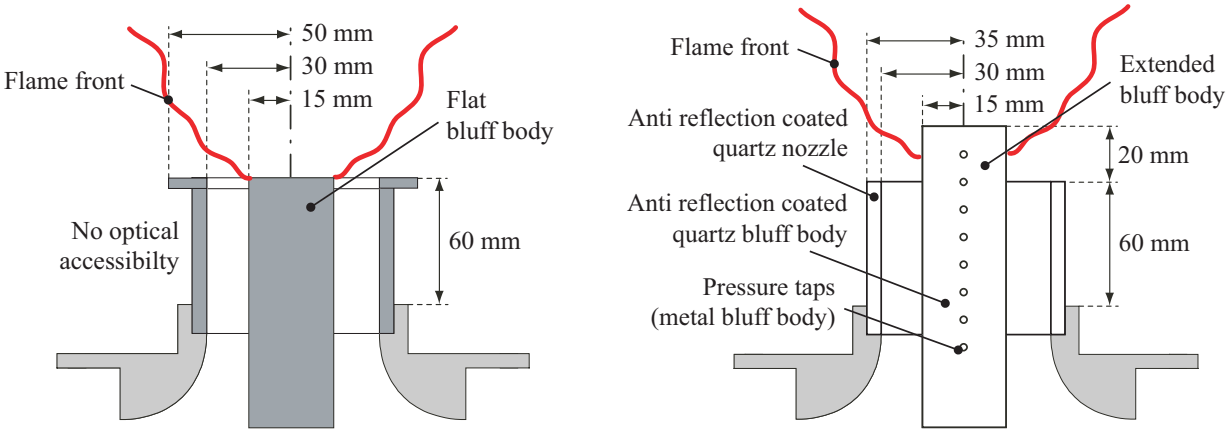

Figure 3.3: Original TECFLAM configuration used by Schneider [173] (left) and modified TECFLAM configuration with optical access and pressure ports on the bluff-body (right)

In addition, the outer nozzle and the central bluff-body were made from quartz to enable an optical access and minimize laser reflections. This was especially helpful in the most interesting region close to the bluff-body where the flame propagates upstream during flashback. Replacement of the metal bluff-body with a quartz one resulted in a significant reduction of the visible and UV stray light and facilitated the optical measurements. Anti-reflection coatings for 532 nm wavelength were applied to the quartz nozzle and also to the quartz bluff-body to further decrease the reflections. This is highly important when the observation angles deviate from 90°, e.g. in Stereo-PIV measurements.

In order to measure the gage pressure on the bluff-body wall, the interior design of the water-cooled metal bluff-body was redesigned to accommodate two pressure transducers. Eight pressure measurement ports with a diameter of 1 mm in increments of 10 mm were axially installed as shown on the right hand side of Fig. 3.3. These were connected to pressure transducers (see Section 4.1.4) by copper tubes with equal length of 300 mm.

3.1.3 Operating Conditions and Flashback Initiation

The operational conditions of the burner during the measurements were based upon the configurations of Schneider [173]. Since the ventilation system of the laser laboratory is limited to a thermal load of $P_{\mathrm{th}} = 30\,\mathrm{kW}$, measurements were restricted to the `PSF30` and `30iso` configuration. However, measurements of higher thermal power were furthermore limited by the capabilities of the diagnostic system. At the 30 kW configurations the system performance to acquire temporally correlated data was nearly exhausted. This will be illustrated in more detail in Section 4.2.3. Thus, the basic reacting configuration `PSF30` were measured with a thermal power of 30 kW and a Reynolds number of 10,000, which was based on the hydraulic diameter. As a reference, the corresponding isothermal configuration `30iso` were furthermore recorded. The isothermal case features the same Reynolds number in an air flow. Differing from Schneider's base configuration with the swirl number $S_{\mathrm{g}} = 0.75$ and the equivalence ratio $\Phi = 0.833$ both parameters were varied to induce flashback. The sets of parameters for the two investigated configurations are shown in Table 3.2.

Stable operation of the burner under laboratory conditions does not naturally lead to flame flashback. There are three methods to trigger the flashback onset:

Table 3.2: Operating configurations of the TECFLAM burner for stable reacting conditions (PSF30) and isothermal conditions (30iso)

Parameter	Symbol	Unit	PSF30	30iso
Thermal Power	P_{th}	(kW)	30	–
Swirl number	S_{g}	(−)	0.75	0.75
Equivalence ratio	Φ	(−)	0.833	–
Methane flow rate	$\dot{V}_{\mathrm{fuel}}$	$(\mathrm{m}_{\mathrm{n}}^3/\mathrm{h})$	3.02	–
Air flow rate	$\dot{V}_{\mathrm{air}}$	$(\mathrm{m}_{\mathrm{n}}^3/\mathrm{h})$	34.9	35.6
Exit bulk velocity	$\overline{u}_{\mathrm{bulk}}$	(m/s)	4.95	4.66
Reynolds number	Re	(−)	9970	9680

- Lowering the Reynolds number reduces the bulk velocity of the approaching flow, thus increasing the ratio of the flame and flow speed. When a critical ratio is reached, the flame propagates upstream against the oncoming flow.
- Increasing the swirl number during operation is another method, investigated by Nauert et al. [141]. Correlations between the critical swirl number and the equivalence ratio as well as the critical swirl number and Reynolds number were experimentally determined.
- The third method was considered additionally in this study: a burner control was employed in LabVIEW® that enabled independent variation of the flow parameters during operation. Flashback could thus be triggered by increasing the equivalence ratio and hence the influence of the heat release while keeping the Reynolds and swirl numbers constant.

A direct result from the correlation of these operation parameters are the stability maps of the TECFLAM burner, presented in Section 5.2. These mark the onset of flashback depending on the operation parameters P_{th}, Re, S_{g}, and Φ.

3.2 Laboratory Infrastructure

The experiments were conducted in the laser laboratory of the department of Reactive Flows and Measurement Techniques (RSM: Reaktive Strömungen und Messtechnik) at the Technische Universität Darmstadt, Germany. The air-conditioned room offered constant environmental conditions for the delicate laser diagnostics hardware as well as for reproducible flashback conditions. The room temperature was held at 21 °C and 30% humidity.

The dry and oil free air for combustion and particle seeding for PIV was supplied at 12 bar by a large pressure vessel via copper tubes and hoses made of polyvinyl chloride that provided a constant air flow without pressure fluctuations. The methane was supplied by standard 50 L gas bottles at 200 bar lasting approximately one hour during stable operation before it had to be replaced. The volumetric flow rates of the three gas streams (air, seeding air, methane) were controlled by calibrated mass flow controllers (Bronkhorst High-Tech B.V., EL-FLOW) integrated into a LabVIEW® control program. The power limitations of the exhaust system were monitored by type K thermocouples measuring the gas temperature in the exhaust system.

Due to the complexity of the optical setup of the applied laser diagnostics, the burner was moved to vary the position of the measurement volume. This was accomplished by a LabVIEW®-

controlled three axes traverse system with individual stepper motor drive mechanism. Thereby the accuracy of absolute positioning was below 20 µm.

The LabVIEW® control software was individually programmed for the TECFLAM application. Besides extra safety features for the flashback experiments a ramp function was implemented that could vary either Φ or Re linearly with time, controlling the three mass flows without changing the other parameter. The accuracy and precision of the control system was tested to be sufficient for the current investigations. Details can be found in [97].

4 Methodology

The following chapter describes the methodology which was applied during the experiments. Non-intrusive laser imaging techniques were primarily used to simultaneously obtain multiple parameters relevant to flashback. These include the flow field, chemiluminescence and intermediate species concentrations. Pressure measurements complement the sophisticated techniques altogether enabling to investigate the interactions between turbulence and chemistry. The first section provides an overview of the physical principles of each diagnostic method. Following this basic introduction, a major part will describe further developments of the originally low speed techniques, of only a few Hertz acquisition rate, towards high speed kilohertz applications. Practical aspects as well as new perspectives on turbulent combustion that come along with fast acquisition rates will be highlighted. These high speed combustion diagnostics have been applied to the TECFLAM burner in various experimental setups which will be presented subsequently. The chapter closes with the processing of the simultaneously acquired multi-parameter data and a discussion on the measurement errors.

4.1 Combustion Diagnostics

Turbulence-chemistry interactions plays a major role in the onset and in the course of upstream flame propagation. This is suggested by the nature of the flashback phenomenon occurring in the premixed configuration of the TECFLAM burner. The utilized combustion diagnostics therefore were selected to capture both, the two- and three-component flow field as well as species concentrations. The latter was used to provide information on the instantaneous location of the thin flame front. The highly non-linear turbulence-flame interactions would be strongly influenced by intrusive methods with finite-sized probes, such as Hot-Wire Anemometry (HWA) and thermocouples. Thus, laser-based techniques were selected that minimally affect the combustion system under investigation during the measurements. On the one hand, this is particularly due to the fact that the number of interacting photons is very small compared to the number of molecules that are involved in the physicochemical processes of the flame. This holds true for purely spectroscopic methods like Laser-Induced Fluorescence (LIF). On the other hand, even in case of a particle seeded flow, as it is necessary using Particle Image Velocimetry (PIV), it was shown that the impact of the laser-illuminated particles on the flow-flame system can be neglected if the seeding properties are properly adjusted.

In the following the applied techniques of *Chemiluminescence* Imaging (CL), *Planar Laser-Induced Fluorescence* of the hydroxyl radical (OH-PLIF), two and three component *Particle Image Velocimetry* (PIV) and supplementing *gage pressure* measurements will be described by their fundamental physical principles. Although simultaneously applied during the measurements, the performance of these techniques will be discussed on their own as a start. The development of Q-switched DPSS lasers (DPSS: Diode-Pumped Solid State) and CMOS cameras (CMOS: Complementary Metal Oxide Semiconductor) has made an enormous leap forward during the last decade. Thereby it enabled to enhance acquisition rates of classical laser diagnostics

from a few Hertz to the kilohertz regime. The various aspects of high speed sampling-enhanced methods and their combination as well as their experimental realization is also a major part of this work and will be presented in a separate section (see Sec. 4.2). Three different experimental setups have been laid out and implemented in and around the TECFLAM burner in the course of the investigations on flashback. These are detailed before this chapter closes with a description of the post processing which has been applied to the acquired multi-parameter data and an assessment of accuracy and precision.

4.1.1 Chemiluminescence Imaging (CL)

Chemiluminescence is the emission of light as a result of a chemical reaction. It can be captured by an optical detector. When using an array detector, e.g. a camera, the technique is called chemiluminescence imaging. In the context of this work it refers to the visible emission of light by the flame. It has been used to qualitatively determine the global flame topology.

In 1856 the Scottish physicist William Swan was the first to study the spectral emission of C_2^* in hydrocarbon flames, the *Swan bands* [198]. Since then quantitative measurements of different luminescent species have been conducted [63]. CL is frequently used to get information about the flame front position and topology. In the recent years CL has further been applied as an indicator of the equivalence ratio and the heat release [114, 118] in gas turbines and laminar premixed methane-air flames. The latter has revealed detailed spatial intensity profiles of reaction zones [107]. The results show reasonable agreements with numerical simulations in the lean and stoichiometric regime. Fuel-rich conditions show disagreements in shape, peak location and emission zone thickness.

During combustion processes a variety of unstable species and radicals is created. Different electronically excited states are populated. The transition of these molecules into a lower energetic state happens by the release of energy which corresponds to the energy difference between the excited and ground state. Intermolecular collision is the main route for this energy transfer and is called *quenching*. However, to a certain extend the emission of light is the process that returns the molecule into its ground state. The signal of the spontaneous emission is called *chemiluminescence* as the energy to excite the molecules is delivered by the chemical reaction. The signal strength is directly proportional to the concentration of electronically exited species.

When burning methane the excited radicals OH^*, CH^* and C_2^* as well as the CO_2^* species are created. The particular energy difference and thus the wavelength of the light corresponds to the two electronic states of the transition. While the structure of triatomic molecules results in many different quantum mechanical states due to a large number of the molecule's vibrational and rotational degrees of freedom, comparably few states exist in diatomic molecules. This results in a broad emission spectrum of the excited CO_2^* molecule, while OH^*, CH^* and C_2^* exhibit discrete emission wavelengths. The energy of the photons $h\nu$ emitted by the transition

$$OH^* \longrightarrow OH + h\nu \tag{4.1}$$

result in a relatively narrow line in the spectrum of an methane-air flame compared to the broad background generated by the CO_2^* luminescence. Fig. 4.1 depicts a typical spectrum of a slightly lean methane-air flame.

To capture the global flame topology during flame flashback, the CL signal has been recorded by a CMOS high speed camera. Details of the experimental setup are given in Section 4.3. The camera recorded the full visible spectrum from $400 - 600$ nm without any additional filter. The

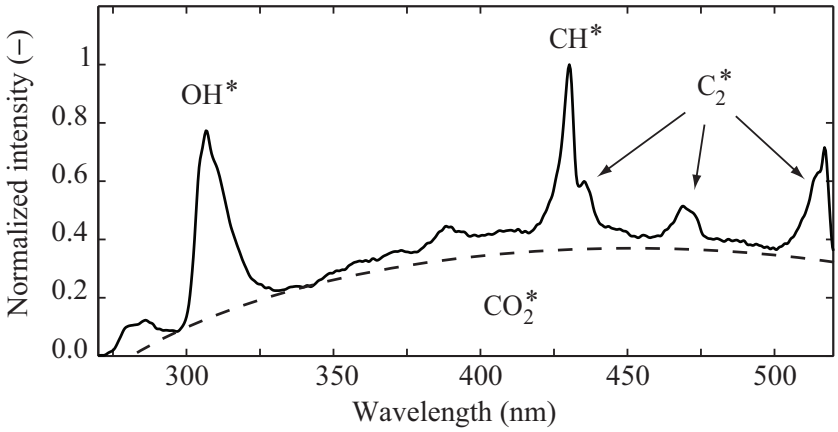

Figure 4.1: CL spectrum of a stoichiometric premixed methane-air flame from Lauer et al. [114]. The narrowband radical emissions from OH^*, CH^*, and C_2^* are superimposed by the broadband emission from CO_2^*.

broadband detection was necessary, since the exposure time at kilohertz repetition rate is very short (≈ 100 µs) thus limiting the number of accumulated photons per frame. Furthermore, no high speed image intensifier was available that could have multiplied the number of photons to yield a reasonable signal when using a filter. Typical for this application are interference filters of 308 ± 10 nm which extract the $X^2\Pi_i(v''=0) \leftarrow A^2\Sigma^+(v'=0)$ and $X^2\Pi_i(v''=1) \leftarrow A^2\Sigma^+$ $(v'=1)$ transitions of OH^* at ≈ 308 nm and ≈ 311 nm, respectively.

CL imaging is a *line-of-sight* method. Thereby, the signal collected by the optical detector can originate from the whole volume which is imaged onto the detector. In contrast to the following measurement techniques the signal does not emanate from a thin measurement volume such as defined by illumination or excitation with a light sheet, but is accumulated along the line-of-sight. Thus, a quantitative determination of the recorded signal is usually difficult except for special cases where Abel inversion [1] is feasible. Therefore it remains a qualitative technique that has been applied in this context to acquire information about the general topology of the flame above and inside the burner's exit nozzle. This is especially helpful when combined with planar techniques, e.g. PLIF or PIV, as it can reveal three-dimensional effects (see Fig. 4.26).

4.1.2 Planar Laser-Induced Fluorescence of OH (OH-PLIF)

In the field of turbulent combustion diagnostics Planar Laser-Induced Fluorescence (PLIF) is a widely used technique to gain information about the physicochemical state of a flame within a planar measurement volume. The most prominent application, which is also utilized within this work, is the observation of the fine scale structure of a flame front by imaging the concentration of the hydroxyl radical (OH). LIF of OH was first observed and published by Wood in 1905 [32]. A review of PLIF and its application in turbulent combustion can be found in [72]

Primarily, LIF is a technique to measure the concentration of minor diatomic species within a reacting system such as OH, CO, NO, CH. However, LIF can also be applied to atoms or larger molecules such as acetone or toluene. In LIF the wavelength of a laser is tuned to an specific absorption line of the molecule of interest. The molecule is thereby excited to a higher electronic state, similar to the excitation through chemical reactions as previously described in Section 4.1.1. When the molecule returns to its ground state it emits a fluorescence photon which

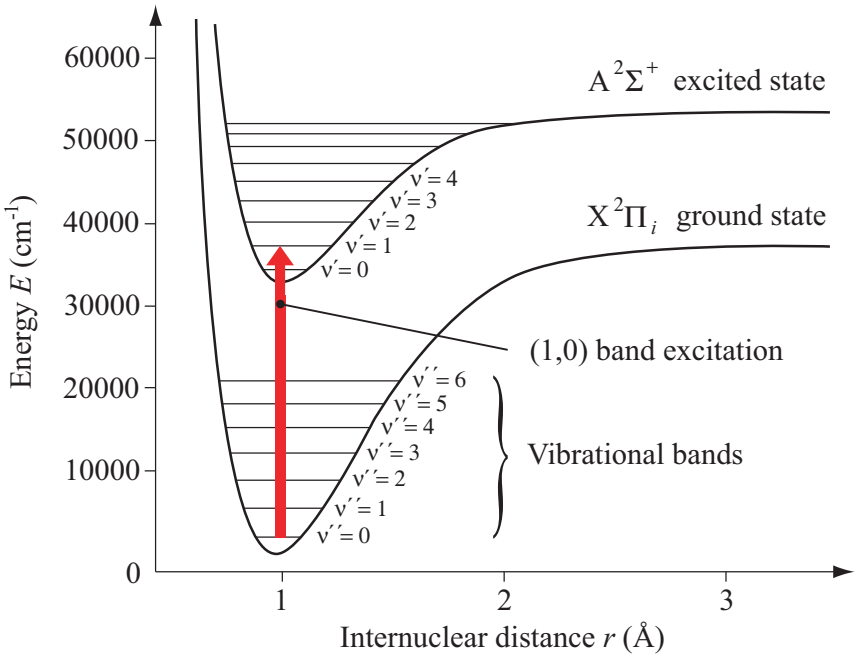

Figure 4.2: Rydberg-Klein-Rees potentials for the A and X electronic states of OH (adapted from Smyth and Crosley [187])

is then collected by an optical detector, such as a photomultiplier. The effective lifetime of the excited states for minor species, such as OH and NO, is only a few nanoseconds [42, 178]. Thus, in terms of turbulent time scales the fluorescence process can be assumed to be instantaneous.

Fig. 4.2 shows the Rydberg-Klein-Rees potentials for the excited (A) and ground (X) electronic states of an OH molecule. The potentials represent the molecule's energy E as a function of the internuclear distance r and the electronic quantum mechanical states. The different electronic states consist of a number of vibronic sub-states called *bands*, which are shown as horizontal lines. The bands differentiate into a number of rotational energy states called *lines*. These are not shown as their separation is very small[9]. For most molecules of interest such as the OH radical, a single photon in the ultra-violet spectrum (UV) is sufficient for excitation, such as the (1,0) band transition marked by the red arrow. However, in the case of other molecules, e.g. CO, single vacuum photons have to be used, which are impractical for the investigation of atmospheric flames. A solution is two-photon LIF which excites the molecule by simultaneous absorption of two photons with half the required energy each.

LIF can be applied as point-wise measurements along a line or two-dimensionally as planar measurement. It is currently widely used throughout the combustion community with an increasing amount of publications utilizing this technique at different pressures and with different aims [106]. Besides the species concentrations LIF is capable of measuring temperature by determining the relative distribution of the molecules' rotational and vibrational states within the measurement volume. The popularity of the technique to measure temperature lies in its relative simplicity compared to single-shot Raman or CARS measurements [106]. Among others, the most common alternative techniques for detecting minor species are resonantly enhanced multi-photon ionization (REMPI), degenerate four-wave mixing (DFWM), cavity ringdown (CRD)

[9] Quantum mechanics describe the molecule's vibrational and rotational degrees of freedom. The molecule's quantum states and their associated energies are calculated by the time-independent *Schrödinger equation* $E\Psi = \hat{H}\Psi$.

spectroscopy, and tunable diode laser (TDL) spectroscopy. The advantage of these techniques is that only the absorption of the laser light is taken into account and no fluorescence signal is needed. Thereby also non-fluorescing species are accessible. However, these techniques are limited to either single point or line-of-sight measurements, which is their the major drawback [187].

Measurements are typically made using pulsed laser systems with a pulse length of $10-100$ ns. Since the laser intensities are relatively high, the produced fluorescence signal discriminates well against the CL radiation, which continuously emits photons. The measured signal S_{LIF} in the linear regime, which is created by a single laser pulse, can be formulated as

$$S_{\mathrm{LIF}} = (VNf_{\mathrm{B}}) \cdot (I_{\mathrm{L}} B_{12} \Gamma_{12,\mathrm{L}}) \cdot \phi \cdot (F_{\mathrm{fl}} \frac{\Omega}{4\pi} \zeta \chi) \cdot t_{\mathrm{L}}. \tag{4.2}$$

The equation has been grouped according to Allison and Partridge [6] to provide a clear physical interpretation in the order of the natural fluorescence measurement process. The first group in Eq. (4.2) represents the number of molecules which can take part in the fluorescence process. Here, V is the excited measurement volume, N the number density of probe species and f_{B} the Boltzmann fraction of molecules in the ground state 1. The latter represents the fraction of molecules in the ground state which are available for excitation. The second group is the probability per time that an available molecule will absorb a laser photon. In the second group, I_{L} is the normalized spectral irradiance of the laser, B_{12} is the Einstein absorption coefficient from the ground level 1 to the excited state 2, and $\Gamma_{12,L}$ is the linewidth integral. The latter represents the overlap between the laser bandwidth and the bandwidth of the absorption line. ϕ is the fluorescence quantum yield and describes the probability of an excited molecule to emit a fluorescence photon when returning to the ground state. The quantum yield is a function of pressure, temperature and the chemical composition in the measurement volume. It shows that for the return to the ground state radiative as well as non-radiative path are available as described for CL. The third group represents the efficiency of the detection system to collect the emitted photons from the measurement volume. Here, F_{fl} is the spectral fraction of the fluorescence emission that overlaps with the bandwidth of the detector. $\Omega/4\pi$ is the solid angle of the collection optics. ζ is the quantum efficiency of the detector to measure a photon and χ is the responsivity of the detection system which relates the measured number of photons to the signal of the detector. Finally, t_{L} is the length of the laser pulse. It should be noted that Eq. (4.2) is only valid in the linear regime where only a fraction of the available molecules within the measurement volume is excited. Otherwise, the equations for saturated LIF apply, which can be found in [32, 106].

The depopulating processes from the excited state, other than the radiative relaxation, need to be considered for absolute measurements of the species concentration. As briefly mention before, this influence is reflected by the fluorescence quantum yield ϕ. Furthermore, a calibration of the measurement system has to be carried out. A lot of research in quantifying and modeling of the non-radiative relaxation processes has been done. However, the accuracy of quantitative OH radical measurements are only in the order of 30 % [62]. Both, the radiative and non-radiative processes for the relaxation of the excited OH molecule are depicted in Fig. 4.3. The energy diagram shows three relevant vibrational bands with their rotational lines for the excitation of the OH molecules and the detected fluorescence at ≈ 308 nm [39]. From the electronic ground state within the $\mathrm{X}^2\Pi_i$ $(v''=0)$ band an excitation into the $\mathrm{A}^2\Sigma^+$ $(v'=1)$ band is happening by absorption of a ≈ 283 nm photon. Due to intermolecular collisions the energy is redistributed throughout the energy levels of the molecule. Rotational energy transfer (RET) redistributes

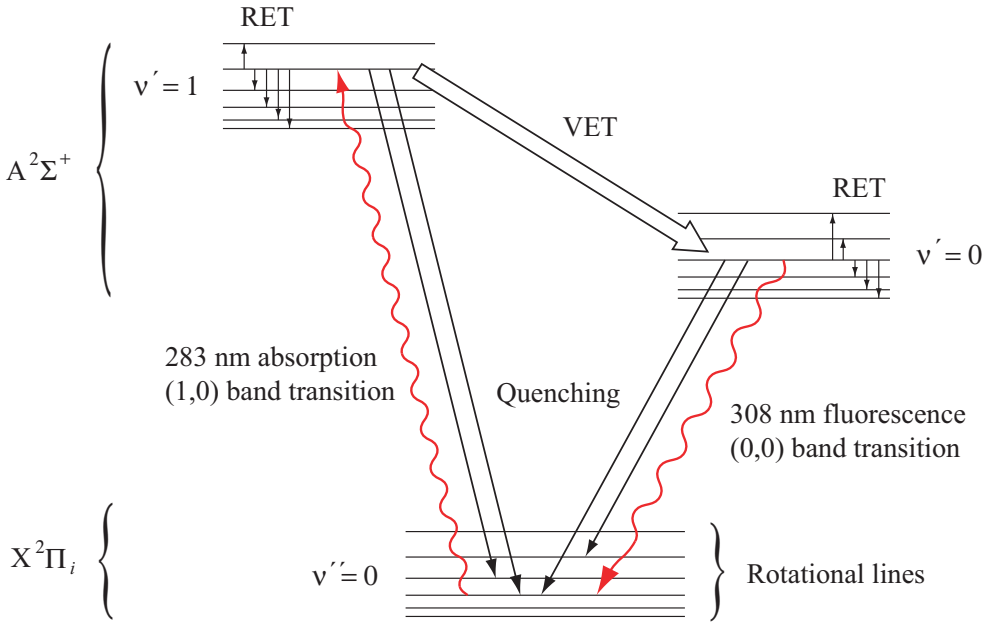

Figure 4.3: Energy levels of the diatomic hydroxyl radical [187]

the population from the initally excited rotational line to other rotational lines with different characteristics within the vibrational band. The non-radiative transfer to the ground state is called *quenching*. This process returns the molecule from any electronic excited state to the ground state. Since quenching is highly dependent on the chemical composition, temperature and pressure, it is most difficult to quantify and model. However, quenching data of OH for quantitative measurements in flames is reported in [148]. At 1 bar the quenching rate is 200–300 times higher than spontaneous emission of fluorescence for most flame species [42]. If the energy of the excited state during the intermolecular collisions exceeds a characteristic limit, the molecule dissociates, which is not shown in Fig. 4.3. Also, energy transfer between the different vibrational bands within the electonic state can occur (VET: Vibrational Energy Transfer). This is an important mechanism for the detection of the OH fluorescence signal. It shifts the fluorescence towards longer wavelengths compared to the excitation wavelength. While the excitation from the ground state had occured at ≈ 283 nm, the fluorescence due to the $(0,0)$ band transition is at ≈ 308 nm. Hence, detection of the light that has undergone VET is better to discriminize against the exicitation wavelength [219] using appropriate filters. Although it is not shown in Fig. 4.3 it should be noted that usually fluorescence from the $(1,1)$ band transition at ≈ 313 nm [39], which is close to the $(0,0)$ band transition, is also recoreded by the detection system.

A certain molecule or species can be identified by its characteristic absorption-emission spectrum. This can be done by scanning the excitation wavelength and detecting the integral emission spectrum of the fluorescence signal. Such an absorption-emission scan for OH is shown in Fig. 4.4 by detecting the emission of the $(0,0)$ and $(1,1)$ band transition at ≈ 308 nm and ≈ 313 nm, respectively. Each line in the spectrum corresponds to one or more rotational lines in the ground state. The relative intensity distribution of lines can be used for thermometry due to the fact that RET is fast compared to the removal of the molecule by a chemical reaction [106]. Experimental and theoretical investigations resulted in the software called LIFBASE [129], which simulates spectra for OH, CO, and NO amongst others. Using the modeled spectra, a specific transition line can be chosen in the experiment by comparing experimentally and com-

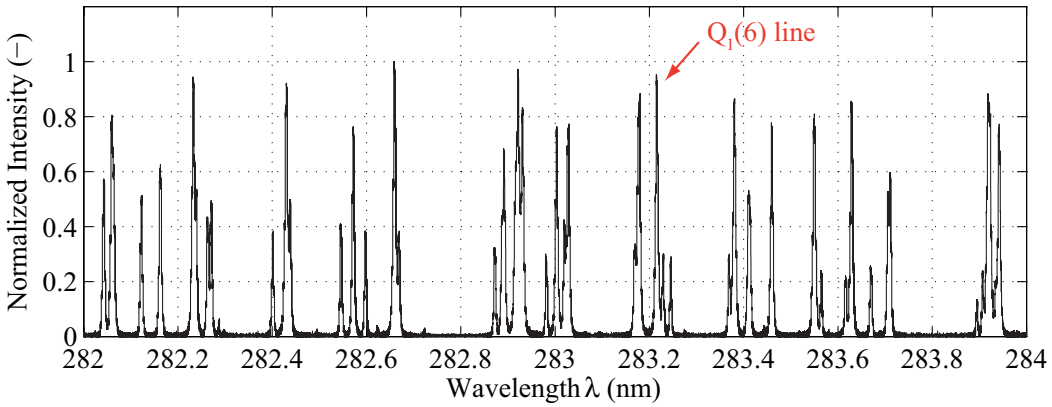

Figure 4.4: Absorption-emission scan of a hydroxyl radical. The scan was recorded with a photo diode and an oscilloscope prior to the PLIF measurements.

putationally determined absorption-emission scans. Although only quantitative measurements have been carried out during this work to obtain the spatial structure of the flame front, care has been taken to select the temperature insensitive $Q_1(6)$ line.

A typical experimental realization for the planar application of LIF using a sheet of light and an array detector is sketched in Fig. 4.5. Planar measurements are convenient to perform by using array detectors, such as intensified CCD or CMOS cameras. The measurement volume is thereby defined through the thickness of the light sheet and the imaging region of the camera. The height of the light sheet is usually adapted to exceed the height of the imaging region, such that fluorescence signal can originate from the full field of view of the camera. Details about laser imaging of scalars in flows can be found in [27]. The light sheet is formed by a cylindrical lens telescope that expands the originally circular beam in one direction. Typical measurement volumes for turbulent combustion experiments are $0.1 - 0.5$ mm thick and up to 10 cm in height. The induced signal is collected at a right angle with an array detector, which is sensitive to the emitted fluorescence wavelength. Due to the fact that silicon-based camera chips usually exhibit high quantum efficiencies only in the visible spectrum, intensified cameras are often used for UV applications. These feature an extended photon absorption in the UV range, due to their cathode base material. The possibility for short gating times of these devices improves the discrimination

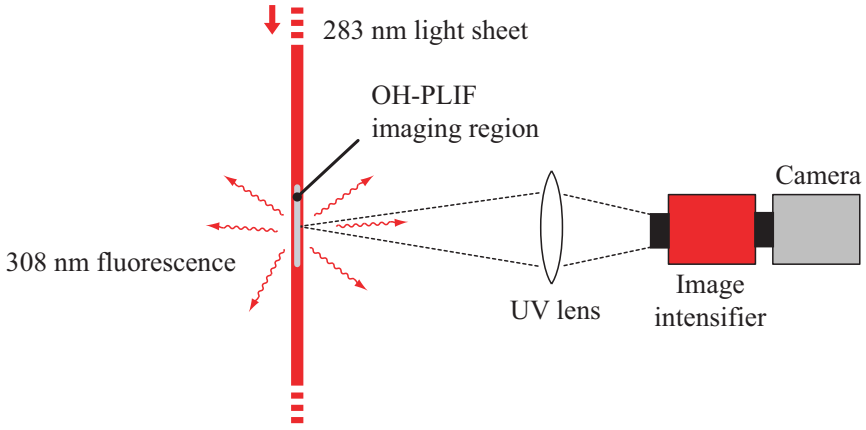

Figure 4.5: General experimental setup for OH-PLIF

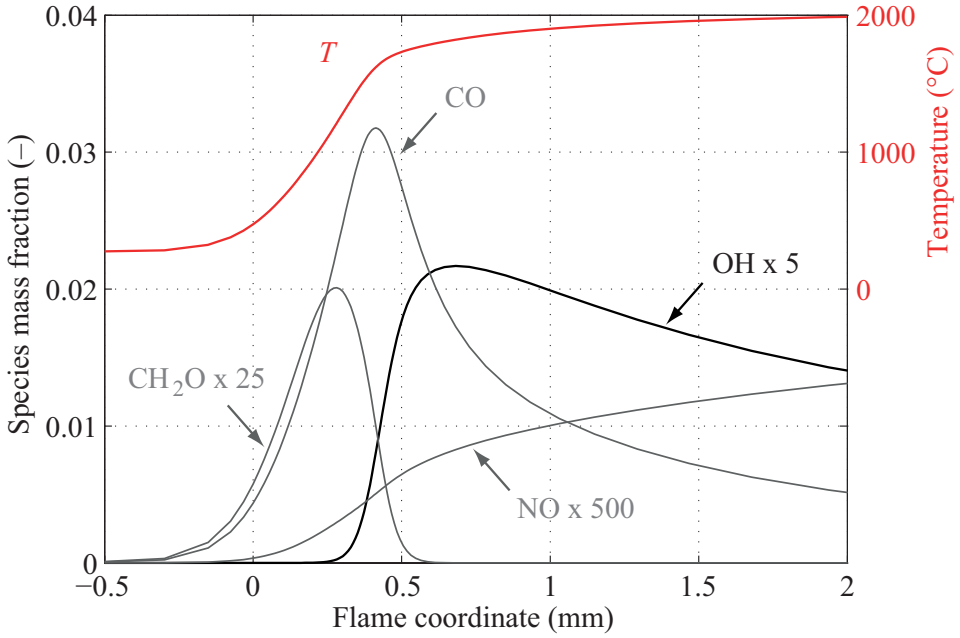

Figure 4.6: Profile of the concentration of the OH radical across the flame front (simulated with CHEM1D [25])

of the LIF signal against the background light, e.g. from CL.

OH-PLIF has been used widely as a flame front marker in premixed flames [44]. The validity for using the qualitative spatial distribution of OH concentrations as a flame front marker is shown in Fig. 4.6. Here, the calculated concentration profiles of various LIF species across a premixed flame front are plotted. The concentration profiles of OH, CO, NO, CH and formaldehyde (CH_2O) together with the temperature across a laminar flamelet were also simulated using CHEM1D. The calculated flamelet of $\Phi = 0.833$ is similar to what can be found during measurements in the TECFLAM burner. It is clearly visible that the steepest gradient in the OH concentration is very close (≈ 100 µm) to the position of the steepest gradient in temperature, which defines the position of the flame front. Further minor species have been plotted that can also be recorded by LIF measurements. Their applications are well documented [32, 106, 187].

4.1.3 2C/3C Particle Image Velocimetry (PIV)

Particle Image Velocimetry (PIV) is a standard and well-established optical measurement technique to capture two or three components of the velocity vectors of a flow field. Hence, only the fundamental aspects are briefly introduced in this section. As a planar technique, it enables to access a flows spatial structures, i.e. vortices, recirculation zones, shear layers, etc.

The influence of PIV on the flow is limited to the injection of small seeding particles. This is the main advantage of PIV compared to intrusive techniques, such as hot-wire anemometry, which include insertion of a probe into the flow. Thus, it is minimally intrusive by the choice of the appropriate seeding material and injection technique. The fundamental principle of this technique is to image the particles while they follow the flow without slip. To obtain velocity information, two images of the seeded flow are recorded with a known time separation Δt. The image is divided into *interrogation areas*. For each interrogation area a displacement vector

$\Delta x_i = x_i(t_0) - x_i(t_0 + \Delta t)$ is determined from the movement of the particles. Hence, a velocity vector $\widetilde{u}_i$ for each interrogation area can be estimated from the displacement vector, the magnification of the imaging system M and the time separation by

$$\widetilde{u}_i = \frac{\Delta x_i}{M \cdot \Delta t}. \tag{4.3}$$

It should be clarified that the displacement estimation is not based on tracking individual particles. This is the case in Particle Tracking Velocimetry (PTV) in which each randomly distributed particle yields a vector information. On the contrary, the displacement in PIV is calculated on a regular grid of interrogation areas by a cross correlation algorithm. The code estimates the most likely shifting distance and direction of the particle field in a certain interrogation area from one image to the following. The cross correlation coefficient for a certain pixel shift in both spatial directions n and m as a function of the interrogation areas' gray values in image one $I(i,j)$ and image two $I'(i,j)$ is given by

$$R_{II'}(m,n) = \sum_i \sum_j I(i,j) I'(i+m, j+n). \tag{4.4}$$

In this relation i and j are the pixel coordinates of the interrogation area in x and y direction, respectively. As a first estimate, the displacement of the particle field is determined by n and m at the maximum of the correlation coefficient $R_{\max}$. Several sophisticated techniques have been developed during the last decade to determine the displacement with a subpixel accuracy [157]. For instance, a three-point Gaussian fit is usually applied to the peak area of the discrete correlation map $R_{II'}(m,n)$ of an interrogation area. Thereby, the maximum of this peak, and hence the particle shift, can be determined with a subpixel accuracy. Other techniques to improve the correlation between the interrogation areas, such as window deformation and multi-pass processing, are detailed by Raffel [157].

Seeding Particles

The tracer particles that are seeded to the flow in combustion PIV are either liquid droplets, such as silicone oils which usually evaporate in the vicinity of the flame, or solid inert particles (MgO, TiO_2). The latter pass the flame front without being altered or having an excessive influence on the flame behavior. In the present study the velocity field ahead of the flame was of interest, thus droplet seeding was sufficient during the flame's upstream propagation. Furthermore, the risk of contaminating the laser laboratory with fine solid particles, which are harmful to the neighboring experimental setups, was minimized. Often di(2-ethylhexyl)-sebacate (DEHS) is used as liquid seeding material. The properties of DEHS are summarized in Table 4.1. Although it starts to evaporate at approximately 485 K, it cannot be used solely to determine a flame front. This will be shown Section 4.4. Similar attempts to detect a flame front through the seeding density jump across the flame ($\rho_\mathrm{u}/\rho_\mathrm{b} = T_\mathrm{b}/T_\mathrm{u} \approx 7$) when instead using solid particles is questionable.

The generation of small droplets of the diameter d_p can be achieved in various ways. For large scale application, such as wind tunnels, high volumetric seeding rates can be achieved by Laskin nozzle seeders [168]. However, single air assist atomizers can be used for smaller applications up to volumetric flow rates of up to 40 m^3/h, such as for the TECFLAM burner [119]. These generate micrometer droplets in the shear region of a jet issuing from an orifice in which the liquid is injected.

Table 4.1: Physical and chemical properties of di(2-ethylhexyl)-sebacate (DEHS) [134]

Hill Formula	$C_{26}H_{50}O_4$	
Solubility	< 0.1 g/L	(20 °C)
Melting point	-55 °C	
Molar mass	426.68 g/mol	
Density	0.91 g/cm^3	
Boiling point	> 250 °C	(1013 hPa)
Vapor pressure	< 0.1 hPa	(20 °C)
Flash point	> 200 °C	

The purpose of using particles in PIV is the Mie-scattering of light. When illuminated, the particles create a pattern of varying intensities throughout the measurement volume. These spatial gradients can be tracked in space from one image to another. Therefore, the Mie-scattering behavior of small particles, which can vary in size, is also of interest. While large particles ($d_p > 100$ µm) scatter the incident light almost homogeneously in all directions, the scattering behavior changes significantly when small particles are illuminated by monochromatic light. Figure 4.7 shows the relative scattering intensities in a logarithmic scale of a 1 and 10 µm particle depending on the observation direction. Two peculiarities can be observed. Firstly, the forward scattering intensities are generally stronger than the backward scattering. Secondly, the signal exhibits large intensity fluctuations with respect to small changes in the observation angle. Hence, PIV in forward scattering configuration can increase the signal intensity by $1-2$ orders of magnitude. This is of advantage especially in Stereo-PIV setups. The advantage of forward scattering applies in particular to high speed applications where laser pulse energies are at least two orders of magnitude smaller compared to the conventional low repetition PIV systems.

From a puristic perspective of general measurement theory the sensor of PIV is the particle itself. It transforms the quantity of interest, i.e. the flow velocity, into a particle velocity. This transformation is already a source of errors and will be discussed in the following. The particle motion in flows can be described by the Basset-Boussinesq-Oseen equation, which is a classical transport equation (see Eq. (2.3)). Its derivation can be found in [30]. For very small particles, such as those used in Laser Doppler Anemometry (LDA) [5] and PIV, the relative velocity, or

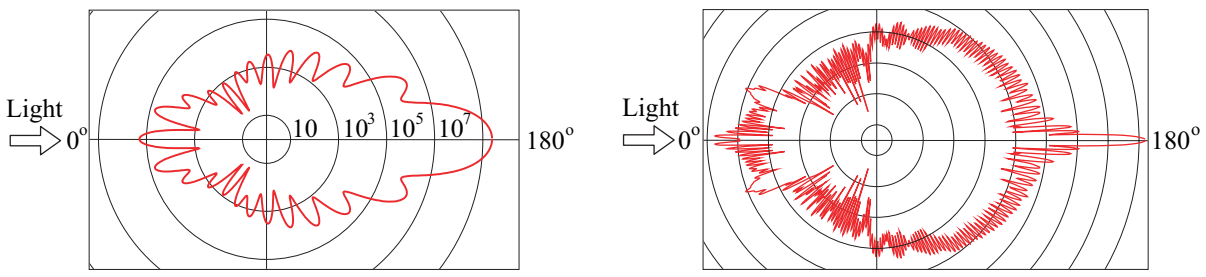

Figure 4.7: Light scattering of 1 µm and 10 µm oil droplets in air at 532 nm [157].

slip velocity, between particle and fluid can be modeled as [203]

$$u_\mathrm{p} - u = \frac{d_\mathrm{p}^2}{18}\frac{(\rho_\mathrm{p} - \rho)}{\mu}\frac{\mathrm{d}u_\mathrm{p}}{\mathrm{d}t}. \tag{4.5}$$

In this equation u_p is the particle velocity, u the velocity of the surrounding fluid, d_p the diameter of the particle, μ the dynamic viscosity of the fluid, ρ_p the density of the particle and ρ the density of the fluid. If the particle is exposed to a gravitational field then $\mathrm{d}u_\mathrm{p}/\mathrm{d}t = g$ and Eq. (4.5) transforms to yield

$$u_\mathrm{g} = \frac{d_\mathrm{p}^2}{18}\frac{(\rho_\mathrm{p} - \rho)}{\mu}g. \tag{4.6}$$

Equation (4.6) describes the velocity defect of a particle u_g due to a gravitational force [157]. For DEHS droplets of $d_\mathrm{p} = 1$ µm in air under normal conditions ($\rho = 0.0012$ g/cm^3) the gravity-induced slip velocity of $u_\mathrm{g} = 100$ µm/s can be estimated. As we will see later in Section 4.4, this error can be neglected compared to the other sources of errors.

According to the Basset-Boussinesq-Oseen equation a velocity difference between the particle and flow can also be the result of high velocity fluctuations. There, the particles cannot follow the fluid anymore due to their inertia [5]. To mathematically describe this effect, it is convenient to introduce the slip s as the normalized slip velocity by

$$s = \left|\frac{u - u_\mathrm{p}}{u}\right|. \tag{4.7}$$

Assuming no interactions between spherical particles as well as a large difference in density between the particles and the fluid $\rho_\mathrm{p}/\rho \gg 1$, Albrecht et al. [5] derived a critical particle frequency f_p. This is a function of the slip and represents the limit for the ability of the particles to follow the fluid motion. It is given as

$$f_\mathrm{p} = \frac{1}{\tau_\mathrm{p}}\frac{1}{2\pi}\sqrt{\frac{1}{(1-s)^2}} - 1. \tag{4.8}$$

Therein τ_p is the particle relaxation time scale, which is given by the expression

$$\tau_\mathrm{p} = \frac{{d_\mathrm{p}}^2}{18}\frac{\rho_\mathrm{p}}{\mu}. \tag{4.9}$$

The relaxation time for DEHS droplets of $d_\mathrm{p} = 1$ µm in air under normal conditions, similar to the conditions in the unburnt flow inside the burner, can be estimated to be $\tau_\mathrm{p} = 29.56$ µs. Assuming a slip of $s = 1$ % the critical frequency for the droplets according to Eq. (4.8) yields f_p = 5.4 kHz.

Another effect can cause errors in combustion applications when measuring flow velocities using particles. Thermophoretic effects will appear due to the heat release of the flame and the associated high temperature gradients [195]. This effect accelerates the particles within the fluid flow towards the cold gas. Thermophoresis stems from the difference of momentum of the hot and cold molecules. The result is a net force within a temperature gradient that pushes the particles down the temperature gradient from the hot to the cold fluid. According to Gomez and Amantini [7, 64] the induced velocity can be estimated by

$$u_\mathrm{T} = (\alpha_\mathrm{T} D)_\mathrm{T} \cdot \left[-\max\left(\frac{\partial T}{\partial x_i}\right)\frac{1}{T}\right] \tag{4.10}$$

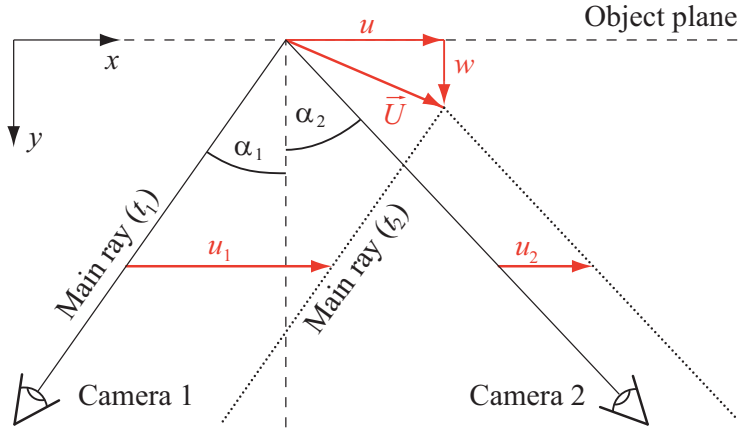

Figure 4.8: Geometrical setup for Stereo-PIV recordings

where $(\alpha_T D)_T$ is the diffusion coefficient of thermophoresis. An induced velocity by thermophoresis of $u_T \approx 0.04$ m/s was estimated by Heeger et al. [76] at the contour of evaporating DEHS droplets ($T = 485$ K). As already mentioned earlier, the relevant region of the flow field for flashback analysis lies ahead of the flame contour where the thermal gradients are much smaller (compare Fig. 2.11).

Stereo-PIV

The major drawback of classical two-dimensional, two-component PIV (2D/2C) is the unknown out-of-plane convection component. Unfortunately, for most of the combustion experiments this component is of paramount importance as turbulence effects are inherently three dimensional. A stringent consequence is the application of advanced PIV techniques. By stereoscopic PIV (Stereo-PIV) a technique is available that enables to additionally obtain the out-of-plane component. Hence, the full velocity vector in a two-dimensional measurement volume can be determined (2D/3C). Furthermore, even volumetric, thus three-dimensional acquisition of velocity data is possible. Examples of 3D/2C techniques are dual plane and scanning PIV, while tomographic and holographic PIV can resolve all components and dimensions (3D/3C) [77]. Within this work Stereo-PIV has been applied and will be briefly presented in the following.

The basic principle is to image the particle displacement from two different directions by separate cameras. The geometrical setup for Stereo-PIV is shown in Fig. 4.8. The different viewing angles α_1 and α_2 result in the measurement of the depicted horizontal in-plane velocity components u_1 and u_2. These values as well as the components v_1 and v_2, which are orientated normal to the sketched plane, can be obtained by

$$u_{1,2} = -\frac{x'_{1,2} - x_{1,2}}{M \cdot \Delta t} \tag{4.11}$$

$$v_{1,2} = -\frac{y'_{1,2} - y_{1,2}}{M \cdot \Delta t}. \tag{4.12}$$

From further geometrical considerations the full set of velocity components (u, v, w) is recon-

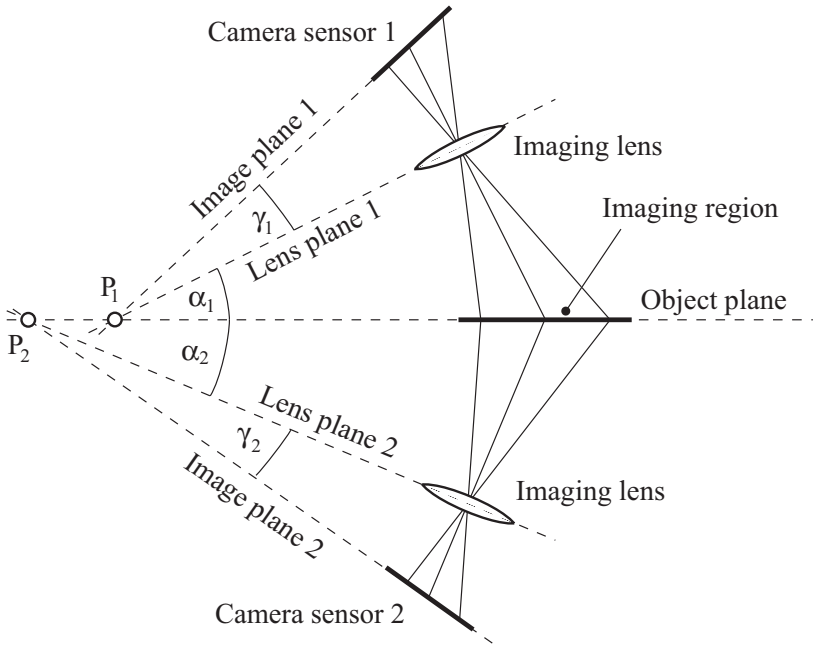

Figure 4.9: Geometrical configuration of the Scheimpflug criterion to establish an oblique focal plane

structed according to the following equations:

$$u = \frac{u_1 \tan\alpha_2 + u_2 \tan\alpha_1}{\tan\alpha_1 + \tan\alpha_2} \tag{4.13}$$

$$v = \frac{v_1 \tan\beta_2 + v_2 \tan\beta_1}{\tan\beta_1 + \tan\beta_2} \tag{4.14}$$

$$w = \frac{u_1 - u_2}{\tan\alpha_1 + \tan\alpha_2} \tag{4.15}$$

$$= \frac{v_1 - v_2}{\tan\beta_1 + \tan\beta_2} \tag{4.16}$$

The values of the viewing angles α_1, α_2, β_1 and β_2 vary with the actual position of the interrogation area. They are determined from a calibration procedure using a reference target and a self calibration procedure, which is detailed below. The system of equations for the reconstruction consists of the three unknown variables u, v and w and the four measured velocities u_1, u_2, v_1 and v_2. Hence, the system is overdetermined. Solving the system in a least square sense, enables a refined estimation of the redundantly acquired in-plane velocity components, with the residuum ε_r as a measure of accuracy. A value of $\varepsilon_r \leq 1$ pix is a minimum requirement for data processing. $\varepsilon_r = 0.1 - 0.5$ pix is feasible for carefully designed setups.

The reconstruction of the out-of-plane velocity component is achieved by using two different projections of a displacement vector, which are obtained from two different directions. The accuracy and precision of the z component estimation increases towards an angle of 90° between both viewing angles. A translational displacement approach with parallel optical axes of the cameras as described by Adrian [3] was not feasible. This was due to the large angle between the cameras and the selected objective lenses. Identical lenses with a focal length of $f \geq 100$ mm are usually used to achieve a distance of at least 400 mm between the flame and the image. This is to prevent the hardware from being damaged by the flame. Furthermore, camera mounts with

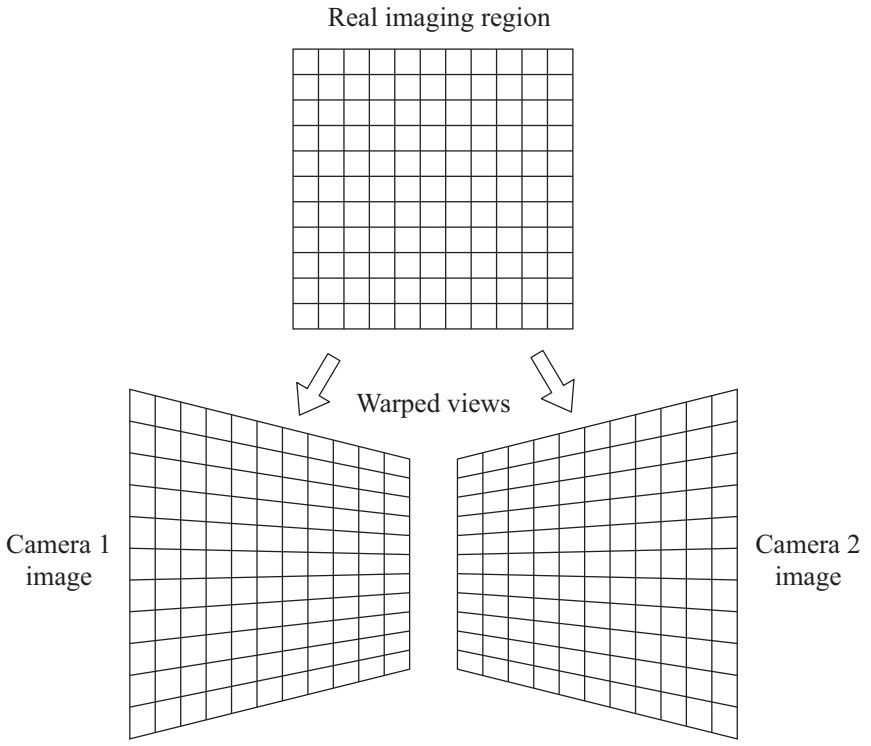

Figure 4.10: Perspective distortion of camera one (left) and two (right) due to oblique viewing angles

an option to shift the lens parallel to the chip are practically not available for scientific cameras. The error of the out-of-plane component is also larger than in the tilted camera configuration [116]. Hence, the tilted camera or angular displacement configuration is usually chosen. In such a configuration the depth-of-field for typical f-numbers (see Section 4.2.4) is not sufficiently large to image the tilted plane properly and blurring in the border regions cannot be avoided. Therefore, a lens adapter has to be used to compensate the effect. The adapter allows to tilt the camera chip at an angle γ such that the Scheimpflug criterion [69] is fulfilled. This is shown in Fig. 4.9 for both cameras. In the Scheimpflug configuration all three principal planes of the object, the lens, and the image intersect in one virtual line.

An inherent phenomenon that occurs at oblique viewing angles is a perspective distortion or warping. This effect leads to an inhomogeneous magnification factor within the image as sketched in Fig. 4.10. Hence, a perspective correction has to be applied in order to compensate the distortion. For this purpose both cameras have to be mapped to a common image space [216] during the data processing. This can be done by imaging a calibration target with a regular, mostly Cartesian, grid of calibration marks. The accuracy of the measurement is directly influenced by the manufacturing tolerances of the used target. Hence, care has to be taken in designing, manufacturing and positioning of the calibration target to achieve a high spatial PIV resolution. The most common mapping functions for the dewarping of the distorted images are the pinhole camera model [4] and a third order polynomial approach. The latter has been described and assessed by Soloff et al. [188] and Willert [217]. Soloff could show that third order polynomials can perform well for correction of lens aberrations. However, recent investigations using Stereo-PIV in cylindrical confinements with large image distortions indicate that polynomials of higher order should be applied. The calibration target in the form of a plate is often

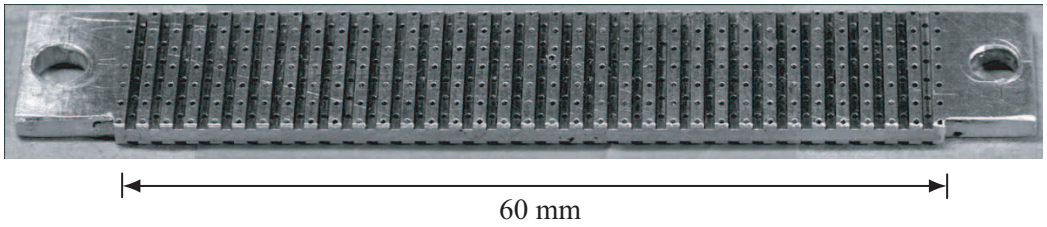

Figure 4.11: Photography of the calibration plate to register and dewarp raw images

additionally used for determining the imaging angles α_1, α_2, β_1 and β_2 and the alignment of the laser sheet with the measurement volume. Figure 4.11 shows the target which was used inside the annular slot of the TECFLAM burner nozzle. Further details about calibration targets can be found in [115].

Experimental Realization

Setting up a PIV system for a specific experiment, such as the flame propagation measurement in the nozzle of the TECFLAM burner, includes several measurement devices. The fundamental devices are a particle seeder, two individual or one dual-cavity, pulsed laser system, and at least one camera with an option for double exposure in the order of microseconds. The laser is used to illuminate the particles in the flow, because it features very high radiation intensities, monochromatic and also parallel light. The coherence of the emitted light is usually not needed and sometimes disadvantageous. It can result in low scattering intensities at certain angles as a consequence of destructive interference (compare Fig. 4.7). With common pulse lengths of $10-100$ ns it is possible to image the moving particles without a motion blur. The sensitivity of non-intensified cameras is usually not sufficient to generate enough signal under continuous illumination at sufficiently small exposure times. The exposure times have to be so short, such that the particles do not move for more than a fraction of a pixel during exposure to avoid the motion blur. Larger movements prevents a definite position, thus, displacement estimation. However, the pulse energy of a laser shot has to be in the order of millijoules or higher to generate enough signal for decent particle imaging. This is of special importance in the case of high speed techniques, where lasers feature much smaller pulse energies than the conventional low repetition systems (see Section 4.2.2). Usually, a wavelength of 532 nm light (green) is used, as high energy Neodymium (Nd) lasers are available and the cameras feature the highest quantum efficiency in this spectral range. Beside the most prominent class of frequency-doubled solid state Nd:YAG lasers (YAG: Yttrium Aluminium Garnet) at 532 nm, recently Nd:YLF (YLF: Yttrium Lithium Fluoride) at 527 nm and Nd:YVO_4 lasers (YVO_4: Yttrium orthovanadate) at 532 nm for high repetition rates are available. The two laser cavities have to be fired independently in order to acquire the two spatially correlated particle images such that the particle shift from one image to the other is optimal (see Section 4.4). For turbulent combustion research Δt is in the order of milliseconds. The light sheet formation is similar to PLIF (see Section 4.1.2) with the additional requirement to keep the loss of particles due to out-of-plane movement below approximately 25%. This is achieved through adjusting the light sheet thickness to the level of out-of-plane velocity at a given Δt.

The camera for imaging the particle field has to fulfill a few specific requirements. Since digital cameras are available, PIV is usually recorded in single frame mode by recording the two illuminating laser shots on two separate images. This has several advantages over the formerly

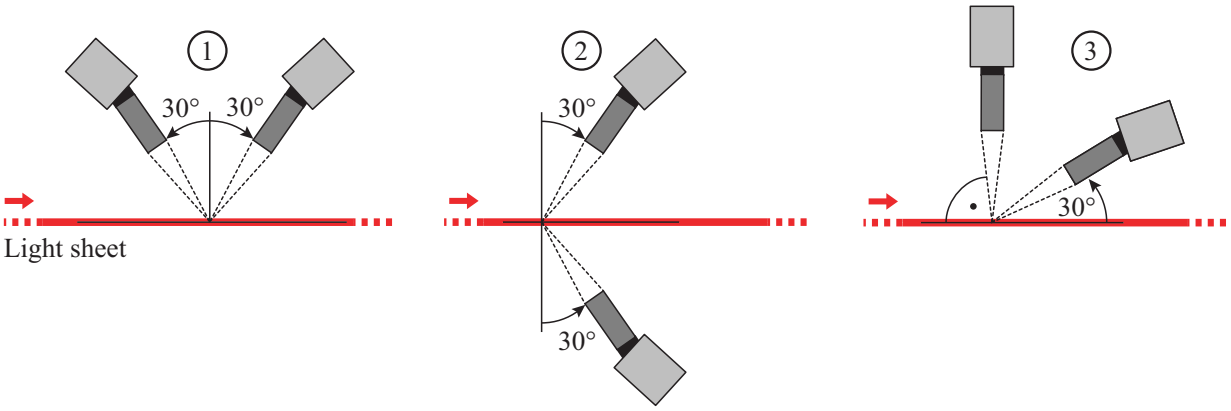

Figure 4.12: Three camera configurations for Stereo-PIV

applied double frame mode [157]. Single frame PIV demands that the camera has to take two images with a time delay in the order of milliseconds (Δt). Interline transfer CCD cameras [79] have been used therefor in the past. With the advent of scientific CMOS cameras (sCMOS) another type of camera is available for this purpose. The imaging of the particle field is done with standard camera lenses, similar to the configuration shown in Fig. 4.5. For a detailed information on laser imaging the reader is referred to [27, 157]. Interrogation area sizes of 32×32 or 16×16 pixels are common for state-of-the-art PIV processing routines. The magnification M of the imaging system has to be adjusted such that at least five particles per interrogation area are imaged in a single-exposure, double-frame recording [95]. Otherwise, a valid correlation peak detection is not feasible, thus decreasing the accuracy and precision of the vector calculation. Obviously, large sensor arrays are advantageous to obtain as many interrogation areas and, therefore, vector data as possible.

The major difference of Stereo-PIV to standard 2C-PIV is the use of two cameras which are at an angle with respect to each other and the measurement plane. Several configurations can be found in literature of which three are shown in Fig. 4.12. The best estimate for the out-of-plane component of the velocity vector is obtained at 90° angle between the two camera's viewing directions. However, this configuration reduces the accuracy of the in-plane components by increasing the deviation from 90° between the measurement plane and camera. An optimum was found by Lawson and Wu [116] at a deviation between $\alpha = 20°$ and 30° for each camera, as shown in the first sketch of Fig. 4.12. At these specific angles the relative displacement error of the in-plane and out-of-plane components is minimized to $3-4\%$ and $1-2\%$ rms, respectively. In terms of signal quality a forward scattering configuration is advantageous, which is shown in the second configuration. Also asymmetric configurations are possible which can become necessary by geometrical restrictions of the flow device or burner (third configuration in Fig. 4.12).

4.1.4 Pressure Measurements

In order to investigate aerodynamic as well as baroclinic mechanisms of flame flashback the measurement of pressure at certain positions within the flow is important for several reasons. From Eq. (2.5) it becomes clear that pressure gradients are a driving force of flow motion. Furthermore, the measurement of the time-trace of static pressure is the most basic measurement technique for detecting and characterizing unstable combustion [118], of which flashback is one

of its most obvious forms. Within this work the following points are of interest regarding the possible influences of pressure on the flashback phenomenon:

- A positive axial pressure gradient can lead to vortex breakdown in swirling flows.
- Close to a bounding surface or wall the pressure gradient affects boundary layer separation.
- Pressure fluctuations is a characteristic indication for thermo-acoustic instabilities.
- Pressure gradients are already utilized to model several flashback mechanisms in straight and rotating flows.

The measurement of the static pressure in combustion applications is typically conducted using water-cooled, piezo-electric pressure transducers with a high-frequency response of up to 250 kHz [118]. From the temporally resolved time series the magnitude, frequency, and phase of the fluctuations can be determined. The pressure transducers should be flush mounted to the inner wall of the combustor to achieve the most accurate results. However, most often this is not feasible due to the combustor design or the risk of exposing the pressure transducers to flame temperatures. Hence, the pressure transducer and the wall have to be isolated by inserting a small-diameter tube with a recess mount in between. In such a configuration the impact of the tube on the measurement has to be taken into account, as it can alter the amplitude and phase of the signal [74]. Further, the effect of the three-dimensional pressure field caused by the flame has to be considered due to the fact that the pressure can only be measured at the wall. It can also modify the phase and amplitude of the measured signal by up to 20 % [117, 126]. Often further simultaneous measurements are conducted which use additional electronic hardware. Therefor, it becomes necessary to electronically filter the pressure signal to eliminate the noise and also higher harmonics as well as to synchronize the various additionally measured signals in time. Thereby, an additional phase delay can be introduced by the filter and has to be taken into account.

4.1.5 Limitations of Conventional Laser Diagnostics and Data Analysis

The current understanding of turbulent combustion processes is based, to a significant extent, on non-intrusive optical diagnostic methods. During the last three decades a variety of diagnostics has been developed and applied to study flow and scalar fields of a very broad range of flames, from generic to practical [105]. The advent of sensitive charge-coupled device (CCD) cameras particularly allowed to measure instantaneous spatial field distributions of up to three velocity components [157] and scalar quantities such as concentration, pressure, temperature [12, 203]. Spatial gradients and correlations became accessible, complementing single-point statistics. First and second statistical moments are commonly deduced from point measurements. The calculation of these statistical moments requires statistically uncorrelated data sampled with data rates larger than

$$f_{\mathrm{uc}} = \frac{2}{\tau_0} \tag{4.17}$$

with τ_0 being the integral time scale [155]. Integral time scales depend on geometrical properties and bulk flow velocities (see Section 2.1.1). Typically, integral time scales are in the order of a

few milliseconds, usually determined by LDA time series measurements [175, 179]. The underlying ensemble should consist of as many independent samples as affordable to achieve a reliable estimation of statistical moments. A characterization by statistical moments is appropriate for statistically stationary combustion processes.

However, to characterize statistically non-stationary combustion processes, such as extinction, ignition or flame flashback, conventional uncorrelated data sampling is unsuitable. Non-stationary processes, or transient events, in turbulent combustion are typically characterized by

- small time scales,
- individual realizations, and
- often unpredictable onset.

Typical time scales are usually in the order of a few milliseconds. These are far smaller than the conventional sampling rates of a few Hertz. Hence, conventional diagnostics is limited to often not more than one measurement per event. Collecting data for statistical analysis can be very time consuming since the experimental preparations for a single event can take from several seconds, in case of reigniting the burner with a lighter, up to days or weeks when large scale rocket engine tests are conducted. Owing to the turbulent nature of technical combustion processes, each instance of a transient event is an individual realization. Therefore, two or more transient events will never have identical velocity or scalar fields during their temporal evolution. The concept of conventional statistics has to be abandoned where hundreds of uncorrelated measurements have to be performed in a quasi-stationary system. Still, there is a need for some kind of statistical approach to uncover underlying physical correlations which is the subject of the present investigations. For example, Fischer et al. [58] have shown how to apply phase averaging with simultaneously-recorded, continuous time traces of pressure. They could show that different oscillation processes in their investigated burner, potentially caused by different physical feedback loops, may have very similar periodic changes in the flow pattern. In internal combustion engine research, crank angle-resolved data evaluation is based on phase averaging of statistically independent measurements, each sampled during a different engine cycle [208]. These techniques work well with processes which are externally controlled or periodic, still being quasi-stationary. Often the beginning of the transient process is not known in advance, e.g. extinction, flashback, auto-ignition, and therefore phase-averaging cannot be applied.

Resolving temporal dynamics is of paramount importance when conventional statistical moments are inappropriate for describing the process. This adds a new perspective to the investigation of transient combustion events. The instrumentation suitable for temporally resolved measurements as well as the concepts for data acquisition, processing and evaluation are presented in the following section.

4.2 High-Speed Laser Imaging Diagnostics

A full temporal resolution of turbulent combustion measurements requires to capture all time scales, including the smallest Kolmogorov and Batchelor time scales. However, in many cases the temporal flame dynamics are driven by large-scale eddies or coherent fluid motions. Examples are auto or spark ignition, flame extinction, flame propagation and stabilization (flashbacks into the nozzles, detached flames), and cycle-to-cycle variations (CCV) in internal combustion

(IC) engines. Such transient events recorded with suitable high-speed diagnostics allow a simple visualization of the process. Quantities such as velocities, time scales and scalar topologies can also be determined. In the physical space, this information provides a clear perspective of the observed processes. This can help to identify underlying mechanisms. Even simple experimental setups to record CL at kilohertz sampling rates provide valuable insights [141, 143, 224].

Identification of distinct flame features generally requires scalar field measurements. Due to its sensitivity at high sampling rates, PLIF is the most commonly used technique for this task. In the following a brief overview on high-speed PLIF and PIV in combustion related applications accompanied by the development of the high-speed instrumentation will be provided.

PLIF at high sampling rates is an emerging technique and complements single or two-point techniques [136, 162, 166, 225]. The pioneering work by Kaminski et al. [92] provided valuable insights into the dynamics of turbulence-chemistry interaction processes. They used a Nd:YAG laser cluster generating a wavelength-tunable pulse burst of up to eight pulses by pumping a dye laser. PLIF signal detection was performed using eight ICCDs integrated into one system (Hadland). Based on this technology, early phases of spark ignition in homogeneous turbulence were investigated [41, 93]. The temporal evolution of flame front wrinkling, which depends on the turbulence level, fuel composition and equivalence ratio, was followed and qualitatively compared to DNS. In a follow up study, high-speed OH-PLIF at 33 kHz was combined with PIV and double-pulsed Rayleigh imaging. Individual extinction events within a turbulent diffusion jet flame (DLR B flame) were correlated with local strain fields and vorticity [80]. This study clearly demonstrated the value of fully 3D velocity vectors, obtained from Stereo-PIV, in avoiding ambiguities due to the out-of-plane motion. The eight-pulse burst laser was also used to study CCV in IC engines [81]. Sequences of fuel tracer or OH radical distributions were monitored during single engine cycles. Local flame front propagation could be deduced by tracking the fuel tracer distribution. By scanning the laser beam perpendicular to the light sheet plane, 3D fuel concentrations could be reconstructed from the multiple, quasi-instantaneous, 2D measurements.

Ongoing research on high repetition rate burst mode laser operation aims at pulse trains containing up to 100 single pulses at high energies. This has been achieved by using a pulse-amplified continuous wave Nd:YAG ring laser and subsequent second or third harmonic generation [223]. By pumping an additional custom-built optical parametric oscillator, Jiang et al. [88] could produce wavelength-tunable high energy laser bursts in the deep UV. Until now, this laser technology was used to demonstrate the feasibility of OH-PLIF at up to 50 kHz in a turbulent hydrogen-air diffusion flames [139] and to study passive scalar mixing by NO-PLIF in a supersonic wind tunnel at 500 kHz sampling rate [89]. Another way to produce adequate laser bursts of up to 200 pulses is by using the second harmonic output of a Q-switched DPSS Nd:YAG laser and subsequent frequency-doubling to 266 nm. Gordon et al. [65] applied this technique to measure mixture fraction in an acetone-seeded flow.

Continuous-pulsed operation of DPSS lasers and camera systems permit cinematographic PLIF imaging techniques. At fixed laser wavelengths, imaging of large fuel tracer and even OH molecules was realized. Smith et al. [185] monitored biacetyl by PLIF at a data acquisition rate of 12 kHz. The data was used to temporally track the fuel distribution in a direct-injection IC engine near the spark plug. Paa et al. [144] used an all-solid-state Yb:YAG disk laser system operated at 343 nm and 1 kHz repetition rate to excite the hot band transition $A^2\Sigma^+(v'=0) \rightarrow X^2(v''=1)$ of OH. With single-pulse energies of 3.7 mJ they were able to produce a reasonable SNR despite the low fluorescence quantum yields. Currently, efforts are being made to excite the A-X (2,0) band with a frequency-quadrupled Nd:YLF laser at 263 nm and 1 kHz repetition rate [31]. So far, reasonable single-shot SNR is prohibited by low pulse en-

ergies of ≈ 50 µJ in combination with a low fluorescence quantum yield. Higher quantum yields for OH excitation can be obtained by tuning the laser wavelength to a strong transition. This can be achieved by using frequency-doubled dye lasers. This was done for the first time by Wäsle et al. [222] to excite OH in the $A^2\Sigma^+(v'=1) \rightarrow X^2(v''=0)$ band at 283 nm and 1 kHz repetition rate. The system was used to study heat release fluctuation in turbulent premixed flames. Single shot energies were ≈ 80 µJ, which allowed for flame front detection at a laser sheet height of 100 mm using a multi-pass cell. Repetition rates of frequency-doubled dye lasers were successively increased up to 5 kHz by Kittler and Dreizler [102]. OH was excited in the same band, improving the SNR remarkably, although the pulse energies were as low as 22 µJ. Since then, due to current DPSS and dye laser development, repetition rates have been increased to 10 kHz and single-pulse energies tunable around 280 nm were increased above 200 µJ.

PIV is an established measurement technique for recording the instantaneous planar flow field [3, 157]. It provides an instantaneous 2D flow field and allows the computation of derivative quantities (e.g. strain rates and vorticity) that provide additional physical insight into combustion processes. The technique is well developed, commercially available and widely used in the field of fluid dynamics. Upatnieks et al. [206] developed a high-speed PIV system that uses a high-speed rotating prism film camera, providing a sufficient combination of frame rate, resolution and sequence length for the study of high Reynolds number turbulent flows. This system was applied to turbulent jet flames at data acquisition rates of 8 kHz. Even higher sampling rates up to 20 kHz were achieved by Williams et al. [220] using a drum film camera. The rapid improvements in CMOS camera technology in recent years has meant that analogue film cameras could be replaced by digital ones while still providing kilohertz frame rates and a sufficiently high resolution. For instance, pixel resolutions of 688×704 pix at 6 kHz were obtained by Müller et al. [140]. These systems have been used widely to study the in-cylinder flow field of IC engines [43, 87, 202]. While most investigations were restricted to motored engine conditions, PIV was demonstrated at 16 kHz in a direct injection fired engine by Fajardo and Sick [50], providing insights into the evolution of the flow field throughout individual cycles. Latest high-speed PIV measurements in engines are summarized by Sick et al. [182]. Furthermore, high-speed PIV has been applied to jet flames [19], opposed jet flames [15, 76] and confined swirled flames [11, 110]. Barbosa et al. [11] for example apply PIV at 12 kHz in a confined swirled flame to identify multiple convective reactive structures associated with combustion instability. These kinds of measurements were extended from two to three components of the flow field in jet flames [19, 194] and confined swirled flames [11, 20].

In the following subsections different aspects of high-speed laser imaging will be highlighted. This begins with a short introduction to the terminology of correlated data sampling in order to clarify commonly misused terms. Subsequently, the technical apparatus to conduct the most important laser imaging diagnostics in flames is presented. Further attention will be paid to the interdependency of the spatio-temporal scales of the process of interest and the camera performance. For very high repetition rates, the potential of measuring volumetric data is discussed, which enables a quasi-4D acquisition. The true strength of high-speed diagnostics by recording multiple parameters simultaneously and corresponding techniques for data processing are addressed prior to closing the section with a prospect of further hardware developments in combustion diagnostics.

4.2.1 Terminology

Whenever a new technique or new concept is introduced it takes a certain time to occupy its place besides existing technologies. During this time also a new specific terminology develops that has to be adopted by the community working with it. This process is usually much slower than the actual application of the novel technique and also accompanied by misinterpretations of existing terminology already in use in similar technological fields. Therefore, a few common mistakes and potential errors in the use of the right terminology will be rectified and clarified, before the technical details of high-speed laser diagnostics are discussed.

Whenever the term *high-speed* is used in this work it refers to *temporally-correlated* acquisition of data. This means that successive data samples contain the same information to a certain amount, which depends on the ratio between the sampling frequency and the time scale of the process under investigation. Hence, the Nyquist criterion can be a measure for correlated data sampling, as shown in Section 4.2.3. With respect to turbulent flows, the term high-speed refers to sampling rates ≥ 1000 Hz. As mentioned above, the sampling rate is the inverse time between two successive measurements, while the temporal resolution (mostly) refers to the duration of time necessary to conduct one measurement. Thus, the time span between data samples cannot be reduced below the temporal resolution without acquiring redundant information.

In analogy to the temporal considerations above, the spatial resolution of an array detector, such as a CMOS camera chip, can therefore be defined by the size of the area which is sensitive to photons. On the other hand the spatial sampling rate is defined by the pixel pitch, which is the size of a full pixel. Widely used CCD arrays of scientific cameras feature a fill factor close to unity. Here, the photo sensitive area covers almost the whole pixel. Hence, spatial sampling rate and resolution are nearly the same and the usually tiny difference can be neglected. However, CMOS array detectors, as integrated in current high-speed cameras, incorporate larger areas of circuitry which is not sensitive to photons. This deficiency is often compensated by the use of micro lenses in front of the pixels. These collect the photons over the whole pixel area and focus them onto the photo-sensitive part of the pixel. Nonetheless, there can be a significant difference in spatial sampling rate and resolution and care has to be taken when the performance of the imaging system is specified.

4.2.2 Apparatus

The following section provides a review of the instruments required for multi-parameter high-speed diagnostics. It starts with the possibilities to generate a burst or a continuous sequence of laser pulses of the appropriate wavelength. Afterwards, the cameras and image intensifiers are presented that detect the photons subsequently emitted from the measurement volume. Finally, a short outlook on the future development of these devices is provided.

Pulsed Laser Sources

Planar high-speed diagnostics with continuously pulsed repetition rates in the multi-kilohertz regime became feasible with the advent of Q-switched, high power, diode laser-pumped, solid-state (DPSS) lasers. They generate quasi-cw power of up to 100 W in the visible spectral range. Subject to cavity design and extra or intra-cavity frequency-doubling, pulse lengths range from five to a few hundred nanoseconds.

The laser specifications required depend on the diagnostic method. PIV is commonly used for flow field measurements. Here, double-pulse laser systems with an adjustable pulse-to-pulse separation independent of the basic repetition rate are required. For moderate turbulent flows with large time scales ($\mathrm{Re} < 10,000$), it is feasible to use fast single-pulse systems. For that purpose, the repetition rate has to be adjusted to match the required temporal pulse-to-pulse separation for the PIV algorithm. The data acquisition rate is predetermined by post-processing steps and is not arbitrary. For 2C (2C) PIV, thin sheets, typically of a few hundred micrometers in thickness, are formed. This demands reasonable M^2 factors [37], concentrating most of the laser energy in the center of the light sheet. For 3C Stereo-PIV, the laser light sheets are usually much thicker, typically in the order of millimeters. Consequently, larger M^2 factors are acceptable. Since laser pulse lengths are usually short, restrictions on pulse lengths in most applications are not stringent, thus lasers with high single-pulse energies should be selected. 2C and 3C high-speed PIV was demonstrated for a number of combustion related configurations [15, 19, 51, 110, 140, 194, 206]. The commercialization of PIV systems has reached a level where many suppliers are able to provide solutions sufficient for high-speed measurements.

Scalar measurements are different to this. Single-pulse energies at high repetition rates are limited to a couple of millijoules when using frequency-converted DPSS lasers. When tunable high-speed dye lasers are used, shot energies are even further reduced to sub-millijoules levels. Therefore, spectroscopic methods with high quantum yields are required for planar scalar field measurements at high sampling rates. So far, Rayleigh scattering and LIF have been demonstrated and applied at multi-kilohertz sampling rates. Rayleigh scattering was restricted in the past to two-point applications using frequency-doubled radiation from DPSS lasers [209, 210]. Although LIF started with one and two-point applications [161] it has been further developed into a planar technique.

PLIF is a technique that is based on resonant excitation. Hence, tunable lasers are mandatory for electronic excitation of small molecules such as OH, CH, NO, or CO [105]. For larger molecules that exhibit broad excitation bands, like formaldehyde [22, 172] or commonly used fuel-tracers such as acetone, biacetyl, or 3-pentanone [177], lasers with fixed emission wavelengths are used.

Formaldehyde or fuel-tracers can be excited electronically by radiation at 355 or 266 nm. These emission wavelengths are easily generated by tripling or quadrupling the fundamental Nd:YAG laser frequency. To generate tunable radiation for excitation of diatomic molecules such as OH, CH, NO, or CO, frequency-doubled or tripled dye lasers are used. Dye lasers are commonly pumped by frequency-doubled or tripled Nd:YAG lasers at 532 or 355 nm, respectively. For low repetition rates, and hence statistically uncorrelated information, Nd:YAG and dye lasers were improved over many years and are commercially available. Laser repetition rates exceeding 1 kHz can be achieved by either pulse bursts with high single pulse energies or continuously-pulsed operation with much lower pulse energies. Initially, pulse bursts that consist of between four and 100 single pulses are generated. Repetition rates within such bursts can be up to megahertz [223] but the repetition rate of the burst itself is typically 10 Hz. Jiang et al. [89] report on pulse bursts of 20 single pulses generated with pulse lengths of approximately 8 ns and pulse energies of up to 400 mJ/pulse at 50 µs spacing (20 kHz). In the next step, tunable radiation was generated at 226 nm with single pulse energies of ≈ 0.5 mJ using an optical parametric oscillator (OPO) and sum-frequency mixing. This allowed for the cinematographic tracking of NO distributions by PLIF in a hypersonic wind tunnel. In Kaminski's et al. earlier approach [92], four double-pulsed Nd:YAG lasers were operated. Using staged frequency doubling, a pulse train of up to eight pulses was emitted from a conjoint port. A single tunable dye

laser was pumped with this pulse train. Pulse-to-pulse separations were 125 µs (8 kHz). After frequency doubling, pulse energies of 1 mJ were achieved at 282 nm.

The second approach takes advantage of recent developments in all-solid-state lasers and new dye lasers specifically designed for continuously pulsed high repetition rate operation. All-solid-state lasers are mostly diode-pumped and Q-switched devices. In contrast to the burst mode approach, laser operation is quasi-continuous. At a repetition rate of 10 kHz, single-pulse energies of approximately 10 mJ are obtained. This is obviously much lower than the magnitude of single-shot energies achieved by burst mode operation. Among the all-solid-state lasers, two types are commercially available that exhibit either pulse durations above 90 ns or below 15 ns. Long-pulse lasers, usually Q-switched by an acousto-optic modulator (AOM), produce lower intensities. Therefore, intra-cavity frequency conversion is required to generate visible or UV light. Pockels cell Q-switched resonators with shorter pulse durations allow for extra-cavity frequency conversion [124]. Other specifications, such as the M^2 factor, can differ significantly as well.

UV laser pulses generated by frequency-tripling or quadrupling of all-solid-state lasers can be used to excite fuel tracers such as acetone [65], biacetyl [186] or combustion intermediates such as OH [144]. In a different approach, frequency-doubled radiation from these all-solid-state lasers can be used to pump tunable dye lasers. The emitted radiation can then be frequency-doubled into the UV range. In contrast to burst mode operation, the main challenge is to pump dye lasers with single-pulse energies below 10 mJ but with quasi-cw power levels up to 100 W. Higher pulse intensities of short-pulsed pump lasers are beneficial, especially for subsequent non-linear frequency conversion into UV. To avoid bleaching of the dye and/or significant triplet-state population that reduces the quantum yield of the fluorescence, the flow rate of the dye solution needs to be increased. Flow rates of these devices are typically up to 12 L/min. In addition, lowest oscillator laser thresholds possible are needed. Based on the most recent laser design, 4 W at 10 kHz were achieved around 283 nm using 50 W pump power (Sirah Credo).

CMOS Cameras and high-speed Image Intensifiers

Planar detection of LIF requires suitable optics and a sensitive array detector. In the case of fluorescence within the UV range, the collection lens needs to be made of quartz or CaF_2 and a UV-sensitive array detector is required. High repetition rates go along with low LIF signal intensities. For this reason, high collection efficiencies are mandatory.

A variety of array detectors suitable for PLIF applications can be operated at high framing rates. An ultra fast framing camera (Hadland) was used for high-speed OH-PLIF, as demonstrated by Kaminski et al. [92]. It consisted of eight independent intensified CCD (ICCD) cameras, each with an 8 bit dynamic range and 576×384 pix. Individual events were imaged onto the respective ICCDs by a special eight-faceted pyramid beam splitter. An additional intensifier was installed in front of the beam splitter at the optical entrance to the camera to increase the UV sensitivity. This camera had a maximum frame rate of 1 MHz but was limited to a sequence of eight images per recording.

The PSI-4 (Princeton Scientific Instruments) framing single-stage ICCD camera is another type of CCD-based camera technology that takes advantage of charge buffers integrated into each pixel (in situ storage). The camera system has up to four image sensors [120]. Each of these four image sensors is composed of an 80×160 pix array. The pixel pitch is 115 µm and each pixel contains its own integrated 28-elements charge buffer, reducing the fill factor to about 50%. The charges and hence the image information is transferred to the buffers with a maximum frame

rate of up to 3 MHz, storing the preceding 28 acquisitions before the stop trigger is released.

Another CCD [49] commercialized by Shimadzu takes advantage of the in situ storage concept. Up to 103 successive frames can be stored with a maximum frame rate of 1 MHz. This increased storage capacity has a fill factor of only 13% at 8 µm pixel pitch. The array consists of 312×260 pix pixels with a nominal dynamic range of 10 bit. In combination with a lens-coupled, intensified relay optic (IRO) these cameras are UV sensitive.

High frame rates can also be achieved with CMOS cameras. The key difference between a CMOS array detector and a CCD is that the charge-to-voltage conversion occurs at each individual pixel. Thus, selective readout of pixel information is possible, resulting in variable regions of interest. In combination with a multitude of Analog-Digital-Converters (ADC), the information readout is parallel rather than serial, as in CCDs. The digitized images are transferred to an on-board memory. For a given image size and dynamic range, the on-board memory limits the number of frames that can be recorded during one run. The largest on-board memories available are currently up to 32 GByte and can record up to a million frames during a single run depending on the number of active pixels. In comparison to CCDs, this feature permits temporal tracking of transients in combustion for much longer durations. This is obviously beneficial, as time intervals of interest, such as during flashback, often spread over a couple of milliseconds. CMOS cameras with the capability of recording sequences of thousands of images have been developed to a state where they are sufficiently sensitive for use in high-speed PIV/PTV applications, which demand a large number of active pixels. Although high frame rates exceeding 500 kHz are possible with CMOS cameras, the number of active pixels is remarkably reduced at these high frame rates, since the pixel readout rate is limited by the number and speed of ADC. This topic will be addressed in more detail in Section 4.2.3. For lower frame rates, i.e. 5 kHz, a mega pixel resolution is commercially available (e.g., Photron Fastcam SA1 or Phantom v12.1). The nominal dynamic range of CMOS cameras can be as high as 14 bit. However, in comparison to CCDs that are available at standards of scientific grade quality, CMOS cameras are characterized and optimized mainly in terms of homogeneity or linearity. This lack of full characterization is due to their mainly industrial application, such as automotive crash tests. These current imperfections of CMOS cameras hamper their use in quantitative scalar imaging. A calibration per pixel has to be performed to account for varying fixed pattern noise, sensitivities and potential non-linearities [212]. Similar to CCDs, CMOS cameras are not UV sensitive. For this reason and for shorter shutter speeds, CMOS cameras are combined with image intensifiers which are either lens or fiber-coupled. For applications with low light intensity levels, such as PLIF at high sampling rates, two-stage intensifiers are commonly used. Present intensifier technology combines a multi-channel plate and a booster that permits frame rates exceeding 20 kHz with minimal electron depletion, which reduces the effective dynamic range.

Future Development

The current trend in the manufacturing industry as well as academia to achieve faster repetition and frame rates and longer burst durations is still unbroken. The need for high powered and fast pulsed laser system in the production process of solar panels with its growing market drives the development of continuously pulsed DPSS lasers. Longer sequences of burst laser systems with pulse energies up to $2\,\mathrm{J/pulse}$ are currently under development [196]. Until recently the readout speed of the few existing high-speed CMOS camera chips have been continuously enhanced, almost doubling the pixel rate every two years. Currently new CMOS chip families are under development, which are expected to continue this trend. Also new low noise scientific grade sC-

MOS technology is being developed. These chips are characterized by a very low dark noise and high sensitivities, which make extremely high SNR feasible. It is expected that the sCMOS technology will be taken up by the high repetition rate applications to produce high-speed camera chips which eliminate the current deficiencies related to high-speed CMOS cameras [212]. Furthermore, faster scan devices for volumetric imaging are under development [213]. The future development of high acquisition rate measurement hardware will continue to extend the perspective of combustion research to even higher levels of turbulence, faster transient processes, and larger three-dimensional measurement volumes.

4.2.3 Interdependency of Spatial and Temporal Scales

Turbulent reacting systems are characterized by different time and length scales. The fundamental concept of various scales of turbulence and chemical reactions have been introduced in Chapter 2. The scales represent the classical characterization of statistically stationary systems. These systems vary from one instant to another, while being stationary in the mean. The potential of high-speed diagnostics to capture transient events by temporally correlated data acquisition introduces additional scales. They are explained in the following and their interdependency with the classical scales of the flow and the flame is shown.

Temporal Scales

Transient processes feature further time and length scales, which have to be taken into account when setting up an experiment. The experimental part of this work focuses on temporally correlated data sampling. The starting point for the discussion on the interdependence of spatial and temporal scales is the relation between three time scales. These are the time scale of the flow field τ_u, the chemical reactions τ_c and the process under investigation τ_pro, such as the transition time from the initial to the final states. In practice Eq. (4.18) holds for most systems of turbulent combustion research

$$\tau_\mathrm{pro} > \tau_u > \tau_\mathrm{c}. \tag{4.18}$$

Depending on the purpose of the experiment one of these time scales limits the sampling rate of the measurement technique to a necessary minimum. This must be fulfilled or exceeded in order to guarantee a successful temporally correlated measurement. For instance, the limiting scale can be the integral time scale of the flow τ_0, when large scale turbulence drives the process of interest. Nonetheless much smaller scales, e.g. the Kolmogorov scale τ_η, can set the limit if autocorrelation functions are of interest. At small Damköhler numbers, where chemistry is slower than turbulent transport processes, one can imagine that even the chemical time scale τ_c can set the minimum sampling rate. The time scale of the process is usually the average duration in which the reacting system passes from the initial to the final state. It does not limit the necessary sample rate, but defines the minimum recording duration t_rec.

From the selected limiting time scale $\tau_\mathrm{limit} = 1/f_\mathrm{s}$ a minimal sampling frequency f_s (in frames per second) can be defined using the Nyquist rate f_N

$$f_\mathrm{s} \geq f_\mathrm{N} = 2 \cdot f_\mathrm{limit} = \frac{2}{\tau_\mathrm{limit}}. \tag{4.19}$$

Applied to single frame high-speed laser imaging setups, such as OH-PLIF, the sampling rate directly sets the repetition rate of the laser and the recording frequency of the camera. It should

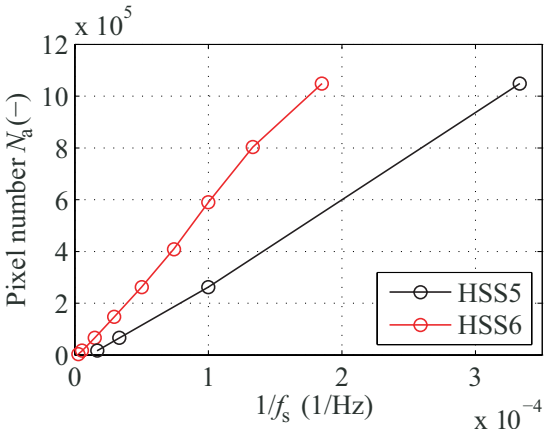

Figure 4.13: Pixel rate diagram for high-speed CMOS cameras

be noted that in case of double frame techniques (e.g. PIV, PTV etc.) the recording frequencies have to be twice as high.

The recently developed high-speed CMOS cameras feature a constant pixel rate recording technique. Thereby, the performance limiting factor of a camera is the maximum number of active pixels that can be read-out in a fixed time interval. This is usually determined by the number of built-in ADCs. The memory architecture of CMOS cameras allows to reduce the number of active pixels on the chip during a recording cycle and hence reduces the readout time at constant pixel rate. Thereby variable recording rates with corresponding active chip areas can be achieved. Hence, the pixel rate R_{pix} can be defined as

$$R_{\mathrm{pix}} = N_{\mathrm{a}} \cdot f_{\mathrm{s}} \tag{4.20}$$

where N_{a} is the number of active pixels per frame. Fig. 4.13 shows the linear relationship between the number of active pixels N_{a} and the inverse sampling rate $1/f_{\mathrm{s}}$ for the possible operation modes of two different CMOS cameras that have been used during the experiments. The pixel rate can be extracted from the inclination of the lines. While the slightly older model HSS5 (HSS: High-Speed Star) has a pixel rate of 123 Gpix/s, the current model HSS6 has been enhanced up to 456 Gpix/s most probably by increasing the number of ADCs. Both cameras are limited to 1024×1024 pix.

Spatial Scales and Spatio-temporal Interdependency

Figure 4.14 shows a generic camera system imaging a measurement volume. The square array detector of $n_x \times n_y$ pixels has a side length of l_{chip}. Each square pixel of side length l_{pix} transforms to a region of the measurement volume of the size $\Delta x = l_{\mathrm{pix}}/M$, where M is the magnification. The term Δx can also be regarded as the pixel resolution, with the unit of meter per pixel. The number of pixels along a column of the array n_x, obtained by the ratio between the size of the chip and the pixels, can also be expressed as a function of the sampling rate using Eq. (4.20)

$$n_x = \frac{l_{\mathrm{chip}}}{l_{\mathrm{pix}}} = \sqrt{\frac{R_{\mathrm{pix}}}{f_{\mathrm{s}}}} \quad \text{with} \quad n_x = n_y. \tag{4.21}$$

The camera's field-of-view l_{FOV}, which limits the physical size of the measurement volume and the acquisition of the largest scales, depends on n_x, pixel size l_{pix}, and the magnification M in the

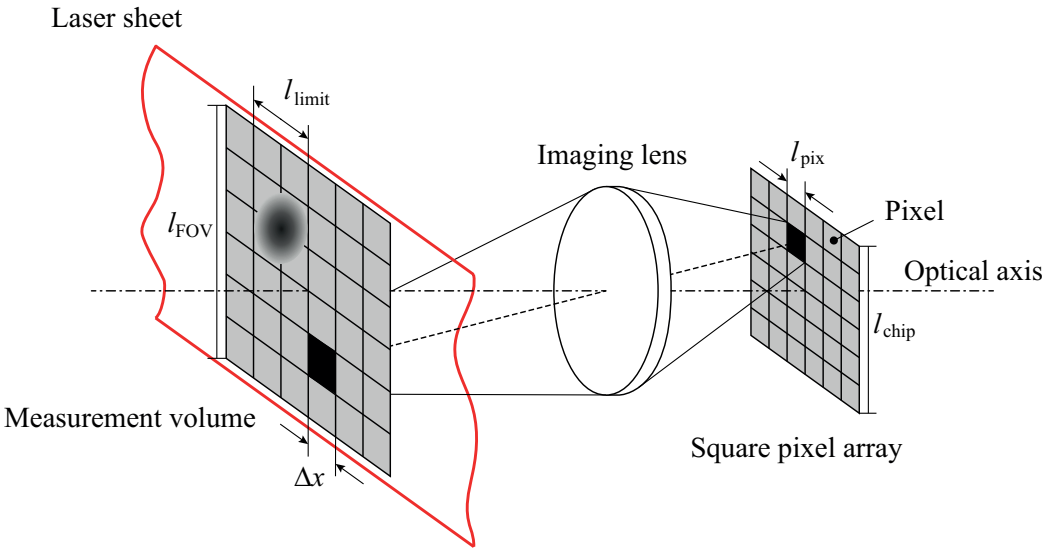

Figure 4.14: Schematic of planar laser imaging using a square array detector

following manner

$$l_{\mathrm{FOV}} = n_x \cdot l_{\mathrm{pix}} \cdot M = n_x \cdot \Delta x. \tag{4.22}$$

The smallest resolved spatial scales l_{limit} can often be related to the time scales of interest by Kolmogorov's hypotheses. These can be defined similarly to the limiting time scale to be

$$2 \cdot \Delta x \leq l_{\mathrm{limit}}. \tag{4.23}$$

By inserting Equations (4.19), (4.22) and (4.23) into (4.21) the dependency of the camera parameter R_{pix} and the spatio-temporal scales of interest can be obtained as

$$\frac{l_{\mathrm{FOV}}}{l_{\mathrm{limit}}} = \frac{1}{2}\sqrt{\frac{R_{\mathrm{pix}} \cdot \tau_{limit}}{2}}. \tag{4.24}$$

It should be noted that the limiting parameter for high-speed imaging experiments as a function of a time scale is expressed as the ratio between the largest observable structures within the field-of-view and the smallest resolved structures, i.e. the spatial dynamic range. The function is shown on the left hand side of Fig. 4.15 for the two camera types that were used.

The magnification of the imaging system can be adjusted by the imaging lens configuration such that the spatial sampling criterion in Eq. (4.23) is met. The magnification of the system for a certain limiting length scale is then calculated as

$$M = \frac{l_{\mathrm{pix}}}{\Delta x} = \frac{2 \cdot l_{\mathrm{pix}}}{l_{\mathrm{limit}}}. \tag{4.25}$$

It is principally possible to adjust the pixel resolution to any pixel size by changing the magnification. Nevertheless, Clemens [27] has shown that the signal acquired by laser imaging experiments is significantly influenced by the magnification of the imaging system. Besides other dependencies the author shows that the signal is proportional to

$$S \propto \frac{M}{(M+1)^2}. \tag{4.26}$$

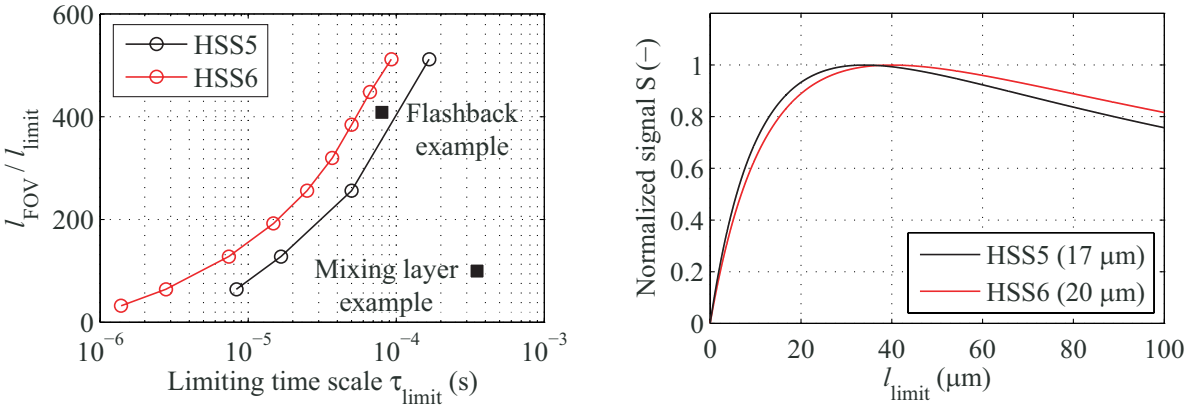

Figure 4.15: high-speed camera performance diagram with spatio-temporal parameters of the experiment on the axes (left) and relative signal intensity as a function of the smallest scales in a high-speed laser imaging experiment (right).

At a magnification of unity the signal is maximized. For a given pixel size of a specific camera, the normalized signal intensity can be calculated using Eq. (4.25) for various limiting length scales by

$$S \propto \frac{2 \cdot l_{\mathrm{pix}}}{l_{\mathrm{limit}}} / \left(\frac{2 \cdot l_{\mathrm{pix}}}{l_{\mathrm{limit}}} + 1 \right)^2 . \tag{4.27}$$

The results for the high-speed cameras are shown on the right hand side of Fig. 4.15. Obviously, the maximum signal is obtained when the limiting length scale is twice the pixel size. At that point the magnification of the system becomes unity.

A last parameter which is of great importance is the earlier mentioned minimum recording duration t_{rec}. It is mandatory to match or even exceed this parameter with the hardware in use to capture the process of interest entirely. Using CMOS cameras, the recording duration t_{rec} is defined by the pixel rate R_{pix} and the total number of pixels N_{tot} that the camera can record as

$$t_{\mathrm{rec}} = \frac{N_{\mathrm{tot}}}{R_{\mathrm{pix}}}. \tag{4.28}$$

The total number of pixels is usually determined by the size of the camera memory. It should be mentioned that Eq. (4.28) only holds when the camera is operated at its maximum pixel rate. If R_{pix} is decreased the recording time is obviously increased. In an experiment it is therefore of advantage to adjust the pixel rate to match the requirements for τ_{limit} and $l_{\mathrm{FOV}}/l_{\mathrm{limit}}$ in order to extend the total recording duration. This is especially helpful if the process of interest happens at an unpredictable point of time. Thus, the hardware has to be triggered randomly and long recording durations are advantageous.

Two Examples: A Mixing Layer and Flame Flashback

The application of the scales diagram in Fig. 4.15, showing the interdependency of spatio-temporal scales and high-speed laser imaging hardware, is illustrated in the following. Two examples of scalar imaging of a mixing layer and flow field imaging during flashback will be discussed. Let us consider mixing in the shear layer between two fluids of different velocity as investigated by Rebollo [160] and depicted in Fig. 4.16. A scalar should be imaged, that varies

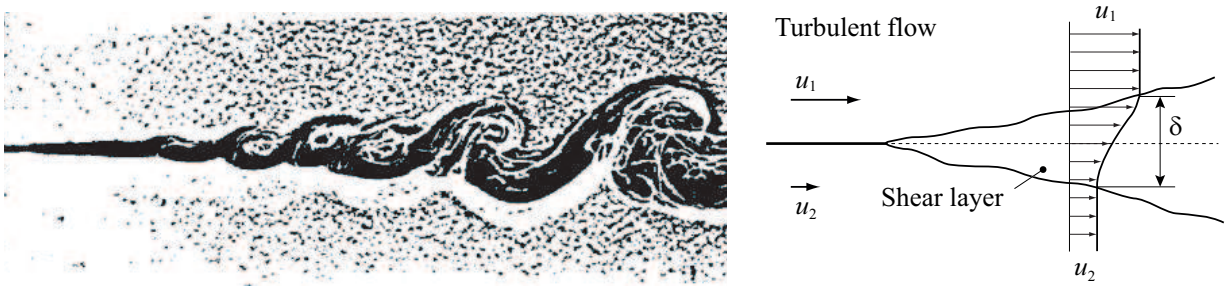

Figure 4.16: Mixing in the shear layer between two fluids [160]

with the concentration ratio between stream one and two. A non-stationary mixing layer with coherent structures of height $\delta(x)$ is formed due to differences in the bulk velocity and the density of the two streams. In the investigated configuration, the increasing shear layer thickness is approximately 1.5 mm at the beginning of the mixing layer. The coherent structures within the layer should be resolved by a factor of 10. Hence, the smallest resolved length scales should be $l_{\text{limit}} = 0.15$ mm. To track the structures over an adequate length, the field-of-view of the camera should be limited to 10 times the minimal shear layer thickness $l_{\text{FOV}} = 10 \times \delta = 15$ mm, which results in a ratio of $l_{\text{FOV}}/l_{\text{limit}} = 100$. The time scale of mixing is estimated from the velocity difference of the two streams $\Delta u = 6\ \text{ms}^{-1}$ and the minimum shear layer thickness to be $\tau_{\text{limit}} = 1.5\ \text{mm}/6\ \text{ms}^{-1} = 250$ ms. The scales diagram in Fig. 4.15 clearly shows that it is possible to capture the phenomenon with both high-speed cameras, while still having the possibility to either increase the field-of-view or the recording rate by an order of magnitude.

In the second example a flow field is investigated with PIV. The process of flashback in the TECFLAM burner, i.e. flame propagation from the top of the bluff-body into the swirler, lasts for about 200 ms. This defines the minimal recording duration t_{rec}. The optical accessibility in combination with the PIV technique allows for a field-of-view of about $l_{\text{FOV}} = 13$ mm. The smallest length scales that should be resolved in the velocity field near the bluff-body should be in the order of 500 µm. In combination with interrogation area sizes of 16×16 pix this results in a limiting length scale of $l_{\text{limit}} = 500\ \mu\text{m}/16 = 31.25\ \mu\text{m}$. Hence, $l_{\text{FOV}}/l_{\text{limit}}$ yields a value of 416. Usually the time scale for a certain process can be estimated in advance and can be used directly as τ_{limit}. In this example, the limiting time scale is estimated based on the time it takes a fluid element to travel through the measurement volume at the axial bulk velocity of $u = 6\ \text{ms}^{-1}$. The flow field should be sampled at least 50 times during the transit time of 2.16 ms. According to Eq. (4.19), it results in a limiting time scale $\tau_{\text{limit}} = 2 \cdot 2.16\ \text{ms}/50 = 86.4\ \mu\text{s}$. From Fig. 4.15 we can extract that the necessary parameters can just be achieved by the HSS6 model. The older HSS5 camera is not able to reach the requirements of 86.4 µs at a ratio of 416. In terms of the signal intensity both cameras with a pixel sizes of 20 and 17 µm, respectively, operate at the theoretical maximum associated with a magnification of $M = 1$. In order to achieve the requirements the HSS6 has to run at the maximum pixel rate of $R_{\text{pix}} = N \cdot f_{\text{s}} = 1024^2\ \text{pix} \cdot 5400\ \text{Hz} = 5.24\ \text{Gpix/s}$. At that rate the camera has a maximum recording duration of 1 s, which is well above the requirement of $t_{\text{rec}} = 200$ ms.

4.2.4 Quasi-4D Acquisition

Instead of increasing the measurement duration, a further remarkable advantage of high-speed acquisition can be utilized if the sampling capabilities of the hardware exceed the requirements.

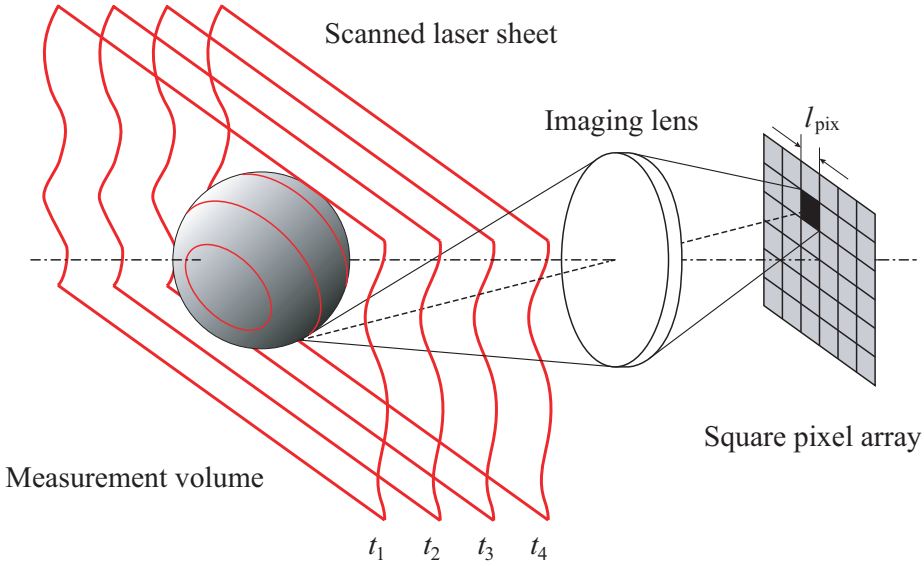

Figure 4.17: Principal setup of a high-speed scanning experiment

Data from multiple parallel volumes (or other geometrical configurations) can be acquired by periodically scanning the light sheet through space with a laser scanning device. Working with a pulsed laser to illuminate or excite the volume, such as in PIV or OH-PLIF, the total measurement volume will be sliced into sections similar to tomographic methods, as known from medical imaging applications [145].

The advantage of volumetric data is obvious in turbulent combustion research. The originally planar imaging technique is enhanced to obtain not only the in-plane gradients and structures, but volumetric structures and gradients in all three spatial directions. Thereby, the spatial resolution of the third dimension depends only on the distance between the slices. It should be noted that a resolution similar to the in-plane measurements is hardly feasible, thus data interpolation techniques need to be applied.

If the measurements are conducted with the appropriate sampling rates, the applied technique can be referred to as *quasi-4D* resolved. It requires the time scales of camera acquisition and laser repetition to be much shorter than the time scales of the system under investigation, such that the requirements of correlated data sampling are fulfilled even with periodical scanning. For turbulent reacting systems this means extreme requirements for the laser and camera hardware, as well as for the scanning device. The latter is required to deliver scanning cycles of a few thousands per second. If these requirements are fulfilled, the phenomenon of interest can be assumed to be *frozen*. This means that no or negligible movement of the flow is occurring while the total measurement volume is scanned.

In principle the technique can enhance all diagnostics using a light sheet to produce a planar signal, which is recorded by a camera normal to the sheet. Mie-scattering by particles, for instance, for coarsely resolved mixing analysis, planar concentrations measurements of OH, CO, and NO by PLIF and even velocity vector data by PIV can be extended to the out-of-plane direction. Nevertheless, the out-of-plane velocity component in PIV still cannot be determined. The technique only allows to estimate gradients of the in-plane velocity components normal to the sheet.

The scanning technique poses further requirements on the laser and detection system. Lasers for high-speed diagnostics usually feature high output powers. However, the pulse energy of

these system is orders of magnitude lower than in conventional systems. This demands large quantum efficiencies and collection angles of the detection optics to reach a reasonable SNR. For example, laser energies of 180 µJ were reported by Kittler et al. [102] in the first publication on high-speed OH-PLIF at 5 kHz. The authors could achieve an SNR of 20 by using large custom made UV lenses with an aperture of $D = 127$ mm at a focal length $f = 158$ mm and a magnification $M = 1$. In typical flame imaging setups the depth of field δ_{DOF} of this lens configuration can be estimated according to Larmore [158] by

$$\delta_{\mathrm{DOF}} \approx 2 \cdot N \cdot l_{\mathrm{pix}} \frac{M+1}{M}. \tag{4.29}$$

With the f-number $N_f = f/d = 1.24$ and the pixel size $l_{\mathrm{pix}} = 20$ µm, Eq. (4.29) results in a depth-of-field $\delta_{\mathrm{DOF}} \approx 100$ µm. In scanning application the depth-of-field defines the maximum scan range. Larger scan ranges in out-of-plane direction result in blurred images with significantly decreases in-plane resolution. The optical system of Kittler and Dreizler [102] could have enabled a scan range of 100 µm which is unfortunately inappropriate for combustion diagnostics. Therefore, the depth-of-field has to be maximized to guarantee a good optical resolution in all slices. According to Eq. (4.29), which is obviously independent of the focal length, δ_{DOF} can be increased by larger f-numbers N_f (associated with a reduced number of collected photons), larger pixels on the chip l_{pix} and magnifications of $M < 1$ (demagnification).

Several different techniques can be applied to generate slices of laser light in the measurement volume. They differ in the most important properties for laser scanning: Photon absorption, maximum scan frequency, maximum scan angle, scanning accuracy and precision, and variability in scan frequency and scan angle. The associated physical principles imply various advantages and disadvantages with respect to these properties. The first class of scanning devices is realized by opto-mechanical scanning. The principle of beam deflection is the mechanical tilting of a reflecting surface, usually a mirror, relative to the incident laser beam. This results in a deflection angle twice the tilting angle. There exist continuously and discontinuously tilting systems. Opto-mechanical scan systems are broadly applied in bar code scanners, laser milling and carving and laser printers. They are easily available and relatively low priced, but are restricted in their maximum scan rate performance by their inertia. Typical representatives of this class are galvanometers, piezo actors and rotating polygons that have scan rates up to kilohertz. Detailed information can be found in the work of Marshall [132] and Sackmann [169].

Time dependent beam deflection can also be achieved by acousto-optical or electro-optical principles. Both principles are based on diffraction [146]. A crystal is mechanically excited by piezo actors. Due to the generated vibrations a density grating is developing in the crystal structure, which causes diffraction of an incident beam. For monochromatic light, this results in an angular deflection of a certain ratio of photons, which is dependent on the power of excitation. The excitation can be controlled in such a way that the incident beam is fully deflected according to a first order diffraction. Typical response times of these acousto-optical modulators (AOM) for beam deflection are 10 µs. It is limited by the inertia of the piezo crystals exciting the deflection crystal. AOMs can be found in pulsed laser systems where they are used to *Q-switch* the resonator [37].

Electro-optical beam deflection is possible by the linear Pockels effect or the quadratic Kerr effect [146]. In certain optical media a constant or varying electric field produces birefringence. Its magnitude varies linearly with respect to the electric field in the Pockels effect and is proportional to the square of the electric field in the Kerr effect. Similar to the acousto-optical effect, the changes in the refractive index lead to diffraction and hence, deflection of monochromatic

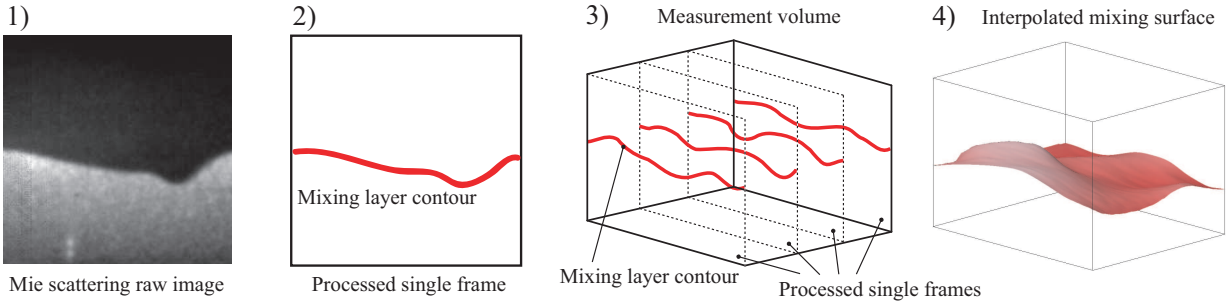

Figure 4.18: Example of volumetric data acquired by a light sheet scanning technique using a galvanometer scanner

light. The response time is solely dependent on the circuit time to create the electric field. This type of device enables scan speeds of more than 10^9 rad/s. Fulfilling the same purpose as AOMs, *Pockels cell* can also be found in resonators of Q-switched lasers.

Additional optics have to be applied in order to parallelize the beams emanating from the scanning device at various angular deflections. The compensation can be achieved by simple single lens setups associated with a relatively poor parallelization quality [213]. Special care has to be taken when designing the optical setup for a scanning experiment. For certain applications with a particular scan angle and focal distance, a few telecentric scan objectives, or f-Θ lenses, are available, which have excellent compensation characteristics [213].

An example of volumetric data acquired by a light sheet scanning technique in combination with Mie-scattering of a particle laden flow is shown in Fig. 4.18. The sequence exemplifies the processing steps to obtain the volumetric information from two-dimensional slices. Starting from the sequence of raw images (1), the contour of the mixing layer between the seeded flow coming from below and the unseeded flow issued from the top is extracted (2). The contour sets for the individual scans are then grouped and positioned relative to each other at the corresponding measurement position. This is determined for each contour by the laser sheet position at the moment of acquisition (3). Finally, the contours in three-dimensional space are interpolated in the third dimension to form a smooth surface of the mixing layer (4). Further application of the scanning technique to obtain volumetric information based on planar measurement techniques can be found in [201].

4.2.5 Multi-Parameter Measurements and Data Conditioning

The greatest potential of high-speed diagnostics lies in quantitative and multi-parameter measurements. By monitoring the spatio-temporal evolution of distinct flame features, such as flame fronts or isocontours of stoichiometric mixture fraction, the laboratory coordinate system can be shifted and transformed into a flame-fixed coordinate system. The flame-fixed coordinate system is moving in physical space due to the transient nature of the non-stationary process under investigation. Then, physical quantities can be treated statistically but are conditioned relative to the distinct flame feature in the flame-fixed coordinate system. For statistically uncorrelated multi-parameter measurements, such as 1D Raman-Rayleigh imaging [12], conditioning is a common procedure. In high-speed multi-parameter imaging, the novelty is the inclusion of time as an additional dimension. Conditioned data recorded during an individual transient event provides completely new information. Mutual interactions between the flame and underlying turbulent

flow fields during their temporal evolution become accessible. This allows the study of the cause and effect chain.

The investigation of turbulence-flame interactions requires simultaneous information on both the flow field and the flame. The change in PIV seeding density due to heat release in flames was used by [194, 207] to determine the flame front. Upatnieks et al. [207] used high-speed PIV at 8 kHz to visualize the time history of the turbulent flow and flame motion to assess theories of flame liftoff in turbulent jet flames. Steinberg et al. [194] used stereoscopic high-speed PIV to reconstruct the 3D flow field of a turbulent premixed flame based on Taylor's hypothesis. Using high-speed PIV in an additional orthogonal plane, the evolution of 3D flow structures and their interaction with the flame was captured. This showed the complexity of 3D flow structures causing straining and wrinkling, contrary to the well-established picture of simple vortex geometry interaction. Although flame front and flow field could be extracted by PIV alone, it is nonetheless desirable to track the flame front using a radical that is generated inside the reaction zone. Konle et al. [110], describe the first application of combined PIV/PLIF at kilohertz sampling rates, using OH as flame front marker. They temporally tracked the relative OH distribution and flow field in a swirled lean premixed flame during flashback. The time-resolved data guided the understanding of the complex transient phenomenon. Böhm et al. [15] combined OH-PLIF and PIV at 5 kHz to study extinction in turbulent opposed jet flames and proposed a multi-dimensional conditioning scheme to allow a comparison of individual extinction events in terms of conditioned statistics. The same setup was used by Heeger et al. [76] to study flame propagation during ignition events in turbulent opposed jet flames. In a study on lifted turbulent jet flames, OH-PLIF was combined with Stereo-PIV, both at 1.5 kHz, such that the out-of-plane motion could be part of the interpretation of the flame dynamics at the flame base [19]. This setup was then extended to 5 kHz sampling rate and applied to lifted jet flames and confined swirling flames [20, 21]. The influence of the flow field on mixing processes can be studied by combining tracer PLIF with PIV. Fajardo et al. [52] demonstrated simultaneous fuel tracer biacetyl PLIF and PIV at a data acquisition rate of 12 kHz in an atmospheric jet, showing instabilities such as vortex shedding. This setup was then applied to a direct-injection IC engine to temporally track the quantitative fuel distribution and flow field at 4.8 kHz [152].

In addition to the necessary instrumentation for high-speed laser imaging, the processing of temporally correlated data brings up several specific challenges. The most obvious challenge is the amount of data that is created during the measurements. As shown in Section 4.2.3 state-of-the-art high-speed CMOS cameras can record up to $10,000\,\mathrm{frames/s}$ at a resolution of 1024×1024 pix. At these settings one second of recording time translates into 10,000 frames that is 8 Gbyte of raw data. It depends strongly on the measurement campaign and the specific aim of the investigations how much data has to be acquired. However, minutes up to hours of raw data usually have to be recorded to gather enough data for statistical analysis. When the onset of the investigated process of interest is not known a priori, experience shows that the amount of data recorded during an experiment increases significantly. The need to store the data redundantly for safety reasons and also legal documentation purposes pose additional requirements on the IT infrastructure and storage capacity. As a consequence, these are often comparable to the requirements of DNS and LES calculations.

Recorded data of several independent events can already give new insights into transient processes and ideas for new models or mechanisms can be generated. However, a comparison of the data from similar processes observed in different experiments as well as comparison of experiments and numerical calculation are only valid when statistical analysis is applied [156]. Hence, individual events cannot be compared due to the unique contribution of turbulence to

each event. To create comparable results conditioning can be applied, which relates the multiple simultaneously acquired parameters to each other [12, 68, 179]. Multi-parameter high-speed imaging diagnostics allows to condition data spatially as well as temporally. It presents a new approach making comparison of transient events feasible. In the following the procedure of the spatio-temporal conditioning will be detailed and possible approaches for comparison to CFD are discussed. The time history of the recorded set of simultaneously acquired data allows for setting a reference time t_0. The selection of t_0 is based on a characteristic state of any of the recorded parameters during the process. For instance, these can be a certain axial position of the flame front during propagation, the time of ignition or extinction or a certain temperature limit. As implied in the examples, the selection is not limited only to predictable events, though they are much easier to capture experimentally. In addition to t_0, the location of occurrence of the investigated phenomenon x_0 is taken into account, as it is also influenced by the large scale turbulence. Here, examples include the flame tip position, the location where quenching is observed first, the position at which a temperature peak is observed, or the center of a vortex. In combustion diagnostics spatial flame front conditioning is most often accomplished by using OH-PLIF. The set of reference parameters, t_0 and x_0, defines a spatio-temporal frame work in which the transient event of interest is fitted into. Hence, all data is referenced according to a fixed point in space and time. This is the reason why this technique is also called *multi-dimensional conditioning*. Nevertheless, individual realizations still cannot be compared, but statistical analysis of the t_0-x_0-conditioned data is feasible.

Recent examples of spatio-temporal conditioning and its application can be found in literature. Böhm et al. [15] used this technique to explore history effects in the extinction of partially premixed flames. They referenced velocity data on the position of the flame front and the location of the first flame breach. This revealed a local strain rate at the flame front exceeding 400 s^{-1} over a duration longer than 4 ms prior to global extinction. In another study on the ignition of partially premixed flames, Heeger et al. [76] could show that edge flame propagation velocities resembled the same values as laminar flame speeds for the corresponding premixed flame by referencing on the edge flame tip and the ignition time. Further examples can be found in [16, 19].

Comparison to CFD Data

Transients from different individual events can be included into conditioned statistics when suitable criteria in the time and space domain are identified. This is an important feature, especially for comparison with numerical simulations, such as LES or DNS. In a general paper on LES, Pope [156] concludes that individual transient events must never be compared. Similar to experiments, this implies that numerical simulation of many individual events is necessary. This is generally limited due to enormous computational costs. However, as shown for simulation of in-cylinder flows studying CCV, this issue can be addressed [66].

A starting point for a statistical comparison of CFD and experiment can be spatio-temporal conditioning on flame front position and a characteristic point in time as presented above. Another criterion can be characteristic frequencies of flow structures such as vortex shedding, precessing vortex cores or pressure fluctuations during thermo-acoustic instabilities. Characteristic time scales can be obtained from the time history of the measured field data. If these time scales are evaluated depending on the spatial location of the control point, the generation of time scale maps is possible. Thereby, the structure of the spatial time scale distribution can be compared to the calculations. In principle, acquisition of time scale maps is also possible by the application of LDA, but the efforts to record a full field make this conventional measurement technique im-

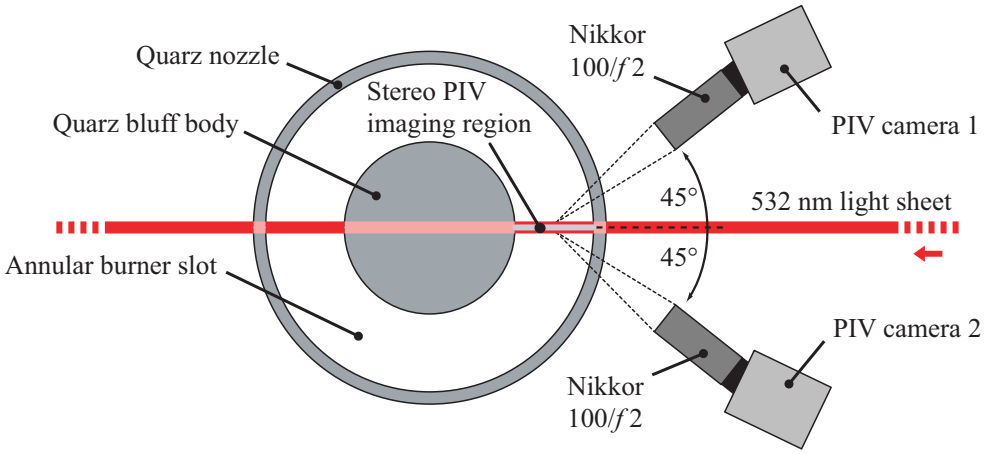

Figure 4.19: High-speed Stereo-PIV setup

practical. Examples of characteristic time scale and frequency maps are shown in Fig. 5.16 and Fig. 5.17, respectively, in Chapter 5.

4.3 Experimental Setups

In this section the three major experimental setups will be explained, which have been built during this work. The background of the applied measurement techniques as well as their extension to kilohertz repetition rates have been explained in the previous chapters. Now, the interplay of the individual aspects of the different measurement techniques to accomplish the capture of flame flashback in a premixed swirl burner will be described. A high-speed Stereo-PIV setup was implemented as a first step to characterize the isothermal flow field including all three components of the velocity vector within the annular slot of the burner nozzle. While recording the in-plane components with classical PIV, the second high-speed setup additionally incorporated OH-PLIF in order to investigate the turbulence-chemistry interactions. Finally, pressure and flame correlation measurements have been conducted to complement the dataset, as pressure is a major driving force behind the fluid motion. The details of the setups will be given in the following.

4.3.1 High-speed Stereo-PIV

The experimental setup for high-speed Stereo-PIV is shown in Fig. 4.19. The flow was seeded with DEHS droplets of ≈ 1 µm in size by an air blast atomizer (Palas GmbH, AKG 2000). The radial measurement volume was illuminated by a Q-switched dual cavity DPSS Nd:YAG laser (Edgewave GmbH, Innolas IS4II-DE). The laser was frequency-doubled and emitted a wavelength of $\lambda = 532$ nm. Both cavities were pulsed simultaneously at a constant repetition rate of 20 kHz to produce an identical illumination of the consecutive frames. Thus, Δt between the shots was set to 50 µs. Both cavities yielded a pulse energy of 1.7 mJ/shot and three cylindrical lenses have been used to form a light sheet of 15 mm height and a thickness of 2 mm according to the method in Raffel et al. [157]. The relatively large thickness is due to the large out-of-plane component of the flow between 5 and 9 m/s. Thereby, the particle loss normal to the light sheet is reduced to acceptable levels. Two high-speed CMOS cameras (Lavision GmbH, HSS6) have

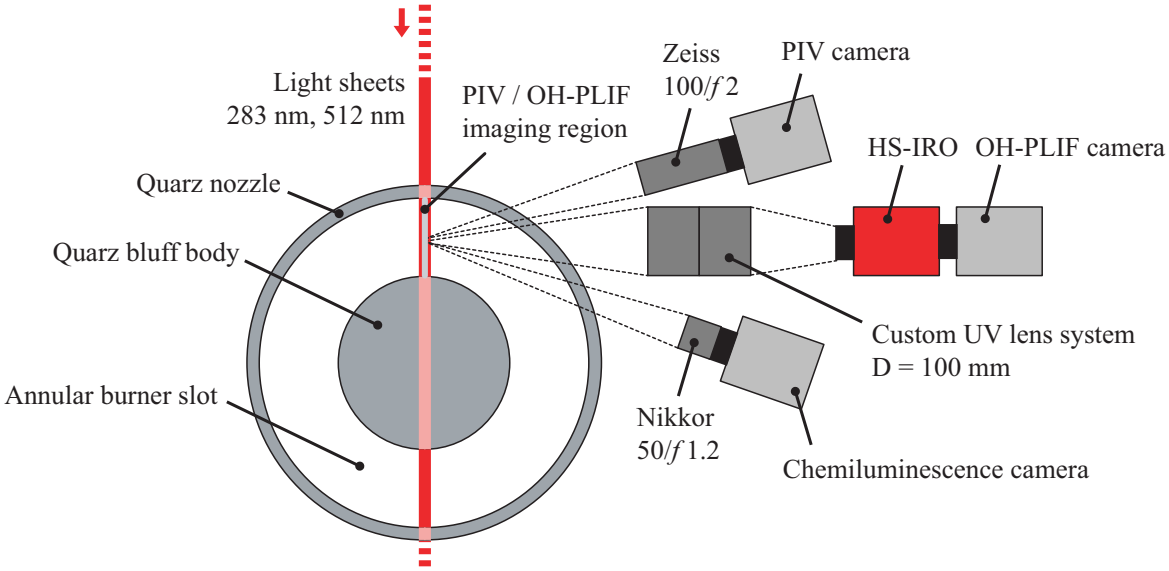

Figure 4.20: Laser imaging setup (2C-PIV, OH-PLIF, CL)

been used to image the signal of the Mie-scattered light from the particles. These allowed the acquisition of 512×512 pix at 20 kHz. The detection angle was 45° in the backward scattering configuration for both cameras. The presence of the bluff-body hindered the use of forward scattering with much higher scattering intensities (compare Section 4.1.3). For the correct focusing on the light sheet, each camera was mounted on a Scheimpflug adapter to account for the obscure observation angle. The measurement volume was imaged by two standard Nikkor objectives ($100/f2$) using an f-stop of 5.6. For the calibration of the system a custom-designed reference target was manufactured that featured two calibration planes and a pattern of 12×12 calibration marks, which was already shown in Fig. 4.11. It was attached to a special mount such that it could be installed very close to the bluff-body wall, where the flame propagation during flashback was expected to happen.

4.3.2 Simultaneous Laser Imaging (OH-PLIF, PIV, and CL)

Three cinematographic measurement techniques were applied simultaneously to gain insight into the mechanism that leads to flashback. These were integrated into two optical setups in radial and tangential configuration. Figure 4.20 shows the radial experimental setup. In addition to PIV and OH-PLIF, information about the global flame position and structure were acquired by recording the CL with a high-speed CMOS camera (Lavision GmbH, HSS6). The imaging region was 60×60 mm^2 covering all of the transparent nozzle. The FIFO (first-in-first-out) architecture of the on-board memory of 8 GByte allowed continuous recording of data and held 20,000 frames at 20 kHz. Spatial matching of the three cameras was performed by imaging a calibration plate. The plate had a carved millimeter square grid and could be mounted inside the quartz nozzle. It was supported by the central bluff-body and was aligned with the laser's path.

In this setup, high-speed PIV was conducted to obtain the planar two component velocity field inside the nozzle in a vertical plane through the axis. Again, the flow was seeded with DEHS oil droplets of similar sizes. The seeding density was 0.08 particles per pixel. Thus, approximately 5 particles were located in each interrogation area of 8×8 pix and approximately 20 particles in an area of 16×16 pix, respectively. The imaging region was 15×15 mm^2 with a pixel resolution

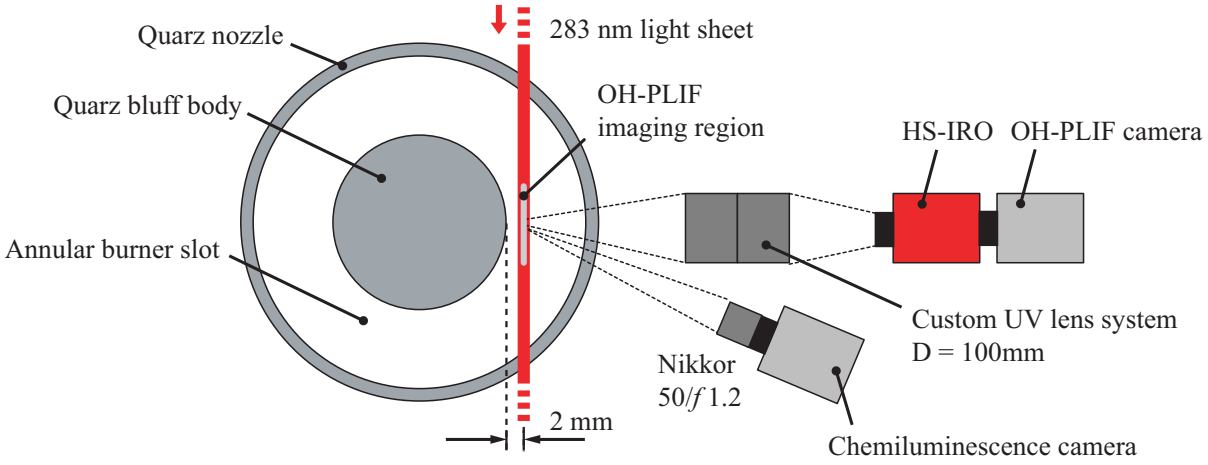

Figure 4.21: Experimental setup with an off-axis measurement plane (OH-PLIF, CL)

of 30 µm. The acquisition rate of the system was 20 kHz with an equidistant time separation of $\Delta t = 50$ µs. A 2 mm thick by 20 mm high light sheet was formed due to the high out-of-plane velocity.

The dataset is complemented by high-speed planar OH-PLIF at 10 kHz, which was acquired inbetween every second PIV double shot. The OH radicals served as a flame front marker and provided information on the position and detailed structure of the flame's leading edge. To excite the $Q_1(6)$ line of OH, a frequency-doubled dye laser was pumped by a frequency-doubled Nd:YLF laser at 532 nm (Edgewave GmbH, Innolas CX16II-E). At 10 kHz, the pump laser was able to deliver 8 mJ/pulse resulting in a quasi continuous wave (quasi-CW) power of 80 W. However, the energy was limited to 5.3 mJ/pulse to protect the system against thermal destruction. The pulse length was approximately 8 ns due to the Pockels cell Q-switch. The dye laser layout includes two separate cuvettes for oscillator and amplifier. Rhodamine 6G in ethanol was used as dye solution to create the required wavelength spectrum around 566 nm. The cuvettes were set at the Brewster angle to minimize the lasing threshold. This setup is easier to align and has better thermal stability than single cuvette designs previously utilized by Kittler and Dreizler [102]. The 566 nm radiation was frequency-doubled by a BBO crystal (BBO: Beta Barium Borate). At the 283 nm for OH excitation, the quasi-CW power at 10 kHz was 2.8 W which yielded 280 µJ/pulse. A 25 mm high and 200 µm thick laser light sheet was formed. This was combined with the PIV laser sheet by a dichroic mirror to overlap with the measurement volume. A two-stage IRO, which was lens coupled to another HSS6, monitored the emitted light. At a repetition rate of 10 kHz, an area of 768×768 pix was active, yielding a resolution of 45 µm. PLIF signals were collected with a head-to-head UV lens system, each with a focal length of $f = 285$ mm and an f-number of $N_f = 2.8$.

In a second setup a similar UV light sheet to the previously used for OH excitation was aligned tangentially to the bluff-body as shown in Fig. 4.21. The distance from the bluff-body wall was set at 2 mm. The flame tip was found to propagate in this region. The surface of the quartz nozzle was tilted with respect to the off-axis light sheet and forced a deflection away from the bluff-body. The beam was directed at a certain angle to compensate for the deflection. This was determined experimentally such that the light sheet inside the nozzle was oriented normal to the observation angle of the camera [61].

Similar to the on-axis setup in Fig. 4.20, CL was recorded with a second camera. PIV was

not applied due to difficulties of interpreting the 2D2C-PIV results in off-axis planes through a rotational flow configuration.

4.3.3 Simultaneous CL–Pressure Setup

Static gage pressure was measured on the surface of the bluff-body using temperature compensated piezo-resistive pressure transducers (Omegadyne Inc. PX409) with a maximum capacity of 2491Pa. The bandwidth of the transmitted direct current (DC) signal was 1 kHz with an accuracy of the measured signal of ± 0.03 % full scale. To accommodate the pressure transducers and protect them from the hot flow, the bluff-body design was modified. Eight pressure measurement ports with a diameter of 1 mm in increments of 10 mm were installed axially in the water cooled bluff-body (see Figures 3.3 and 5.1). These were connected to pressure transducers with a recess mount by copper tubes with equal length of 300 mm. The time lag of the signal due to the length of the tube was estimated from the speed of sound under normal conditions to be 0.87 ms. The total measurement period was 1 s and started shortly before flashback. As confirmed by high-speed imaging, flame upstream propagation occurs in a small fraction of a second. Hence this period was certainly long enough to capture the whole flashback event. The analogue voltage signal was digitized and recorded using a digital oscilloscope (Tektronix, DPO5000 Series) at 2 MHz sampling rate.

Information about the global flame position and structure were acquired by recording CL imaging with a high-speed CMOS camera (Lavision GmbH, HSS5) at 5 kHz frame rate. The imaging region was 60×60 mm^2, covering the entire transparent nozzle. These measurements were conducted with simultaneous and temporally correlated acquisition of the pressure transducer signals.

An optical reference signal was generated by a light-emitting diode (LED) for temporal matching of the CL images and the pressure time series. The photo diode was driven by a TTL (TTL: Transistor-Transistor-Logic) pulse generator (Quantum Composers 9500+) and directed towards the bluff-body such that a reflection could be observed by the camera. The supply voltage was recorded on a separate channel of the digital oscilloscope. Detailed information on the matching procedure are presented in the next section.

4.4 Multi-Parameter Data Processing, Accuracy and Precision

The processing techniques to obtain the quantities of interest from the raw data of the single techniques are discussed in this section. Further, the method to relate the simultaneously acquired information to each other by matching them onto a common time and space is presented. After describing the experimental setups in the previous section, the processing techniques of CL imaging, OH-PLIF, 2C-PIV, Stereo-PIV (3C-PIV) as well as time series analysis are detailed. Finally, the data matching procedures will be explained.

CL Imaging

The CL imaging was conducted without filter to obtain a SNR ratio which enabled to capture the global structure of the flame. Due to the fact that no filters were used, several sources of

unwanted signal had to be eliminated during the processing of the images. The three main contributions were laser reflections, stray light from the laboratory and reflections of the flame itself on the bluff-body and nozzle walls. The first two contributions were stationary, thus did not change during the recording of a sequence. The unwanted signal could be removed by a background subtraction code implemented in MATLAB®. Therefor, a series of 1000 temporally uncorrelated images with running lasers was recorded. This was conducted without the presence of the flame and its CL emissions. From this series the mean image was produced and subtracted from every single frame of a flashback series. The variance of the background image was only a few counts in each pixel due to the shot-to-shot stability of the laser systems. Nevertheless, the contribution of the reflections of the flame on the bluff-body and nozzle walls could not be removed as they were the result of the measured signal itself and varied unpredictably in space and time. However, the global structure of the flame, which was primarily of interest, could be obtained. The unwanted signal was created in the outer regions of the measurement volume, which were of minor importance.

OH-PLIF

For exact flame front detection a threshold-based edge detection of the OH-PLIF signal was implemented. The OH radical is created inside the reaction layer of the premixed flame and slowly decays in the post flame zone. Hence, the reaction front can be interpreted as the line of the steepest gradient of OH signal in the recorded images (see Fig. 2.11). To automatically locate the steepest gradient in an image, an algorithm was implemented in MATLAB®, which segmented the images into binary regions of 1 and 0. The segmentation was based on a threshold which was determined for each frame individually. This was accomplished by taking the mean value between the highest signal very close to the reaction front and the lowest signal in the unburnt mixture region. The boundary between these regions was defined as the flame front. An image normalization had to be carried out before the segmentation could be conducted. The OH signal is linearly proportional to the exciting laser intensity, which is non-uniform orthogonal to the beam propagation direction. The spatial non-uniformity of the laser excitation was corrected through normalizing each OH-PLIF image by the laser intensity profile. The profile was obtained from a sequence of post-flashback OH signal, in which the OH signal was homogeneously filling the measurement volume. The sequence was similarly acquired as in the CL background correction. The local laser intensity was resembled by an average image of the sequence. This was used to correct for the local excitation intensity by dividing each frame of a flashback sequence by the mean intensity frame. This step prepared the OH-PLIF image for the boundary extraction. Through the processing, the detailed structure of the flame was obtained in periods when the leading edge passed the measurement volume.

2C-PIV

The 2C-PIV data was processed with the MATLAB®-based open source code MATPIV [197], which was further developed by Böhm et al. [14]. Interrogation areas of 8×8 pix and 16×16 pix were used, giving a physical resolution of 250µm and 500µm, respectively. Thereby, velocity measurements close to the bluff-body wall were feasible. Due to equidistant time steps, all subsequent image pairs could be processed, yielding a temporal resolution of 20 kHz. A flow field comparison between the interrogation area sizes showed no significant change in the resulting

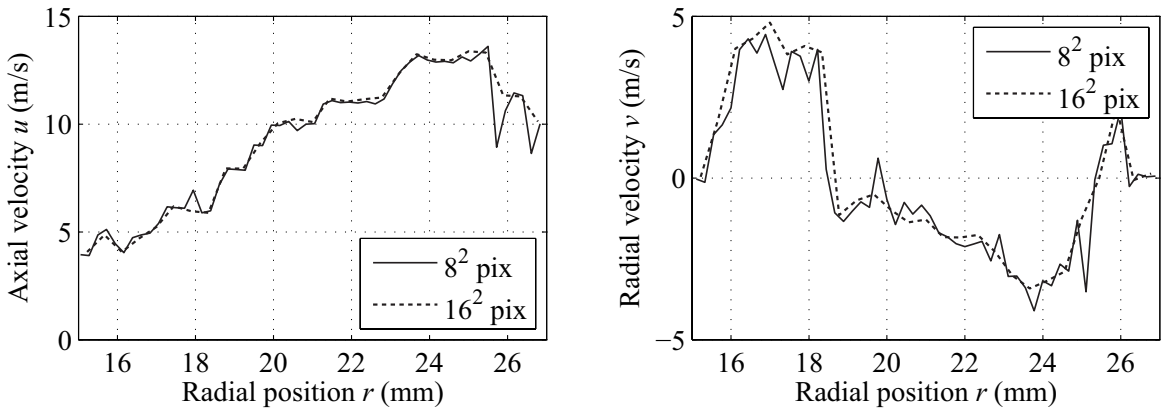

Figure 4.22: Comparison of 8×8 pix vs. 16×16 pix interrogation area size during PIV processing: Single shot radial profiles.

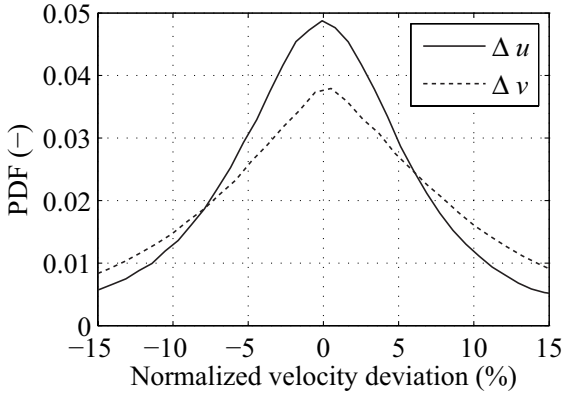

Figure 4.23: Comparison of 8×8pix vs. 16×16 pix interrogation area size during PIV processing: Distribution of the relative deviation

vectors. Figure 4.22 shows an example of radial single shot profiles of the u and v component of the velocity vector based on the two different interrogation areas.

The exemplary results for the two different interrogation areas show a rather good agreement, though the smaller interrogation area size exhibits more fluctuations in the v component. To quantify the difference a statistical analysis has been carried out. Therefor, a subset of 100 statistically independent frames with a time separation of $\Delta T = 100 \cdot \Delta t = 5$ ms has been selected from an isothermal sequence consisting of 10,000 vector fields. This was processed at 16×16 pix and 8×8 pix interrogation area size. From the finer resolved 8×8 pix subset every second vector was omitted in the analysis to adapt to the coarser resolved 16×16 pix subset. The absolute difference was calculated between each of the 86,400 vectors ($100 \times 32 \times 27$) of the two sets containing $u_{i,8}$ and $u_{i,16}$ and normalized by the root mean square value of all velocities of each set according to

$$\Delta u_{i,\mathrm{norm}} = \frac{u_{i,8} - u_{i,16}}{(u_{\mathrm{rms},8} + u_{\mathrm{rms},16})/2} \tag{4.30}$$

$$\Delta v_{i,\mathrm{norm}} = \frac{v_{i,8} - v_{i,16}}{(v_{\mathrm{rms},8} + v_{\mathrm{rms},16})/2}, \tag{4.31}$$

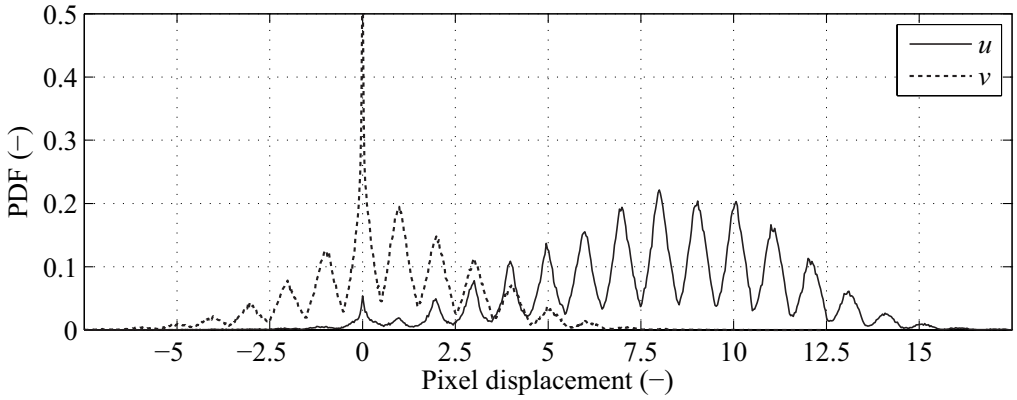

Figure 4.24: Pixel displacement histogram from a 2C-PIV dataset showing the effect of peak locking.

Here, the normalization values $(u_{\mathrm{rms},8} + u_{\mathrm{rms},16})/2$ and $(v_{\mathrm{rms},8} + v_{\mathrm{rms},16})/2$ where determined to be 3.07 m/s and 2.13 m/s, respectively. Thereby, the full width at half maximum of the normalized deviation between the 16×16 pix and the 8×8 pix subset could be estimated to be 12.5 % (0.38 m/s) for the u component. The v component resulted in a FWHM of the deviation of 15 % (0.32 m/s). The higher deviation of the v component can be attributed to the lower velocity fluctuations in the radial direction.

The probability density functions for the deviations of u and v are shown in Fig. 4.23. A symmetric shape for both velocity components can be observed. This indicates that no systematic error is introduced when refining the resoltution from 16×16 pix down to 8×8 pix interrogation area size. The recorded PIV data was conservatively evaluated at 16×16 pix interrogation area size. Hence, the comparison signifies the good raw data quality. The PIV configuration, including seeding density and light sheet thickness, was adequately setup such that reasonable data was still obtained at a quarter of the reference interrogation area size for the given levels of out-of-plane motion.

The effect of peak locking [203] could not be avoided by the modified MATPIV code as it can be seen in Fig. 4.24. The effect can be attributed to particle images which were too small [157]. As a consequence, the three-point Gaussian peak estimator was unsuited to find the exact location of the particle at the subpixel scale. Attempts to reduce this effect by defocussing the particles, such that they occupied larger areas of the detector, was not successful. On the contrary, it led to a decrease of valid velocity vectors. As a consequence, the absolute error for the estimation of the velocity components was conservatively determined by half a pixel displacement, which translates to 15 µm in physical space, at $\Delta t = 50$ µs to be ± 0.3 m/s. Although a velocity dataset with minimal peak locking is desirable, the resulting vector component accuracy was sufficient to investigate the flashback mechanism as it will be presented in Chapter 5.

In addition to the velocity vectors, a contour of the evaporating droplets by the heat release of the flame was detected. This could be compared to the flame front detection from the OH-PLIF data. The image processing of the particle images was similar to the flame front detection in the OH-PLIF images except for a prior smoothing filter that removed the steep gradients between the particles. This was accomplished by a large circular, non-linear median filter which preserved the edges between the particle-laden and particle-free regions. Image normalization to compensate the influence of the spatial beam profile as well as the contour detection process were applied

similar to the OH-PLIF processing.

Stereo-PIV

In contrast to 2C-PIV, the Stereo-PIV data was processed by the dedicated commercial software Davis® by LaVision GmbH. The software features the latest processing techniques to acquire the most accurate and precise results. The performance of the code compared to several other commercial and non-commercial software for PIV is published in the PIV Challenge [191–193]. The code features multi-pass processing, dynamic window deformation, subpixel estimation, image dewarping, and a self calibration algorithm which is essential for Stereo-PIV processing [115]. The need for a self calibration is due to a misalignment between the light sheet and the target which cannot be avoided. The method to compensate this is called *disparity correction*. It is applied after the two camera images have been mapped onto a common physical space. Afterwards the correction algorithm calculates the disparity between the two particle images of camera one and two using a cross correlation algorithm. The resulting disparity field is subsequently used to remap the previously calculated dewarping functions for both cameras, such that the particles overlap. Further details can be found in the work of Wieneke [215]. In the course of the PIV data processing an iterative disparity correction has been applied that repeated the remapping of the image coordinates three times. The resulting average disparity field was $\ll 1$ pixel.

An example of a processed dataset is shown in Fig. 4.25. The dataset to obtain a three-component vector field consists of the raw images of the two cameras from time step t_0 and t_1 (4 images in the top left corner). Strong laser reflections on the bluff-body superpose the scattered light from the particles due to oblique viewing angle of the cameras. A global background subtraction from averaged particle images was applied to eliminate the laser reflections. The result is shown in the top right corner of Fig. 4.25. A sliding background filter of 8×8 pix was added to remove the remaining large scale intensity inhomogeneities in the particle field without removing the sharp gradients of the particles themselves. Thereafter, the cross-correlation algorithm was applied to determine the displacement field. A two-pass PIV processing scheme was applied starting at 64×64 pix, which reduced to 32×32 pix in the second pass. The vector field was determined with an overlap of 75%. This yielded a resolution of 64×62 vectors with a spatial sampling rate of 231 μm/vector. The vector map from the raw images, which exhibts scattered spureous vectors, is shown in the bottom left corner of 4.25. In the course of the vector post processing, two filters have been applied to remove spurious vectors and interpolate the information in the resulting gaps with the surrounding vectors. The removal was performed if the current vector components differed from the ensemble average of the surrounding eight pixels by more than twice the standard deviation of the ensemble. Finally, the successive interpolation was carried out if the difference was smaller than 3 times the standard deviation. The bottom right part of Fig. 4.25 shows the final processed vector field that has been used for further analysis.

Time Series Analysis

From the velocity, CL and pressure data, time series at several control points have been recorded, which are marked in Fig. 5.1 as red dots. These time series have been processed by spectral analysis to obtain characteristic coherent frequencies in the signal. In case of the velocity time series from the 2C-PIV measurements the autocorrelation function was calculated. Thereby, coherent structures of the flow field were revealed as exemplified on the left hand side in Fig. 5.5. A Fourier transformation of the autocorrelation function yields the power spectral density (PSD)

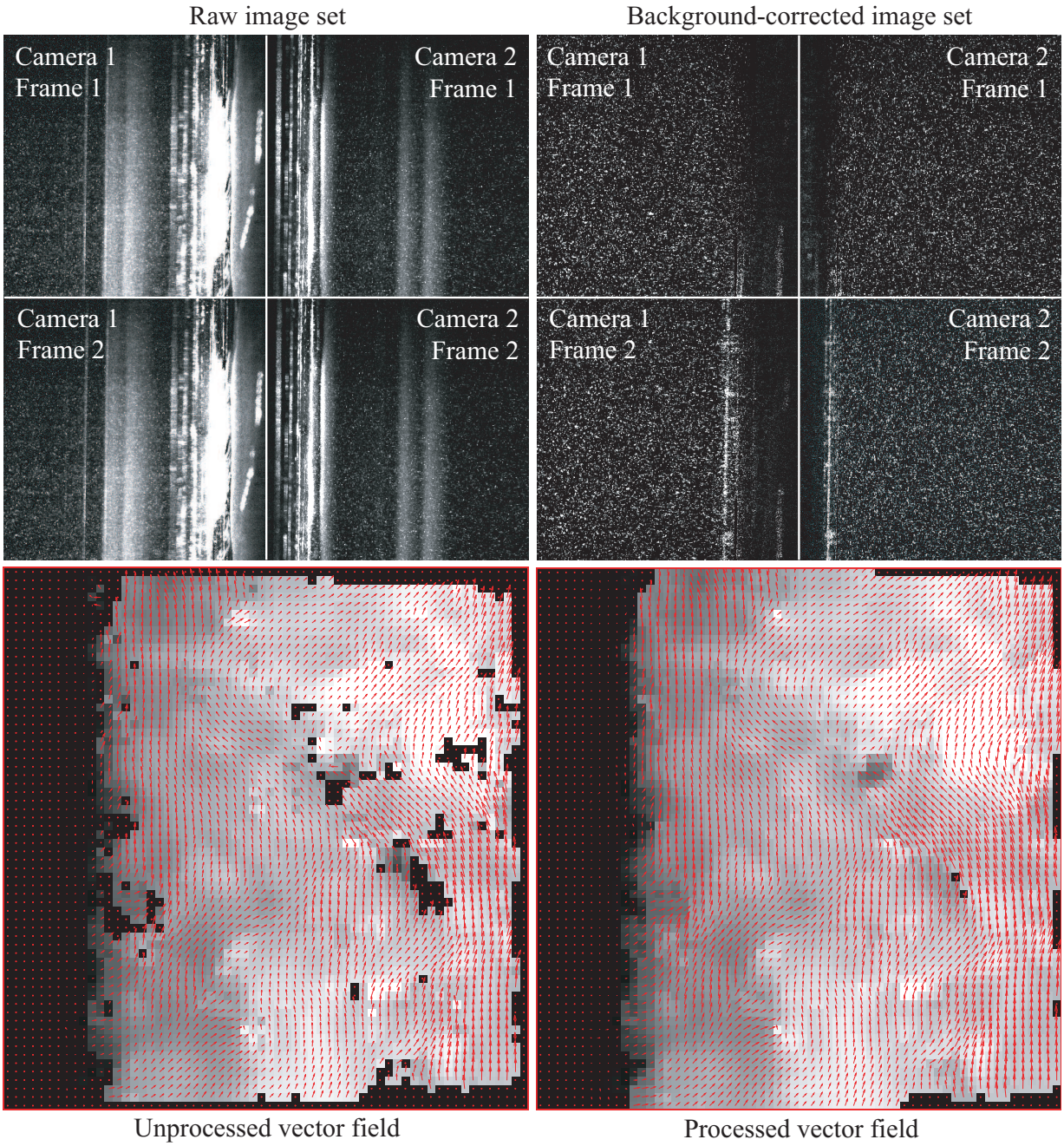

Figure 4.25: Example of a Stereo-PIV single shot dataset. Upper left quarter: Stereoscopic raw image set. Upper right quarter: Background-subtracted image set. Lower left quarter: Resulting flow field from raw image set. Lower right quarter: Final flow field from background-corrected image set for data analysis.

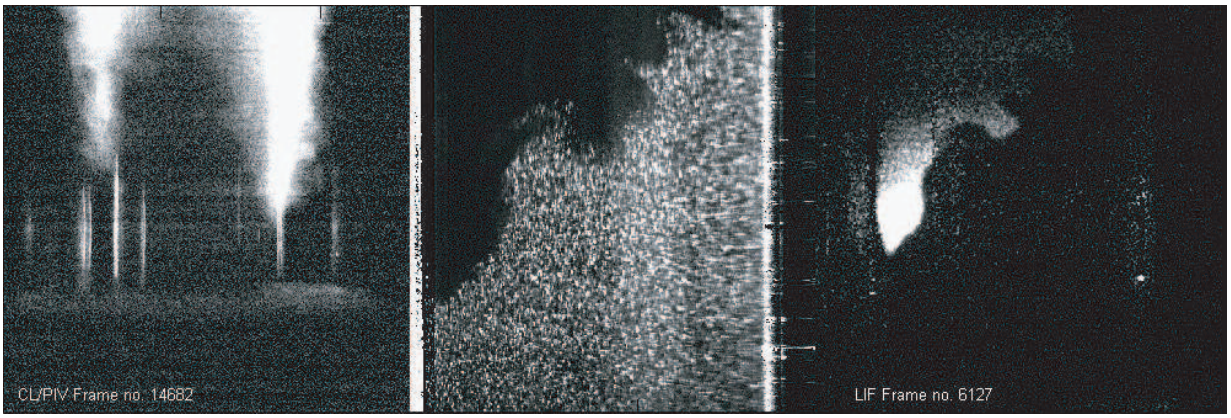

Figure 4.26: Multi-parameter raw data sample including wide field CL.

with the predominant frequencies appearing as peaks in the spectrum in Fig. 5.5 (right hand side). Similarly, the CL signal time series were processed.

For the pressure signal, a refined spectral analysis had to be applied. Noise from the circuitry of the measurement equipment was removed by a Gaussian filter. The very short transition time of the flame between stable burning and flashback ≈ 100 ms (see left hand side of Fig. 5.6) results in a poor spectral resolution using conventional spectral analysis. Parametric, or model based, methods of spectral analysis were therefore used [94]. These methods improve the spectral resolution of the short-length data compared to that obtained by standard techniques, which are non-parametric. Briefly described, the method models the available information within the short period, such that it can be extrapolated to longer time spans, thus increasing the spectral resolution.

Data Matching

In the simultaneous laser imaging experiment, including PIV, OH-PLIF and CL as well as the pressure-flame front correlation measurements, simultaneous data from different measurement systems was recorded. To combine the data, a matching procedure in space and time was applied.

Spatial matching of the data for the pressure-flame correlations was straightforward. The measurement ports in the bluff-body wall were visible in the CL images due to reflections of CL signal on the bluff-body wall. Hence, the measured gage pressure could easily be related to the flame front position by finding the corresponding pressure port in the CL images. The position error was conservatively estimated to be < 100 µm. In order to synchronize the pressure time series to the CL sequence an optical trigger was applied. The supply voltage of an LED with a very short rise time was simultaneously recorded by the oscilloscope for the data acquisition of the pressure transducers. The stop trigger for the measurement system was connected to the supply voltage of the LED. Thereby, with a known delay of the stop trigger, a light pulse could be generated close to the end of the recording sequence. This was captured synchronously by the camera as well as the pressure recording system through the rise in the supply voltage. Hence, the matching error was only a fraction of the exposure time.

Spatio-temporal matching of the PIV, OH-PLIF and CL datasets was achieved by a common calibration plate, similar to those described in Section 4.1.3. An example of the raw dataset of

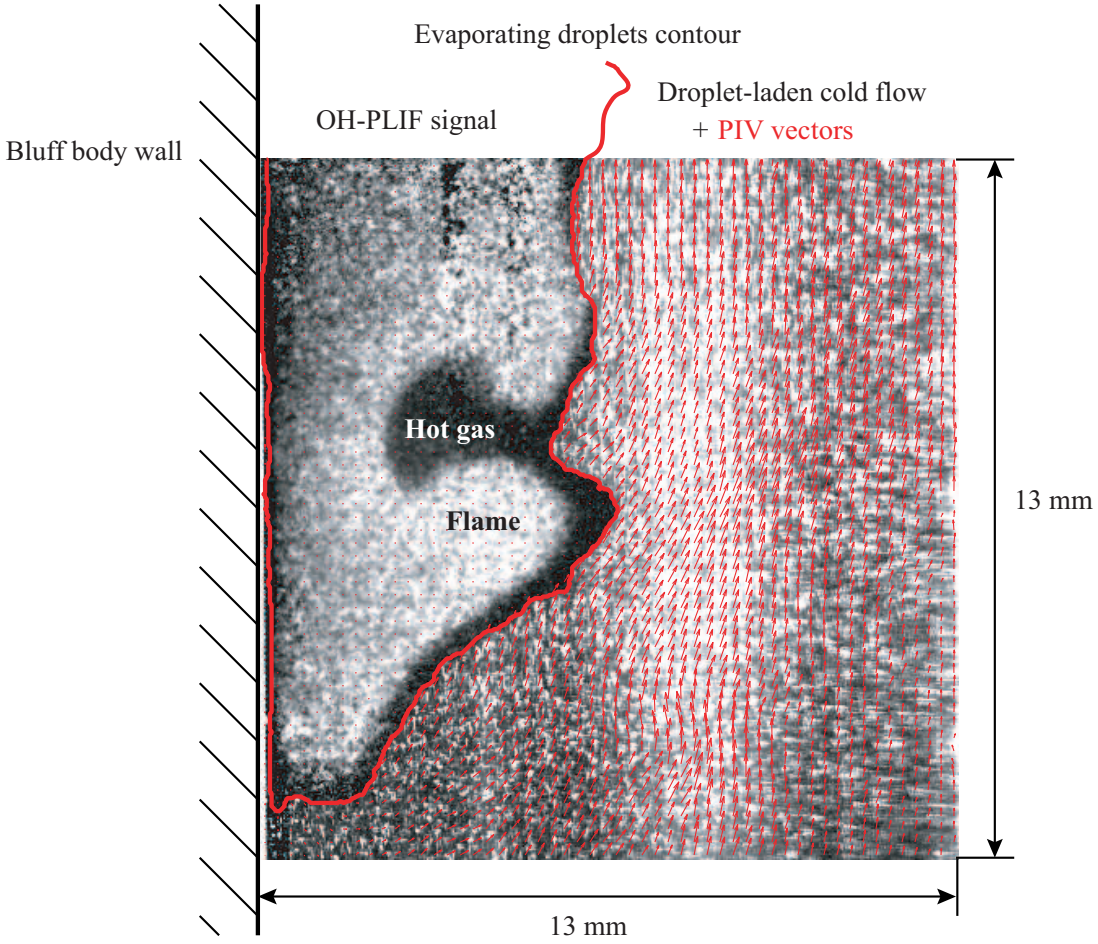

Figure 4.27: Processed multi-parameter data sample. The lines of evaporation are marked by a red line. In the vector field, the background displays the particle field. The gray scale in the flame region is linked to OH concentration but is not quantified in this example.

a single time step is shown in Fig. 4.26. The wide field CL (left image) shows the global flame structure with a leading flame tip on the right hand side of the bluff-body. Further, the PIV and OH-PLIF images (central and right image) show the magnified tip region in which a detailed flame structure can be observed. Reference images of the calibration plate with its markings were taken with each measurement system. The PIV and OH-PLIF data was matched with a cross correlation-based subpixel algorithm implemented in MATLAB®. Based on the pixel resolution of the OH-PLIF data, which was resolved coarser than the particle images, a matching error of < 23 µm was achieved. The off-axis experiment was only conducted for visualization purposes, thus no subpixel camera matching was applied in the post-processing. The CL data was not matched spatially to the others. It was recorded to classify the global flame behavior with respect to the flame structure in the smaller measurement volume of PIV and OH-PLIF. Temporal matching was achieved by synchronizing the recording frequencies of the different cameras by an external pulse generator and also utilizing the lasers' capability of random triggering. Thereby, a single pulse of particle illumination and OH excitation in the recorded sequence was omitted simultaneously. In the post processing the corresponding dark frames, which contained no signal, could be assigned to each other. As the CL camera also recorded reflections of the PIV laser, this camera could be temporally matched by the same method.

A single frame from the processed laser imaging dataset is presented in Fig. 4.27. Due to the difference in recording rates, every second PIV image pair has a corresponding OH-PLIF image. The latter was superimposed on the processed PIV vector field. The instant displayed captures a moment where a flame front is passing through the measurement plane close to the bluff-body wall on the left hand side of the image. The image window spans from the bluff-body to the nozzle wall on the right. The image center is located 30 mm below the nozzle exit. The seeded oil droplets evaporate in the vicinity of the flame front. The lines of evaporation are marked by a red line in this figure. In the vector field, the background displays the particle field. The gray scale in the flame region is linked to OH concentration but is not quantified in this example.

Several features of this image should be noted. First, the OH-PLIF image highlights the importance of the simultaneously applied measurement techniques. The distorted flame front can be seen clearly in the OH signal. This distortion is not observed in the evaporated droplet contour because the oil droplets do not re-form after evaporation. It is essential to know the location of the flame front, not just the evaporated droplet region, to be able to correctly identify the flame behavior.

Second, the spatial resolution and the quality of the PIV measurement technique have enabled valid velocity measurements to within less than a millimeter away from the bluff-body wall. This feature is important in evaluating the flashback mechanisms that are linked to boundary layer and near-wall flow phenomena. The thickness of the turbulent boundary layer is expected to be in the order of 1 mm for the flows considered here.

The third important feature of the experiment is the inclusion of the large scale CL imaging. In this turbulent, swirling flow, there is significant out-of-plane motion of the fluid. Further, during the milliseconds leading up to flashback, the flame motion can be quite chaotic. Consequently, it can be challenging to determine which gross flame structures and behaviors are occurring, even from a temporally correlated sequence of two dimensional slices. As the CL imaging is a line-of-sight technique rather than purely two dimensional and the whole nozzle area is monitored, it is possible to include more detailed information in the conditioning and interpretation of the results.

5 Results and Discussion

In this chapter the results are presented and discussed. In Section 2.3 the most relevant flashback mechanisms found in the literature for the TECFLAM burner were presented. It was noted that so far not much attention has been paid to the flashback mechanisms of burners with central bluff-body. The interactions of the swirling flow field with the flame requires to measure the velocity field and the flame front position inside the burner nozzle simultaneously. This allows to condition the flow field data with respect to the moving flame front, which is crucial for the analysis of the transient nature of flashback phenomena. Further, this demands the use of high-speed diagnostics to track the flow field and the flame while moving upstream into the swirl generator. In Section 4.4 the focus was on the experimental techniques as well as the new approach in combustion diagnostics to acquire temporally correlated data together with the corresponding processing. The results presented in this chapter provide insights to the phenomenon of flashback in premixed swirl burners with a central bluff-body utilizing the new approach. Special attention will be given to the process of upstream flame propagation. One major aspect of the results presented in this chapter is the new perspective on turbulent flames obtained from multi-parameter planar high-speed diagnostics.

Figure 5.1 provides an overview of the various measurement volumes of the simultaneous multi-parameter experiments from which the results have been produced. First, the three different stabilization points of the flame, recorded by means of wide field CL, are discussed. The following section presents the operating regions of the TECFLAM burner with respect to the onset of flashback. The obtained stability maps are compared to the flashback model of Konle and Sattelmayer [112]. The main focus of this chapter is on the results of the upstream flame propagation by planar multi-parameter high-speed measurements. Here, a frequency analysis of the large-scale coherent structures are presented, recorded at the control points marked as red dots in Fig. 5.1. Further results of the wide field CL sequences inside the nozzle exit as well as correlations of this dataset with the results of the pressure traces will be detailed. The isothermal and the reacting flow fields from the on-axis laser imaging setup as well as the off-axis setup, including the narrow field CL recordings, will be presented. They result in the formulation of a flashback prototype and a new hypothesis of upstream flame propagation for this type of burner. Finally, this hypothesis is classified within the framework of the existing flashback mechanisms.

5.1 Flame Stabilization Points

The burner was externally ignited by a sparker at a Reynolds number of $\mathrm{Re} = 10,000$, a swirl number of $S_g = 0.75$ and an equivalence ratio of $\Phi = 0.833$ according to the `PSF30` configuration. In a fraction of a second a stable burning flame developed anchoring above the bluff-body. This state represents the first global stabilization point. Through a constant increase in swirl number, the anchoring point of the flame starts to move upstream. It stabilizes at the bluff-body wall near the exit of the outer nozzle (intermediate stabilization point) before it finally flashes back into the swirl generator. This is the final stabilization point. Figure 5.2 provides a visual

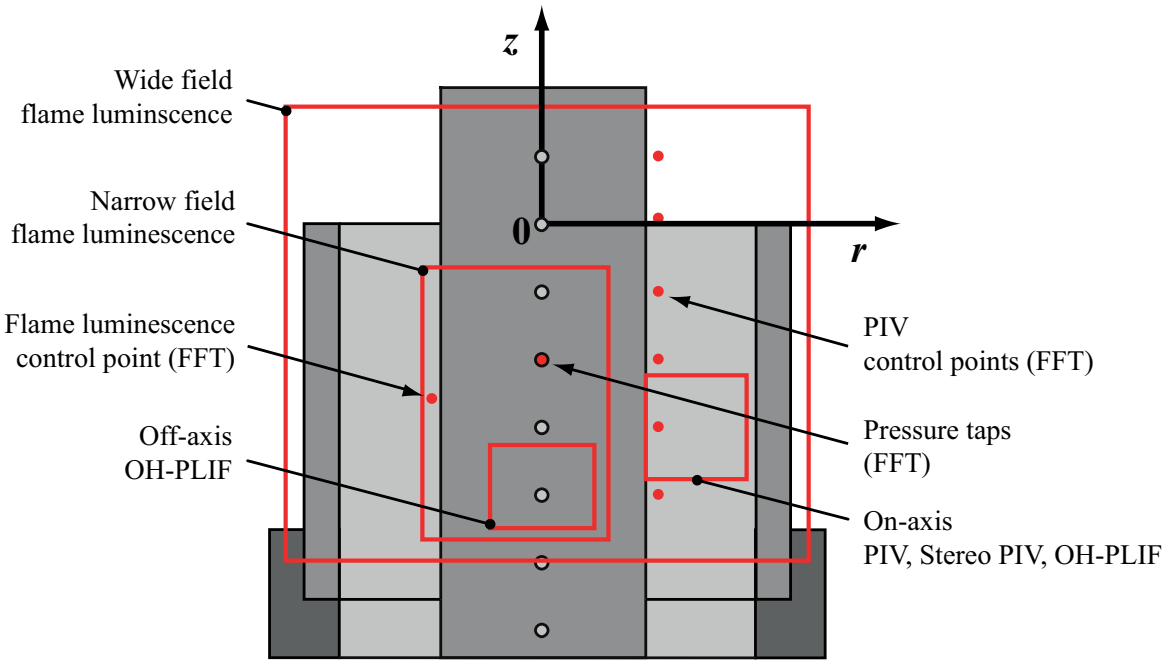

Figure 5.1: Overview of the various measurement volumes

impression of the three different stabilization points through imaging the visible and near UV spectra. The image on the left hand side of Fig. 5.2 shows the flame in the stable PSF30 configuration ($\Phi = 0.833, \mathrm{Re} = 10,000, S_g = 0.75$). It was anchored at the rim of the central bluff-body. A precessing motion of the flame was observable.

Increasing the geometrical swirl number S_g to values in a range between 0.8 and 1.0, a flame tip was formed that left the rim of the bluff-body and moved upstream. As it is obvious from the second image of Fig. 5.2 the flame stabilized freely in the diverging flow field beside the shell of the bluff-body. The stabilization point, in the following referred to as *meta-stable*, was highly transient, meaning that the flame tip intermittently moved up and down by up to 30 mm along the bluff-body. Thereby, it strongly precessed around the bluff-body. The average leading edge flame position depended sensitively on the swirl number.

At approximately $S_{g,crit} = 1.0$ only a slight increase of the swirl could cause the flame to reach back into the annular slot. When the critical swirl number was met or passed the flame suddenly flashed back into the nozzle and stabilized upstream at the swirler assembly. The two images on

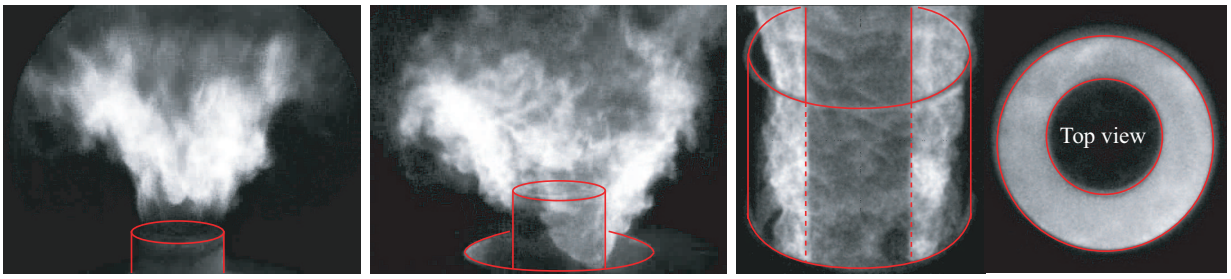

Stable ($S_g < 0.8$) Meta stable ($0.8 < S_g < 1$) After flashback ($S_g > 1$)

Figure 5.2: Instantaneous CL images of the three flame stabilization points.

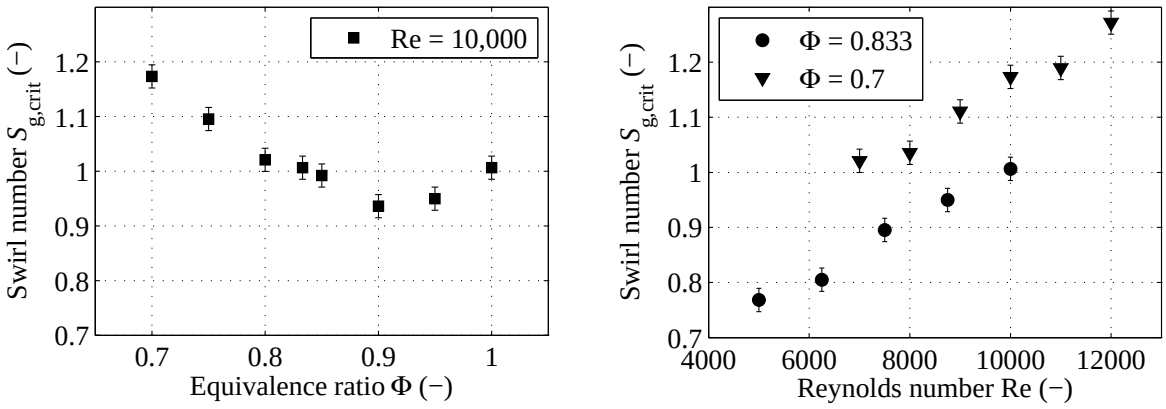

Figure 5.3: Stability limits of the modified TECFLAM burner. The critical swirl number is plotted as a function of the equivalence ratio (left) and the Reynolds number (right)

the right hand side of Fig. 5.2 shows the CL after the flashback. In this mode a thermo-acoustic instability was observed producing a rumbling sound at 133 ± 10 Hz [141].

5.2 Stability Maps

For a global characterization of flame stability, the equivalence ratio and the Reynolds number were varied. The left hand side of Fig. 5.3 shows the critical geometrical swirl number $S_{g,crit}$ for a fixed Reynolds number of $10,000$ based on the hydraulic diameter and the bulk nozzle exit velocity. At the right hand side $S_{g,crit}$ is presented for two fixed equivalence ratios but varying Reynolds numbers. Operation of the flame in the regions below the experimental data points corresponds to statistically stable conditions, the regions above the data points correspond to flashback. The maximum thermal load of the rig was restricted to 30 kW due to limitations in the laboratory environment. For $\Phi = 1$, this was reached at $\mathrm{Re} = 10,000$. Therefore, higher Reynolds numbers or richer mixtures were not investigated.

$S_{g,crit}$ decreases monotonically in the range of $\Phi = 0.7$ to 0.9 . This finding can be attributed to the influence of the density jump between unburned and burnt gases across the flame front (ρ_u/ρ_b). Flame propagation speed along a fine vortex was shown to depend on (ρ_u/ρ_b) [8–10, 26, 34, 71, 75, 171, 205]: According to the theories in Section 2.3 an increasing value of the density jump increases the axial pressure gradient as well as the baroclinic torque. In both classes of flashback initiation the density jump was identified as a major parameter driving the premixed flame into the vortex. The higher the density jump, the larger is the negative axial velocity generated by a positive axial pressure gradient or azimuthal vorticity. In a later study by Domingo and Vervisch [40] the latter finding was confirmed for cases where turbulence was superimposed on the vortex interacting with the flame.

Further, starting in the lean regime of Φ the laminar flame speed s_l increases while approaching stoichiometric conditions. With respect to Eq. (2.76) this facilitates the upstream propagation as the flame itself can propagate faster against the approaching flow. However, $S_{g,crit}$ increases again when exceeding $\Phi = 0.9$ and reaches a value of $S_{g,crit} = 1.0$ at $\Phi = 1.0$. This finding is in contrast to the explanations above as the largest density jump as well as the highest flame speeds are expected to occur closer to $\Phi = 1.0$. The present data, however, is insufficient to draw any

conclusive explanation for this observation.

At $\Phi = 0.833$ the critical swirl number was $S_{g,crit} = 1.0$. This corresponds to a 25 % increase relative to the original nozzle geometry [141] (see left hand side of Fig. 3.3) and can be attributed to changes in the flow field by the extended bluff-body. The critical swirl number increases approximately linearly with the Reynolds number at a fixed equivalence ratio as shown on right hand side of Fig. 5.3. From this finding one can conclude that larger bulk velocities retard the onset of flashback. The propagation speed in vortex tubes was furthermore found to be proportional to the maximum circumferential velocity w_{max} [10, 26, 34, 75]. The proportionality factor is a positive function of the density jump across the flame and the swirling strength of the vortex (expressed by ω_{max}). Based on numerical simulations, Hasegawa et al. [75] showed that the dependence of the proportionality factor on the Reynolds number is a rather weak function (compare their Fig. 8 [75]). If it is assumed that their findings for non-turbulent vortex tubes can be transferred to the present case, increasing Reynolds numbers only marginally increase the negative axial velocity generated by azimuthal vorticity. Drawing the balance between increased axial momentum, due to higher Reynolds numbers, and negative axial momentum, due to azimuthal vorticity, net negative flame propagation into the annular slot is obtained only when swirl is increased. This mechanism broadens the region of stable operation at higher Reynolds numbers to higher values of $S_{g,crit}$.

The flashbacks were also induced by changes in stoichiometry, increasing Φ by 0.01 /s at a constant swirl number of $S_g = 1.05$ and Reynolds number $Re = 10,000$. Starting from a stable state at $\Phi = 0.75$, the flame transitions from the stable to the meta-stable state and then undergoes flashback. The value for Φ_{crit} (referring to when flashback occurs) was recorded for multiple realizations of the same Reynolds number. The number of realizations chosen depends on the variation of Φ_{crit}. The experiment was repeated until the variance did not change significantly over the last three realizations. The average value for a constant Reynolds number was calculated from 13 to 21 flashback realizations. The critical equivalence ratio was measured for Reynolds numbers ranging from 6,000 to 10,000. Figure 5.4 shows the reciprocal equivalence ratio $1/\Phi_{crit}$ plotted versus the thermal power at the moment of flashback. A total of 280 flashbacks were conducted to determine these stability limits. The open circles represent individual flashbacks, and red markers represent the mean values for constant Reynolds number.

A lot of effort has been made to predict the stability limits of lean premixed swirl combustors. Kröner et al. [113] derived a model for high-power combustors (100 kW and large Reynolds numbers). In successive studies, this model was refined and extended to smaller combustors and lower Reynolds numbers by Konle and Sattelmayer [112]. The refined model is based on a Damköhler criterion which compares turbulent and chemical time scales and is calibrated for each burner. The turbulent time scale s_t can be defined as

$$\tau_t = \frac{l_0}{u'_{rms}} \propto \frac{L}{\overline{u}}. \tag{5.1}$$

This is a commonly used integral definition for turbulent flows [155], where l_0 is the turbulent length scale, u'_{rms} is the velocity fluctuations, $\overline{u}$ is the mean velocity and L is a characteristic diameter. The chemical time scale τ_c represents the time that the reaction needs to consume the volume of unburned gases between the recirculation bubble tip and the flame front. This assumes a propagating flame following an IRZ in a confined swirl flow. The time scale can be modeled as

$$\tau_c = \frac{\Delta x_c}{s_t} \propto \frac{\Delta x_c}{s_l}. \tag{5.2}$$

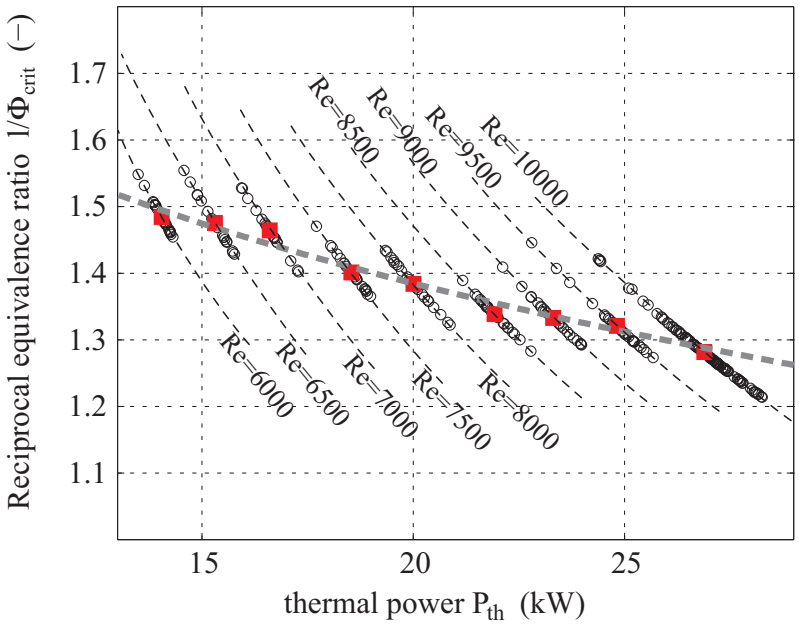

Figure 5.4: Critical equivalence ratio dependency on thermal power. The open circles represent individual flashbacks, and red markers represent the mean values for constant Reynolds number. The dashed line denotes the predicted flashback limits by Konle and Sattelmayer [112].

Here, Δx_c is the distance between the most upstream point of the recirculation bubble and the flame tip. s_t denotes the turbulent flame speed while s_l represents the laminar flame speed. The ratio of these time scales gives a burner specific constant which can be calculated from the burner parameters of a measurement of Φ_{crit} and is defined as

$$\frac{\tau_c}{\tau_t} \sim \frac{\Delta x_c \cdot \overline{u}}{s_l \cdot L} = C_b. \tag{5.3}$$

Once C_b is experimentally determined it can be used to predict the stability limits of the whole parameter space of the burner. Originally developed for swirl burners without central bluff-body, the model has been tested with the current dataset of flame flashback parameters. The dashed gray line in Fig. 5.4 represents the stability limit for the model presented in Konle and Sattelmayer [112]. The limits, modeled by the scaled Damköhler criterion, also agree well with the experimental results for the investigated swirl burner with bluff-body. However, it should be noted that it is not a predictive model as the model constant C_b is calibrated by data from the experiment itself. Thus, the mechanism of the flashback phenomenon remains unidentified.

5.3 Upstream Flame Propagation

After the general characterization of the flashback phenomenon, the focus of the next section is on the mechanism of upstream flame propagation, which is a possible reason for global flashback. The experiments have shown that it is a highly complicated matter, being the result of interactions between coherent flow structures, turbulence, and heat release. The section is therefore divided into results showing the existence of precessing vortex cores (PVC), analysis of the isothermal flow field, and the flow field during flashback. The section concludes with a hypothesis for the underlying mechanism that drives the upstream propagation of the flame tip.

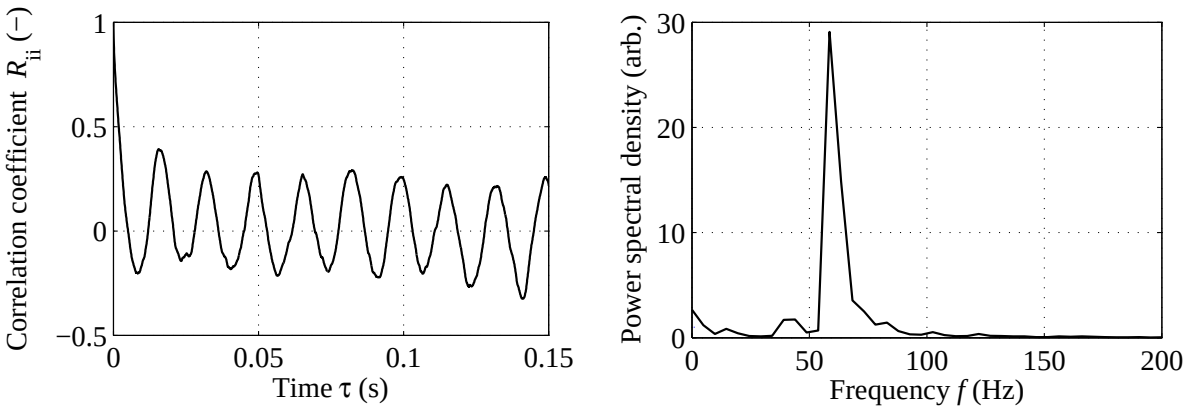

Figure 5.5: Example of a temporal autocorrelation function of an axial velocity time series at $z = -30\,\text{mm}, r = +17\,\text{mm}$ inside the nozzle (left). Power spectral density after Fourier transformation of the temporal autocorrelation function (right)

5.3.1 Frequency Analysis of Large-Scale Coherent Structures

The analysis of time series measured at several control points inside the burner exit nozzle (see Fig. 5.1) revealed the existence of large scale coherent structures. These appeared in the time series of pressure measurements, CL, and the velocity field. Further, the coherent structures are observed in the isothermal configuration `30iso`, as firstly discovered by Schneider [174], and also during reacting conditions in the course of flashback.

Isothermal Configuration

From previous experiments by Schneider et al. [174], PVC-like structures were identified in the isothermal flow configurations of the burner with the swirl number ranging between $S_g = 0.75$ and $S_g = 2.0$. Using the Fourier-transform of the temporal auto-covariance function, coherent structures can be identified. These are revealed by distinct peaks in the power spectral density (PSD), which represent the coherent frequency of these flow structures such as a PVC [155]. In contrast to the experiments considered in this work, the data from Schneider were captured with Laser Doppler Velocimetry [3] above the exit nozzle. Further, the bluff-body was flush-mounted at the nozzle exit whereas the current measurements featured a bluff-body which extended from the nozzle exit by 20 mm (see Section 3.3).

Time series analysis of the axial velocity component at a control point inside the nozzle close to the bluff-body wall produces slightly lower coherent frequencies compared to data from Schneider. A frequency range between 34 and 44 Hz could be determined from four different measurement heights inside the nozzle (see Table 5.1) at a swirl number of $S_g = 1.05$. These were obtained by calculating the PSD of the normalized auto-covariance function. Schneider's data shows similar frequencies of 38 and 56 Hz at $S_g = 0.75$ and 1.4, respectively.

There are three possible reasons for the slight shift to lower frequencies in this study. First, the difference in the burner exit geometry can have an impact on the non-stationary flow field. Second, the measurement location in this experiment is inside the nozzle near the bluff-body wall while Schneider was measuring outside the nozzle in the shear layer of the flow. Finally, the limited recording duration of 1 s for a time series (20,000 samples at 20 kHz) leads to an uncertainty of ± 5 Hz in the frequency range of interest. A sample of the temporal autocorrelation

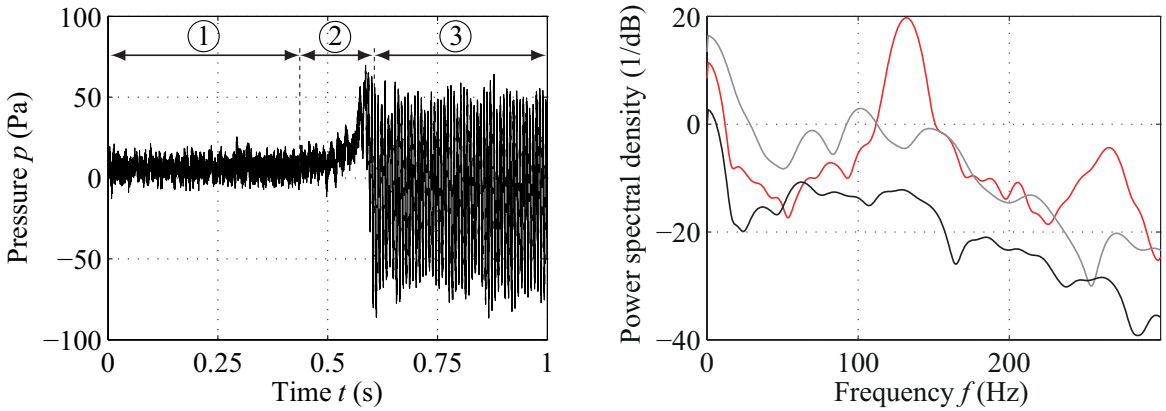

Figure 5.6: Pressure history recorded at the pressure port at $z = -30$ mm, 1: before flashback, 2: transition period, 3: after flashback (left). Power spectral density of periods 1-3, black: 1, gray: 2, red: 3. (right)

function and the corresponding PSD for a time series measurement is shown in Fig. 5.5. The distinct peak in the PSD corresponds to the coherent fluid motion, which is also visible as a sinusoidal modulation of the autocorrelation function.

Reacting Configuration – Flashback

Figure 5.6 shows a pressure history measured 20 mm upstream of the nozzle exit. This time trace can be divided into three distinctive time intervals. The first part extends from the beginning of the measurement for about 400 ms. Within this time the flame is still downstream of the pressure measurement port. This interval includes very low amplitude oscillations, featuring an average gage pressure in this part which is slightly positive. As the second interval begins, the fluctuations start to grow and quickly reach large amplitudes. This part is a transition between interval one and three and lasts approximately 100 ms. Flame upstream propagation occurs in a fraction of this period. Finally, organized pressure oscillations develop. These are self-sustaining limit-cycles which continue until the flame is extinguished by shutting off the fuel line. This qualitative trend was observed in all flashback realizations.

Spectral analysis of the time trace reveals that the oscillations in the first part happen in a range of frequencies, which is shown in the PSD of Fig. 5.6. As can be seen in this figure, there is no dominant frequency in this period and the pressure fluctuations are essentially random.

The second time interval is short compared to the other two and lasts for ≈ 100 ms. For the investigated burner configurations this is approximately ten times the flow-through duration of the exit nozzle. Using conventional spectral analysis in such a short period results in a poor spectral resolution. Parametric (model based) methods of spectral analysis were therefore used [94]. These methods improve the spectral resolution of the short length data compared to that obtained by standard techniques (non-parametric) [94]. Applying these techniques to the second interval shows that the spectrum of the second interval tends to have more well-defined peaks. Thus, the pressure fluctuations happen at more distinctive frequencies compared to the first interval. The main oscillation frequencies are 70, 102 and 146 Hz. The relations between the found values suggest a fundamental frequency of 35 Hz. This could not be confirmed in the spectrum of this interval due to the limited length, thus limited spectral resolution. However, this frequency is

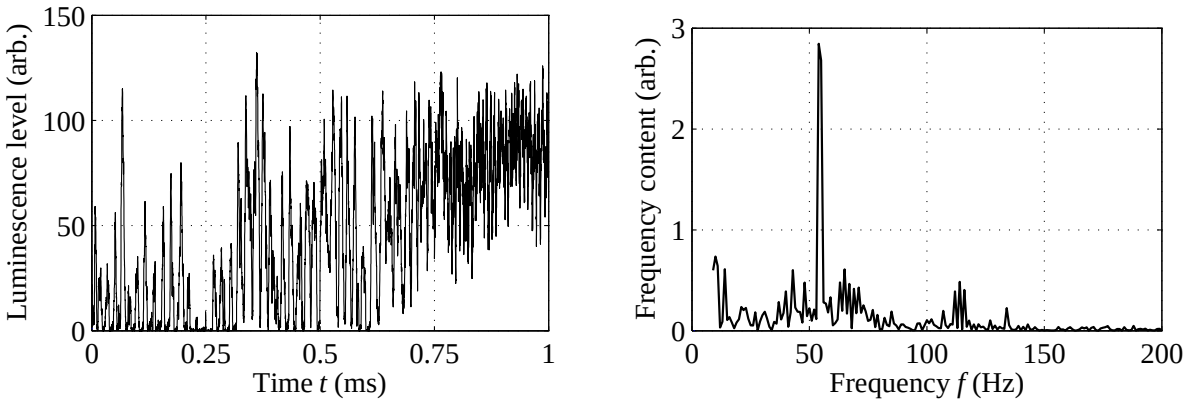

Figure 5.7: CL time series at the control point $z = -25$ mm, $r = +16$ mm inside the burner's exit nozzle (left). Power spectral density of the luminescence time series during flashback (right)

similar to what was found in the velocity time series.

The spectrum of the third part of the pressure trace includes a single frequency at 130 Hz and its harmonic at 260 Hz. This is a clear indication of a thermo-acoustic instability. A further discussion will be given in Section 5.4 and additional results in Section 5.3.3 will clarify these measurement results.

Coherent frequencies were also observed in CL sequences inside the burner nozzle. These were recorded during propagation from the meta-stable state down into the swirler. The details on the flame topology and movement will be discussed later in Section 5.3.2. At this point the focus is on the analysis of the luminescence intensity time series at a fixed reference location (see Fig. 5.1) inside the nozzle. On the left hand side of Fig. 5.7 such an example time series shows the intermittent occurrence of CL at the control point. As an example power spectrum of the luminescence signal, the right hand side of Fig. 5.7 shows a distinct peak at 58 Hz. This frequency resembles the rate at which the flame spins around the bluff-body. Analysis of the total number of recorded data sets revealed a mean frequency of 58 ± 3 Hz $(68\ \%)$.

The same analysis was also applied to time series of reacting configurations using PIV data. No modifications of the analysis scheme had to be applied to the stable burning configuration ($S = 0.75,\ U = 0.833,\ \mathrm{Re} = 10,000$) as the flame was burning far away from the measurement location.

During flashback the flame moves upstream into the nozzle through the measurement volume. Because the flame evaporates the droplets used for velocity determination, the time series was divided into two parts in a previous step: A sequence before the first evaporation of droplets (*pre*-series) and the time span thereafter (*post*-series). By this measure the evaluation of the pre-series determines the frequency of coherent structures in the flow up to the point when the flame moves through the measurement volume. In contrast, the post-series analysis gives information about the precessing frequency of the flame. The characteristic frequencies are summarized in Table 5.1.

[10] Measurements from Schneider [173].

Table 5.1: Summary of the measured coherent frequencies.

Configuration	Swirl no. S_g $(-)$	Axial position (mm)	Frequency f_c (Hz)	Technique
Isothermal[10]	0.75	$+1$	38	LDV
Isothermal[10]	1.4	$+1$	56	LDV
Isothermal[10]	2.0	$+1$	76	LDV
Isothermal	1.05	-40	39	PIV
Isothermal	1.05	-30	34	PIV
Isothermal	1.05	-20	44	PIV
Isothermal	1.05	-10	34	PIV
Stable	0.75	$+1$	55	PIV
Flashback (pre)	1.05	-20	$48-60$	PIV
Flashback (post)	1.05	-20	$53-60$	PIV
Flashback	1.05	-20	58	CL
Flashback (phase 1)	1.05	-20	-	pressure
Flashback (phase 2)	1.05	-20	70, 102, 146	pressure
Flashback (phase 3)	1.05	-20	130, 260	pressure

Discussion

The frequency of ≈ 39 Hz in the isothermal case is similar to the frequencies measured by Schneider. The data shows that coherent structures exist inside the nozzle. This indicates that their origin is either the swirl generator or the influence of the recirculation zone downstream. In the reacting cases, Schneider could not measure any coherent frequency content above the nozzle at $z = +1$ mm, $r = +25$ mm close to the flame front. Probably, the increase in viscosity dampens out the coherent motion there. However, the coherent motion can still be seen in the velocity dataset upstream of the flame. There, a higher frequency of ≈ 50 Hz is detected when compared to the isothermal case. It shows that these coherent motions still exist in the flow upstream of the flame's position.

No significant increase in frequency is observable when going from $S = 0.75$ to $S = 1.05$, considering the velocity data during flashback (PIV, pre-series). This is in contrast to the observed isothermal cases by Schneider. These show a gradual increase in frequency when going to higher swirl numbers. The results of the velocity post-series as well as the CL data frequencies show that the flame's precessing motion highly correlates with the flow's coherent frequency. This indicates a strong influence of the underlying flow field on the motion of the flame.

The single frequency of 130 Hz in the pressure signal after flashback is in complete agreement with the previous measurements of CL. These results show the same frequency of 130 Hz after flashback when the flame stabilized inside the burner [141]. Thus, the flame after flashback develops a thermo-acoustic instability and the pressure fluctuations go under limit-cycles. However, through examination of the pressure history and the corresponding spectra it is not clear at which stage the thermo-acoustic instabilities are initiated. The crucial question here is whether this instability leads the upstream flame motion or lags it. In the first case the thermo-acoustic instability can be a driving mechanism of flashback. However, if thermo-acoustic instability follows the flame flashback, it is simply a consequence of the modification of the flow field and has

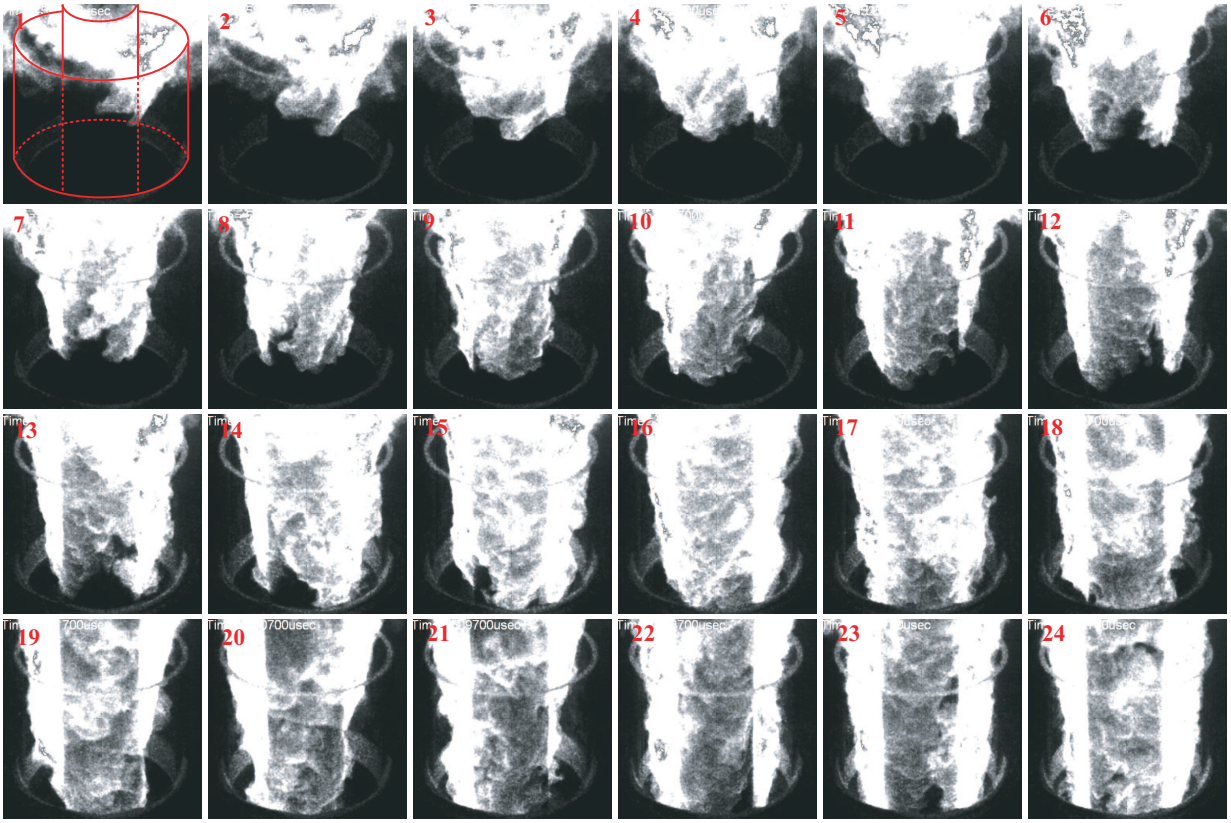

Figure 5.8: Sequence of CL imaging during flashback viewed from an inclined perspective.

no significant impact. To clarify this, correlations of pressure and CL have been measured that are presented in the following section.

5.3.2 CL Inside Exit Nozzle

To obtain a closer view on the flame dynamics inside the burner, temporally resolved CL sequences were monitored through the glass nozzle as detailed in Section 5.3.2. Figure 5.8 shows snapshots of the flame dynamics in steps of 1 ms at an inclined viewing angle. Notice that the data rate was 10 kHz. Only every tenth exposure is shown in the sequence spanning 23 ms. The propagation of the flame tip from the nozzle's exit upstream into swirl generator can be observed. In the course, the wrinkled structure of the flame is clearly visible. From this viewing angle the flame seems to be characterized by highly irregular motion at the leading edge.

Figure 5.9 shows a sequence of CL viewed from the side to provide a better impression of the flame's leading edge position. The sequence covers an equivalent time span of 23 ms, showing every tenth exposure. The starting point of the sequence shows the flame stabilization region located inside the annular slot. The flame precessed clockwise around the bluff-body. Flashback was associated with a rather small flame region identified as the flame tip. This is highlighted by an arrow in the image at $t = 9$ ms (image no. 10). A characteristic V-shaped form in circumferential direction can be observed. The flow dilatation just upstream the flame tip was expected to accelerate the flow at neighboring radial and circumferential locations once the flame tip was located partly in the annular slot. The flame tip subsequently moved upstream during the precession in a very fast manner. In this individual example, the global propagation speed (in fixed

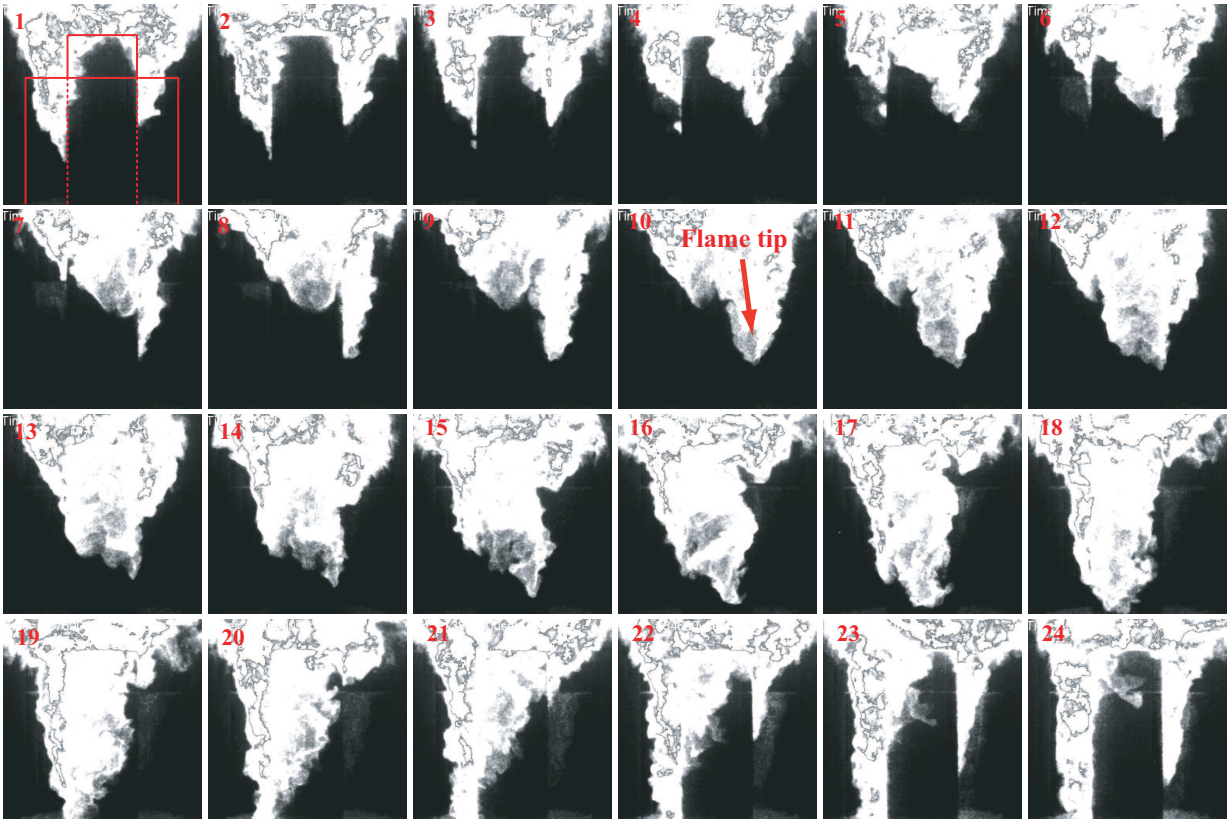

Figure 5.9: Sequence of CL imaging during flashback viewed from the side.

laboratory coordinates) of the leading edge in negative axial direction was nearly 3 m/s. In other individual realizations, propagation speeds up to 12 m/s were observed. In contrast, Nauert et al. [141] conservatively estimated the turbulent flame speed to be less than 2.1 m/s, based on Eq. (2.70) and Gouldin's model for the turbulent flame surface area ratio [67]. Hence, flashback cannot be caused by the trivial mechanism of bulk velocity flashback where the turbulent flame speed globally exceeds the axial bulk velocity of the flow according to Eq. (2.76). Instead, the very high upstream propagation speeds of the flame tip in the vicinity of the bluff-body wall indicate a boundary layer separation. Thus, a strong flow reversal is expected to convect the flame upstream and lead to the large magnitude of upstream propagation compared to the relatively low flame speed. However, at the end of the sequence shown in Fig. 5.9 the flame was anchored inside the swirler assembly similar to the example shown on the right hand side of Fig. 5.2.

From the combined off-axis OH-PLIF/CL data, several sequences can be extracted that reveal coherent flame structures. During the transition from meta-stable flame to full flashback, flame *tails* form in what appear to be PVC structures inside the nozzle. An example of such a sequence is given in Fig. 5.10. The structure is similar to that which Domingo and Vervisch [40] observed in DNS calculations of a flat flame front entering a tubular vortex. A needle-shaped flame tip is visualized by the OH-PLIF, propagating against the main flow direction (bottom right to top left). Domingo and Vervisch showed that a flame can propagate faster inside a vortex tube than outside due to the generation of a toroidal structure of vorticity. This structure can make between 10 and 20 revolutions of the nozzle, descending deeper into the burner until the flame wraps completely around the bluff-body and the flame tails dip completely into the plenum. The process can last for hundreds of milliseconds, while many different flow and flame structures are observable.

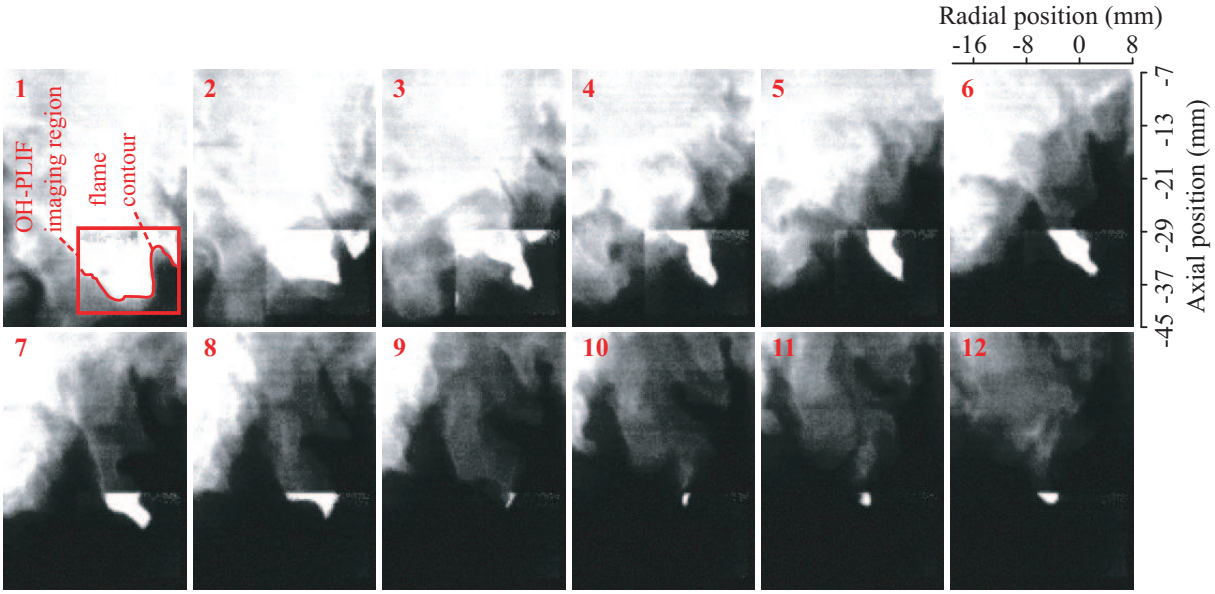

Figure 5.10: Sequence of a typical flame trail that propagates towards the oncoming flow (OH-PLIF is superimposed on narrow field CL)

5.3.3 CL–Pressure Correlations

Pressure measurements were done simultaneously with high-speed CL imaging at 5 kHz to precisely clarify the behavior of the pressure field during flashback. Figure 5.11 shows a sequence of flame images at various stages of flame flashback. In this measurement the camera system was synchronized with the data acquisition system through an optical trigger. The time axis appearing in the pressure trace shows the time relative to this trigger and therefore includes negative values. It is clear from Fig. 5.11 that, as expected, the recorded pressure is negative (image a) when the flame is far downstream of the measurement port. As the flame upstream propagation continues and reaches close to the measurement point, the pressure starts to rise (images b and c). This gain of pressure continues as the flame front passes over the pressure measurement port (images d and e). Although not shown in this figure, re-exposure of the measurement point to non-reactive flow results in a drop of the gage pressure. Thus, the simultaneous pressure and CL imaging indicates that the static pressure increases behind the reactive front.

This behavior of the pressure field is in agreement with the theory of vortex bursting and flame back pressure [84, 85]. According to the theories, the pressure rise across the flame front can be derived from the angular momentum conservation [34] as

$$\Delta p = \rho_u w_{max}^2 \left[1 - \left(\frac{\rho_b}{\rho_u} \right)^2 \right]. \tag{5.4}$$

Equation (5.4) predicts a pressure gain of between $20-50$ Pa considering the present experimental conditions with an axial bulk velocity of 5 m/s and swirl number of about $S_g = 1$. These values are similar to those measured in the present investigation. Interestingly, previous measurements of the pressure behind a flame front propagating in a vortex tube [84] show qualitative similarities to the present results.

Similar images of flame flashback show that such correlations between the pressure and flame propagation continues until the flame reaches the bottom of the nozzle. At this stage the whole

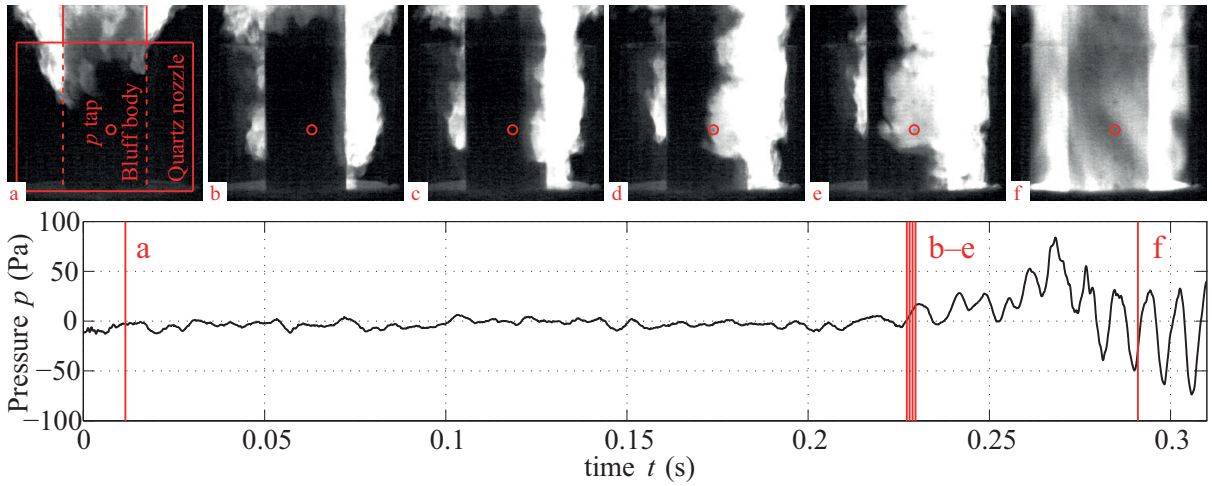

Figure 5.11: Sequence of CL images with the corresponding pressure at the bluff-body wall marked by the red circle

length of the nozzle is filled by the reacted flow. Strong pressure pulses are initiated under this condition and very quickly grow in amplitude in less than 50 ms. This is then followed by pressure limit-cycles (image (f)). It is therefore inferred that thermo-acoustic instability is established only after the flame flashback. Thus, under the investigated conditions the thermo-acoustic instability seemed to be a subsequent result of the flashback and is not, by itself, a significant driving mechanism.

The gain of pressure across the flame can have important influences upon the upstream flame propagation. It acts as a support of the front propagation against the incoming flow [85]. In general, this is a known mechanism for enhancement of the flame propagation speed in vortical flows [84] (see Section 2.3). In the present study the existence of the bluff-body adds further complexities to the problem. The most significant effects are the modification of the vortex and the introduction of the boundary layer. High-speed flame imaging clearly shows that the flame propagates close to the surface of the bluff-body. It is therefore most probable that the state of the boundary layer greatly affects the flame flashback. On the other hand, the present results indicate the development of an adverse pressure gradient on the surface of the bluff-body. This results in the depletion of the momentum flow and may ultimately separate the boundary layer. The flame can then readily propagate in the resultant low velocity region. Nonetheless, in the absence of simultaneously acquired data on the flow velocity, this remains as a possibility. Nevertheless, separate three-component velocity field data was recorded as well as simultaneously acquired two-component flow fields and the detailed flame front position. These results are presented in the following section.

5.3.4 Flow Field Analysis

High-speed 2C-PIV and high-speed Stereo-PIV have been applied to gain insight into the mechanism for upstream propagation of the flame, which ultimately leads to flashback. Firstly, the flow field recorded by Stereo-PIV under isothermal conditions will be discussed. It serves as a reference to the observations in the reacting case when the propagating flame influences the flow characteristics. Here, the influence of the swirl number on the flow field is assessed through the determination of the out-of-plane component of the velocity vectors. Measurements with 2C-

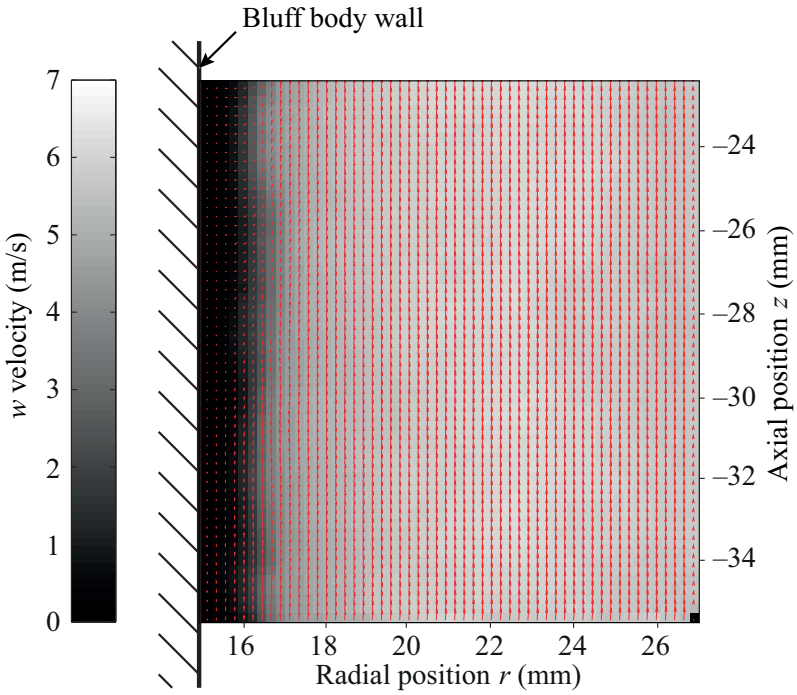

Figure 5.12: Mean vector field at $S_g = 1.05$. The in-plane components are indicated by arrows, while the out-of-plane component is shown in the background.

PIV were available and a comparison of the in-plane components between 2C and Stereo-PIV was conducted. Furthermore, the temporal correlated data allows for advanced comparison techniques to CFD data. The data of the flame front propagating through the measurement volume provides insights into the mechanism of upstream propagation. Here, 2C-PIV has been applied along with OH-PLIF to observe the flow-flame interactions as close as possible to the wall, where the additional influence on the boundary layer is relevant. The section closes with a summary of the observations in form of a flashback prototype. This resembles the characteristic features of an upstream propagating flame tip.

Isothermal Flow Field Analysis

To assess the influence of the chemical reactions on the flow field in the burner configuration `PSF30`, the corresponding isothermal configuration `30iso` at the mean critical swirl number of $S_g = 1.05$ has been characterized using Stereo-PIV. The measurement volume was chosen according to the location within the nozzle where the influence of the nozzle's inflow and outflow phenomena on the flame upstream propagation was expected minimal. The measurement volume was chosen approximately 30 mm below the exit of the outer nozzle (see Fig. 5.1). This location was approximately halfway between the inlet and the outlet.

In order to provide an overview of the entire flow field, Fig. 5.12 shows the resulting mean velocity field from 200 temporally uncorrelated instantaneous velocity fields as shown in Fig. 4.25. The arrows represent the magnitude and direction of the in-plane components $\overline{u}$ and $\overline{v}$ in z and r direction, respectively, while the grayscale map in the background represents the out-of-plane component $\overline{w}$. The mean flow field in axial direction along the 13 mm section inside the annular slot is very homogeneous in all three components. It furthermore does not comprise any struc-

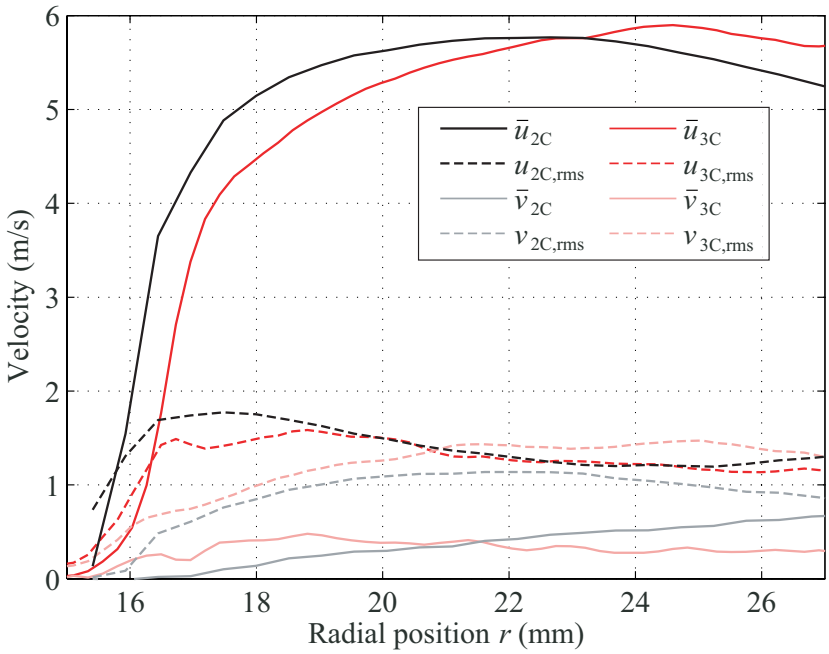

Figure 5.13: Comparison of the in-plane velocity data between 2C and Stereo-PIV measured at $z = -30$ mm axial position.

tures besides a decreasing gradient in $\overline{u}$ and $\overline{w}$ towards the bluff-body wall. The mean radial velocity $\overline{v}$ is close to zero in the entire domain. Note that the measured flow field does not cover the entire slot width from radial position between 15 and 30 mm. This is due to the reflections on the outer nozzle as well as the curvature of the glass, which results in an increasing glass surface inclination towards the camera at larger radii.

The detailed radial profiles of the in-plane components at $z = -30$ mm are shown in Fig. 5.13. While the red lines represent data that has been recorded using Stereo-PIV (3C), the black lines represent results acquired by conventional 2C-PIV. The magnitudes of the mean values as well as the fluctuations in terms of the root mean square show very good agreements. However, the location of the maximum gradient in the axial velocity component $\overline{u}$ differs significantly by approximately 0.5 mm. This effect can be attributed to the influence of the strong laser reflections close to the bluff-body wall, which extend much further into the imaging region (see raw images in Fig. 4.25). These were due to the oblique viewing angles of the stereoscopic cameras. During the Stereo-PIV processing, it could be observed that apparently valid vectors were often equal to zero. This does not mean the particles did not move in this region, but the image was overexposed by laser reflections, which left remaining structures after the background correction. These structures do not move and create high values during the cross-correlation, hence resulting in zero velocity values. This behavior will be referred to as *zero forcing* in the following. The contribution of unphysical zero values reduces the mean velocity already in regions were the axial flow velocity is still quite high. This behavior can be seen in the profiles from the 2C-PIV. Also, the fluctuations $u_{3C,rms}$ decrease due to the zero forcing. Additionally, the radial component exhibits some minor differences. Firstly, it should be noted that from continuity considerations, when compressibility effects are neglected, zero velocities for both measurement techniques are expected along the radius. No recirculation zone can be observed that can in-

duce a mean lateral velocity component. Further, it is most unlikely that a recirculation zone will develop in the region of $r > +26.5$ mm which could not be imaged. This is because the axial pressure gradients, which can lead to a recirculation, are expected to be smaller in the outer region than close to the bluff-body (see Section 2.1.2). The deviation from zero is almost constantly $+0.3$ m/s for the 3C results. When examining the 2C results it can be found that $\bar{v}$ increases linearly towards larger radii. A slight off-axis position of the light sheet results in a non-normal circumferential component of the flow such that part of the out-of-plane component is transferred to the radial component. However, this type of laser misalignment cannot cause the observed behavior since the misalignment influence is larger at smaller radii. Thus, a linearly decreasing velocity profile would be generated. An apparently increasing radial velocity profile can also be created due to the presence of the swirl. Since the seeding particles have a higher density than the surrounding fluid, they experience a larger centrifugal force which accelerates them outwards. As a consequence, this leads to an accumulation of particles, thus higher seeding densities, at larger radii. This phenomenon was not observed during the experiments. Thus, the measured radial velocity profile is probably real as two typical sources of error can be excluded. Unfortunately, no calibration data for this configuration is available such that the obtained velocities can be validated. Nonetheless, while Stereo-PIV suffers from laser reflections at the wall the 2C-PIV has the great advantage to acquire reasonable velocities close to the bluff-body, where flame upstream propagation is occurring.

The great advantage of Stereo-PIV is the determination of the out-of-plane component of the flow, which is of major importance in rotational flows (see Section 2.1.2). This technique has been applied to obtain a clearer picture of the isothermal flow field as well as to provide a dataset that can be used for validation purposes of CFD calculations. Two datasets have been recorded at the reference axial height $z = -30$ mm.

The first dataset consists of temporally uncorrelated data to obtain the mean velocities and fluctuations for increasing swirl numbers. These were varied between the standard configuration with $S_g = 0.75$ and the maximum swirl number of $S_g = 1.40$ which could be technically recorded by the selected PIV approach. Again 200 instantaneous vector fields have been averaged to acquire the mean and root mean square profiles shown in Fig. 5.14. Therein, the out-of-plane component w is marked as red, while the in-plane components u and v are in black and gray, respectively. Again, it should be mentioned that the data at the locations closer to the bluff-body than 2 mm ($r < 17$ mm) should be considered mindfully due to the risk of misinterpretation. The out-of-plane component shows the expected trend. While the swirl is increased the magnitude of w also increases. Starting from a maximum circumferential velocity w_{max} of approximately 5 m/s at $S_g = 0.75$, a maximum of 8.5 m/s is reached at $S_g = 1.4$. It is interesting to note that the form of the profile also changes. While being relatively flat at 5.5 m/s, the profile at $S_g = 0.95$ starts to form a peak from $S_g = 1.05$ on that moves from the inner to the outer radius as the swirl is further increased. As a consequence the axial component is influenced by this behavior. The u profile starts out flat, hence the swirl resembles a solid body rotation until $S_g = 0.95$. There, the axial velocity of the inner region closer to the bluff-body starts to decrease, while the outer velocities increase. This changes the relatively structured appearance at lower swirl numbers. The maximum measured mean axial velocity never exceeds 6 m/s. Obviously, this change of structure occurs close to the critical swirl number for flashback. However, no conclusions can be made due to the lack of valid data close to the bluff-body. Furthermore, it should be emphasized at this point that flashback process is highly stochastic and interpretation of unconditioned mean values with respect to transient phenomena is doubtful. This draws the attention to the velocity fluctuations. Though the mean velocities between the three components vary in magnitude from

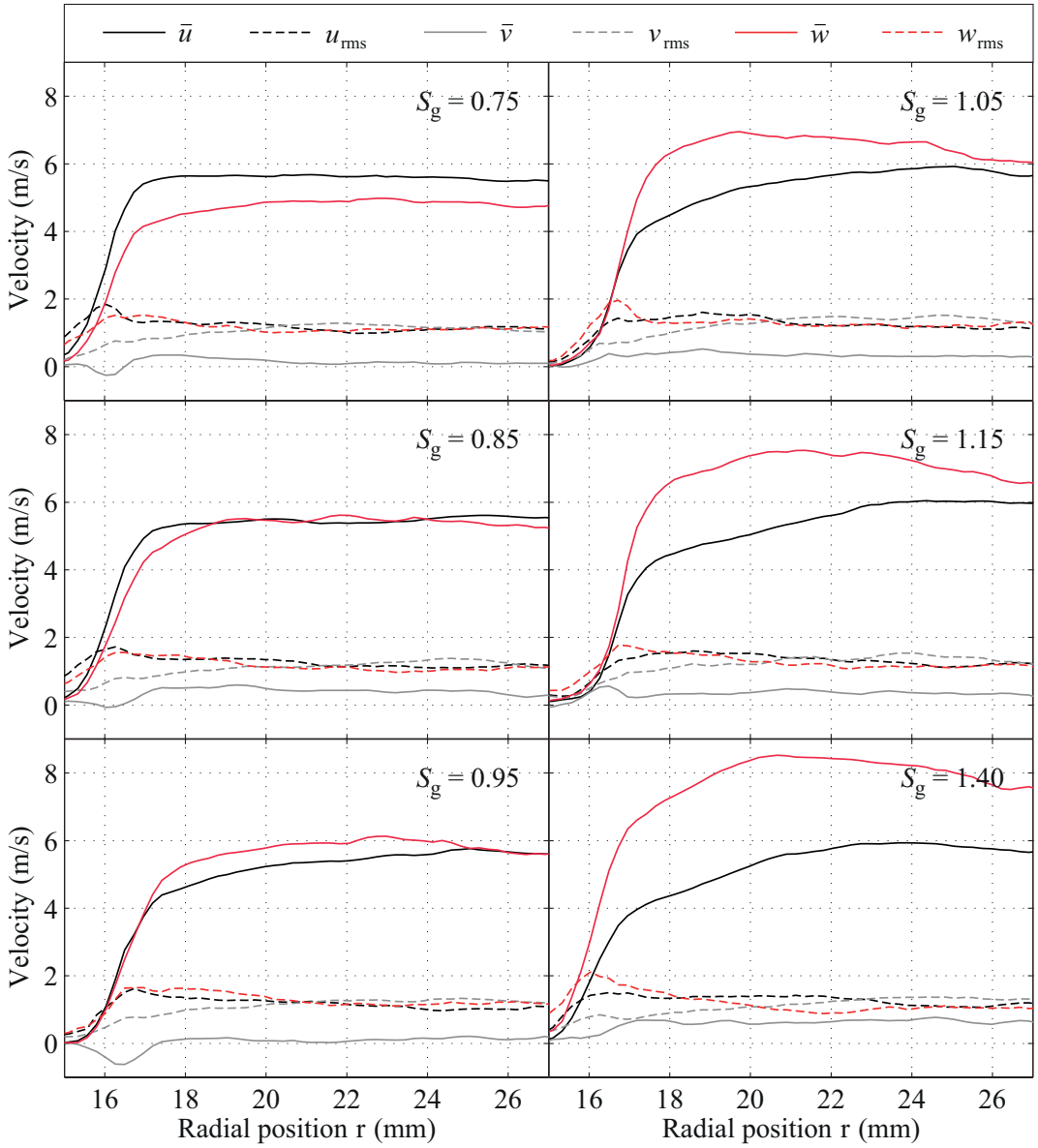

Figure 5.14: Radial profiles of the isothermal flow field inside the burner nozzle.

0 to more than 8 m/s, the level of fluctuations remains relatively constant. The root mean square values of all components are between 1 and 1.5 m/s over the entire measured radius.

Until now, no advantage has been drawn from the use of a high-speed measurement technique and all of the stereo data could have been produced by a conventional 10 Hz Stereo-PIV system. However, the second set of data acquired by high-speed Stereo-PIV provides a valuable tool for the validation of numerical calculations such as LES results. A sequence of 1 s duration at 20 kHz sampling rate has been recorded at the critical swirl number $S_g = 1.05$ for `30iso`. From each of the three components of $62 \times 64 = 3968$ vectors the time series of 20,000 samples has been subsequently analyzed. Here, the autocorrelation function and the integral time scale τ_0 was determined for the u, v, and w data at the first zero crossing (see Section 4.4 and Fig. 5.15).

In Fig. 5.16 the resulting time scales throughout the measurement volume have been mapped as grayscales. The large map on the left hand side shows the results of the axial velocity compo-

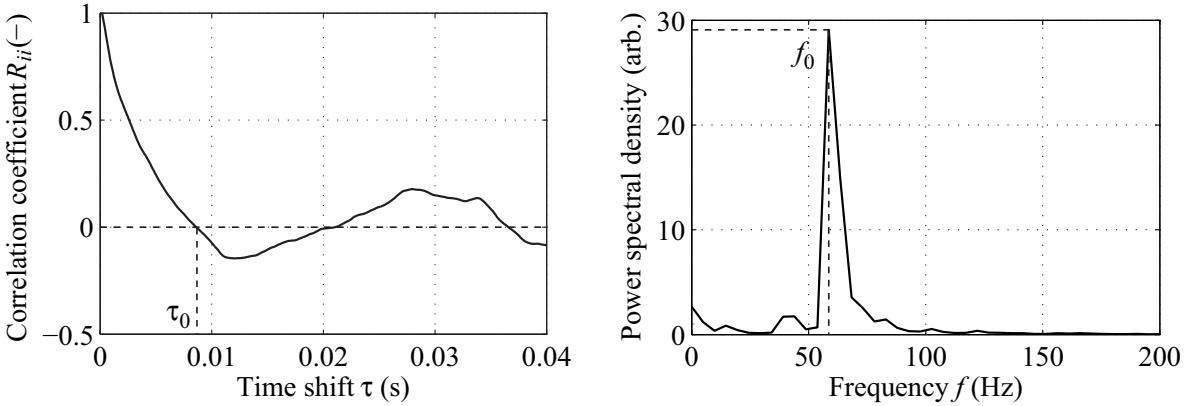

Figure 5.15: Map processing examples: An autocorrelation function at a control point within the integral time scale maps in Fig. 5.16 (left) and a sample spectrum from within the maps of coherent frequencies in Fig. 5.17 (right).

nent. Axially oriented stripes of constant time scales can be observed that are above 25 ms close to the bluff-body. The time scales decrease as the distance to the bluff-body increases down to approximately 5 ms. However, localized spots of strongly differing time scales can be found. In the other two components, shown in the small time scale maps at the right hand side, no obvious structures are prominent. Nonetheless, along the bluff-body wall a relatively homogeneous axial distribution in the *u* and *w* components can be found which indicate a correlation between them. All three maps are characterized by large regions of constant time scale. It can be concluded, that the predominant time scale for the *v* component is approximately 5 ms, while the *w* component exhibits time scales that are three times higher incorporating smaller islands of shorter time scales.

In order to compare coherent structures, which are of paramount interest in non-stationary simulations, further time series analysis has been applied. In a second processing step a Fourier transformation revealed the coherent frequency with the strongest energy content in the example spectrum shown in Fig. 5.15. The peak search in the spectral domain had to be limited to the range above 30 Hz. This was due to the length of the time series that led to an unacceptable temporal resolution below this limit.

Similar to the integral time scale maps, Fig. 5.17 shows maps of the local dominant frequency for each component of the velocity vectors. Again, the maps comprise large regions of constant frequencies which are between 40 and 170 Hz for all components with small islands of frequencies that exceed 250 Hz. While the radial component data shows no clear structure, a large region close to the bluff-body can be observed in the axial and circumferential data which is significantly lower than the bulk frequency of the rest of the field. The coherent frequency of these larger areas are approximately 80 and 40 Hz for the *u* and *w* component data, respectively. Nevertheless, structures close to the bluff-body can still be the result of reduced data quality in this region. A measure to quantify the significance of the found frequency compared to the rest of the peaks in a spectrum has to be defined in order to clarify this uncertainty. This issue has not been further addressed within this work. However, measures to quantify the significance of the characteristic local frequency could be based upon peak height ratios of the Fourier spectra.

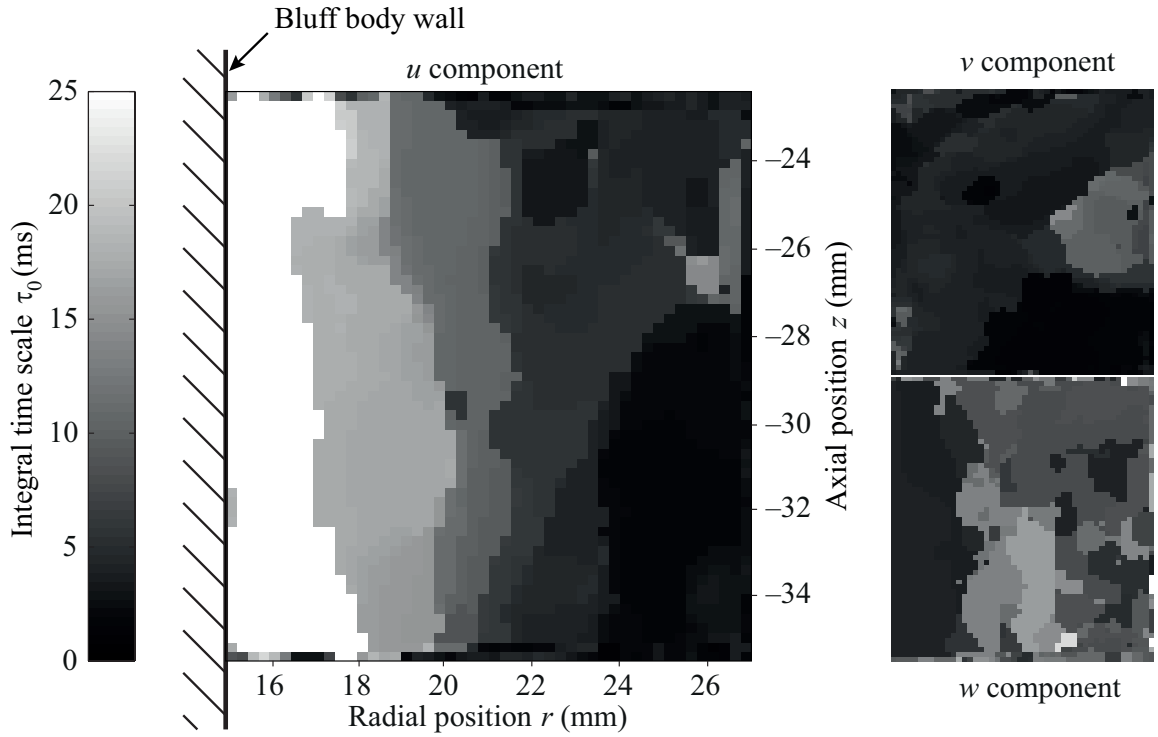

Figure 5.16: Map of local integral time scales obtained from time series of each vector component.

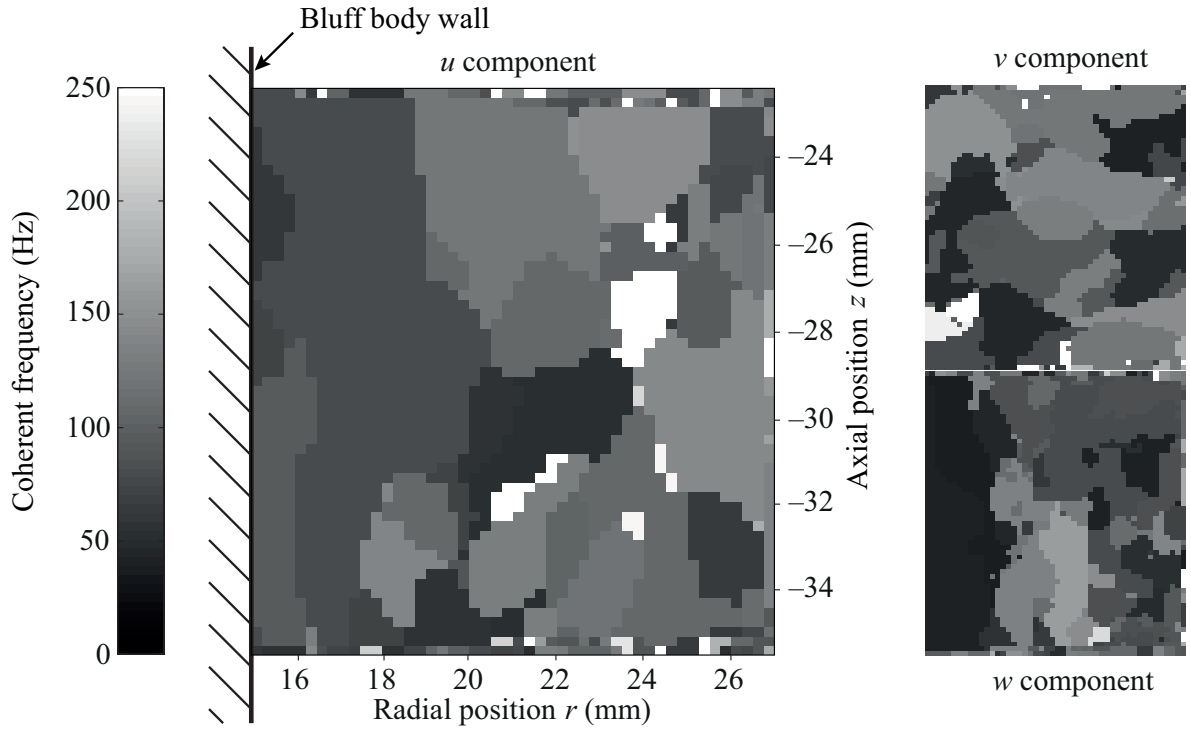

Figure 5.17: Map of predominant local coherent frequency obtained from time series of each vector component.

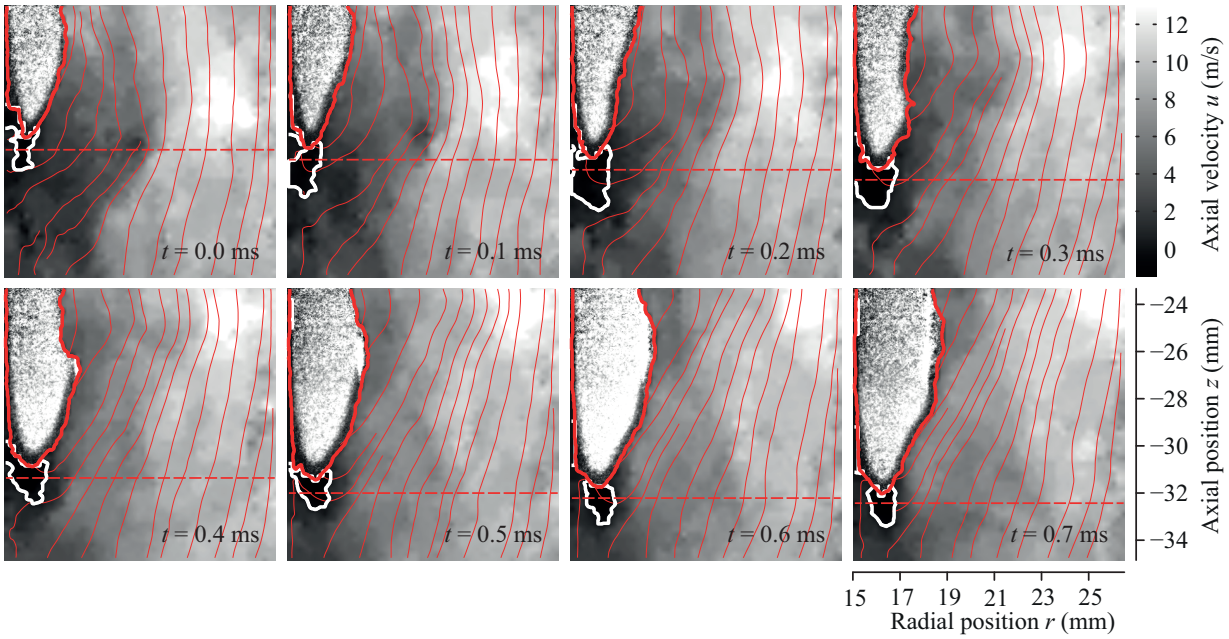

Figure 5.18: Sequence of images with upstream axial motion of the flame front lead by a negative axial velocity zone (enclosed in a thick white line). The red solid line denotes evaporated droplet region. The OH-PLIF image is superimposed on this region. The thin red lines are streamlines. The dashed red line denotes locations used for conditional velocity profiles

Flow Field Analysis during Flashback

With the combined OH-PLIF/PIV/CL measurements, data sequences of the evolution of the velocity field during flame propagation could be recorded inside the nozzle within a millimeter close to the bluff-body. Such a sequence is shown in Fig. 5.18. Eight consecutive OH-PLIF/PIV shots are displayed in which the flame tip propagates monotonically upstream while a region of negative axial flow (outlined in white in the images) precedes the flame tip.

The reduced and negative velocities within 2 mm of the inner wall can be clearly seen in a mean velocity profile conditioned on the location 1 mm upstream of the flame tip (Fig. 5.20). The low root mean square values highlight the consistency of this event. Observation of the CL imaging confirms that the overall flame base appears to be progressing upstream. It is remarkable that the root mean squares remain low close to the inner wall and the approaching flame front. It signifies the quality of the resolution of the technique and the efforts to minimize near-wall reflections while retaining a high SNR in the Mie-scattering images. The outer wall mean axial velocity does not return to zero near the wall due to the blurring loss of information from the lensing effect of the quartz nozzle in this region. De-warping algorithms were applied but there is an increased uncertainty in this region.

CL is an important tool for attempting to interpret the results [14, 16]. In the 14 flashback events recorded in detail, many different flame motions and events were observed. Specifically, sequences exist where apparent upstream motion is observed without negative velocities occurring near the inner wall of the nozzle, as shown in Fig. 5.19. An analysis of the CL data shows that in some cases it is not apparent that the flame base is actually progressing upstream. In fact, the data shows a sequence of slices through a V-shaped flame tail that is being convected around the bluff-body. Flow field divergence is still visible around the flame event and the OH-PLIF

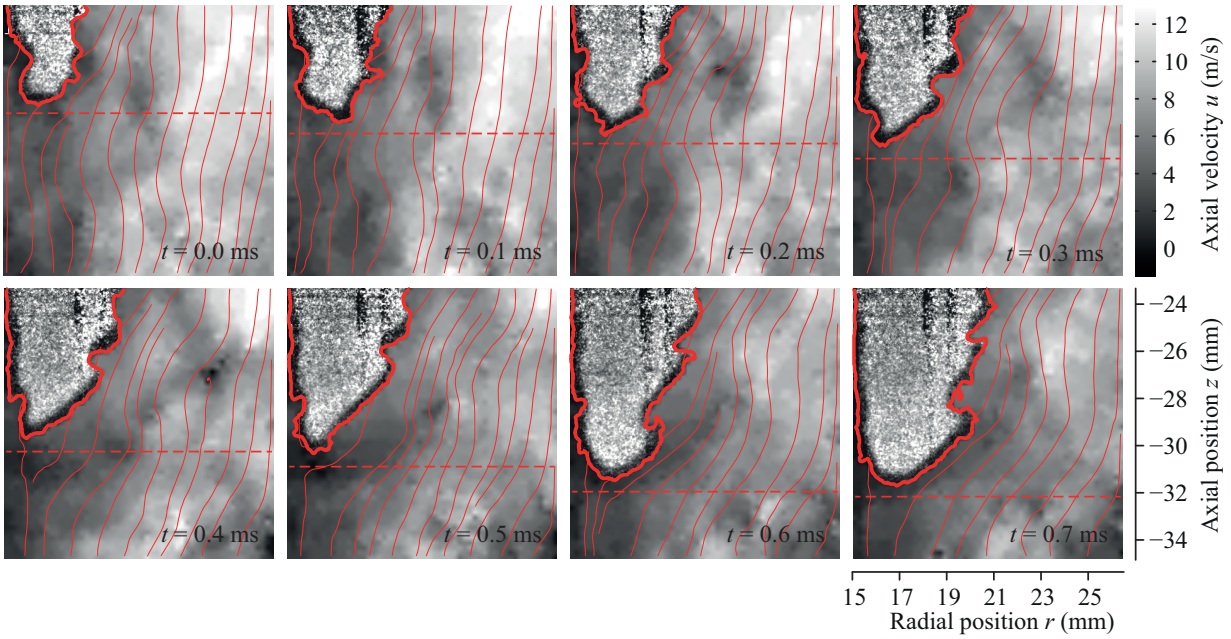

Figure 5.19: Sequence of images with upstream axial motion of flame front which is not preceded by a negative axial velocity zone. The red solid line denotes evaporated droplet region. The OH-PLIF image is superimposed on this region. The thin red lines are streamlines. The dashed red line denotes locations used for conditional velocity profiles.

confirms there is definitely a flame front in the sequence.

The corresponding axial velocity mean and RMS profiles display what appears to be a thickened boundary layer on the nozzle's inner wall (see Fig. 5.20). An almost constant axial velocity region of approximately 5.5 m/s in the main flow can be found following a decrease in the velocity when approaching the inner wall.

The temporal resolution is very important in understanding the data collected in this investigation. For this flow, there is a big difference between the inter-frame correlation of image sequences taken at 5 kHz and those taken in this experiment at 10 and 20 kHz. For this flow, with significant swirling out-of-plane motion and a moderate Reynolds number, 10 kHz is close to the minimum required to resolve the integral flow structures. Regarding the out-of-plane component of the velocity, careful design of the experiment has enabled the key flow structures and events to be resolved even without the third velocity component. However, this addition to the experiment would be very useful as it can be used to condition the in-plane velocity components.

The Flashback Prototype

After analysis of all recorded flashback data, where the flame enters the measurement volume, the sequences could be divided into two categories. The first category of the sequences showed the *convection*-type upstream propagation of the flame without negative axial velocity region at the flame tip. These sequences do not contain interesting information about the driving mechanism of upstream flame propagation resulting in flashback.

The second category reveals a flame motion that follows a region of negative axial velocity. This indicates an upstream propagation of the leading edge inside the measurement plane. The typical characteristics of these in-plane *propagation*-type sequences are summarized in Fig. 5.21

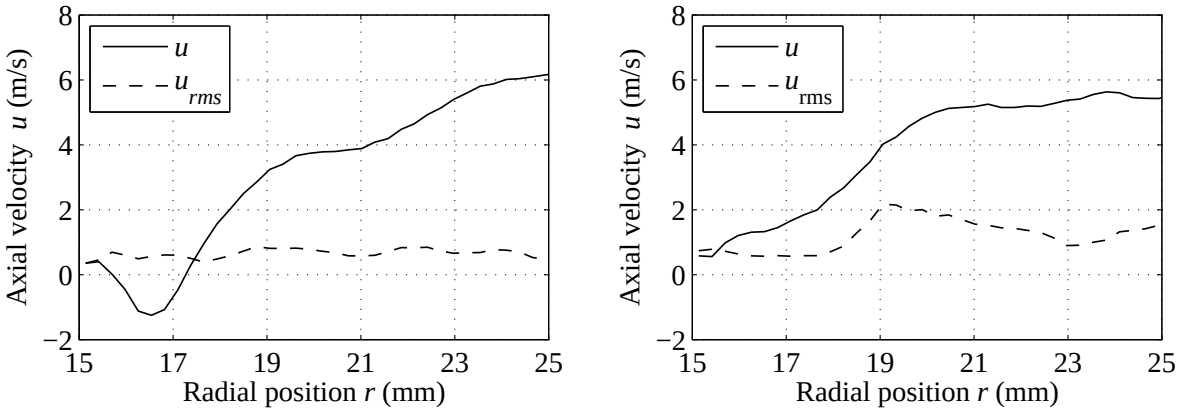

Figure 5.20: Conditional mean and RMS axial velocity, 1 mm upstream of the flame tip. Left hand side: negative axial velocities upstream of the flame tip. Right hand side: upstream motion of the flame front is not found in conjunction with a negative axial velocity zone.

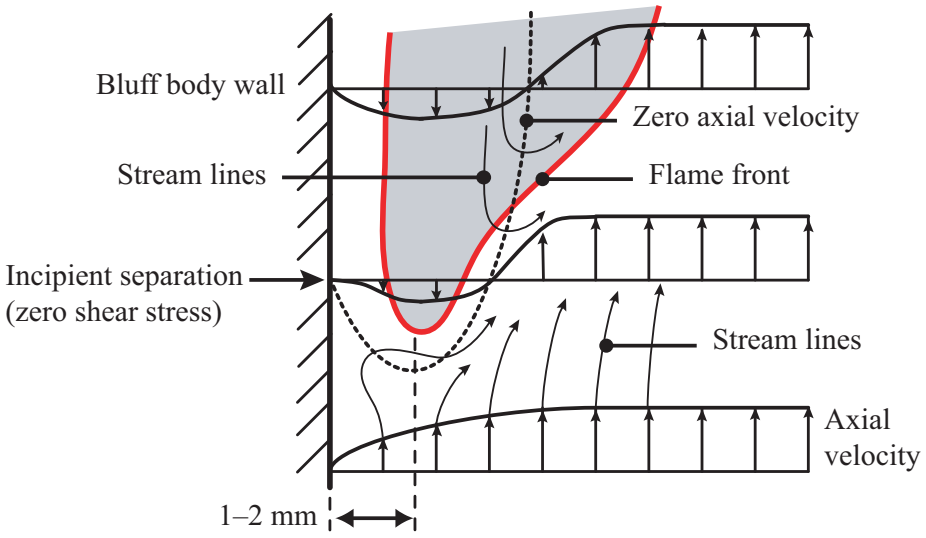

Figure 5.21: Schematic of propagation prototype which characterizes upstream flame propagation inside the nozzle.

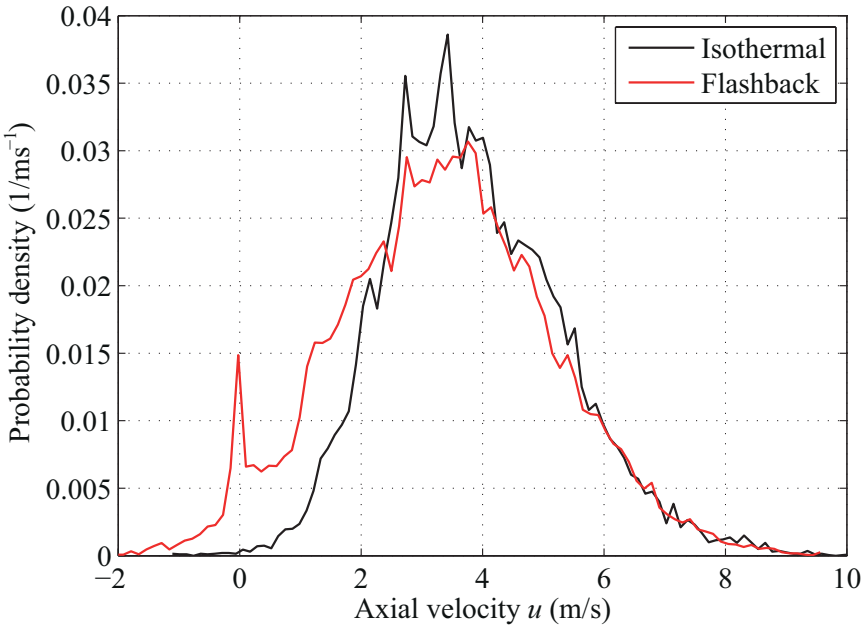

Figure 5.22: Histograms of axial velocity component at control point close to inner bluff-body wall inside the nozzle for isothermal and reacting conditions.

and referred to as the propagation prototype. The upstream flame propagation is characterized by:

1. V-shaped flame topology in radial and circumferential direction

2. Leading edge 1 – 2 mm from bluff-body wall

3. Axial velocity deceleration up to boundary layer separation and flow reversal near bluff-body wall preceding the upstream flame propagation

4. Flame motion following the region of low axial flow velocity

The influence of the chemical reaction on the flow field becomes clear when a histogram of the axial velocity is considered (see Fig. 5.22). It is taken from the PIV dataset at a control point approximately 1 mm away from the inner bluff-body wall ($r = 16$ mm) at $z = -25$ mm axial distance from the nozzle exit. The time series of the isothermal configuration, which has the same flow parameters as the reacting series with flashback, spans 1 s giving 20,000 samples at a repetition rate of 20 kHz. In the case of flashback, three pre-series were taken into account to approximately match the total number of data samples. The data shows that in the case of isothermal flow no negative axial velocities exist. In contrast, a significant number of negative axial velocities were measured during flashback. The artificial peak at zero velocity is an effect of statistically occurring erroneous vectors from the PIV analysis that could not be removed. Nevertheless, the histogram clearly displays the influence of combustion on the flow field and the link to the mechanism of upstream propagation.

5.3.5 A New Flashback Hypothesis

Many different flashback theories can be found in the literature of which the most relevant have been summarized in Section 2.3. These predict the premixed flame propagation speed inside a vortex tube based on various types of mechanisms. Phenomena of combustion inside vortex tubes can be found in many types of gas turbine combustors. However, the mechanisms are inappropriate for swirl burners featuring a central bluff-body, which changes the flow field drastically. A boundary layer is introduced which can interact with the flame. The various flashback theories in the literature do not include both possibilities, the swirl and a boundary layer, to enable flashback. Thus, the experiments conducted during this work aimed for the understanding of flashback in a swirled flow with central bluff-body. Although a large dataset of combined scalar and vector information could be recorded, the driving mechanism of upstream propagation that causes flame flashback cannot be determined yet. This is due to the complexity of the phenomenon, which includes interactions of turbulence, large coherent flow structures, a boundary layer, and chemical reaction. A hypothesis can still be formulated despite a limited experimental view that lacks the information of all three velocity components together with the thermo-kinetic state of the gas mixture in all three dimensions close to the bluff-body wall.

The flow field time series of the flashback indicates that the flame propagates upstream when the boundary layer on the inner wall is separated or close to separation. A thick boundary layer with low momentum is a requirement for the flame to propagate upstream. The flame speed of the fuel-air mixture has to be higher than the local fluid velocity at a sufficiently large distance from the wall to prevent quenching due to heat transfer and radical loss to the wall. Figure 5.21 sketches the separation of the boundary layer from the inner wall of the annulus and the subsequent upstream propagation of the flame. The separation of the boundary layer from a flat wall is linked to the existence of an adverse pressure gradient, i.e., the rise in static pressure in streamwise direction. Possibly, the flame interacts with the flow field through the static pressure field. In this case, the flame affects the static pressure field by producing an adverse pressure gradient of sufficient strength to cause flow separation on the inner wall of the annulus. This enables the flame to propagate upstream. Thereby, it can further increase the strength of the adverse pressure gradient or shift the location of the adverse pressure gradient in upstream direction.

To support this latter possibility, Fig. 5.23 sketches the burner exit region in an x-r-coordinate system. The thick red line denotes the location of the main reaction zone during stable combustion. At the same time, the pressure along a line through the points (A), (B) and (C) (at $r = R_\mathrm{o}$ along the outer wall) and along a line through the points (a), (b) and (c) (at $r = R_\mathrm{i}$ along the inner wall) is considered. The static pressure along these lines is indicated on the left hand side of Fig. 5.23. There is a pressure difference $\Delta p > 0$ between the outer wall and the inner wall. The magnitude of Δp follows from the simplified momentum equation in radial direction Eq. (2.83). Assuming $p = p(x,r)$ and a constant mean tangential velocity $\overline{\omega}$,

$$\Delta p = p(x,R_\mathrm{o}) - p(x,R_\mathrm{i}) = \int_{r=R_\mathrm{i}}^{r=R_\mathrm{o}} \frac{\partial p}{\partial r}\mathrm{d}r = \int_{r=R_\mathrm{i}}^{r=R_\mathrm{o}} \frac{\rho\overline{\omega}^2}{r}\mathrm{d}r. \tag{5.5}$$

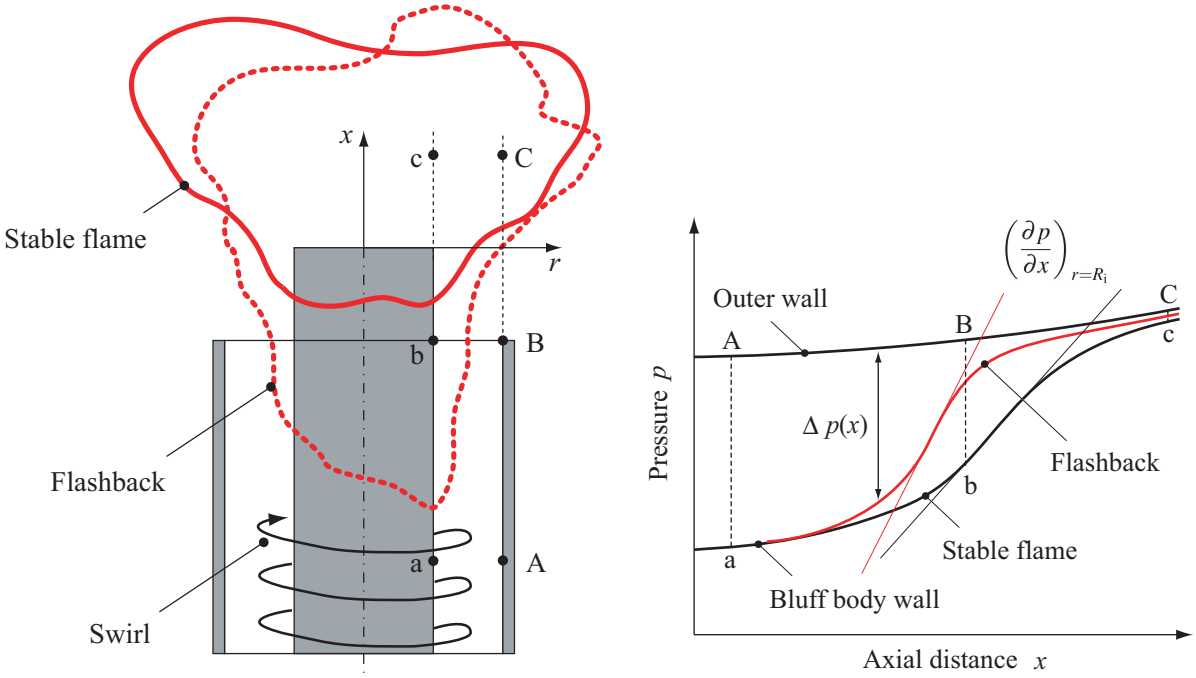

Figure 5.23: Schematic of proposed mechanism of flashback within premixed swirl burners with central bluff-body. The burner exit region (left) and axial pressure profiles at the bluff-body and the outer nozzle (right) are shown.

Taking the partial derivative for the stream coordinate x one obtaines

$$\left(\frac{\partial p}{\partial x}\right)_{r=R_o} - \left(\frac{\partial p}{\partial x}\right)_{r=R_i} = \int_{r=R_i}^{r=R_o} \frac{\partial(\rho\overline{\omega}^2)}{\partial x}\frac{\mathrm{d}r}{r} \tag{5.6}$$

$$= \int_{r=R_i}^{r=R_o} \left\{\overline{\omega}^2\frac{\partial\rho}{\partial x} + \rho\frac{\partial\overline{\omega}^2}{\partial x}\right\}\frac{\mathrm{d}r}{r} \tag{5.7}$$

$$= \int_{r=R_i}^{r=R_o} \left\{\overline{\omega}^2\frac{\partial\rho}{\partial x} + 2\rho\overline{\omega}\frac{\partial\overline{\omega}}{\partial x}\right\}\frac{\mathrm{d}r}{r}. \tag{5.8}$$

This determines the stream pressure gradient along the inner wall as

$$\left(\frac{\partial p}{\partial x}\right)_{r=R_i} = \left(\frac{\partial p}{\partial x}\right)_{r=R_o} - \int_{r=R_i}^{r=R_o} \left\{\overline{\omega}^2\frac{\partial\rho}{\partial x} + 2\rho\overline{\omega}\frac{\partial\overline{\omega}}{\partial x}\right\}\frac{\mathrm{d}r}{r} \tag{5.9}$$

The above expression shows that the stream pressure gradient along the inner wall can be larger than the gradient along the outer wall. This is due to a decrease of the density in streamwise direction and/or a decrease of the tangential velocity in streamwise direction. When the swirling fuel-air mixture exits the burner, it mixes intensely with the ambient air. This intense mixing decreases the tangential velocity component, thus lowering the pressure difference between the inner and outer wall (see Eq. (5.5)) while increasing the streamwise pressure gradient (see

Eq. (5.9)). The pressure difference Δp further decreases if points (c) and (C) are in regions with hot products because the density ρ_b there is low.

If the flame can locally propagate upstream into the nozzle, induced by an interaction with a PVC (as shown previously and denoted by the dashed red line in Fig. 5.23), the pressure difference between the inner and outer walls will be strongly reduced compared to when stabilization occurs above the burner mouth. This is caused by the effect of the low density of the hot products (see Eq. (5.5)). The decrease of the density in the streamwise direction, i.e. $\partial\rho/\partial x > 0$, increases the pressure gradient along the inner wall (see Eq. (5.9)). This could lead to a static pressure distribution as sketched by the red line in the diagram on the right hand side of Fig. 5.23. Furthermore, it would imply that the adverse pressure gradient is larger at a location further upstream, which results in earlier boundary layer retardation and an increase in boundary layer thickness. This promotes the upstream propagation of the flame after which the process is self-exciting, resulting in flashback. In subsequent studies additional measurements of the axial pressure gradient along the bluff-body wall could provide data in order to prove this theory.

5.4 Discussion and Classification of the Hypothesis

Three different states of flame stabilization of the premixed swirl burner were classified in this work. At low swirl numbers, the flame stabilizes on top of the bluff-body. Sufficiently high swirl numbers influence the flame to move upstream and stabilize at the shell of the bluff-body while precessing around it. A small increase of the swirl number causes the flame to rapidly move into the annular slot which results in flame flashback.

The critical swirl number was investigated for several configurations, which were summarized as stability limits. These show very good agreement with a calibrated flashback model by Konle and Sattelmayer [112].

Using an optically transparent nozzle the phenomenon of flashback of a turbulent, premixed, swirling flame was investigated experimentally by time-correlated, simultaneously acquired PIV, OH-PLIF, and CL data at kHz repetition rates. The measurements were complemented by the acquisition of the static gage pressure fluctuations at the bluff-body wall. The burning velocity was found much lower than the measured flashback propagation speeds. Hence, the objective was to elucidate the physical mechanisms responsible for upstream flame propagation.

Close inspection of flame images during upstream propagation revealed that the static pressure increases behind the flame front. This was in keeping with the theory of vortex bursting [85]. The gain of pressure across the flame front imposes an adverse pressure gradient in the direction of flame propagation. This is expected to cause boundary layer thickening or separation which, in turn, facilitates the upstream flame propagation.

In the course of the measurements, oscillations in pressure grow and lead to large amplitude fluctuations. These have a dominant frequency which match very well the previously measured CL data under the same experimental conditions [141]. The beginning of the apparently simultaneous occurrence of acoustic instability could be distinguished from the flame flashback. The results show that thermo-acoustic instabilities are a subsequent result and do not initiate the flashback. This is not obvious as the end of the flashback process and the beginning of the acoustic instability are only separated by milliseconds. Thus, the time difference cannot be distinguished without adequate combined high-speed diagnostics.

OH-PLIF at 10 kHz and PIV at 20 kHz were reported. The simultaneous flow field and flame position measurements revealed that flashback in this configuration is often associated with neg-

ative axial velocities upstream of the flame tip. The tip itself has a characteristic topology, being V-shaped in circumferential and radial direction (see Fig. 5.9 and Fig. 5.19, respectively). Located closely to the bluff-body wall at a distance of $1-2$ mm, the flame tip propagates upstream following a large region of flow reversal in the course of a boundary layer separation. Comparing the histograms of axial flow velocities in the isothermal and reacting case, further evidence for the influence of the flame's heat release on the flashback mechanism is found. Isothermal configurations do not show these negative velocities, but contain large coherent structures of ≈ 55 Hz which can also be found during flashback.

Hence, the driving mechanism lies in an interaction between three dimensional large-scale coherent motion, turbulence, and chemical reaction and cannot be determined precisely due to its overwhelming complexity. Nevertheless, a hypothesis for the propagation mechanism was presented. This can be categorized principally in the class of aerodynamically driven flashback (see Section 2.3.3). It is based on the generation of a adverse pressure gradient along the vortex axis in the presence of the flame. The magnitude of this pressure gradient is a function of the circumferential velocity and the fluid density according to Eq. (5.9). Exceeding a critical pressure gradient leads to boundary layer separation and flow reversal. This enables the flame to follow the separation upstream along bluff-body wall while providing a steep density gradient that maintains the pressure gradient to separate the boundary layer. Therefore, the current mechanism cannot solely be classified as aerodynamically driven, but also comprises characteristics of classical boundary layer flashback.

Finally, it should be mentioned that the two classes of mechanisms, based aerodynamics and baroclinity, come to play by a combination of density and pressure gradients, that are not aligned parallel in space. For future classifications it might be more reasonable to distinguish the models by the utilized form of the considered conservation equations. However, at least both mechanisms comprise a baroclinic effect according to its definition [17, 183].

6 Conclusions and Future Work

This thesis investigated flame flashback in a lean premixed swirl burner with central bluff-body using high-speed multi-parameter laser imaging diagnostics. Thereby, statistics of flame front-conditioned data of the velocity field and gage pressure at the bluff-body wall were obtained. In the course of the experimental investigations, the conventional laser imaging techniques were enhanced towards multi-kilohertz sampling rates. Furthermore, the concepts of quasi four-dimensional data acquisition and multi-dimensional data conditioning, which emerge from planar high-speed measurements, were elaborated and discussed.

6.1 Conclusions

Beginning with the theory of the transport equations in fluid dynamics, the characteristics of classical turbulence were introduced. The concept of spectral energy transfer from large scale production to small scale dissipation in the turbulence cascade was explained along with the theory to estimate the important spatio-temporal scales. The influence of swirl on the flow field was illustrated, which induces the vortex breakdown phenomenon and large scale coherent structures, such as precessing vortex cores. To complement the background on relevant flow theory, a brief introduction to boundary layer flows was provided. Regarding the involved chemistry, the oxidation of methane from the perspectives of one-step chemistry and reaction kinetics were detailed. From the latter perspective, the six mechanisms of nitric oxides formation were successively pictured and reduction strategies were presented. Lean premixed combustion was illuminated as it is the most effective primary reduction strategy for gas turbine combustors. The concept of turbulent flame speed was explained and premixed combustion regimes as well as premixed flamelets were discussed briefly. Summarizing previous investigations in premixed combustion, the different mechanisms of flashback due to thermo-acoustic instabilities, propagation in boundary layers, and in the core flow were classified.

The TECFLAM burner was described with an emphasis on the movable block swirl generator and the modifications to the original design. These were implemented to obtain an optical access into the burner nozzle as a fundamental requirement for the applicability of laser diagnostics. The burner parameters of the investigated isothermal and reacting flow conditions as well as the procedures to induce flashback were explained.

The measurement principles along with typical parameters of the various combustion diagnostics were illustrated. Further, their limitations in investigating unpredictable transient processes were emphasized. The measurement techniques included

- Chemiluminescence imaging to capture the global flame structure,
- Planar Laser-Induced Fluorescence of OH radicals for fine scale flame front detection,
- Two- and three-component Particle Image Velocimetry to characterize the flow field, and
- Wall pressure measurements on the bluff-body.

The extension of these techniques to temporally correlating data acquisition by using high-speed lasers and cameras was described. Details of the apparatus suitable for planar high-speed measurements were given and recent developments were reviewed. The interdependency of the spatial and temporal scales was investigated and a method to visualize the camera performance with respect to the scales of interest was developed. The application was demonstrated and implications of various camera parameters on the recorded signal were discussed. Furthermore, the concept of quasi four-dimensional data acquisition by laser sheet scanning was exemplified by an non-stationary mixing layer experiment using Mie-scattering of oil droplets. Different methods for laser scanning were briefly presented, hardware requirements of lasers and cameras were stated, and limitations with respect to the depth-of-field of the collection optics were discussed. The recent work using planar multi-parameter imaging was summarized and multi-dimensional data conditioning was presented as a technique to statistically compare unpredictable transient events from one experiment to another as well as to data from computational fluid dynamics. Multi-parameter measurements were applied in three different experimental setups. Subsequently, the data processing for each technique as well as the multi-parameter data matching was detailed. Further, the accuracy and precision were estimated and discussed. From the analysis of the various recorded datasets the following results were obtained:

- Three stabilization points of the flame base for the `PSF30` condition were characterized: The ordinary stabilization on top of the bluff-body for low swirl numbers ($S_g < 0.85$), a meta-stable location while the flame tip is precessing around the bluff-body near the exit of the burner nozzle ($0.85 < S_g < 1.05$) and a stabilization inside the swirl generator following flame flashback ($S_g > 1.05$).

- Stability maps of the burner's parameter field with respect to Reynolds number, thermal power, swirl number and equivalence ratio were generated from over 200 individual measurements of flashback initiation. The data shows an increased propensity to flashback at equivalence ratios around $\Phi = 0.9$ and the opposite behavior with increasing Reynolds numbers. Comparison of the dataset to a recently refined flashback model based on the Damköhler number by Konle and Sattelmayer [112] revealed excellent agreement. However, the model is not predictive and must be calibrated by a reference flashback condition.

- Frequency analysis of the measurements conducted within the burner nozzle revealed the existence of large scale coherent flow structures. Velocity, chemiluminescence, and pressure time series recorded under isothermal as well as reacting conditions prior, during, and after flashback yielded a set of characteristic frequencies. At the critical swirl number of 1.05 the lowest measured frequencies at approximately 40 Hz in the velocity data could be attributed to the isothermal flow which supplemented previous measurements of Schneider et al. [174]. In the presence of the flame, the coherent structures exhibited higher frequencies at approximately 55 Hz. Nevertheless, the pressure signal revealed strong acoustic oscillations under limit-cycle at 130 Hz.

- Correlations of flame structure from chemiluminescence imaging and simultaneous measurements of pressure time series showed that the limit-cycle oscillations were a subsequent result of upstream flame propagation and did not initiate the process.

- Analysis of the global flame tip location revealed propagation speeds against the oncoming flow that exceeded the estimated turbulent flame speed.

- The characterization of the isothermal flow field by stereoscopic three-component PIV showed a significant impact of the increasing circumferential velocity w on the axial momentum by increasing the swirl number from $S_g > 0.95$ on. A comparison to two-component PIV showed rather good agreement in the center region of the annular slot of the nozzle. Regions close to the bluff-body suffered from laser light reflections and the oblique viewing angle of the stereoscopic configuration.

- Spatio-temporal conditioned data from the reacting conditions revealed a negative recirculation zone bubble upstream of the flame tip with a diameter of up to $2.5 - 3$ mm. The flame was following the bubble upstream at a velocity of $\approx 1.5\,\mathrm{m/s}$ for the considered flashback events. Based upon these findings, a flashback prototype was formulated that featured a characteristic geometry and propagation parameters.

- A hypothesis for flashback in swirled flows with central bluff-body was postulated and classified in the framework of existing flashback mechanisms.

For the first time, simultaneously recorded and temporally resolved experimental data on the velocity field and scalar information close to the wall inside a burner nozzle was acquired. It appears that the recorded data of flashback phenomenon supports theories based on aerodynamics, baroclinity and boundary layers [84]. However, due to the high complexity of the flow and flame in combination with optical accessibility issues, putting forward a definite mechanism remains as a task of future investigations.

6.2 Future Work

It is expected that the continuation of experimental investigations with high-speed measurement techniques will help to elucidate further aspects of the flashback problem. Combined measurements of the velocity field, flame front position, and pressure will contribute to understand the mechanism of upstream flame propagation in swirl burners with central bluff-body, such as the TECFLAM burner. Especially simultaneous velocity and pressure data within the thickened boundary layer 2 – 3 mm away from the bluff-body wall is supposed to provide valuable insights into the underlying physics. Additional effects of the flame on the flow field can be investigated in the burnt region downstream of the flame front through using solid particle seeding for PIV. Finally, accurate measurements of the axial gage pressure gradient along the bluff-body wall can help to verify the presented hypothesis.

The complexity of the flow geometry necessitates the acquisition of three-dimensional data. Tomographic PIV [47] seems to be a potential candidate to measure three-dimensional volumes including all components of the velocity vector. Laser scanning techniques for planar diagnostics, such as PLIF, can be extended to higher scan rates and larger volumes by developing stronger and faster-pulsed lasers as well as faster scanners and cameras. Nonetheless, the reflections on the nozzle and bluff-body walls will render these investigations a difficult task.

Bibliography

[1] ABEL, N. H. *Oeuvres Completes*. Johnson Reprint Corp., New York, 1988.

[2] ACHESON, D. J. *Elementary fluid dynamics*. Oxford applied mathematics and computing science series. Clarendon Press, Oxford University Press, New York, Oxford, 1990.

[3] ADRIAN, R. J. Particle-imaging techniques for experimental fluid-mechanics. *Annual Review of Fluid Mechanics 23* (1991), 261–304.

[4] ADRIAN, R. J., AND WESTERWEEL, J. *Particle Image Velocimetry*. Cambridge Aerospace Series. Cambridge University Press, Cambridge, New York, 2011.

[5] ALBRECHT, H.-E., BORYS, M., DAMASCHKE, N., AND TROPEA, C. *Laser doppler and phase doppler measurement techniques*. Experimental fluid mechanics. Springer, Berlin, New York, 2003.

[6] ALLISON, S. W., AND PARTRIDGE, W. P. *Laser-Induced Fluorescence Imaging*. John Wiley & Sons, Inc., 2002.

[7] AMANTINI, G., FRANK, J. H., SMOOKE, M. D., AND GOMEZ, A. Computational and experimental study of standing methane edge flames in the two-dimensional axisymmetric counterflow geometry. *Combustion and Flame 147*, 1-2 (2006), 133–149.

[8] ASATO, K., TAKEUCHI, Y., AND KAWAMURA, T. Fluid dynamic effects of flame propagation in a vortex ring. In *Eleventh Australasian Fluid Mechanics Conference* (1992), pp. 167–170.

[9] ASHURST, W. T. Flame propagation along a vortex: The baroclinic push. *Combustion Science and Technology 112* (1996), 175–185.

[10] ATOBILOYE, R. Z., AND BRITTER, R. E. On flame propagation along vortex tubes. *Combustion and Flame 98*, 3 (1994), 220–230.

[11] BARBOSA, S., SCOUFLAIRE, P., AND DUCRUIX, S. Time resolved flowfield, flame structure and acoustic characterization of a staged multi-injection burner. *Proceedings of the Combustion Institute 32* (2009), 2965–2972.

[12] BARLOW, R. S. Laser diagnostics and their interplay with computations to understand turbulent combustion. *Proceedings of the Combustion Institute 31* (2007), 49–75.

[13] BARNETT, H. C., AND HIBBARD, R. R. Basic considerations in the combustion of hydrocarbon fuels with air. Tech. rep., NACA report, 1959.

[14] BÖHM, B., GEYER, D., DREIZLER, A., VENKATESAN, K. K., LAURENDEAU, N. M., AND RENFRO, M. W. Simultaneous PIV/PTV/OH PLIF imaging: Conditional flow field statistics in partially premixed turbulent opposed jet flames. *Proceedings of the Combustion Institute 31* (2007), 709–717.

[15] BÖHM, B., HEEGER, C., BOXX, I., MEIER, W., AND DREIZLER, A. Time-resolved conditional flow field statistics in extinguishing turbulent opposed jet flames using simultaneous highspeed PIV/OH-PLIF. *Proceedings of the Combustion Institute 32* (2009), 1647–1654.

[16] BÖHM, B., HEEGER, C., GORDON, R. L., AND DREIZLER, A. New perspectives on turbulent combustion: Multi-parameter high-speed planar laser diagnostics. *Flow Turbulence and Combustion 86*, 3-4 (2011), 313–341.

[17] BJERKNES, V. Über einen hydrodynamischen Fundamentalsatz und seine Anwendung besonders auf die Mechanik der Atmosphäre und des Weltmeeres. *Kongl. Sven. Vetensk. Akad. Handlingar 31* (1898), 1–35.

[18] BORGHI, R. *On the structure and morphology of turbulent premixed flames*. Plenum Press, New York, 1985, pp. 117–138.

[19] BOXX, I., HEEGER, C., GORDON, R., BÖHM, B., AIGNER, M., DREIZLER, A., AND MEIER, W. Simultaneous three-component PIV/OH-PLIF measurements of a turbulent lifted, C_3H_8-Argon jet diffusion flame at 1.5 khz repetition rate. *Proceedings of the Combustion Institute 32* (2009), 905–912.

[20] BOXX, I., STOHR, M., CARTER, C., AND MEIER, W. Sustained multi-khz flamefront and 3-component velocity-field measurements for the study of turbulent flames. *Applied Physics B 95*, 1 (2009), 23–29.

[21] BOXX, I., STOHR, M., CARTER, C., AND MEIER, W. Temporally resolved planar measurements of transient phenomena in a partially pre-mixed swirl flame in a gas turbine model combustor. *Combustion and Flame 157*, 8 (2010), 1510–1525.

[22] BÄUERLE, B., HOFFMANN, F., BEHRENDT, F., AND WARNATZ, J. Detection of hot spots in the end gas of an internal combustion engine using two-dimensional LIF of formaldehyde. In *Proceedings of the Combustion Institute* (1994), vol. 25, pp. 135–141.

[23] CHANAUD, R. C. Observations of oscillatory motion in certain swirling flows. *Journal of Fluid Mechanics 21*, 01 (1965), 111–127.

[24] CHATTERJEE, P. *A Computational Fluid Dynamics Investigation of Thermoacoustic Instabilities in Premixed Laminar and Turbulent Combustion Systems*. PhD thesis, Virginia State University, 2004.

[25] CHEM1D. A one-dimensional laminar flame code, developed at Eindhoven University of Technology, <www.combustion.tue.nl/chem1d>, 2011.

[26] CHOMIAK, J. Dissipation fluctuations and the structure and propagation of turbulent flames in premixed gases at high reynolds numbers. *Proceedings of the Combustion Institute 16* (1977), 1665–1673.

[27] CLEMENS, N. T. *Flow Imaging*. John Wiley & Sons, Inc., 2002.

[28] COHEN, J. M. Experimental investigation of near-blowout instabilities in a lean, premixed step combustor. In *34th AIAA Aerospace Science Meeting and Exhibit* (1996).

[29] CORREA, S. M. A Review of NO_x Formation Under Gas-Turbine Combustion Conditions. *Combustion Science and Technology 87*, 1-6 (1993), 329–362.

[30] CROWE, C. T., SOMMERFELD, M., AND TSUJI, Y. *Multiphase flows with droplets and particles*. CRC Press, Boca Raton, Fla., 1998.

[31] CUNDY, M. E., AND SICK, V. Hydroxyl radical imaging at khz rates using a frequency-quadrupled Nd:YLF laser. *Applied Physics B 96*, 2-3 (2009), 241–245.

[32] DAILY, J. W. Laser-induced fluorescence spectroscopy in flames. *Progress in Energy and Combustion Science 23*, 2 (1997), 133–199.

[33] DAMKÖHLER, G. Der Einfluss der Turbulenz auf die Flammengeschwindigkeit in Gasgemischen. *Zeitschrift für Elektrochemie und angewandte physikalische Chemie 46*, 11 (1940), 601–626.

[34] DANESHYAR, H., AND HILL, P. G. The structure of small-scale turbulence and its effect on combustion in spark-ignition engines. *Progress in Energy and Combustion Science 13*, 1 (1987), 47–73.

[35] DAOU, J., AND MATALON, M. Flame propagation in poiseuille flow under adiabatic conditions. *Combustion and Flame 124*, 3 (2001), 337–349.

[36] DE SWART, J. A. M., GROOT, G. R. A., VAN OIJEN, J. A., TEN THIJE BOONKKAMP, J. H. M., AND DE GOEY, L. P. H. Detailed analysis of the mass burning rate of stretched flames including preferential diffusion effects. *Combustion and Flame 145*, 1-2 (2006), 245–258.

[37] DEMTRÖDER, W. *Laser spectroscopy*, 4th ed. Springer, Berlin, 2008.

[38] DERY, R. J. Development of a combustion wave in a flowing gas. *Proceedings of the Combustion Institute 3* (1949), 235.

[39] DIEKE, G. H., AND CROSSWHITE, H. M. The ultraviolet bands of the hydroxyl radical (OH). *Journal of Quantitative Spectroscopy & Radiative Transfer 2*, 2 (1962), 97–199.

[40] DOMINGO, P., AND VERVISCH, L. DNS of partially premixed flame propagating in a turbulent rotating flow. *Proceedings of the Combustion Institute 31* (2007), 1657–1664.

[41] DREIZLER, A., LINDENMAIER, S., MAAS, U., HULT, J., ALDEN, M., AND KAMINSKI, C. F. Characterisation of a spark ignition system by planar laser-induced fluorescence of OH at high repetition rates and comparison with chemical kinetic calculations. *Applied Physics B 70*, 2 (2000), 287–294.

[42] DREIZLER, A., TADDAY, R., MONKHOUSE, P., AND WOLFRUM, J. Time and Spatially-Resolved Lif of Oh $A^2\Sigma^+(v' = 1)$ in Atmospheric-Pressure Flames Using Picosecond Excitation. *Applied Physics B 57*, 1 (1993), 85–87.

[43] DRUAULT, P., GUIBERT, P., AND ALIZON, F. Use of proper orthogonal decomposition for time interpolation from PIV data – Application to the cycle-to-cycle variation analysis of in-cylinder engine flows. *Experiments In Fluids 39*, 6 (2005), 1009–1023.

[44] ECKBRETH, A. C. *Laser diagnostics for combustion temperature and species*. Energy and engineering science series. Abacus Press, Tunbridge Wells, Kent ; Cambridge, Mass., 1988.

[45] EDENHOFER, O., PICHS-MADRUGA, R., AND SOKONA, Y. IPCC Special Report on Renewable Energy Sources and Climate Change Mitigation. Tech. rep., Intergovernmental Panel on Climate Change, 2011.

[46] EICHLER, C., AND SATTELMAYER, T. Experiments on flame flashback in a quasi-2d turbulent wall boundary layer for premixed methane-hydrogen-air mixtures. *Journal of Engineering for Gas Turbines and Power-Transactions of the ASME 133*, 1 (2011).

[47] ELSINGA, G. E., SCARANO, F., WIENEKE, B., AND VAN OUDHEUSDEN, B. W. Tomographic particle image velocimetry. *Experiments in Fluids 41*, 6 (2006), 933–947.

[48] ESCUDIER, M. P., BORNSTEIN, J., AND ZEHNDER, N. Observations and LDA Measurements of Confined Turbulent Vortex Flow. *Journal of Fluid Mechanics 98*, May (1980), 49–63.

[49] ETOH, T. G., POGGEMANN, D., KREIDER, G., MUTOH, H., THEUWISSEN, A. J. P., RUCKELSHAUSEN, A., KONDO, Y., MARUNO, H., TAKUBO, K., SOYA, H., TAKEHARA, K., OKINAKA, T., AND TAKANO, Y. An image sensor which captures 100 consecutive frames at 1,000,000 frames/s. *IEEE Transactions On Electron Devices 50*, 1 (2003), 144–151.

[50] FAJARDO, C., AND SICK, V. Flow field assessment in a fired spray-guided spark-ignition direct-injection engine based on uv particle image velocimetry with sub crank angle resolution. *Proceedings of the Combustion Institute 31* (2007), 3023–3031.

[51] FAJARDO, C., AND SICK, V. Development of a high-speed UV particle image velocimetry technique and application for measurements in internal combustion engines. *Experiments In Fluids 46*, 1 (2009), 43–53.

[52] FAJARDO, C. M., SMITH, J. D., AND SICK, V. Sustained simultaneous high-speed imaging of scalar and velocity fields using a single laser. *Applied Physics B 85*, 1 (2006), 25–30.

[53] FALER, J., AND S., L. Disrupted states of vortex flow and vortex breakdown. *Physics of Fluids 20* (1977), 1385–1400.

[54] FEFFERMAN, C. L. Existence and smoothness of the navier-stokes equation, 2000.

[55] FICK, W., GRIFFITHS, A. J., AND O'DOHERTY, T. Visualisation of the precessing vortex core in an unconfined swirling flow. *Optical Diagnostics in Engineering 2*, 1 (1997), 19–31.

[56] FINE, B. The flashback of laminar and turbulent burner flames at reduced pressure. *Combustion and Flame 2*, 3 (1958), 253–266.

[57] FINE, B. Effect of initial temperature on flash back of laminar and turbulent burner flames. *Industrial and Engineering Chemistry 51*, 4 (1959), 564–566.

[58] FISCHER, A., BAKE, F., HEINZE, J., DIERS, O., WILLERT, C., AND ROHLE, I. Off-line phase-averaged particle image velocimetry and OH chemiluminescence measurements using acoustic time series. *Measurement Science & Technology 20*, 7 (2009).

[59] FREITAG, M. *On the simulation of premixed combustion taking into account variable mixtures*. Dissertation, Technische Universität Darmstadt, 2007.

[60] FRITZ, J., KRÖNER, M., AND SATTELMAYER, T. Flashback in a swirl burner with cylindrical premixing zone. *Journal of Engineering for Gas Turbines and Power-Transactions of the ASME 126*, 2 (2004), 276–283.

[61] GANUZA, L. *Experimental investigation of flame flashback in a swirl burner by means of planar laser-induced fluorescence*. Master thesis, Technische Universität Darmstadt, 2008.

[62] GARLAND, N. L., AND CROSLEY, D. R. On the Collisional Quenching of Electronically Excited OH, NH, and CH in Flames. In *Twenty-first Symposium (International) on Combustion* (1986), p. 1693.

[63] GAYDON, A. G., AND WOLFHARD, H. G. *Flames, their structure, radiation, and temperature*, 4th ed. Chapman & Hall ; Wiley, London, New York, 1979.

[64] GOMEZ, A., AND ROSNER, D. E. Thermophoretic effects on particles in counterflow laminar diffusion flames. *Combustion Science and Technology 89*, 5-6 (1993), 335–362.

[65] GORDON, R. L., HEEGER, C., AND DREIZLER, A. High-speed mixture fraction imaging. *Applied Physics B 96*, 4 (2009), 745–748.

[66] GORYNTSEV, D., SADIKI, A., KLEIN, M., AND JANICKA, J. Large eddy simulation based analysis of the effects of cycle-to-cycle variations on air-fuel mixing in realistic DISI IC-engines. *Proceedings Of The Combustion Institute 32* (2009), 2759–2766.

[67] GOULDIN, F. C. An application of fractals to model premixed turbulent flames. *Combustion and Flame 68* (1987), 249–266.

[68] GREGOR, M. A., SEFFRIN, F., FUEST, F., GEYER, D., AND DREIZLER, A. Multi-scalar measurements in a premixed swirl burner using 1D Raman/Rayleigh scattering. *Proceedings of the Combustion Institute 32* (2009), 1739–1746.

[69] GROSS, H. *Handbook of optical systems*. Wiley-VCH, Weinheim, 2005.

[70] GUPTA, A. K., LILLEY, D. G., AND SYRED, N. *Swirl flows*. Energy and engineering science series. Abacus Press, Tunbridge Wells, Kent, 1984.

[71] HANSON, R. J., AND THOMAS, A. Flame development in swirling flows in closed vessels. *Combustion and Flame 55*, 3 (1984), 255–277.

[72] HANSON, R. K., SEITZMAN, J. M., AND PAUL, P. H. Planar laser-fluorescence imaging of combustion gases. *Applied Physics B 50*, 6 (1990), 441–454.

[73] HARRIS, M. E., GRUMER, J., VON ELBE, G., AND LEWIS, B. Burning velocities, quenching, and stability data on nonturbulent flames of methane and propane with oxygen and nitrogen. In *Symposium on Combustion and Flame, and Explosion Phenomena* (1949), vol. 3, pp. 80–89.

[74] HARRJE, D. T., AND REARDON, F. H. *Liquid propellant rocket combustion instability*. Scientific and Technical Information Office, National Aeronautics and Space Administration, 1972.

[75] HASEGAWA, T., MICHIKAMI, S., NOMURA, T., AND GOTOH, D. Flame development along a straight vortex. *Combustion and Flame 129*, 3 (2002), 294–304.

[76] HEEGER, C., BÖHM, B., AHMED, S. F., GORDON, R., BOXX, I., MEIER, W., DREIZLER, A., AND MASTORAKOS, E. Statistics of relative and absolute velocities of turbulent non-premixed edge flames following spark ignition. *Proceedings of the Combustion Institute 32* (2009), 2957–2964.

[77] HINSCH, K. D. Three-dimensional particle velocimetry. *Measurement Science & Technology 6* (1995), 742–753.

[78] HOFFMANN, S. *Untersuchungen des Stabilisierungsverhaltens und der Stabilitätsgrenzen von Drallflammen mit innerer Rückstromzone*. Dissertation, Universität Karlsruhe, 1994.

[79] HOLST, G. C., AND LOMHEIM, T. S. *CMOS/CCD sensors and camera systems*, 2nd ed. JCD Publishing ; SPIE, Winter Park, FL ; Bellingham, Wash., 2011.

[80] HULT, J., MEIER, U., MEIER, W., HARVEY, A., AND KAMINSKI, C. F. Experimental analysis of local flame extinction in a turbulent jet diffusion flame by high repetition 2-D laser techniques and multi-scalar measurements. *Proceedings of the Combustion Institute 30* (2005), 701–709.

[81] HULT, J., RICHTER, M., NYGREN, J., ALDEN, M., HULTQVIST, A., CHRISTENSEN, M., AND JOHANSSON, B. Application of a high-repetition-rate laser diagnostic system for single-cycle-resolved imaging in internal combustion engines. *Applied Optics 41*, 24 (2002), 5002–5014.

[82] HUSSAIN, A. K. M. F. Coherent structures and turbulence. *Journal of Fluid Mechanics 173* (1986), 303–356.

[83] INTERNATIONAL ENERGY AGENCY. Key world energy statistics 2011. Tech. rep., International Energy Agency (IEA), 2011.

[84] ISHIZUKA, S. Flame propagation along a vortex axis. *Progress in Energy and Combustion Science 28*, 6 (2002), 477–542.

[85] ISHIZUKA, S., HAMASAKI, T., KOUMURA, K., AND HASEGAWA, A. Measurements of flame speeds in combustible vortex rings: Validity of the back-pressure drive flame propagation mechanism. In *Symposium (International) on Combustion* (1998), vol. 27, pp. 727–734.

[86] JANICKA, J., AND SADIKI, A. Large eddy simulation of turbulent combustion systems. *Proceedings of the Combustion Institute 30* (2005), 537–547.

[87] JARVIS, S., AND HARGRAVE, G. K. A temporal PIV study of flame/obstacle generated vortex interactions within a semi-confined combustion chamber. *Measurement Science & Technology 17*, 1 (2006), 91–100.

[88] JIANG, N., LEMPERT, W. R., SWITZER, G. L., MEYER, T. R., AND GORD, J. R. Narrow-linewidth megahertz-repetition-rate optical parametric oscillator for high-speed flow and combustion diagnostics. *Applied Optics 47*, 1 (2008), 64–71.

[89] JIANG, N. B., WEBSTER, M. C., AND LEMPERT, W. R. Advances in generation of high-repetition-rate burst mode laser output. *Applied Optics 48*, 4 (2009), B23–B31.

[90] JOHNSTON, H. S. Atmospheric ozone. *Annual Review of Physical Chemistry 43* (1992), 1–32.

[91] JOOS, F. *Technische Verbrennung*. Springer, Berlin Heidelberg New York, 2006.

[92] KAMINSKI, C. F., HULT, J., AND ALDEN, M. High repetition rate planar laser induced fluorescence of OH in a turbulent non-premixed flame. *Applied Physics B 68*, 4 (1999), 757–760.

[93] KAMINSKI, C. F., HULT, J., ALDEN, M., LINDENMAIER, S., DREIZLER, A., MAAS, U., AND BAUM, M. Spark ignition of turbulent methane/air mixtures revealed by time-resolved planar laser-induced fluorescence and direct numerical simulations. *Proceedings of the Combustion Institute 28* (2000), 399–405.

[94] KAY, S. M., AND MARPLE, S. L. Spectrum analysis – a modern perspective. *Proceedings of the IEEE 69*, 11 (1981), 1380–1419.

[95] KEANE, R. D., AND ADRIAN, R. J. Theory of cross-correlation analysis of PIV images. *Applied Scientific Research 49*, 3 (1992), 191–215.

[96] KECK, O., MEIER, W., STRICKER, W., AND AIGNER, M. Establishment of a confined swirling natural gas/air flame as a standard flame: Temperature and species distributions from laser raman measurements. *Combustion Science and Technology 174*, 8 (2002), 117–151.

[97] KEIM, M. *Experimentelle Bestimmung der Rückschlaggrenzen eines vorgemischen Drallbrenners*. Studienarbeit, Technische Universität Darmstadt, 2007.

[98] KETELHEUN, A., OLBRICHT, C., HAHN, F., AND JANICKA, J. NO Prediction in Turbulent Flames Using LES/FGM With Additional Transport Equations. *Proceedings of the Combustion Institute 33*, 2 (2011), 2975–2982.

[99] KHITRIN, L., MOIN, P., SMIRNOV, D., AND SHEVCHUK, V. Peculiarities of laminar- and turbulent-flame flashbacks. In *Tenth Symposium (International) on Combustion* (1965), pp. 1285–1291.

[100] KÜHNE, J., KETELHEUN, A., AND JANICKA, J. Analysis of sub-grid PDF of a progress variable approach using a hybrid LES/TPDF method. *Proceedings of the Combustion Institute 33*, 1 (2011), 1411–1418.

[101] KIESEWETTER, F., KONLE, M., AND SATTELMAYER, T. Analysis of combustion induced vortex breakdown driven flame flashback in a premix burner with cylindrical mixing zone. *Journal of Engineering for Gas Turbines and Power-Transactions of the ASME 129*, 4 (2007), 929–936.

[102] KITTLER, C., AND DREIZLER, A. Cinematographic imaging of hydroxyl radicals in turbulent flames by planar laser-induced fluorescence up to 5 khz repetition rate. *Applied Physics B 89*, 2-3 (2007), 163–166.

[103] KLEWER, C. *Numerische Berechnung von Verbrennungslärm und thermoakustischen Instabilitäten*. Dissertation, Technische Universität Darmstadt, 2011.

[104] KÜNNE, G., KETELHEUN, A., AND JANICKA, J. LES modeling of premixed combustion using a thickened flame approach coupled with FGM tabulated chemistry. *Combustion and Flame 158*, 9 (2011), 1750–1767.

[105] KOHSE-HÖINGHAUS, K., AND JEFFRIES, J. *Applied Combustion Diagnostics*. Taylor & Francis, New York, 2002.

[106] KOHSEHOINGHAUS, K. Laser techniques for the quantitative detection of reactive intermediates in combustion systems. *Progress in Energy and Combustion Science 20*, 3 (1994), 203–279.

[107] KOJIMA, J., IKEDA, Y., AND NAKAJIMA, T. Basic aspects of OH(A), CH(A), and C_2(d) chemiluminescence in the reaction zone of laminar methane-air premixed flames. *Combustion and Flame 140*, 1-2 (2005), 34–45.

[108] KOLMOGOROV, A. The local structure of turbulence in incompressible viscous fluid for very large reynolds numbers. *Dokl. Akad. Nauk. SSSR 30* (1941), 301–305.

[109] KONLE, M. *Verbrennungsinduziertes Wirbelaufplatzen in moderat turbulenten Drallströmungen*. Dissertation, Technische Universität München, 2010.

[110] KONLE, M., KIESEWETTER, F., AND SATTELMAYER, T. Simultaneous high repetition rate PIV-LIF-measurements of CIVB driven flashback. *Experiments In Fluids 44*, 4 (2008), 529–538.

[111] KONLE, M., AND SATTELMAYER, T. Interaction of heat release and vortex breakdown during flame flashback driven by combustion induced vortex breakdown. *Experiments In Fluids 47*, 4-5 (2009), 627–635.

[112] KONLE, M., AND SATTELMAYER, T. Time scale model for the prediction of the onset of flame flashback driven by combustion induced vortex breakdown. *Journal of Engineering for Gas Turbines and Power-Transactions of the ASME 132*, 4 (2010).

[113] KRÖNER, M., SATTELMAYER, T., FRITZ, J., KIESEWETTER, F., AND HIRSCH, C. Flame propagation in swirling flows – effect of local extinction on the combustion induced vortex breakdown. *Combustion Science and Technology 179*, 7 (2007), 1385–1416.

[114] LAUER, M., AND SATTELMAYER, T. On the adequacy of chemiluminescence as a measure for heat release in turbulent flames with mixture gradients. *Journal of Engineering for Gas Turbines and Power-Transactions of the ASME 132*, 6 (2010).

[115] LAVISION GMBH. Product manual for DaVis 7.2, 2007.

[116] LAWSON, N. J., AND WU, J. Three-dimensional particle image velocimetry: Error analysis of stereoscopic techniques. *Measurement Science & Technology 8*, 8 (1997), 894–900.

[117] LEE, D. H., AND LIEUWEN, T. C. Acoustic near-field characteristics of a conical, premixed flame. *Journal of the Acoustical Society of America 113*, 1 (2003), 167–177.

[118] LEE, J. G., AND SANTAVICCA, D. A. Experimental diagnostics for the study of combustion instabilities in lean premixed combustors. *Journal of Propulsion and Power 19*, 5 (2003), 735–750.

[119] LEFEBVRE, A. H. *Atomization and sprays*. Combustion,. Hemisphere Pub. Corp., New York, 1989.

[120] LEMPERT, W. R., WU, P. F., MILES, R. B., ZHANG, B., AND LOWRANCE, J. L. Pulse-burst laser system for high-speed flow diagnostics. In *34 th AIAA Aerospace Science Meeting* (1996).

[121] LEUCKEL, W. Swirl intensities, swirl types and energy losses of different swirl generating devices. Tech. rep., IFRF Doc Nr. G 02/a/16, Ijmuiden, 1967.

[122] LEUCKEL, W., AND FRICKER, N. Characteristics of Swirl-Stabilized Natural-Gas Flames, Part 1: Different Flame Types and Their Relation to Flow and Mixing Patterns. *Journal of the Institute of Fuel 49*, 399 (1976), 103–112.

[123] LEWIS, B., AND VON ELBE, G. *Combustion, flames, and explosions of gases*, 3rd ed. Academic Press, Orlando, 1987.

[124] LI, D. J., MA, Z., HAAS, R., SCHELL, A., SIMON, J., DIART, R., SHI, P., HU, P. X., LOOSEN, P., AND DU, K. M. Diode-pumped efficient slab laser with two Nd:YLF crystals and second-harmonic generation by slab LBO. *Optics Letters 32*, 10 (2007), 1272–1274.

[125] LIEUWEN, T., AND ZINN, B. T. The role of equivalence ratio oscillations in driving combustion instabilities in low NOx gas turbines. *Proceedings of the Combustion Insititute 27* (1998), 1809–1816.

[126] LIEUWEN, T., AND ZINN, B. T. On the experimental determination of combustion process driving in an unstable combustor. *Combustion Science and Technology 157* (2000), 111–127.

[127] LIZORKIN, P. I. *Fourier transform*. Encyclopaedia of Mathematics. Springer, Berlin, 2002.

[128] LUCCA-NEGRO, O., AND O'DOHERTY, T. Vortex breakdown: a review. *Prog. Energy Combust. Sci. 27* (2000), 431–481.

[129] LUQUE, J., AND CROSLEY, D. R. LIFBASE: Database and spectral simulation program (Version 1.5). Tech. rep., 1999.

[130] LYON, R. K., AND COLE, J. A. A reexamination of the RapreNOx process. *Combustion and Flame 82*, 3-4 (1990), 435–443.

[131] MALTE, P. C., AND PRATT, D. T. Role of energy-releasing kinetics in NOx formation: fuel-lean, jet-stirred co-air combustion. *Combustion Science and Technology 9*, 5-6 (1974), 221–231.

[132] MARSHALL, G. F. *Handbook of optical and laser scanning*. Optical Engineering. Marcel Dekker, New York, 2004.

[133] MCCORMACK, P. D. Combustible vortex rings. *Proceedings of the Royal Irish Academy Section a-Mathematical Astronomical and Physical Sciences 71*, 6 (1971), 73–83.

[134] MERCK KGAA. Chemicals database, <http://www.merck-chemicals.de>, 2011.

[135] METZ, B. AND INTERGOVERNMENTAL PANEL ON CLIMATE CHANGE: WORKING GROUP III. *Climate change 2007: mitigation of climate change: contribution of Working Group III to the Fourth assessment report of the Intergovernmental Panel on Climate Change*. Cambridge University Press, Cambridge ; New York, 2007.

[136] MEYER, T. R., ROY, S., ANDERSON, T. N., MILLER, J. D., KATTA, V. R., LUCHT, R. P., AND GORD, J. R. Measurements of OH mole fraction and temperature up to 20 khz by using a diode-laser-based UV absorption sensor. *Applied Optics 44*, 31 (2005), 6729–6740.

[137] MIDGLEY, K., SPENCER, A., AND MCGUIRK, J. J. Unsteady flow structures in radial swirler fed fuel injectors. *ASME Conference Proceedings 2004*, 41669 (2004), 375–384.

[138] MILLER, J. A., AND BOWMAN, C. T. Mechanism and modeling of nitrogen chemistry in combustion. *Progress in Energy and Combustion Science 15*, 4 (1989), 287–338.

[139] MILLER, J. D., SLIPCHENKO, M., MEYER, T. R., JIANG, N. B., LEMPERT, W. R., AND GORD, J. R. Ultrahigh-frame-rate OH fluorescence imaging in turbulent flames using a burst-mode optical parametric oscillator. *Optics Letters 34*, 9 (2009), 1309–1311.

[140] MÜLLER, S. H. R., BÖHM, B., GLEISSNER, M., GRZESZIK, R., ARNDT, S., AND DREIZLER, A. Flow field measurements in an optically accessible, direct-injection spray-guided internal combustion engine using high-speed PIV. *Experiments In Fluids 48*, 2 (2010), 281–290.

[141] NAUERT, A., PETERSSON, P., LINNE, M., AND DREIZLER, A. Experimental analysis of flash back in lean premixed swirling flames: Conditions close to flash back. *Experiments in Fluids accepted* (2007).

[142] NEWAC. NEWAC Technologies – highly innovative technologies for future aero engines. Tech. rep., New Aero Engine Core Concepts (NEWAC), 2009.

[143] NG, W. B., CLOUGH, E., SYED, K. J., AND ZHANG, Y. The combined investigation of the flame dynamics of an industrial gas turbine combustor using high-speed imaging and an optically integrated data collection method. *Measurement Science & Technology 15*, 11 (2004), 2303–2309.

[144] PAA, W., MULLER, D., STAFAST, H., AND TRIEBEL, W. Flame turbulences recorded at 1 khz using planar laser induced fluorescence upon hot band excitation of OH radicals. *Applied Physics B 86*, 1 (2007), 1–5.

[145] PARKER, J. R., AND ATTIA, E. N. Object reconstruction from slices for vision. In *Computer Graphics International, 1999. Proceedings* (1999), pp. 58–64.

[146] PASCHOTTA, R. *Encyclopedia of laser physics and technology*. Wiley-VCH, Weinheim, 2008.

[147] PATANKAR, S. V. *Numerical heat transfer and fluid flow*. Series in computational methods in mechanics and thermal sciences. Hemisphere Pub. Corp.; McGraw-Hill, Washington; New York, 1980.

[148] PAUL, P. H., DURANT, J. L., GRAY, J. A., AND FURLANETTO, M. R. Collisional electronic quenching of OH $A^2\Sigma$ $(v' = 0)$ measured at high temperature in a Shock-Tube. *Journal of Chemical Physics 102*, 21 (1995), 8378–8384.

[149] PETERS, N. Laminar flamlet concepts in turbulent combustion. *Proceedings of the Combustion Institute 21* (1986), 1231–1250.

[150] PETERS, N. The turbulent burning velocity for large-scale and small-scale turbulence. *Journal of Fluid Mechanics 384* (1999), 107–132.

[151] PETERS, N. *Turbulent combustion*. Cambridge University Press, Cambridge, 2000.

[152] PETERSON, B., AND SICK, V. Simultaneous flow field and fuel concentration imaging at 4.8 khz in an operating engine. *Applied Physics B 97*, 4 (2009), 887–895.

[153] POINSOT, T., CANDEL, S., AND TROUVE, A. Applications of direct numerical simulation to premixed turbulent combustion. *Progress in Energy and Combustion Science 21*, 6 (1995), 531–576.

[154] POINSOT, T., AND VEYNANTE, D. *Theoretical and numerical combustion*. Edwards, 2005.

[155] POPE, S. B. *Turbulent Flows*. Cambridge University Press, Cambridge, 2000.

[156] POPE, S. B. Ten questions concerning the large-eddy simulation of turbulent flows. *New Journal of Physics 6* (2004), 35.

[157] RAFFEL, M., WILLERT, C. E., T., W. S., AND KOMPENHANS, J. *Particle image velocimetry: a practical guide*, 2nd ed. Springer, Heidelberg ; New York, 2007.

[158] RAY, S. F. *Applied photographic optics: lenses and optical systems for photography, film, video, and electronic imaging*, 2nd ed. Focal Press, Oxford; Boston, 1994.

[159] RAYLEIGH, J. W. S. *The theory of sound*. Macmillan and co., London,, 1878.

[160] REBOLLO, M. R. *Analytical and esperimental investigation of a turbulent mixing layer of different gases in a pressure gradient*. Phd thesis, California Insitute of Technology, 1973.

[161] RENFRO, M. W., GUTTENFELDER, W. A., KING, G. B., AND LAURENDEAU, N. M. Scalar time-series measurements in turbulent $CH_4/H_2/N_2$ nonpremixed flames: OH. *Combustion and Flame 123*, 3 (2000), 389–401.

[162] RENFRO, M. W., KLASSEN, M. S., KING, G. B., AND LAURENDEAU, N. M. Time-series measurements of CH concentration in turbulent CH_4/air flames by use of picosecond time-resolved laser-induced fluorescence. *Optics Letters 22*, 3 (1997), 175–177.

[163] REPP, S., SADIKI, A., SCHNEIDER, C., HINZ, A., LANDENFELD, T., AND JANICKA, J. Prediction of swirling confined diffusion flame with a Monte Carlo and a presumed-PDF-model. *International Journal of Heat and Mass Transfer 45*, 6 (2002), 1271–1285.

[164] REYNOLDS, O. An experimental investigation of the circumstances which determine whether the motion of water shall be direct or sinuous, and of the law of resistance in parallel channels. *Philosophical Transactions of the Royal Society 174*, 0 (1883), 935–982.

[165] RICHARDSON, L. F. *Weather prediction by numerical process*. University Press, Cambridge, 1922.

[166] ROY, S., KULATILAKA, W. D., RICHARDSON, D. R., LUCHT, R. P., AND GORD, J. R. Gas-phase single-shot thermometry at 1 khz using fs-CARS spectroscopy. *Optics Letters 34*, 24 (2009), 3857–3859.

[167] RUTAR, T., AND MALTE, P. C. NOx formation in high-pressure jet-stirred reactors with significance to lean-premixed combustion turbines. *Journal of Engineering for Gas Turbines and Power-Transactions of the ASME 124*, 4 (2002), 776–783.

[168] SABROSKE, K. R., HOYING, D. A., AND RABE, D. C. Laskin nozzle particle generator, U.S. Patent 5,498,374, 1996.

[169] SACKMANN, D. *Design and setup of a high-speed scan mirror for three-dimensional recordings of flow fields*. Bachelor thesis, Technische Universität Darmstadt, 2010.

[170] SAGAUT, P. *Large eddy simulation for incompressible flows: an introduction*. Springer, 2006.

[171] SAKAI, Y., AND ISHIZUKA, S. The phenomena of flame propagation in a rotating tube. In *Proceedings of the Combustion Institute* (1996), vol. 26, pp. 847–853.

[172] SCHIESSL, R., PIXNER, P., DREIZLER, A., AND MAAS, U. Formaldehyde formation in the endgas of Otto engines: Numerical simulations and quantitative concentration measurements. *Combustion Science and Technology 149*, 1-6 (1999), 339–360.

[173] SCHNEIDER, C. *Über die Charakterisierung von Turbulenzstrukturen in verdrallten Strömungen*. PhD thesis, Technische Universität Darmstadt, 2003.

[174] SCHNEIDER, C., DREIZLER, A., AND JANICKA, J. Fluid dynamical analysis of atmospheric reacting and isothermal swirling flows. *Flow Turbulence and Combustion 74* (2005), 103–127.

[175] SCHNEIDER, C., DREIZLER, A., JANICKA, J., AND HASSEL, E. P. Flow field measurements of stable and locally extinguishing hydrocarbon-fuelled jet flames. *Combustion and Flame 135*, 1-2 (2003), 185–190.

[176] SCHNEIDER, C., REPP, S., SADIKI, A., DREIZLER, A., AND JANICKA, J. The effect of swirling number variation on turbulent transport and mixing processes in swirling recirculating flows: Experimental and numerical investigations. In *2nd International Symposium on Turbulent Shear Flow Phenomena* (2001), vol. 3.

[177] SCHULZ, C., AND SICK, V. Tracer-LIF diagnostics: quantitative measurement of fuel concentration, temperature and fuel/air ratio in practical combustion systems. *Progress in Energy and Combustion Science 31*, 1 (2005), 75–121.

[178] SCHWARZWALD, R., MONKHOUSE, P., AND WOLFRUM, J. Fluorescence lifetimes for nitric-oxide in atmospheric-pressure flames using picosecond excitation. *Chemical Physics Letters 158*, 1-2 (1989), 60–64.

[179] SEFFRIN, F., FUEST, F., GEYER, D., AND DREIZLER, A. Flow field studies of a new series of turbulent premixed stratified flames. *Combustion and Flame 157*, 2 (2010), 384–396.

[180] SEINFELD, J. H., AND PANDIS, S. N. *Atmospheric chemistry and physics: from air pollution to climate change*, 2nd ed. J. Wiley, Hoboken, N.J., 2006.

[181] SHIH, W., LEE, J., AND D., S. Stability and emissions characteristics of a lean premixed gas turbine combustor. In *Proceedings of the Combustion Institute* (1996), vol. 26, pp. 2271–2278.

[182] SICK, V., DRAKE, M. C., AND FANSLER, T. D. High-speed imaging for direct-injection gasoline engine research and development. *Experiments In Fluids 49*, 4 (2010), 937–947.

[183] SILBERSTEIN, L. Über die Entstehung von Wirbelbewegungen in einer reibungslosen Flüssigkeit. *Bull. Int. l'Acad. Sci. Cracovie, Compt. Rend. Séances Année* (1898), 280–290.

[184] SMITH, G., GOLDEN, D. M., FRENKLACH, M., MORIARTY, N. W., EITENEER, B., GOLDENBERG, M., BOWMAN, C. T., HANSON, R. K., SONG, S., GARDINER, W. C., LISSIANSKI, V. V., AND QIN, Z. Gas Research Institute GRI Mech 3.0, <http://www.me.berkeley.edu/gri_mech/>, 2011.

[185] SMITH, J. D., AND SICK, V. Crank-angle resolved imaging of biacetyl laser-induced fluorescence in an optical internal combustion engine. *Applied Physics B 81*, 5 (2005), 579–584.

[186] SMITH, J. D., AND SICK, V. Quantitative, dynamic fuel distribution measurements in combustion-related devices using laser-induced fluorescence imaging of biacetyl in iso-octane. *Proceedings of the Combustion Institute 31* (2007), 747–755.

[187] SMYTH, K. C., AND CROSLEY, D. R. *Detection of minor species with laser techniques*. Taylor & Francis, New York, 2002, ch. Two.

[188] SOLOFF, S. M., ADRIAN, R. J., AND LIU, Z. C. Distortion compensation for generalized stereoscopic particle image velocimetry. *Measurement Science & Technology 8*, 12 (1997), 1441–1454.

[189] SOMERS, B. *The simulation of flat flames with detailed and reduced chemical models*. PhD thesis, Technische Universiteit Eindhoven, 1994.

[190] SPURK, J. H., AND NURI, A. *Fluid Mechanics*, 2nd. ed. ed. Springer, Berlin, 2008.

[191] STANISLAS, M., OKAMOTO, K., AND KAHLER, C. Main results of the first international PIV challenge. *Measurement Science & Technology 14*, 10 (2003), 63–89.

[192] STANISLAS, M., OKAMOTO, K., KAHLER, C. J., AND WESTERWEEL, J. Main results of the second international PIV challenge. *Experiments In Fluids 39*, 2 (2005), 170–191.

[193] STANISLAS, M., OKAMOTO, K., KAHLER, C. J., WESTERWEEL, J., AND SCARANO, F. Main results of the third international piv challenge. *Experiments In Fluids 45*, 1 (2008), 27–71.

[194] STEINBERG, A. M., DRISCOLL, J. F., AND CECCIO, S. L. Measurements of turbulent premixed flame dynamics using cinema stereoscopic PIV. *Experiments In Fluids 44*, 6 (2008), 985–999.

[195] SUNG, C. J., LAW, C. K., AND AXELBAUM, R. L. Thermophoretic effects on seeding particles in ldv measurements of flames. *Combustion Science and Technology 99*, 1-3 (1994), 119–132.

[196] SUTTON, J. Private communication, 2011.

[197] SVEEN, J. K. An introduction to MatPIV v.1.6.1, <http://www.math.uio.no/~jks/matpiv>, 2004.

[198] SWAN, W. On the prismatic spectra of the flames of compounds of carbon and hydrogen. *Transactions of the Royal Society of Edinburgh 21* (1857), 411–430.

[199] SYRED, N. A review of oscillation mechanisms and the role of the precessing vortex core (PVC) in swirl combustion systems. *Progress in Energy and Combustion Science 32*, 2 (2006), 93–161.

[200] SYRED, N., AND M., B. J. Damping of precessing vortex cores by combustion in swirl generators. *Acta Astronautica 17*, 4-5 (1972), 783–&.

[201] THUROW, B. S., LYNCH, K., WILLIAMS, S. T., AND MELNICK, M. B. 3d flow imaging using a mhz-rate pulse burst laser system. In *15th Int Symp on Applications of Laser Techniques to Fluid Mechanics* (2010).

[202] TOWERS, D. P., AND TOWERS, C. E. Cyclic variability measurements of in-cylinder engine flows using high-speed particle image velocimetry. *Measurement Science & Technology 15*, 9 (2004), 1917–1925.

[203] TROPEA, C., YARIN, A. L., AND FOSS, J. F. *Springer handbook of experimental fluid mechanics*. Springer, Berlin, 2007.

[204] TURNS, S. R. *An introduction to combustion: concepts and applications*, 2nd ed. McGraw-Hill series in mechanical engineering. WCB/McGraw-Hill, Boston, 2000.

[205] UMEMURA, A., AND TOMITA, K. Rapid flame propagation in a vortex tube in perspective of vortex breakdown phenomena. *Combustion and Flame 125*, 1-2 (2001), 820–838.

[206] UPATNIEKS, A., DRISCOLL, J. F., AND CECCIO, S. L. Cinema particle imaging velocimetry time history of the propagation velocity of the base of a lifted turbulent jet flame. *Proceedings of the Combustion Institute 29* (2002), 1897–1903.

[207] UPATNIEKS, A., DRISCOLL, J. F., RASMUSSEN, C. C., AND CECCIO, S. L. Liftoff of turbulent jet flames – assessment of edge flame and other concepts using cinema-piv. *Combustion and Flame 138*, 3 (2004), 259–272.

[208] VOISINE, M., THOMAS, L., BOREE, J., AND REY, P. Spatio-temporal structure and cycle-to-cycle variations of an in-cylinder tumbling flow. *Experiments in Fluids 50*, 5 (2011), 1393–1407.

[209] WANG, G. H., CLEMENS, N. T., AND VARGHESE, P. L. High-repetition rate measurements of temperature and thermal dissipation in a non-premixed turbulent jet flame. *Proceedings of the Combustion Institute 30* (2005), 691–699.

[210] WANG, G. H., CLEMENS, N. T., AND VARGHESE, P. L. Two-point, high-repetition-rate Rayleigh thermometry in flames: Techniques to correct for apparent dissipation induced by noise. *Applied Optics 44*, 31 (2005), 6741–6751.

[211] WARNATZ, J., MAAS, U., AND DIBBLE, R. *Combustion*. Springer Verlag, Berlin, 1999.

[212] WEBER, V., BRÜBACH, J., GORDON, R. L., AND DREIZLER, A. Pixel-based characterization of CMOS high-speed camera systems. *Applied Physics B 103*, 2 (2011), 421–433.

[213] WEINKAUFF, J. *Design, Implementation and Test of a High Speed Laser Scanning System*. Master thesis, Technische Universität Darmstadt, 2011.

[214] WHO WORKING GROUP. Health aspects of air pollution with particulate matter, ozone and nitrogen dioxide. Tech. rep., World Health Organization (WHO), 2003.

[215] WIENEKE, B. Stereo-PIV using self-calibration on particle images. *Experiments in Fluids 39*, 2 (2005), 267–280.

[216] WILLERT, C. Stereoscopic digital particle image velocimetry for application in wind tunnel flows. *Measurement Science & Technology 8*, 12 (1997), 1465–1479.

[217] WILLERT, C. E. Assessment of camera models for use in planar velocimetry calibration. *Experiments in Fluids 41*, 1 (2006), 135–143.

[218] WILLIAMS, F. A. *Turbulent Combustion*. Society for Industrial and Applied Mathematics, 1985, ch. 3.

[219] WILLIAMS, L. R., AND CROSLEY, D. R. Collisional vibrational energy transfer of OH ($A^2\Sigma^+$ ($v' = 1$)). *Journal of Chemical Physics 104*, 17 (1996), 6507–6514.

[220] WILLIAMS, T. C., HARGRAVE, G. K., AND HALLIWELL, N. A. The development of high-speed particle image velocimetry (20 khz) for large eddy simulation code refinement in bluff body flows. *Experiments in Fluids 35*, 1 (2003), 85–91.

[221] WOLFRUM, J. Formation of nitrogen oxides on combustion. *Chemie Ingenieur Technik 44*, 10 (1972), 656–&.

[222] WÄSLE, J., WINKLER, A., AND SATTELMAYER, T. Spatial coherence of the heat release fluctuations in turbulent jet and swirl flames. *Flow Turbulence and Combustion 75*, 1-4 (2005), 29–50.

[223] WU, P. F., LEMPERT, W. R., AND MILES, R. B. Megahertz pulse-burst laser and visualization of shock-wave/boundary-layer interaction. *AIAA Journal 38*, 4 (2000), 672–679.

[224] XIONG, Y., ROBERTS, W. L., DRAKE, M. C., AND FANSLER, T. D. Investigation of pre-mixed flame-kernel/vortex interactions via high-speed imaging. *Combustion and Flame 126*, 4 (2001), 1827–1844.

[225] ZHANG, J. Y., VENKATESAN, K. K., KING, G. B., LAURENDEAU, N. M., AND RENFRO, N. W. Two-point time-series measurements of minor-species concentrations in a turbulent nonpremixed flame. *Optics Letters 30*, 23 (2005), 3144–3146.